CHIROPTICAL SPECTROSCOPIC STRUCTURAL DETERMINATION OF ORGANIC, INORGANIC AND BIOMOLECULES

By

Ana Grozdan Petrović

Dissertation

Submitted to the Faculty of the

Graduate School of Vanderbilt University

in partial fulfillment of the requirements

for the degree of

DOCTOR OF PHILOSOPHY

in

Chemistry

December, 2007

Nashville, Tennessee

Approved:

Professor Prasad L. Polavarapu

Professor Eva Harth

Professor Terry Lybrand

Professor Carmelo Rizzo

Professor Michael Stone

To My Loving Parents,
Gordana and Grozdan Petrović

ACKNOWLEDGEMENTS

I would first like to express my gratitude to my research advisor Professor Prasad Polavarapu, who introduced me to the world of research by giving me the opportunity to work in his laboratory even as an undergraduate summer student. Throughout my graduate study at Vanderbilt University, he has provided me with invaluable guidance. I learned much from his helpful suggestions and advices. I thank him for his support and for helping future opportunities open-up for me. I would also like to acknowledge my Ph.D. committee: Dr. Eva Harth, Dr. Terry Lybrand, Dr. Carmelo Rizzo, and Dr. Michael Stone. I thank each one of them for their encouragement, support, and advices that have helped me grow as a scientist.

I would also like to thank to the members of Dr. Polavarapu's research group: Dr. Ganesh Shanmugam, Dr. Jiangtao He, and Dr. Peng Zhang for many valuable and helpful discussions about various aspects of research.

I appreciate the dedication of our research collaborators, without whom some of this research would not be possible. They are Dr. Jozef Drabowicz from the Polish Academy of Sciences (Chapters II, V and VI), Dr. Daniel A. Armstrong from Iowa State University (Chapters III and V), Dr. Albert F. Cotton from Texas A&M University (Chapter III), and Dr. Padmanabhan Balaram from the Indian Institute of Science (Chapter X).

Funding from the NSF (CHE0092922) has supported this research and is gratefully acknowledged. Computational work was partially supported by the

National Center for Supercomputing Applications under TG-CHE060063T and utilized the NCSA IBM P690 system. Teaching Assistantship from Vanderbilt University is greatly appreciated.

I would like to express gratitude to my Whitman College professors Dr. Allison Calhoun and Dr. Frank Dunnivant who have inspired me to become a Chemist. Their friendly and educational mentorship will always be an example for me as an educator and a scientist.

Besides gaining knowledge and research experience during my graduate study, I am happy to say that I have developed several lifetime friendships. Ioanna Ntai has been the closest friend of mine and has offered tremendous help and support. I could always count on Ioanna for her valuable input both inside and outside of the laboratory. I have been very lucky to have her as a friend and will miss her friendship when I move. My friends Lyrad Smallwood and Rachel Snyder have also made my life in Nashville pleasant and colorful and I am very grateful to have them as friends. Heather Day has been a wonderful friend as well. She has unselfishly provided suggestions for improving my writing style.

I would also like to thank and acknowledge Daniel and Maria Mallory, my American host family, who have welcomed me into their home and helped me immensely in realizing my “American dream”.

Finally, my family in Serbia and Yugoslavia has been the greatest support to me…

My uncles ujka-Stole, cika-Mircek, ujka-Branko; aunts ujna-Jasmina, strina-Mirjana, ujna-Jelka; cousins Margarita, Maja, Rince, Misa, Nanad; great-

aunts nana-Ankica, nana-Silvica and great-uncle deda-Vladica have given me support not only in these past four years, but also all the ones that came before. I like to acknowledge all of them.

My brother Vojislav has given me a tremendous support and love. He has the amazing ability to lift me up when I am feeling down. His jokes and laughter gave me strength.

I like to express gratitude to my grandma Dragica Petrović “Omama” and grandma Margarita Aleksievska “Nana” whose incredible love during childhood and through the years encourages and comforts me. They are both an inspiration to me in all areas of my life.

Most especially I would like to thank my parents, mom Gordana and dad Grozdan…no words can possibly express my gratitude for everything they have given me. They provided me the kind of unconditional love and support that makes all things possible. All my accomplishments are thanks to two of them.

TABLE OF CONTENTS

LIST OF TABLES

LIST OF FIGURES

CHAPTER I

CHIROPTICAL SPECTROSCOPIC METHODS

Introduction

The field of research associated with investigation of chirality or optical activity has undergone a remarkable development[1-4] over the last three decades, maturing to an area of major scientific and economic interest. This progress has been inevitable considering that an overwhelming majority of molecules as well as molecular and biological systems are chiral. Chirality has strong repercussions[3] on development of drugs, agrochemicals, food additives, fragrances, new materials and catalysts. Understanding the activity of chiral systems and identifying the utility of chiral compounds necessitate chiral separations and structural investigations. A dominant investigation-effort pertains to developing and implementing methods for reliably assigning stereochemistry, which includes determination of the absolute configuration and conformation(s) of chiral molecules.

The presence of chirality in a molecule is experimentally identified by its ability to rotate a plane polarized light. The origin of chirality on a molecular level can be associated with the presence of: a) one or more stereogenic centers (center chirality); b) twisting-arrangement of certain moieties (helical chirality) and/or c) symmetry associated with C_n, D_n, T, O or I point-group[5,6] (point-group chirality). Determination of the absolute configuration of a chiral molecule involves specification of the spatial arrangement of the atoms or functional

groups that distinguishes it from its mirror image. For example, the absolute configuration of molecules which exhibit conventional center chirality is specified by assigning enantiomers to either (*R*)- or (*S*)-configuration. Knowing absolute configuration means knowing if the (+)-enantiomer at 589nm is (*R*)- or (*S*)-configured. If the $(+)_{589}$-enantiomer is (*R*)-configured, the $(-)_{589}$-enantiomer must be (*S*)-configured. For large biopolymers, such as homopolynucleotides, the absolute configuration is determined by the sense of the helical-twist within the polymer-backbone (left-handed vs. right-handed helix). The determination of conformation, on the other hand, encompasses knowledge of all dihedral angles, angles and bond lengths within the molecule in addition to the identification of all intra- or inter-molecular hydrogen bonding interactions under the conditions of interest.

The interest in stereochemistry of chiral compounds and its consequences is not a new phenomenon. The significance of being able to establish the stereochemistry is manifested through the recognition that different diastereomers and enantiomers of the same chiral molecule can have vastly different chemical activity and reactivity as well as biological and physiological effects. Numerous examples portraying the importance of a reliable stereochemical assignment can be found in current pharmaceutical development processes. A neglect to make a stereochemical assignment or an incorrect assignment can lead to tragic consequences[7,8] as in the case of S-(–)-thalidomide. This drug was administered for the treatment of morning sickness in the late 1950s without awareness of its stereochemistry. The (S)-configured

thalidomide resulted in numerous cases of birth defects, while the (R)-configuration was determined to have no apparent side-effects.

Many methods have been applied over the years to address the need for reliable stereochemical assignment. One of the oldest methods is asymmetric or stereoselective synthesis[2] which involves a series of well-understood synthetic steps to obtain a chiral molecule of known absolute stereochemistry. However, it is often difficult to achieve such synthesis with a high enantiomeric purity. X-ray crystallography provides definitive stereochemical assignment, but is limited in scope due to the requirement to grow quality crystals of a pure enantiomer. NMR and MS techniques[9] can be sensitive to chirality, but only by using supplementary chiral reagents that form diastereomeric complexes with the chiral molecules of interest. Due to the advances in both instrumentation and quantum mechanical methods, chiroptical spectroscopic methods have emerged as an important tool that provides both reliability and ease in establishing stereochemical assignments. Chiroptical methods are spectroscopic methods that probe different aspects of optical activity. The three complementary, yet non-redundant[10] chiroptical techniques used in investigations comprising this dissertation are: Vibrational Circular Dichroism (VCD), Electronic Circular Dichroism (ECD), and Optical Rotatory Dispersion (ORD).

This chapter includes a description of the fundamentals for the three chiroptical techniques and the methodology used in applying them for stereochemical elucidation. The chapters that follow pertain to either

implementation of these methods or an effort associated with improving their implementation.

The Origin of a Chiroptical Response

The interaction of electromagnetic radiation with a chiral sample gives rise to a chiroptical response. Different types of chiroptical methods probe optical activity with a different type of radiation and its polarization. There are two main types of polarizations: linear and circular. The electric-field vectors for linear (E) and circular (E_L and E_R) polarizations are given in Figure 1-1. For a linearly polarized light, the electric field vector (E) remains in the same plane of polarization while its magnitude changes in a sinusoidal manner. In the case of circularly polarized light, the magnitude of electric field vector is constant, but its direction changes. The electric field vector of the left circularly polarized beam (E_L) rotates counterclockwise, while of the right circularly polarized beam (E_R) rotates clockwise. One way of viewing[11] linearly polarized light is as a superposition of left and right circularly polarized components with equal amplitudes and phases with equal magnitude, but opposite sign. The two vectors E_L and E_R inscribe equal angles ($\omega = -\omega'$) in time and their resultant vector E translates the motion of the plane-polarized wave along x-axis (Figure 1-1A).

Upon passing through an optically active sample, the circularly polarized components are changed in two aspects. Firstly, differing indices of refraction of left and right circular polarizations (birefringence phenomenon)[11] result in differential velocities of propagation through an optically active medium. The

outcome of the differential velocity of E_R and E_L is that the phase of their rotation is no longer equivalent ($\omega \neq -\omega'$). Although resultant vector E is still linearly polarized, its plane of polarization is rotated by an angle α (Figure 1-1B). This angle α is an angle of an observed optical rotation and the overall phenomenon represents the basis for an ORD method. Secondly, molar absorptivities of right and left circular polarizations are non-equivalent when passing through a chiral sample. The two circular polarizations are absorbed by different extents and while E_R and E_L components are still circularly polarized, their magnitudes are no longer equal. Concomitantly, the polarization of the resultant vector E is no longer linear, yet elliptical (Figure 1-1C). The degree of ellipticity is an indirect measure of circular dichroism (CD). The phenomenon of differential absorption of left vs. right circular polarizations is the basis for VCD and ECD methods.

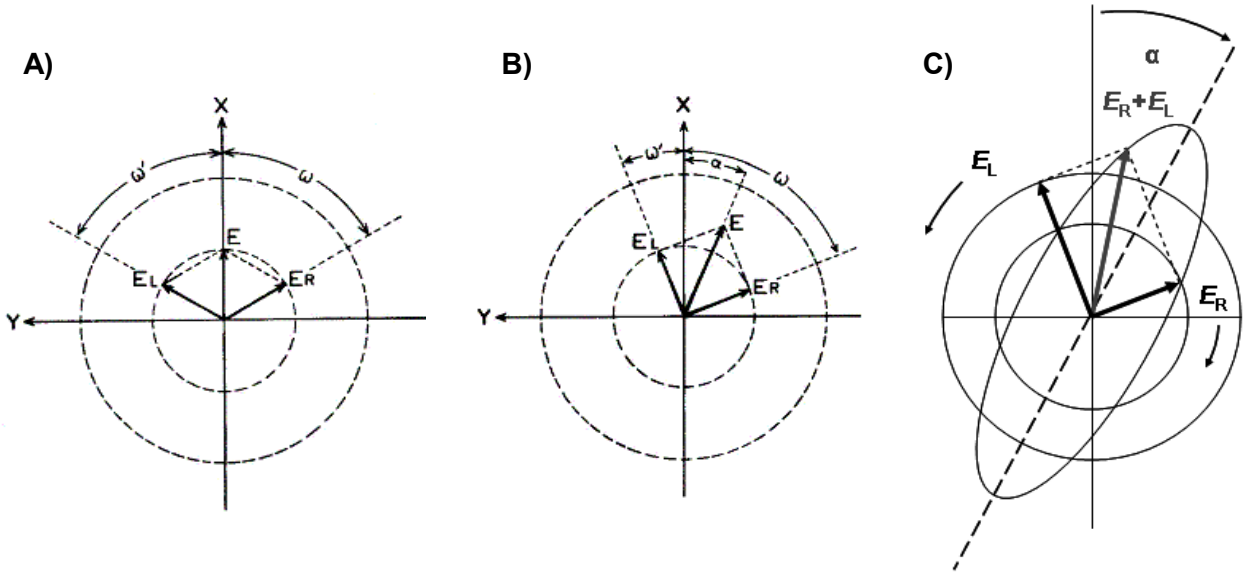

Figure 1-1: A) Plane-polarized light resolved into two circularly polarized components. B) The birefringence-induced rotation of a linear-polarization for an angle α as a result of passing through a chiral sample. C) The change of a linear-polarization into elliptical-polarization as a result of differential absorption of the two circularly polarized components by a chiral sample.

Vibrational Circular Dichroism (VCD)

Conceptually, VCD can be viewed as the extension of circular dichroism into the realm of vibrational transitions, probed by infrared radiation. From an experimental standpoint, VCD measures the differential response of a chiral molecule to the modulation of infrared polarization between right and left circularly polarized states. During the VCD measurement only individual vibrational transitions are probed within a ground electronic state. Intensities arise from a set of 3*n*–6 normal vibrational modes in a molecule, where *n* is the number of atoms. Mathematically, the differential response that defines VCD can be expressed via relation $\Delta A = A_L - A_R$, where A_L and A_R are absorbances of the left and right circularly polarized radiation, respectively. It is a common practice to express infrared absorption intensity and corresponding VCD intensity as molar absorptivity (ε) and differential molar absorptivity ($\Delta\varepsilon$) in units of $L \cdot mol^{-1} \cdot cm^{-1}$. Using the Beer-Lambert law, the absorption components of left and right circularly polarized light can be given as:

$$A_L = \varepsilon_L \cdot C \cdot l \qquad (1-1)$$

$$A_R = \varepsilon_R \cdot C \cdot l \qquad (1-2)$$

where C is concentration (in mol/L) and l represents pathlength (in cm). A rearrangement leads to expression for the differential molar absorptivity, given as:

$$\Delta\varepsilon = \varepsilon_L - \varepsilon_R = \frac{(A_L - A_R)}{l \cdot C} = \frac{\Delta A}{l \cdot C} \qquad (1-3)$$

Most VCD instruments in current use are based on the Fourier Transform method[12-14]. The schematic diagram of a VCD instrument is given in Figure 1-2. Light from a polychromatic mid-infrared source is passed through a Michelson interferometer, which generates different frequencies of radiation via a moving mirror. The light exiting the interferometer is firstly linearly polarized by means of a linear polarizer and subsequently circularly polarized via a photoelastic modulator (PEM). PEM_1 functions based on stress-induced birefringence and it introduces a 90° phase difference between two orthogonal linearly-polarized components comprising the net linearly polarized light. As the linearly polarized light passes through PEM_1 it is converted into alternating left and right circularly polarized components. The alternation frequency[9] is ~37 KHz for ZnSe optical element. The alternating circularly polarized light is passed through a chiral sample, then PEM_2 and finally focused onto a liquid-nitrogen cooled HgCdTe detector. PEM_2 is implemented[15] in a newer-generation of VCD instruments to remove artifacts associated with linear birefringence. The electronic signal at the detector contains a high frequency (AC) and a low frequency (DC) component. The AC component arises from a differential absorption of left vs. right circular polarization, while the DC component comes from intensity modulation in the interferometer. The two components are separated using an electronic filter. The AC component is processed by a lock-in-amplifier, which is tuned to the frequency of the PEM. After performing a Fourier Transform on both AC and DC components, the VCD signal is extracted as the ratio of AC and DC components. During the VCD measurement, the corresponding absorption spectrum is

simultaneously collected. The absorption intensity is derived from a DC component.

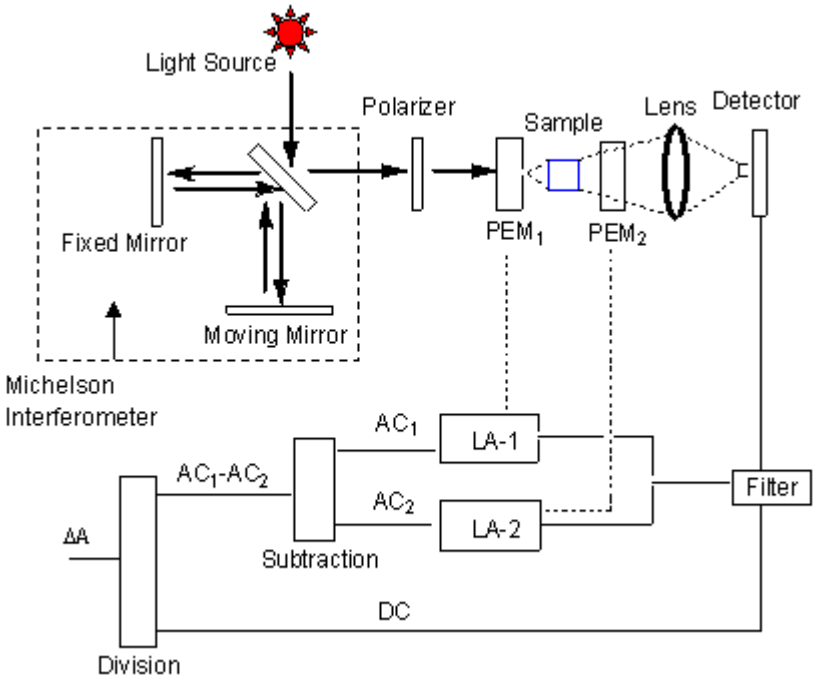

Figure 1-2: Schematic diagram of a VCD instrument.

In the quantum-mechanical treatment[16,17], the intensity of absorption and VCD bands are determined though parameters known as dipole strength (D_i) and rotational strength (R_i), respectively. The expressions for these two parameters are given in Equations 1-4 and 1-5:

$$D_i = \left| \langle \psi_{0,0} | \hat{\mu} | \psi_{0,i} \rangle \right|^2 \qquad (1-4)$$

$$R_i = \mathrm{Im}[\langle \psi_{0,0} | \hat{\mu} | \psi_{0,i} \rangle \cdot \langle \psi_{0,i} | \hat{m} | \psi_{0,0} \rangle] \qquad (1-5)$$

where $\psi_{0,0}$ and $\psi_{0,i}$ represent wavefunctions of ground and excited (i^{th}) vibrational-state within the ground electronic-state. $\hat{\mu}$ and $\hat{m}$ stand for electric dipole moment and magnetic dipole moment operators, while "Im" stands for "imaginary part of".

Relations[16,17] between dipole strength and rotational strength (both in esu^2cm^2) to molar absorptivity and differential molar absorptivity are given in Equations 1-6 and 1-7:

$$D_i = 91.76 \cdot 10^{-40} \cdot \int \frac{\varepsilon(\nu)}{\nu} d\nu \approx \frac{91.76 \cdot 10^{-40}}{\nu_i} \cdot \int \varepsilon(\nu) d\nu \qquad (1-6)$$

$$R_i = 22.94 \cdot 10^{-40} \cdot \int \frac{\Delta\varepsilon(\nu)}{\nu} d\nu \approx \frac{22.94 \cdot 10^{-40}}{\nu_i} \cdot \int \Delta\varepsilon(\nu) d\nu \qquad (1-7)$$

where $\varepsilon(\nu)$ is the molar absorptivity and $\Delta\varepsilon(\nu)$ is differential molar absorptivity (both in $L \cdot mol^{-1} \cdot cm^{-1}$), while ν_i is the frequency (in cm^{-1}) at the i^{th} band maximum. Furthermore, the Lorentzian band-shape is often used for simulating a VCD trace and its expression is given in Equation 1-8. Designation σ_i is a bandwith (in cm^{-1}) at the half of maximum band height.

$$\Delta\varepsilon(\nu) = \frac{\sigma_i^2}{(\nu - \nu_i)^2 + \sigma_i^2} \Delta\varepsilon_i \qquad (1-8)$$

Substitution of Equation 1-8 into Equation 1-7 and subsequent rearrangement leads to an expression for $\Delta\varepsilon_i$, as given below:

$$\Delta\varepsilon_i = \frac{\nu_i \cdot R_i \cdot 10^{40}}{22.94 \cdot \sigma_i \cdot \pi} \qquad (1-9)$$

Plotting of $\Delta\varepsilon_i$ vs. ν leads to generation of a theoretical VCD trace in a form comparable to an experimental trace. The comparison between experimental and theoretical VCD traces is one of the implementations of chiroptical methods that allows for a stereochemical assignment.

Electronic Circular Dichroism (ECD)

ECD is an extension of the circular dichroism principle into the realm of electronic transitions, probed by the UV-visible radiation. From an experimental standpoint, ECD measures the differential response of a chiral molecule to the modulation of UV-visible radiation between right and left circularly polarized states. An experimental ECD trace is obtained by expressing differential absorption as a differential molar absorptivity $\Delta\varepsilon$ (in $L \cdot mol^{-1} \cdot cm^{-1}$) and plotting it vs. wavelength λ (in nm).

In the early literature, stereochemical interpretations of numerous organic compounds have been accomplished based on empirical rules for correlating ECD spectra with the absolute configuration. For example, one of the most widespread empirical rules has been an exciton chirality method also known the coupled oscillator method[11,18]. The exciton chirality method is generally applied to molecules that contain two identical chromophores. Such molecules typically exhibit a bisignate ECD couplet originating from oppositely signed electronic transitions involving symmetric and antisymmetric combination of individual

chromophore wavefunctions. The application of the exciton method allows for a positive ECD couplet to be associated with stereochemistry where the two choromphores constitute a right-handed screw sense. The negative ECD couplet is diagnostic of a left-handed screw sense. However, the application of this method is problematic for molecules where the electronic transitions of the two identical chromophores are not well separated from the transitions of other moieties in the molecule. In other words, the exciton chirality method is not always applicable[16]. A combinatorial application of experimental and theoretical ECD methods allows for reliable stereochemical elucidation, regardless of the complexity of the ECD spectrum.

In the quantum mechanical expression[16] for ECD, intensity is given via rotational strength R_k (in esu^{2}cm^2). Equation 1-10 is similar to VCD-pertaining Equation 1-5, yet the designations ψ_0 and ψ_k are for the ground and excited electronic-state wavefunctions. In Equation 1-11, λ_k (in nm) is a wavelength at the k^{th} band maximum.

$$R_k = \mathrm{Im}[\langle\psi_0|\ \hat{\mu}\ |\psi_k\rangle \cdot \langle\psi_k|\ \hat{m}\ |\psi_0\rangle] \qquad (1-10)$$

$$R_k = 22.94 \cdot 10^{-40} \cdot \int \frac{\Delta\varepsilon(\lambda)}{\lambda} d\lambda \approx \frac{22.94 \cdot 10^{-40}}{\lambda_k} \cdot \int \Delta\varepsilon(\lambda) d\lambda \qquad (1-11)$$

An expression for differential molar absorptivity ($\Delta\varepsilon_k$) in terms of calculated rotational strength (R_k) can be obtained via combination of Equation 1-11 with either Lorentzian or Gaussian band-shape relations, depending on the choice for ECD spectral simulation. Plotting of $\Delta\varepsilon_k$ (in L·mol^{-1}·cm^{-1}) vs. λ (in nm) leads to generation of an ECD trace in a form comparable to the experimental trace. The

comparison of the ECD traces is another of implementations of chiroptical methods that allows for a stereochemical assignment.

Optical Rotatory Dispersion (ORD)

Observed optical rotation (α) is a measure of the rotation of linearly polarized light after it passes through a chiral sample[19-21]. This property has been routinely used for characterizing optically active organic compounds, especially in terms rotation of sodium-D-line at 589 nm wavelength. In order to make optical rotation applicable beyond just chiral-characterization, this chiroptical property needs to be detected as a function of a range of wavelengths. When optical rotation is measured in a wavelength range that is away from an electronic transition wavelength, termed the nonresonant region, the optical rotation decreases with increasing wavelength. When optical rotation is measured in a wavelength range that encompasses or is near an electronic transition, termed the resonant region, the sign of optical rotation inverts at the center of the ECD band maximum. For a positive ECD signal, optical rotation displays what is known[2,11] as a positive Cotton effect, where optical ration is positive at a higher wavelength and becomes negative at a lower wavelength. The crossover point is typically close to the position of maximum ECD intensity. For a negative ECD signal, optical rotation displays a negative Cotton effect as a function of wavelength. ORD exploits the overall phenomenon that the value of optical rotation exhibited by a chiral molecule varies with the wavelength of light passing through the molecule.

It should be noted that besides displaying a wavelength-dependence, optical rotation also inherently depends on concentration and temperature of the solution. The concentration-dependence can be a constant, linear, quadratic, or a polynomial function (typically no higher than third-power). The best-fitted dependence[22] can be found by measuring optical rotation at four or more different concentrations.

Figure 1-3 shows a schematic of a polarimeter, which measures optical rotation. Monochromatic light is first linearly polarized and then directed towards a cell containing solution of an optically active sample. Most commercial polarimeters are equipped with monochromatic sources at several discrete wavelengths, typically: 633, 589, 546, 435, 405, and 365 nm. The light exiting the sample is directed to a linear-polarization analyzer and finally to a detector. When the axis of the polarizer and that of the analyzer are perpendicular, no light reaches the detector and this condition is referred[5] to as the null point. In the presence of an optically active sample, the polarization of light is rotated, consequently resulting in the deviation from the null point. In order to obtain the optical rotation reading, the analyzer is rotated to a new position to achieve the null point. The magnitude and the direction of rotation necessary for reestablishing the null point provide the value of observed rotation.

A useful form of optical rotation is referred to as specific rotation, [α]. At a given wavelength (λ) and temperature (t), specific rotation is given as:

$$[\alpha]_{\lambda}^{t} = \frac{\alpha}{l \cdot \rho} \qquad (1-12)$$

where α is observed rotation (in deg), l is a pathlength (in dm) and ρ is the sample-density (in g/mL). The specific rotation is reported in units $deg \cdot mL \cdot dm^{-1} \cdot g^{-1}$. Another useful version of the optical-rotation parameter is known as the intrinsic rotation, which represents the value of specific rotation at the limit of zero concentration (infinite dilution). Intrinsic rotation[22] can be determined as the y-intercept of the best-fitted function for specific rotation vs. concentration data. Determining the value of intrinsic rotation is useful for a more quantitative comparison of experimental and theoretical ORD data. Since the theoretical model is typically based on an isolated chiral molecule, the determination of intrinsic rotation is the corresponding experimental value of interest.

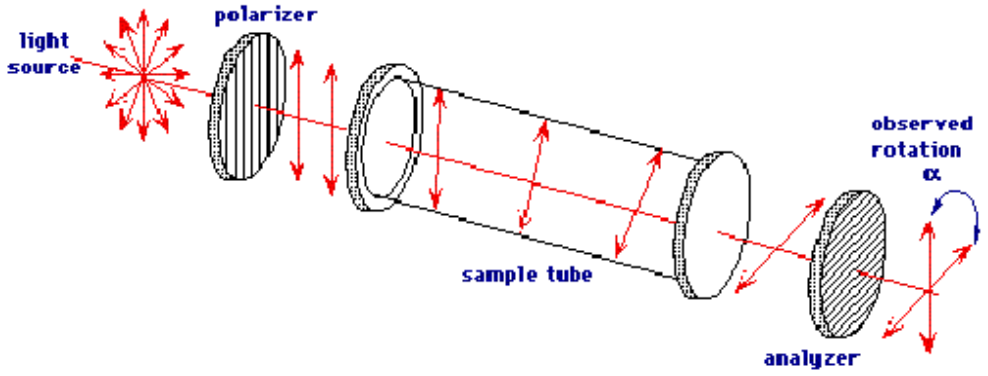

Figure 1-3: The schematic diagram of a Polarimeter.

ORD[23] represents the measure of specific/intrinsic rotation as a function of wavelength. As is the case for VCD and ECD methods, implementing ORD as a structural tool mandates correlation of empirical data with a quantum mechanical prediction of this property.

In quantum mechanical methods[24-28], specific rotation in deg·mL·dm^{-1}·g^{-1} is given by:

$$[\alpha(\lambda)] = 13.43 \cdot 10^{-5} \cdot \frac{\beta(\lambda)}{\lambda^2 \cdot M} \qquad (1-13)$$

where λ is wavelength (in cm), M is molar mass (in g/mol) and $\beta(\lambda)$ is optical rotatory parameter (in bohr^4, 1 bohr = 5.29177·10^{-11} m). The optical rotatory parameter needed for the theoretical prediction of $[\alpha(\lambda)]$ can be expressed[27] as:

$$\beta(\lambda) = \frac{1}{3} \cdot \left[\beta_{xx}(\lambda) + \beta_{yy}(\lambda) + \beta_{zz}(\lambda)\right] \qquad (1-14)$$

where each of its additive-contributions [$\beta_{xx}(\lambda), \beta_{yy}(\lambda), \beta_{zz}(\lambda)$] is related to the electric dipole–magnetic dipole polarizability tensor, leading to expressions[29] such as:

$$\beta_{xx}(\lambda) = \frac{1}{h \cdot \pi \cdot c^2} \sum_{k \neq 0} \frac{\lambda^2 \cdot \lambda_k^2}{\lambda^2 - \lambda_k^2} \cdot \mathrm{Im}[\langle \psi_0 | \ \hat{\mu}_x \ | \psi_k \rangle \cdot \langle \psi_k | \ \hat{m}_x \ | \psi_0 \rangle] \qquad (1-15)$$

In Equation 1-15, h is Planck's constant (6.62607·10^{-27} esu·s·cm^{-1}), π is a constant (3.143), and c is the speed of light (2.9979·10^{10} cm·s^{-1}). Further, $\lambda_k = h \cdot c/(E_k - E_0)$, where E_0 and E_k represent the unperturbed energies of ground and excited states, respectively. Designations ψ_0 and ψ_k represent the ground and excited (k^{th}) electronic state wave functions respectively, while $\hat{\mu}_x$ and $\hat{m}_x$ stand for electric and magnetic dipole moment operators respectively. A graph of $[\alpha(\lambda)]$ vs. λ gives a predicted ORD trace. A comparison of overall trends associated

with empirical and predicted ORD traces is another chiroptical method that allows determination of stereochemistry.

Interdependence of ORD and ECD via the Kramers-Kronig Transform

Even though the quantum mechanical predictions of ECD and ORD involve different algorithms and both predictions and measurements can be accomplished independently, it is important to note that ORD and ECD are related via the Kramers-Krong (KK) transform[29,30] . If one of these two properties is measured or predicted as a function of wavelength then, in principle, the second can be obtained via a KK transform. The need for KK transform can be present in cases where either predicting theoretical ORD spectra is computationally expensive or obtaining experimental ORD spectra is challenging. If wavelength at which optical rotation is to be predicted lies in a resonant region (*vide infra*), the quantum mechanical expression for optical rotation becomes what is what is known as “singular”. In the case of singularity, optical rotation and hence ORD cannot be reliably determined without inclusion[29] of lifetimes of excited states, which greatly increases the computational expense. Additionally, obtaining an experimental ORD trace is difficult when samples are highly colored.

In the KK transform, the ECD intensity is expressed in terms of molar ellipticity [$\theta(\mu)$] at wavelength μ, while ORD intensity is expressed in terms of molar rotation [$\varphi(\lambda)$] at wavelength λ. Equation 1-16 provides conversion from customary differential molar absorptivity $\Delta\varepsilon(\mu)$ in L·mol^{-1}·cm^{-1} into molar ellipticity [$\theta(\mu)$] in deg·cm^2 ·dmol^{-1}. Similarly, Equation 1-17 provides conversion from

customary specific rotation [$\alpha(\lambda)$] in deg·mL·dm^{-1}·g^{-1} into molar rotation [$\varphi(\lambda)$] in deg·cm^2 ·dmol^{-1}. The designation *M* is for molar mass (in g/mol).

$$[\theta(\mu)] = 3298.8 \cdot \Delta\varepsilon(\mu) \qquad (1-16)$$

$$[\varphi(\lambda)] = [\alpha(\lambda)] \cdot \frac{M}{100} \qquad (1-17)$$

The KK transform from molar ellipticity [$\theta(\mu)$], associated with an ECD signal, to molar rotation [$\varphi(\lambda)$], associate d with an ORD signal, is given[29] by Equation 1-18:

$$[\varphi(\lambda)] = \frac{2}{\pi} \cdot \int_0^{\infty} [\theta(\mu)] \cdot \frac{\mu}{\lambda^2 - \mu^2} d\mu \qquad (1-18)$$

For practical purposes, the limit of the integral involved is typically truncated to a smaller region. Further, the integral has a singularity condition when $\lambda = \mu$. To overcome the singularity, different numerical methods have been proposed for evaluating the integral. Among these methods, the one[31] by Ohta and Ishida has been suggested[29] as the best choice for implementation because: a) it provides least deviation from the exact KK transform; b) electronic ECD can be converted to ORD without the need for spectral curve-fitting; c) theoretical ECD with either Gaussian or Lorentzian band-shapes can be converted to ORD in both resonant and non-resonant regions.

When the ECD spectrum is available at constant intervals of *h* with the wavelengths and spectral intensities at these intervals given as μ_j and [$\theta(\mu)$],

where j=1,2,3,…N, the numerical method by Ohta and Ishida allows for approximation of the KK transform as:

$$[\varphi(\lambda)] = \frac{2}{\pi} \cdot \int_0^{\infty} [\theta(\mu)] \cdot \frac{\mu}{\lambda^2 - \mu^2} d\mu \approx \left(\frac{2}{\pi}\right) \cdot (2h) \cdot \left(\frac{1}{2}\right) \cdot \sum_j^{\#} \left[\frac{[\theta(\mu_j)]}{\lambda - \mu_j} - \frac{[\theta(\mu_j)]}{\lambda + \mu_j} \right] \qquad (1-19)$$

In the above relation, the summation $\sum^{\#}$ uses alternate data points to avoid the singularity situation when $\lambda = \mu$. If the wavelength λ associated with molar rotation $[\varphi(\lambda)]$ corresponds to an odd data number, then the summation is carried over the even data numbers and *vice versa*.

Another expression that demonstrates the interrelation between ORD and ECD is the sum-over-states (SOS) expression[27,32] given by Equation 1-20. In this Equation, λ_n is the wavelength at the maximum intensity of n^{th} ECD band, while σ_n is the half-width at half the maximum height of that band. R_n is the rotational strength (in esu^{2}cm^2) associated with the ECD intensity.

$$[\varphi(\lambda)] = \frac{0.915 \cdot 10^{42}}{2} \cdot \sum_n \lambda_n \cdot \left[\frac{(\lambda - \lambda_n)}{(\lambda - \lambda_n)^2 + \sigma_n^2} - \frac{(\lambda + \lambda_n)}{(\lambda + \lambda_n)^2 + \sigma_n^2} \right] \cdot R_n \qquad (1-20)$$

The implementation of the KK transform method along with the use of SOS relation is demonstrated and evaluated in Chapter IV.

Complementarities of the Three Chiroptical Methods

An important question recently raised[10] is whether the application of all three chiroptical methods is necessary for a reliable stereochemical assignment. Three situations can be considered, each advocating a simultaneous application

of all three methods: 1) The first scenario pertains to cases where all three methods lead to the univocal and unambiguous stereochemical assignment. In such cases independent cross-verification via the three methods is beneficial because it increases the confidence-level of the assignment; 2) The second type of situation pertains to cases where one of the methods may reveal additional information. This situation is an outcome of the fact that each chiroptical method probes optical activity in a slightly different manner. For example, electronic transitions and vibrational transition do not necessarily survey the same structural aspects of chiral molecules; 3) The third scenario pertains to cases where determination of stereochemistry via one of the methods is not as unambiguous as via the remaining two.

The arguments justifying the simultaneous application of all three chiroptical methods are strengthened by the observation that the advantages and disadvantages of the three methods complement each other in a manner that produces overall a very powerful approach for the structural elucidation of chiral molecules. The description[10] of the complementary nature of the three chiroptical methods is the following: a) Vibrational transitions are numerous and better resolved than electronic transitions and so additional conformations may be identified via VCD that may not be apparent from ECD or ORD; b) Despite the presence of a large number of vibrational transitions, many of them may not exhibit significant measurable VCD signal for some chiral molecules; c) ECD and ORD are typically measured at much lower concentrations (even up to a factor of 1000) than those used for VCD; d) Due to a somewhat limited wavelength region

probed via ECD or ORD, a change in conformation may lead to oppositely signed traces, which may be incorrectly interpreted with opposite absolute configuration. The potential for such ambiguity is removed with VCD since it is highly unlikely that the sign of a large number of bands would invert as a result of change in conformation; e) The ECD method has the limitation[1] that it can be applied only in the UV-visible absorption range, whereas the ORD method is equally well applied to molecules that have no optically active chromophore in the wavelength region to be studied; f) ORD in the UV-visible region can be influenced by ECD bands in the vacuum region where experimental measurements are not simple. Application of Kramers-Kronig transform can lead to the identification of the ECD bands that are not experimentally easily accessible.

Several of the projects incorporated into this dissertation demonstrate that simultaneous application of the three methods is essential as it provides missing information or a solution to an ambiguous conclusion.

The Methodology of a Stereochemical Assignment

Regardless of which of the three chiroptical methods is under consideration, the methodology for a stereochemical assignment typically involves five main steps: 1) The first step is building a theoretical model for a chiral molecule under study with an arbitrarily chosen, yet known absolute configuration. For a molecule with *n* stereogenic centers there are 2^n diastereomers, half of which are mirror images of the other half. This implies that 2^{n-1} diastereomers necessitate computational consideration. The chiroptical data

for the mirror-image diastereomers can be obtained by multiplying predicted VCD, ECD, and optical rotation intensities by (–1); 2) The second step is performing a conformational search and then geometry optimization (energy minimization) for all feasible conformations. Conformational search involves systematic variation of all dihedral angles that are associated with rotatable bonds. Those combinations of dihedral-angles that result in steric clashes of functional groups are eliminated and do not undergo geometry optimization; 3) The third step involves the comparison of conformational parameters (bond lengths, angles, and dihedral angles) as well as electronic energies for the conformations that have converged as a result of the geometry optimization. The relative fractional population of the converged nonequivalent conformations can be determined via the Boltzmann distribution relation[33], as given in Equation 1-21. The conformations with nonzero relative population undergo predictions of the three chiroptical properties. The output of the VCD calculation lists Gibbs free energies, which allow a more accurate determination of the relative populations. Additionally, a VCD output that does not contain imaginary frequencies indicates that the considered conformation represent either local or global minima on the potential energy surface. The presence of imaginary frequencies in a VCD output is indicative of a transition-state rather than a stable conformation. 4) For molecules that contain more than one stable conformation, step four involves generation of population-weighted chiroptical spectroscopic traces. The relative populations obtained from Gibbs free energies are considered for this step; 5) The final step involves the comparison of the experimentally and theoretically

obtained traces in order to make the stereochemical assignment. Quantum-mechanically predicted chiroptical traces for different plausible structures (configurations and conformations) of a molecule under investigation are compared to the corresponding experimental spectra of the same molecule with an unknown structure. The predicted trace that best matches with the experimental trace reveals the structure of that chiral molecule under experimental conditions.

$$P_i = \frac{N_i}{N_0} = e^{-(E_i - E_0)/RT} \qquad (1-21)$$

In the above provided Boltzmann relation, the fractional population of conformer i needs to satisfy the condition $\sum_i P_i = 1$. Further, E_i and E_0 are energies of two conformers, R is the gas constant and T is the temperature.

In the end, it should be noted that theoretical chiroptical predictions included in this dissertation were carried out using either Gaussian 98[34] or 03[35] software packages. The details associated with the quantum mechanical level of theory and basis set chosen will be provided in each chapter involving chiroptical predictions.

CHAPTER II

ABSOLUTE CONFIGURATION OF C_2–SYMMMETRIC SPIROSELENURANE: 3,3,3′,3′-TETRAMETHYL-1,1′-SPIROBI[3H,2,1]-BENZOXASELENOLE

Introduction

In the field of organic synthesis, considerable interest[36] has been devoted to the preparation of optically active, spirocyclic, hypervalent compounds containing a sulfur, tellurium or selenium as the central atom. This interest has arisen due to the recognition that until relatively recently very few compounds of this kind have been characterized in an optically active form and, therefore, a substantial amount of important stereochemical information has been lacking. Spiroselenuranes constitute a family of hypervalent selenium compounds that exhibit trigonal bipyramidal geometry and display chirality due to molecular dissymmetry. Examples of previously studied spiroselenuranes are 3,3′-spirobi-(3-selenaphthalide), **1** (Figure 2-1) and its 7-carboxy derivative. Compound **1** was first synthesized by Lesser and Weiss[37] and the synthesis was later reinvestigated by Dahlen and Lindgren[38]. Okazaki[39] *et al.* accomplished the synthesis of 1,5-dioxa-4-selenaspiro[3.3]heptanes, a type of a spiroselenurane bearing two oxaselenetane rings. Koizumi *et al.* have prepared[40] a few enantiomerically pure spiroselenuranes and spirotelluranes using the 2-exo-hydroxy-10-bornyl group as a chiral ligand. Recently, Drabowicz and coworkers have reported[41] the synthesis of 3,3,3′,3′-tetramethyl-1,1′-spirobi[3*H*,2,1]-benzoxaselenole oxide, **2** (Figure 2-1), and determined its absolute configuration using X-ray crystallography. They have also synthesized[42] 3,3,3′,3′-tetramethyl-

1,1′-spirobi[3*H*,2,1]-benzoxaselenole, **3** (Figure 2-1), but its absolute configuration has not yet been determined.

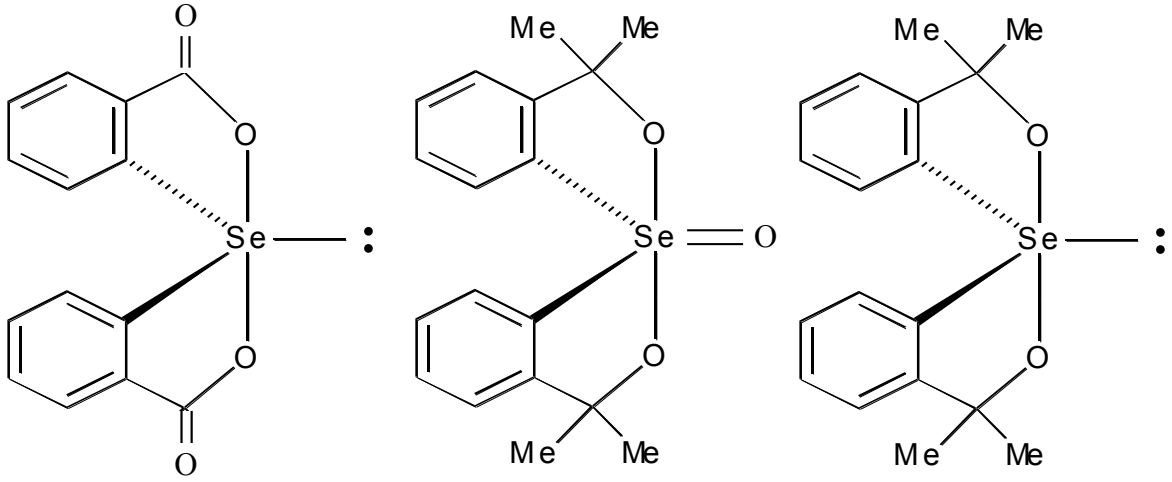

$(-)_{589}$-(*S*)-**1** $(+)_{589}$-(*S*)-**2** $(-)_{589}$-(*S*)-**3**

Figure 2-1: The chemical structures of 3,3′-spirobi-(3-selenaphthalide), **1**, 3,3,3′,3′-tetramethyl-1,1′-spirobi[3*H*,2,1]-benzoxaselenole oxide, **2** and 3,3,3′,3′-tetramethyl-1,1′-spirobi[3*H*,2,1]-benzoxaselenole, **3.**

In the light of continued interest in investigating the stereochemistry of hypervalent compounds containing a central selenium atom, the research presented here uses chiroptical methods to determine the absolute configuration and the dominant conformation of **3**. The stereochemical assignments have been previously made for **1** and **2**, which have structural resemblances with **3** (Figure 2-1). The enantiomer of **1** with negative optical rotation at 589 nm was assigned[36] (*S*)-configuration, while the enantiomer of **2** with negative optical rotation at 589 nm has been[41] assigned (*R*)-configuration. This chapter examines the absolute

configuration of **3**, as determined by comparing experimental and theoretical chiroptical data (VCD, ECD, and ORD).

Experimental Section

Synthesis and Resolution: Compound **3** in racemic form has been synthesized at Lodz by means of a one step reaction[42] of diethyl selenite and the Grignard reagent derived from orthobromcumyl alcohol. Drabowicz and coworkers[42] have demonstrated resolution of enantiomers of **3** on a Chiralpak AS column with the first and second eluted enantiomers exhibiting negative ($[\alpha]_D$ = –20, CH_2Cl_2) and positive ($[\alpha]_D$ = +21, CH_2Cl_2) rotations, respectively. Following this approach, the enantiomeric separation was carried out at Wyeth laboratories on a Chiralpack AS analytical column (20·250mm), using 10% IPA and 90% hexane as the mobile phase at room temperature. Since the sign of optical rotation changes at shorter wavelengths, the $(+)_{589}$- and $(-)_{589}$-enantiomers of **3** are identified by their rotation at 589 nm in CH_2Cl_2 solvent.

VCD, ECD, and ORD Spectra: The absorption and VCD spectra were recorded on a commercial Fourier Transform VCD spectrometer, Chiralir, in the 2000-900 cm^{-1} region. The VCD spectra were recorded with three hour data collection time at 4 cm^{-1} resolution. Spectra were measured in CH_2Cl_2 solvent at 0.075M and 0.086M concentration for $(-)_{589}$- and $(+)_{589}$-enantiomers respectively. The sample was held in a variable pathlength cell with BaF_2 windows and a path length of 110 μm. In the absorption spectrum presented, the raw solvent absorption was subtracted out. In the VCD spectrum presented, the VCD spectrum of the solvent was eliminated indirectly by subtracting the VCD spectra

of two enantiomers and then scaling the intensities ½. The ECD spectra were recorded on a Jasco J720 spectropolarimeter using 0.01 cm pathlength and CH_2Cl_2 solvent. The optical rotations at six discrete wavelengths (633, 589, 546, 436, 405, and 365 nm) have been measured in CH_2Cl_2 using an Autopol IV polarimeter.

Calculations: The geometry optimizations, vibrational frequencies, absorption and VCD intensities for spiroselenurane were calculated using Gaussian 98 program[34]. The calculations were based on density functional theory (DFT) method with B3LYP functional, using 6-31G* basis set. The theoretical absorption and VCD spectra of (*R*)-**3** were simulated with Lorentzian band shapes and 5 cm^{-1} half-width at one-half of the peak height. Since 6-31G* predicted band positions are higher than the experimental values, the DFT vibrational frequencies were scaled with 0.9613 factor. The ECD and ORD calculations have been undertaken with the same level of theory as for VCD using Gaussian 03 program[35]. The theoretical ECD intensities of the first 12 electronic transitions are used to simulate the ECD spectra for (*S*)-**3** using gaussian band shapes and 20 nm half-width at 1/e of peak height.

Results and Discussion

The stereoisomers available to a molecule can have a dramatic effect on its activity and reactivity. In some cases an ensemble of stereoisomers may be responsible for an observed behavior. Therefore, it is important to account for all possible low-energy stereoisomers. The conformational rigidity of **3** restricts the

consideration to only two different isomers (Figure 2-2). Although NMR data for **3** have been reported[42], the predominance of one or both of these isomers has not been established. Therefore we investigated the two isomers, trans- and cis-, differing in the dihedral angle labeled as D(5-4-1-3). The trans-isomer with D(5-4-1-3) = 5.6° (Figure 2-2a) has C_2-symmetry and was obtained from geometry optimization of the structure possessing coordinates acquired from spiroselenurane's crystal structure[42]. The cis-isomer (Figure 2-2b) considered has no symmetry and is characterized by the dihedral angle D(5-4-1-3) = −105.6°. The initial structure for cis-isomer has been obtained via manual search for possible low energy conformations.

The converged dihedral angle, D(5-4-1-3), optimized electronic energies, and relative populations are listed in Table 2-1. Due to the rigidity of spiroselenurane structure, it is not surprising that among the two isomers under consideration only one is dominant. Based on the DFT predicted electronic energies, and calculated relative Boltzmann populations thereby calculated, the trans-isomer with D(5-4-1-3) = 5.6° is seen to be dominant.

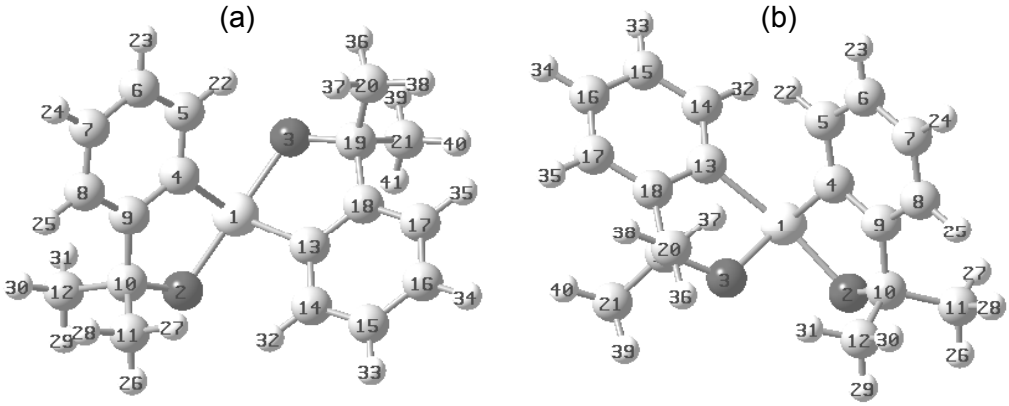

Figure 2-2: B3LYP/6-31G* optimized structures of two stereoisomers of **3**. (a) trans-isomer with D(5-4-1-3) = 5.6°, (b) cis-isomer with D(5-4-1-3) = -105.6°.

The converged dihedral angle, D(5-4-1-3), optimized electronic energies, and relative populations are listed in Table 2-1. Due to the rigidity of spiroselenurane structure, it is not surprising that among the two isomers under consideration only one is dominant. Based on the DFT predicted electronic energies, and calculated relative Boltzmann populations thereby calculated, the trans-isomer with D(5-4-1-3) = 5.6° is seen to be dominant.

Table 2-1: B3LYP/6-31G* predictions of optimized dihedral angles, energies and relative populations of the two isomers of **3**.

Conformations	Dihedral angle[a] D(5-4-1-3) (°)	Electronic Energy (Hartree)	Population (%)
trans-isomer	5.6	-3247.768804	100
cis-isomer	-105.6	-3247.735673	0

[a]for atom numbering see Figure 2-2.

Specification of the absolute configuration[18,43,44] of the structure used in theoretical calculation is based on established convention for spirane compounds[18]. In order to specify the absolute configuration, atoms surrounding the selenium are assigned priority designations (Figure 2-3). Labels a_1 and a_2 carry higher priority than b_1 and b_2. The atoms labeled as “a” and “b” with the same subscripts designate the pair of atoms sharing the same ring. Placing the lowest priority group (b_2) in the back, away from the observer, and following the sequence a_1-a_2-b_1, gives a clockwise rotation and hence, (*R*)-configuration for the structure used in calculations. The same (*R*) absolute configuration for this

structure can be designated by the modification of the Cahn-Ingold-Prelog rules[45] proposed by Martin and Balthazor[46].

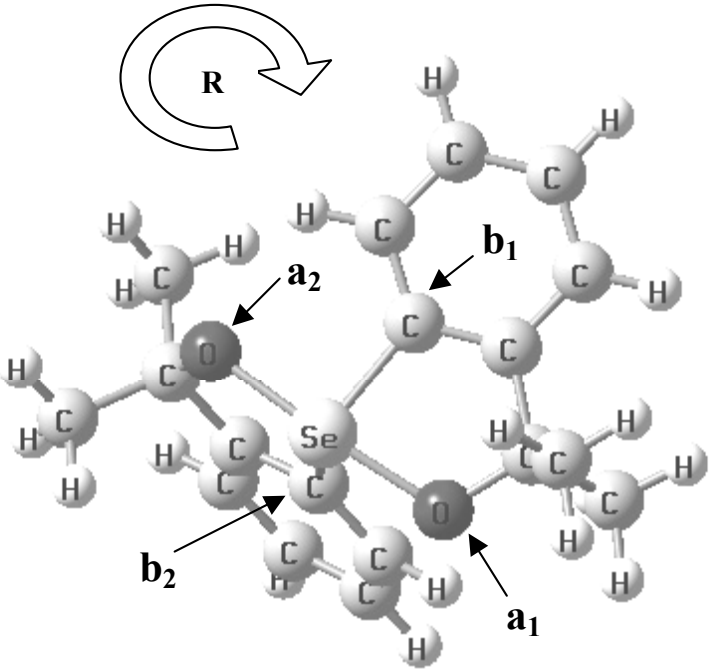

Figure 2-3: Priority designations aiding the configurational assignment for the structure used in theoretical calculations on **3**.

The theoretical vibrational spectra are compared to the corresponding experimental spectra in Figures 2-4 and 2-5. It is well known that the B3LYP/6-31G* calculated frequencies are larger than the observed frequencies, and therefore need to be scaled. Even after scaling there will be differences between calculated and observed frequencies due to inaccuracies at the level of theory used and due to anharmonic effects in the experimental frequencies. Therefore, the correlation between predicted and experimental spectra is normally made by following spectral patterns (that is higher intensity bands in the experimental

spectra correspond to higher intensity bands in the predicted spectra etc). The region between ~1300 and 1246 cm^{-1} is not shown in the experimental spectra due to interference from high intensity absorption band of solvent. Consequently, this region of the experimental spectrum cannot be compared to the predicted spectrum. The absorption bands in the predicted spectrum show one to one correspondence with the absorption bands in the experimental spectrum of **3**. For example, the high intensity experimental bands at 953 and 1155 cm^{-1} correspond to the analogous high intensity bands in the predicted spectrum at 946 and 1151 cm^{-1}.

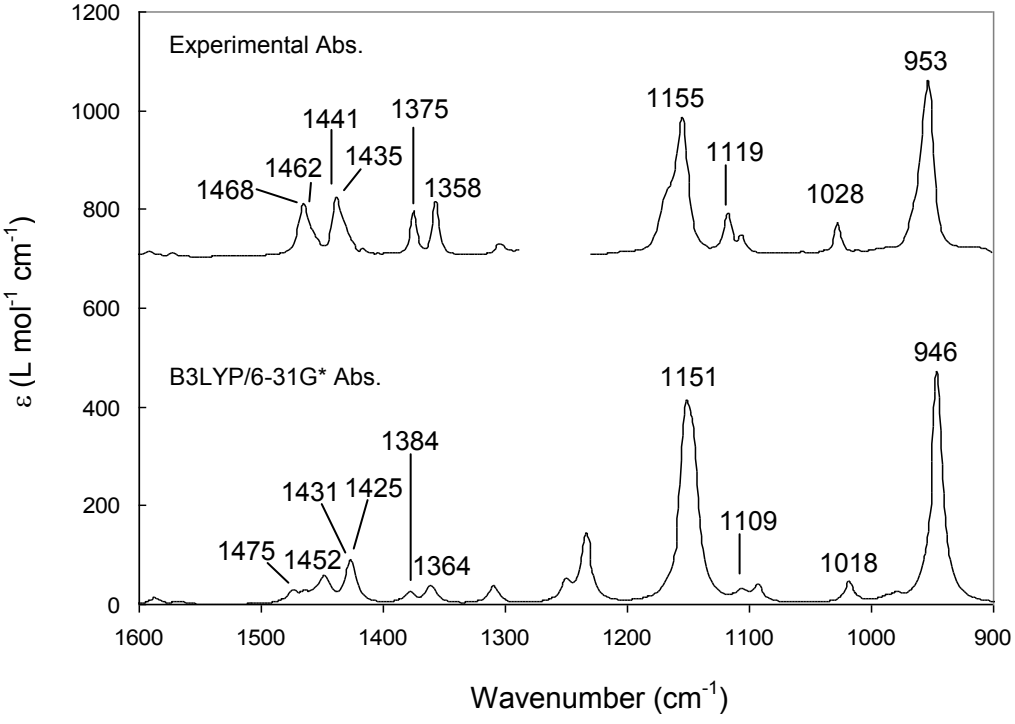

Figure 2-4: Comparison of experimental absorption spectrum of $(+)_{589}$-**3** with the predicted absorption spectrum (B3LYP/6-31G*) of (*R*)-**3**.

The significant VCD bands (Figure 2-5) in the observed VCD spectrum of $(+)_{589}$-**3** at concentration of 0.086M can be seen as three bisignate couplets: a couplet with positive band at 953 cm^{-1} and negative at 966 cm^{-1}; a second couplet with negative band at 1115 cm^{-1} and positive band at 1119 cm^{-1}; a third couplet with positive band at 1155 cm^{-1} and negative band at 1173 cm^{-1}. The corresponding couplets in the predicted spectrum can be seen at 946/959 cm^{-1}, 1102/1109 cm^{-1} and 1151/1168 cm^{-1}. The vibrational origin of these couplets in the predicted spectrum are as follows. In the first couplet, the positive VCD band at 946 cm^{-1} has contributions from three different vibrations, with dominant contribution coming from anti-symmetric C-O stretching vibration; the negative band at ~959 cm^{-1} is due to symmetric C-O stretching vibration. The second couplet originates from phenyl C-H rocking vibrations with the negative VCD at 1102 cm^{-1} and positive VCD at 1109 cm^{-1} coming, respectively, from symmetric and anti symmetric modes. In the third couplet, the positive VCD band at 1151 cm^{-1} has contributions from five different vibrations, with C-CH_3 stretching and phenyl C-H bending vibrations making major contributions; the negative VCD band at 1168 cm^{-1} originates from C-CH_3 stretching coupled with C-O stretching.

The abovementioned three bisignate VCD features observed for $(+)_{589}$-**3** are reproduced in the predicted VCD spectrum of (*R*)-**3**. The predicted VCD spectrum for (*S*)-**3** would be a mirror image to that of (*R*)-**3** and would not agree with the experimental VCD spectrum for $(+)_{589}$-**3**. The nice agreement seen between predicted VCD spectrum of (*R*)-**3** and experimental VCD spectrum of

$(+)_{589}$-**3** indicates that the absolute configuration is $(+)_{589}$-(*R*) or equivalently $(-)_{589}$-(*S*).

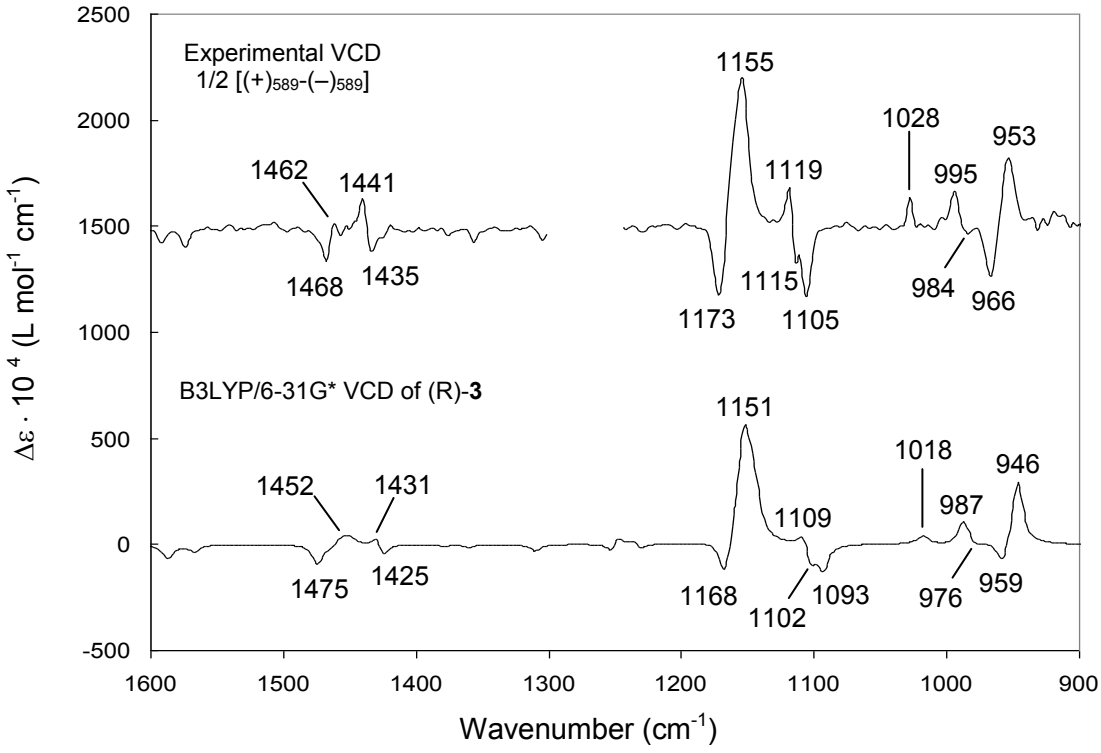

Figure 2-5: Comparison of experimental VCD spectrum of $(+)_{589}$-**3** with the predicted VCD spectrum (B3LYP/6-31G*) of (*R*)-**3**.

The experimental ECD spectrum obtained for $(-)_{589}$-**3** in CH_2Cl_2 (Figure 2-6) is similar to the same spectrum measured by Drabowicz and coworkers[6b] in hexane. The predicted ECD spectrum for (*S*)-**3,** obtained from that for (*R*)-**3** by multiplying with (–1), is compared to the experimental ECD spectrum of $(-)_{589}$-**3**. The predicted spectrum for (*S*)-**3** and experimental ECD spectrum for $(-)_{589}$-**3** display an overall positive ECD in the ~210 to 300 nm region, suggesting that the absolute configuration is $(-)_{589}$-(*S*) or equivalently $(+)_{589}$-(*R*). The origin of ECD

features in spiroselenuranes has not been identified before in the literature. We have analyzed the molecular orbital coefficients obtained in the ECD calculation at B3LYP/6-31G* level and found that all of the first 12 electronic transitions calculated are associated with lone pairs of electrons on either Se or O atoms. The lowest energy electronic transition is associated with lone pair electrons on selenium.

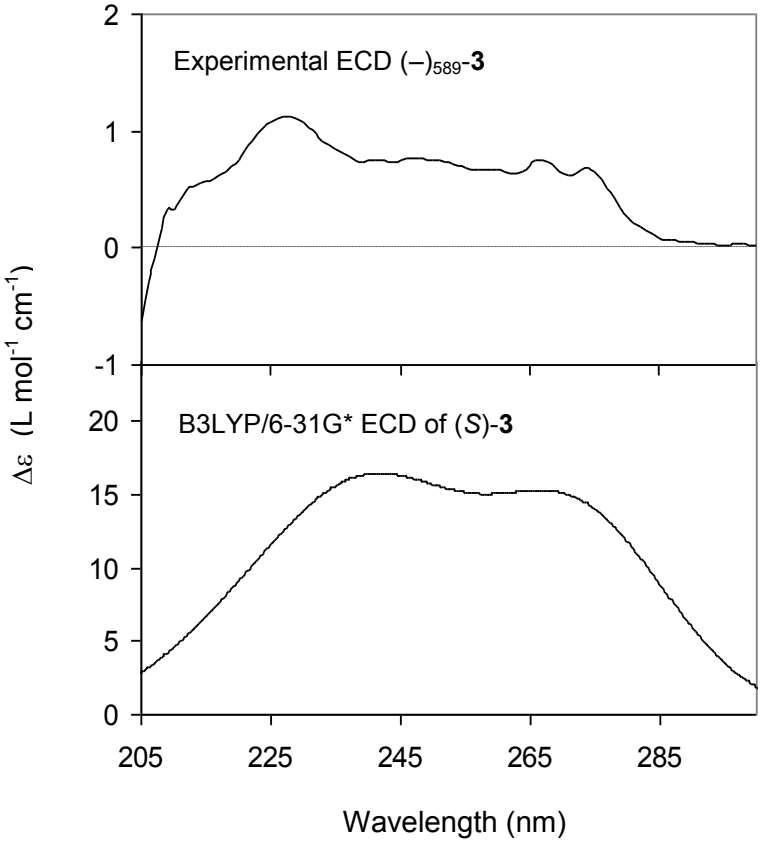

Figure 2-6: B3LYP/6-31G* predicted ECD spectrum for (*S*)-**3** (bottom) and experimental (top) ECD spectrum of $(-)_{589}$-**3.**

The predicted ORD for (*S*)-**3**, obtained from that for (*R*)-**3** by multiplying with (–1), is compared to the corresponding experimental ORD measured in CH_2Cl_2 for $(-)_{589}$-**3** in Figure 2-7. The experimental specific rotations for $(-)_{589}$-**3** at longer wavelengths are negative, but change sign at ~ 475 nm and increase in magnitude at shorter wavelengths. The same trend is seen in the predicted values for (*S*)-**3**, although the crossover point in predicted ORD is different from that in experimental data, because of the inaccuracies in electronic transition wavelengths predicted at B3LYP/6-31G* level. Nevertheless, a nice correlation seen in the trends of predicted and experimental ORD data provides another verification that the absolute configuration of **3** is $(+)_{589}$-(*R*) or $(-)_{589}$-(*S*). Since the first eluted enantiomer on Chiralpack AS analytical column has negative optical rotation at 589 nm in CH_2Cl_2 it is concluded that the (*S*)-enantiomer of **3** elutes first on this column.

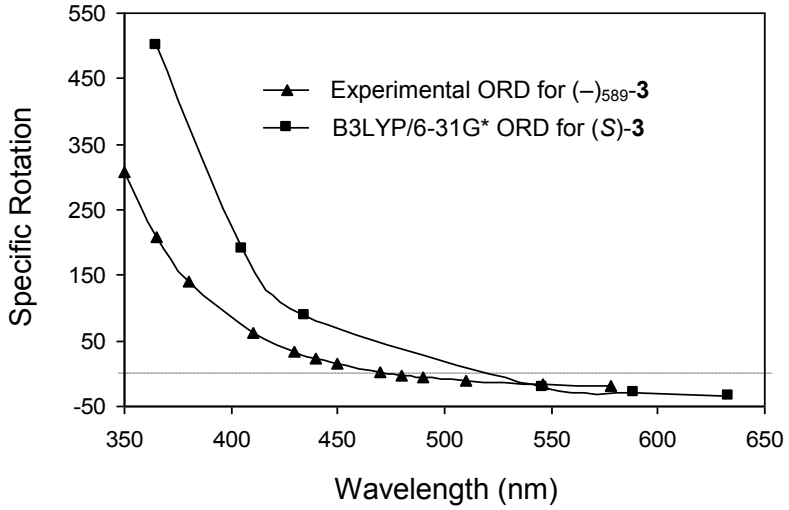

Figure 2-7: Comparison of ORD predicted for (*S*)-**3** using B3LYP/6-31G* with experimental data of $(-)_{589}$-**3**.

It is interesting to note that the absolute configuration for **3**, $(+)_{589}$-(*R*), determined here is opposite to that determined[41] for **2**, $(-)_{589}$-(*R*), using X-ray crystallography, but is same as that determined[36], $(-)_{589}$-(*S*), for **1**. The ECD spectra of $(-)_{589}$-**3** and $(-)_{589}$-**2** are also significantly different. The chemical constitutional difference between spiroselenuranes **3** and **2**, namely a lone pair in **3** vs. oxygen atom in **2** attached to selenium, must be the source for change in the sign of rotation for a given configuration. Very recently, the absolute configurations of the spirosulfuran and the spirotellurane with structures analogous to **3** were deduced to be the same as that of **3** [$(+)_{589}$-(*R*) or $(-)_{589}$-(*S*)] on the basis of the dirhodium-NMR-method.[47]

Conclusion

Due to its rigid structure, spiroselenurane is stable as trans-isomer. The agreement between the theoretical and experimental chiroptical parameters, namely VCD, ECD and ORD leads to the conclusion that the absolute configuration of 3,3,3′,3′-tetramethyl-1,1′-spirobi[3*H*,2,1]-benzoxaselenole is $(+)_{589}$-(*R*) and $(-)_{589}$-(*S*), where $(+)_{589}$ and $(-)_{589}$ are the signs of observed rotations at 589 nm in CH_2Cl_2 solvent. Since the first eluted enantiomer on Chiralpack AS analytical column, with 10% IPA and 90% hexane as the mobile phase at room temperature, has negative optical rotation at 589 nm in CH_2Cl_2 it is concluded that the (*S*)-enantiomer of **3** elutes first on this column. Furthermore, this work demonstrates the first combined use of VCD, ECD and ORD

techniques, complimenting each other, to assign the absolute configurations with increased confidence.

CHAPTER III

ABSOLUTE CONFIGURATION OF TRINICKEL(II) COMPLEX OF DIPYRIDYLAMINE ($Ni_3(dpa)_4Cl_2$) WITH A HELICAL CHIRALITY

Introduction

Synthesis and investigation of metal-complexes plays a significant role in modern chemistry since this class of compounds is known for its relevance in various chemical technologies. Some of these technologies include application of metal-complexes in photochemical processes, catalysis and enantioselective synthesis of metallopharmaceuticals.[48,49] Recent interest[50] in molecular electronics and photonics has further inspired many studies with metal-complexes as the basis of new functional materials. In this respect, one of the particularly interesting subclasses of metal-complexes is an assembly of linear metal core surrounded by poly(pyridylamide) ligands (Figure 3-1). The metals Cr (*n* = 0-2), Co (*n* = 0-2), Ni (*n* = 0-3), Cu (*n* = 0), Ru (*n* = 0), and Rh (*n* = 0) have been incorporated into complexes of this type, where designation *n* indicates the repetition-number of pyridylamide segments. Such elongated complexes[51-55] with extended metal-atom chains have received attention due to their potential for acting as molecular wires in molecular-electronics devices. Some of the properties of these complexes, especially for *n* = 0, have been studied in detail[56-59]. The ligand for *n* = 0 is designated “dpa” as derived from di(2-pyridyl)amido anion.

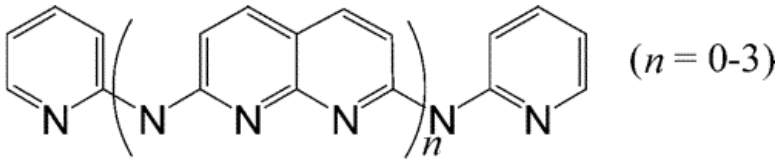

Figure 3-1: Poly(pyridylamide) Ligands.

The poly(pyridylamide)-based subset of inorganic molecules is additionally interesting because they display a helical chirality, which entails helical winding of the four insulating polypyridyl ligands around the central metal wire. The direction of helical twist of dpa-ligands along the (N-N^{-}-N)-axis, as displayed in Figure 3-2, allows for distinguishing the absolute configuration of the enantiomers. In a helical system, *P* and *M* stand for positive and negative as they relate to the dihedral angle along the axis. Likewise, *P* and *M* designations relate to clockwise and counterclockwise rotation, respectively, in order to overlap the pyridine ring in the front with the one in the back when viewing along the axis.

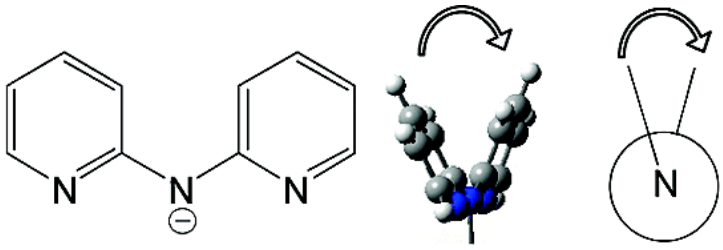

Figure 3-2: Representation of the *P*-helicity of Dipyridyl Ligands.

Separation of the enantiomers and subsequent determination of the absolute configuration of any chiral molecule is desired due to often-encountered

differences in chemical behaviors and properties exhibited by the two enantiomeric species. These differences imply the possibility for versatile applications of the two enantiomers. Extensive efforts to obtain single crystals of the individual enantiomers of this class of inorganic molecules were unsuccessful. However, Armstrong *et al.* has recently accomplished the first-ever enantiomeric separation of nickel analog[53-55] ($Ni_3(dpa)_4Cl_2$) of this special class of chiral metal-complexes. The separation of the two enantiomers was achieved[60] by a preparative chromatographic procedure using a macrocyclic glycopeptide-based chiral stationary phase.

Two different views of this D_4-symmetric nickel-complex, designated as **1**, are displayed in Figure 3-3. This chapter describes the use of chiroptical methods as a reliable and simple approach for establishing the helical-chirality of **1** for the first time. The joint use of three chiroptical techniques not only increases the confidence of the structural assignment, but also provides information on both vibrational and electronic origins of optical activity.

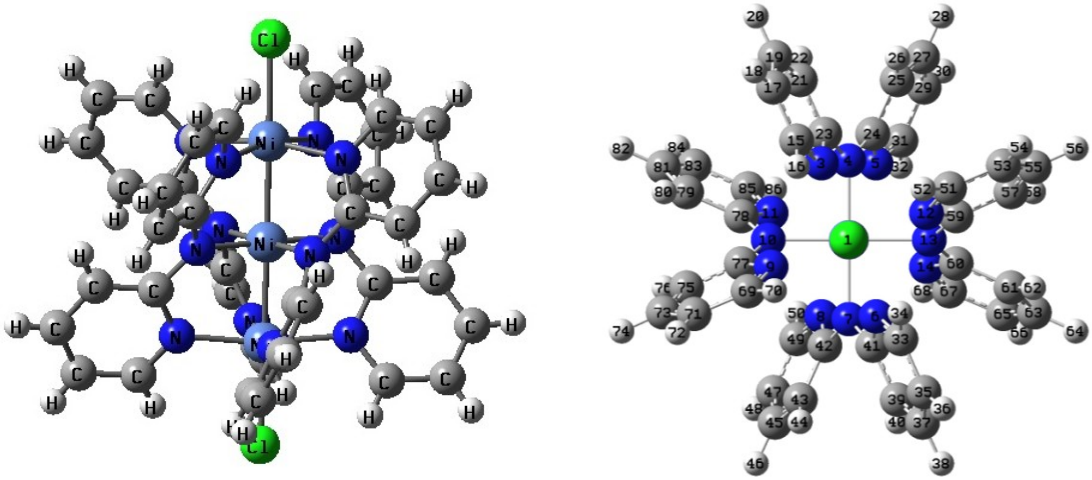

Figure 3-3: Two different views of this D_4-symmetric $Ni_3(dpa)_4Cl_2$ (**1**).

Experimental Section

Synthesis and Resolution: The intensely purple-colored **1** was synthesized and both enantiomers have been provided to us via collaboration with Armstrong *et al*. and Cotton *et al*. It should be noted that in the course of the chromatographic separation, the replacement of Cl by OH occurs. The $(+)_{589}$-enantiomer is the second eluted peak, while the $(–)_{589}$-enantiomer is the first eluted peak. The labels $(+)_{589}$ and $(–)_{589}$ are employed to designate the signs of optical rotation (OR) of the enantiomers at 589 nm.

VCD, ECD, and ORD Spectra: The vibrational absorbance and VCD spectra of $(+)_{589}$-**1** and $(–)_{589}$-**1** were recorded in the mid-infrared spectral region, from 2000-900 cm^{-1}, with one hour data collection time, at 8 cm^{-1} resolution. Recording was accomplished on a commercial Fourier transform VCD spectrometer Chiralir. Spectra were measured in a demountable cell with CaF_2 windows and 200 μm pathlength spacer. The concentration used was ~ 0.0126 M in $CHCl_3$ solvent environment. Solvent spectra were subtracted out in order to eliminate the solvent absorbance bands and establish the zero-baseline. The frequency region ~ 1238 to 1196 cm^{-1} has been excluded due to presence of a strong solvent absorption band in this region. ECD spectra were recorded on a Jasco J720 spectrometer in the 200 to 800 nm region, using 0.01 cm pathlength cell. The concentration was ~ 0.00129 M in $CHCl_3$ solvent. OR as a function of concentration has been measured on Autopol IV polarimeter, using 1.0 dm cell. OR measurements were made at all wavelengths accessible by Autopol IV polarimeter: 633, 589, 546, 436, 405, and 365 nm. Solutions of $(+)_{589}$ and $(–)_{589}$-**1**

in $CHCl_3$ solvent were prepared by successive dilutions from the parent stock solution. These concentration-dependent studies have resulted in data points ranging in concentrations from ~ 0.00013 to 0.000013 g/ml for $(-)_{589}$-enantiomer and from ~ 0.000181 to 0.0000181 g/ml for $(+)_{589}$-enantiomer. The intrinsic rotation, was extracted from the optical rotations at different concentrations as described before[22].

Calculations: The geometry optimizations and calculation of vibrational frequencies, vibrational absorptions (VA), VCD and ECD intensities were undertaken with Gaussian 03 program[35]. Geometry optimization was first carried out with the B3LYP functional. The same functional was also used for the VA and VCD calculations. On the basis of previous experience,[61] the BHLYP functional, which uses an increased admixture of Hartree-Fock exchange in time-dependent DFT calculations, was employed for ECD prediction. The LANL2DZ basis set[62] was used for all computations. A Kramers-Kronig transform of the calculated ECD intensities has provided the ORD spectrum[29]. The theoretical absorption and VCD spectra were simulated with Lorentzian band shapes and a 5 cm^{-1} half-width at half-peak height. The calculated vibrational frequencies have been scaled by a factor of 0.9613. The theoretical ECD spectrum was simulated from the first 50 singlet→singlet electronic transitions using Gaussian band shapes and a 20 nm half-width at 1/*e* of peak height.

Results and Discussion

From a theoretical standpoint, **1** represents a convenient target for study because it displays a conformational rigidity. The interlocking of eight pyridine rings through N-Ni bonding inhibits the conformational degrees of freedom. The chirality induced by the D_4-symmetry and helical twisting of dpa-ligands around the three collinear Ni-metals differs from customary chirality associated with one or more chiral centers. The helical twist of dpa-ligands makes **1** unique and attractive target for chiroptical study.

The D_4-symmteric theoretical model of **1** has been obtained by taking the structural coordinates from the reported X-ray crystallographic data[53]. Upon geometry optimization of the theoretical model, the calculation of chiroptical properties has been undertaken. The fact that no imaginary frequencies were found among calculated vibrational frequencies reinsures that the optimized structure represents minima on the potential energy surface.

Panel A in Figure 3-4 shows the observed VA spectrum from 1100 to 1750 cm^{-1} and the calculated spectrum for the *P*-enantiomer. Thirteen absorption bands are labeled and exhibit one-to-one correspondence with the experimental spectrum. The assignments of normal-mode vibrations giving rise to the labeled bands are provided in Table 3-1, with the numeric designations of atoms provided in Figure 3-3. The computation was done on $Ni_3(dpa)_4Cl_2$, and no account was taken of the fact that some axial OH groups were present in the experimental sample. This is why the Ni-O-H bending mode at ~ 1700 cm^{-1} is not in the computed spectrum. The ~ 1190-1240 cm^{-1} gap corresponds to strong

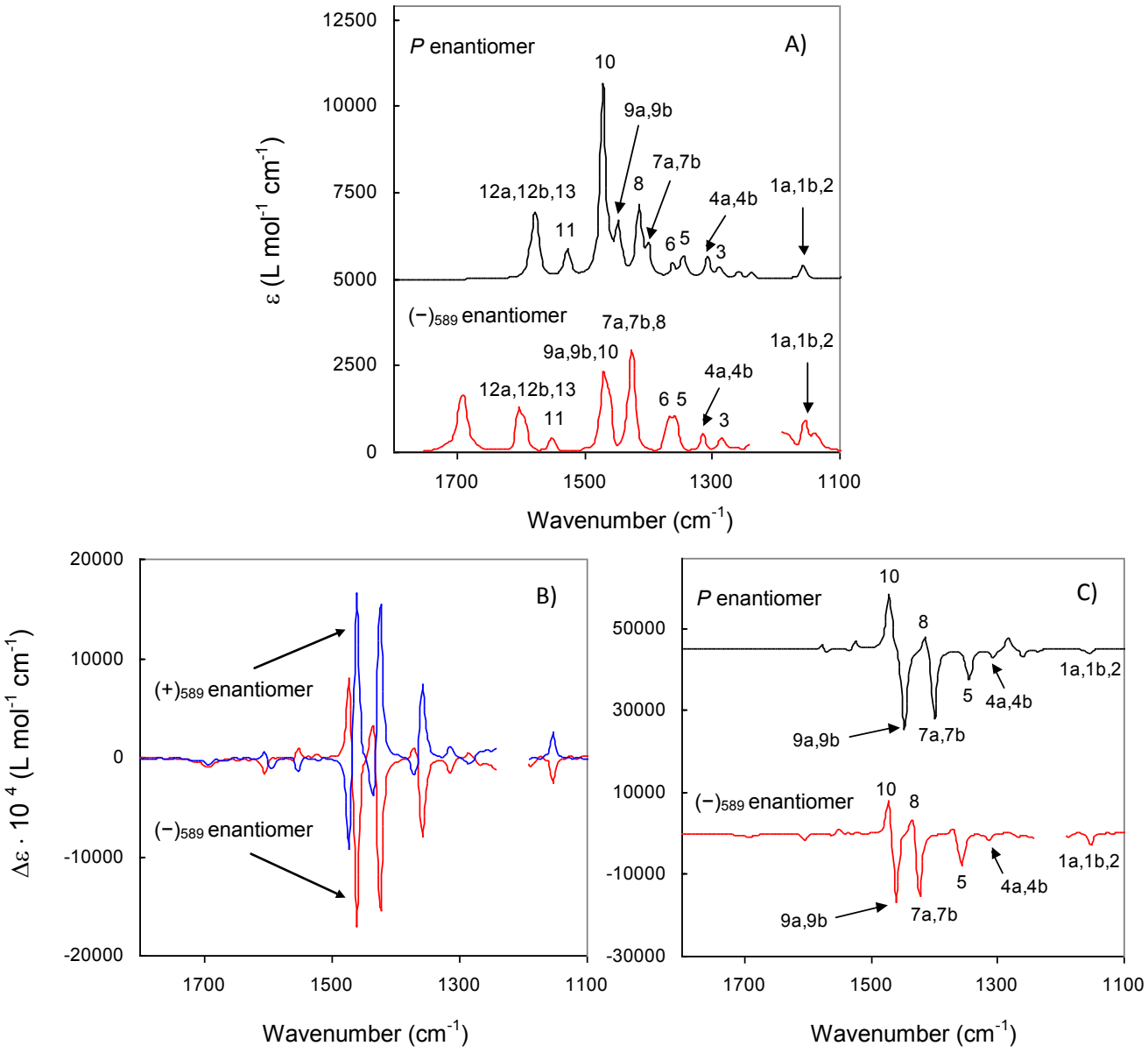

Figure 3-4: VA (panel A) and VCD spectra of **1**. The experimental VCD spectra are shown for both enantiomers in panel B. Calculated spectra for *P*-**1** (topmost trace in panels A and C) were obtained with B3LYP/LANL2DZ.

absorption interference from the $CHCl_3$ solvent. Panel B of Figure 3-4 shows the mirror-image VCD spectra of the $(+)_{589}$- and $(–)_{589}$-enantiomers of **1**. The fact that the two enantiomers display good-quality mirror-image signals throughout the entire mid-IR region confirms the high enantiomeric purity of the sample. In panel

C, the VCD spectrum of the $(-)_{589}$-enantiomer is compared with the VCD spectrum calculated for the *P*-enantiomer and all of the labeled peaks display a highly satisfactory qualitative match. The high degree of loyalty between measured and calculated spectra provides high certainty to the configurational assignment as *P*-$(-)_{589}$.

Table 3-1: Vibrational frequencies and vibrational descriptions for $Ni_3(dpa)_4Cl_2$.

Band Number[a]	Experimental frequency (cm^{-1})	Calculated frequency[b] (cm^{-1})	Vibrational description[c]
1a,1b	1142	1157	scissoring vibrational mode among H-C-C-H groups of rings.
2	1153	1157	
3	1284	1289	bond stretching between N3-C15, N5-C31, N6-C33, N8-C49, N9-C69, N11-C85, N12-C51, N14-C67.
4a,4b	1315	1308	symmetric stretching of C23-N4-C24, C41-N7-C42, C77-N10-C78, C59-N13-C60 with bond stretching between N3-C15, N5-C31, N6-C33, N8-C49, N9-C69, N11-C85, N12-C51, N14-C67, as well as some rocking of H-C-C-H groups of rings.
5a,5b	1358	1344	pronounced asymmetric stretching of C23-N4-C24, C41-N7-C42, C77-N10-C78, C59-N13-C60 with some ring breathing modes and rocking of H-C-C-H groups of rings.
6	1369	1362	asymmetric stretching of C23-N4-C24, C41-N7-C42, C77-N10-C78, C59-N13-C60 with ring breathing modes and some rocking of H-C-C-H groups of rings.
7a,7b	1423	1402	asymmetric stretching of C23-N4-C24, C41-N7-C42, C77-N10-C78, C59-N13-C60 with bond stretching between N3-C15, N5-C31, N6-C33, N8-C49, N9-C69, N11-C85, N12-C51, N14-C67, as well as some rocking vibrational mode among H-C-C-H groups of rings.
8	1435	1416	asymmetric stretching of C23-N4-C24, C41-N7-C42, C77-N10-C78, C59-N13-C60 with some rocking vibrational mode among H-C-C-H groups of rings.
9a,9b	1462	1448	asymmetric stretching of C23-N4-C24, C41-N7-C42, C77-N10-C78, C59-N13-C60 with stretching of N3-C23, N5-C24, N6-C41, N8-C42, N9-C77, N11-C78, N12-C59, N14-C60 as well as wagging of H-C-C-H groups of rings.
10	1473	1473	asymmetric stretching of C23-N4-C24, C41-N7-C42, C77-N10-C78, C59-N13-C60 with some ring breathing modes.

Table 3-1, cont.:

11	1551	1527	asymmetric stretching of C15-C17=C19-C21, C25-C27=C29-C31, C33-C35=C37-C39, C43-C45=C47-C49, C51-C53=C55-C57, C61-C63=C65-C67, C69-C71=C73-C75, C79-C81=C83-C85.
12a,12b	1605	1578	asymmetric stretching, within rings, between N3=C15-C17, N5=C31-C29, N6=C33-C35, N8=C49-C47, N9=C69-C71, N11=C85-C83, N12=C51-C53, N14=C67-C65 and also stretching between C19=C21-C23, C24-C25=C27, C37=C39-C41, C42-C43=C45, C55=C57-C59, C60-C61=C63, C73=C75C-C77, C78-C79=C81.
13	1605	1578	asymmetric stretching, within rings, between N3=C15-C17, N5=C31-C29, N6=C33-C35, N8=C49-C47, N9=C69-C71, N11=C85-C83, N12=C51-C53, N14=C67-C65 and also stretching between C19=C21, C25=C27, C37=C39, C43=C45, C55=C57, C61=C63, C73=C75C, C79=C81.

[a]see Figure 3-4 for band numbers;
[b]scaled by 0.9613;
[c]The atom numbers for **1** are given in Figure 3-3.

The mirror-image ECD spectra of the $(+)_{589}$- and $(-)_{589}$-enantiomers of **1** and their comparison to the predicted ECD spectrum for the *P*-enantiomer are shown in Figure 3-5. From the correspondence in the ECD pattern, which consists of a negative band at a higher wavelength and a negative-couplet at a lower wavelength, it is clear that the $(-)_{589}$-enantiomer has *P*-helicity, in agreement with the conclusion from the VCD results. Based on reviewing predicted molecular orbital coefficients, the origin of the three dominant ECD signals can be attributed to ligand-to-metal charge transfer transitions (LMCT). These transitions are expected[63] to give rise to signals in the wavelength region around ~ 300 nm. It has been indicated[63] that complexes that exhibit LMCT often have intense coloring, which is the case for a dark-purple **1** under investigation.

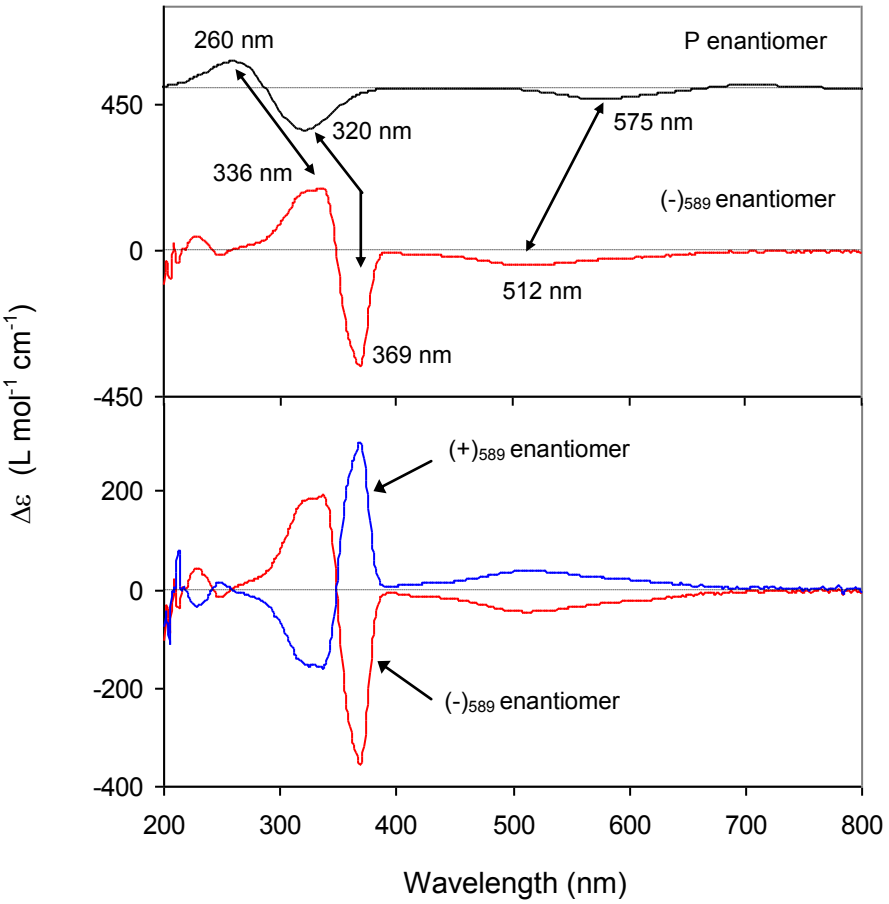

Figure 3-5: ECD spectra of **1**. Experimental ECD spectra are shown for both enantiomers in the bottom panel. The predicted spectrum for *P*-**1** (topmost trace) was obtained with time-dependent BHLYP/LANL2DZ.

The experimental ORD spectrum in the 400-650 nm region for the $(-)_{589}$-enantiomer shown in Figure 3-6 exhibits a negative-positive-negative feature, which is reproduced by the ORD predicted for the *P*-helical structure. Since wavelength range at which OR is measured (633 - 365 nm) is in a resonant region, meaning near the wavelength of the electronic transitions, the quantum mechanical predictions of ORD have been avoided[29]. Instead, the predicted ORD spectrum has been obtained via Kramers-Kronig transform of the predicted ECD

data. As for the ECD, the predicted positive ORD maximum at 533 nm and zero crossing positions at 458 and 573 nm are shifted from the corresponding positions (436, 414, and 500 nm, respectively) in the experimental ORD. These shifts are not unusual because it is well-known[64] that DFT calculations do not yield accurate wavelengths for the electronic transitions.

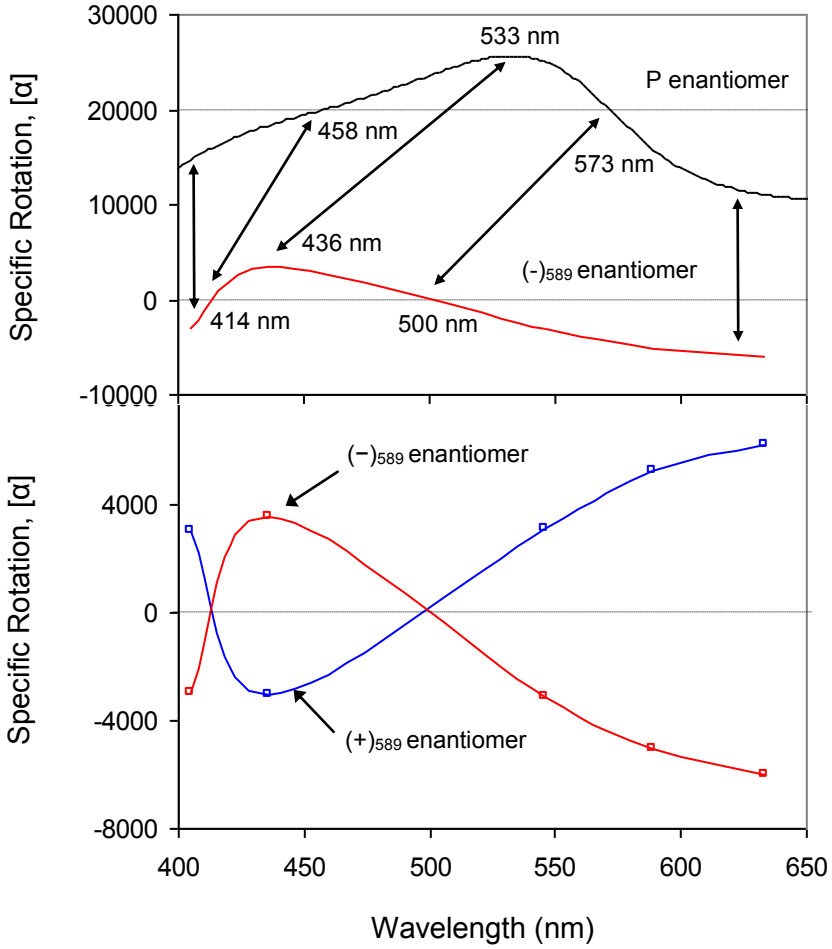

Figure 3-6: ORD spectra of **1**. The bottom panel shows experimental spectra for the two enantiomers, while the top panel shows a comparison between the predicted ORD for the *P* enantiomer of **1** and the experimental spectrum for the $(-)_{589}$ enantiomer of **1**.

Conclusion

Due to its relatively rigid structure, trinickel(II) complex of dipyridylamine ($Ni_3(dpa)_4Cl_2$) exhibits one dominant helical conformation in solution. The highly satisfactory reproduction between the theoretical and experimental chiroptical spectra (VCD, ECD, and ORD) leads to the indisputable conclusion that the $(-)_{589}$-enantiomer of **1** has the *P*-helical configuration and, conversely, the $(+)_{589}$-enantiomer of **1** has the *M*-helical configuration. This work contributes to the evidence that chiroptical methods can be used as a reliable probe of the absolute configuration for chiral metal-complexes.

CHAPTER IV

ABSOLUTE STEREOCHEMISTRY OF CHIRAL BIPHENANTHRYLS: 2,2'-DIPHENYL-[3,3'-BIPHENANTHRENE]-4,4'-DIOL

Introduction

Substituted biphenanthryl compounds are of importance because the biphenanthryl groups are present in a variety of natural and synthetic compounds; they provide expanded opportunities for chiral recognition and have the necessary skeleton needed for chiral molecular motors[65,66]. For example, 1,1',2,2',3,3',4,4'-octahydro-4,4'-biphenanthrylidine skeleton was used for a molecular motor[65,66]. In addition, biphenanthryl molecules also belong to an important class of chiral polycyclic aromatic hydrocarbons with significant environmental interest. In chemical synthesis, the group of compounds that contain phenanthryl groups are considered to have an important role. In particular, 2,2'-diphenyl-[3,3'-biphenanthrene]-4,4'-diol, also known as VAPOL, and its derivatives have been identified[67-69] as highly effective enantioselective catalysts and ligands. Their utility spans a range of asymmetric reactions such as Diels-Alder[70,71], imino-aldol[72], and aziridination[73-75] reactions. Numerous studies have solidified[76] the evidence that biphenanthryl compounds induce asymmetric reactions over a wide range of substrates and provide high yields. Enantiopure species and the knowledge of their absolute configurations are needed for applications in asymmetric syntheses.

The conformation (dihedral angle between the two phenanthryl groups) has not been determined unambiguously for substituted biphenanthryl molecules

in general, although that information is necessary to establish the absolute configuration. As such there are two contradictory assignments[77-79] made for the absolute configurations of 3,3'-dihydroxy-4,4'-biphenanthryl and 3,3'-methoxy-4,4'-biphenanthryl. The absolute configurations for 10,10'-dihydroxy-9,9'-biphenanthryl, 10,10'-dimethoxy-9,9'-biphenanthryl, 2,2'-dihydroxy-1,1'-biphenanthryl, 2,2'-methoxy-1,1'-biphenanthryl have been suggested[80,81] in the literature, but they have not yet been independently confirmed.

There are no prior VCD studies on biphenanthryl compounds. The molecule closest to biphenanthryl class of molecules that has been studied by VCD is 1-(9-phenanthryl)ethylamine[82]. In that work, the vibrational bands originating from methyl antisymmetric deformation and NH_2 deformations have been discussed, but the vibrations originating from phenanthryl group have not been. Infrared spectra of phenanthrene single crystals were reported by several authors[83-86] but some uncertainties in vibrational assignments remain. The infrared spectra of phenanthrene and alkyl-substituted phenanthrenes in CS_2 or $CHCl_3$ solvents were reported[87] to contain intense absorption bands at 1600 and 1500 cm^{-1}. Also the 1500-900 cm^{-1} region was reported to be dense with several bands appearing in this region. The bands at 870, 810 and 730 cm^{-1} were noted to be influenced by substitution. However, there is no discussion on the assignment of vibrations of phenanthrene group. The vapor phase infrared spectra of phenanthrene were reported by *Cane et al*. and with the help of density functional theoretical predictions, vibrational assignments were suggested[88]. The infrared spectrum of phenanthrene predicted with B3LYP

functional were compared to the gas phase infrared spectrum[89] or single crystal infrared spectrum[90]. In all of these papers the focus was on identifying the symmetry representation of the observed bands, but vibrational mode descriptions were not provided. Thus there is a need for understanding the vibrational modes of phenanthrene itself. No literature reports could be found on the vibrational spectroscopy of biphenanthryl compounds.

The electronic spectra of phenanthrene have been analyzed[91,92] in detail using C_{2v} point group symmetry. However, the irreducible representations of this point group are not used by the ECD community for specifying the electronic states. Instead, the spectroscopic notation of Platt[93,94] is used for the analysis of ECD spectra. The five lowest energy electronic transitions, namely ^1L_b at 353 nm, ^1L_a at 303 nm, ^1B_b at 254 nm, ^1C_b at 212 nm and ^1B_a at 187 nm have been identified[93,94] in the visible spectrum. Of these ^1B_b transition is the most intense and is polarized along the long-axis of phenanthrene. Thus to apply exciton chirality ECD method[18] for chiral biphenanthryl compounds one looks for ^1B_b absorption band and analyzes the associated bisignate ECD band. A positive bisignate ECD couplet associated with ^1B_b band indicates that the long axes of two phenanthryl groups make a right handed screw sense; a negative bisignate ECD couplet indicates left handed screw sense[18]. However, for practical applications the identification of ^1B_b band might not be easy when this band overlaps with those from other electronic transitions appearing in the same wavelength range. The exciton chirality method[18] is useful for rigid molecules and when transitions associated with chromophores under consideration are isolated

(not overlapped by the transitions from the remaining parts of the molecule). However, in majority of the cases, a given molecule may exist in different conformations and the electronic transitions of chromophores under consideration need not be well separated from other transitions in the molecule. Thus there are situations where exciton chirality method may not be easily applicable. Some of the substituted biphenanthryl molecules are representatives of such difficult examples for the application of exciton chirality method. As an illustration of the difficulties in assigning the absolute configuration of phenathryl compounds using exciton chirality ECD method a few examples noted in the literature are summarized here. 1) Hattori *et al.*[81] assigned (+)-(a*R*) configuration for 1,1'-biphenanthryl-2,2'-diol, based on the formation mechanism of cyclic diester with 1,1'-binaphthalene-2,2'-dicarbonyldichloride. The (a*R*) configuration of 1,1'-biphenanthryl-2,2'-diol has two long axes oriented with negative chirality, so the authors expected a negative ECD couplet for ^1B_b transition, but a positive ECD couplet was found for (+)-1,1'-biphenanthryl-2,2'-diol and its methoxy derivative. This discrepancy was thought to arise from the overlap with a second transition polarized along the short axis. Thus biphenanthryl molecules are considered to be difficult to analyze[81] with the exciton chirality ECD method. As a result, the exciton chirlaity method is known to have limited applicability for the compounds containing phenanthrene chromophores. 2) Based on ^{1}H NMR studies the absolute configuration of 1-(9-phenanthryl)-2-naphthoic acid and 1-(9-phenanthryl)-2-naphthalene methanol were assigned as (–)-(a*S*). The exciton chirality ECD method required several assumptions because the observed ECD

spectra of these compounds gave complex ECD patterns and it was not clear which ECD band corresponds to which electronic transition. Based on chemical correlation and X-ray results, the configurational assignment was reversed[95] as (+)-(a*S*). 3) For assigning the absolute configuration of 1-(9-phenanthryl)ethylamine, a bichromophoric derivative obtained by complexing 1-(9-phenanthryl)ethylamine with naphthimido chromophore was synthesized. The exciton chirality ECD method suggested the configuration of 1-(9-phenanthryl)ethylamine to be (+)-(a*S*). But this assignment had to be reversed[82] based on: a) the stereochemical outcome of catalytic hydrogenation; b) VCD studies on 1-(9-phenanthryl)ethylamine; and c) ECD studies on Zn-porphyryn complex, where all three methods suggested (+)-(a*R*) assignment. Thus the exciton chirality ECD method could not be used[82] for determining the absolute configuration of 1-(9-phenanthryl)ethylamine. To give a balanced view, it should be mentioned that exciton chirality ECD method did provide easier assignment for the absolute configuration in some cases. For 4,4'-biphenanthrene-3,3'-diol, and its thiol analogue, a simple negative ECD couplet was found to be associated with the ^1B_b absorption band and this couplet did correlate with the absolute configuration[96]. Nevertheless, it should be remembered that this method is prone to give incorrect absolute configuration when a) observed ECD is complicated (because ^1B_b band is overlapped with other electronic transitions); b) it is not clear which electronic transition is responsible for which ECD band; and c) the predominant conformation (dihedral angle 3-4-4'-3' in the case of 4,4'-biphenanthryl) is not known.

In place of exciton chirality ECD method, semi-classical theoretical models such as Devoe's polarizability model[97] have also been applied[96] for biphenanthryl compounds in the literature. However these models are approximate in nature and do not enjoy the reliability required for sound interpretation in the current times.

Optical rotation at 589 nm is routinely reported by synthetic chemists whenever a compound is synthesized. However ORD data are not routinely reported. There are no prior experimental reports, nor theoretical studies, on the ORD spectra of any of the biphenanthryl compounds.

From the literature survey provided in the previous paragraphs, it is clear that there are wide gaps in the spectroscopic and structural information on chiral molecules containing biphenanthryl groups. The latest developments in chiroptical spectroscopic methods can be used to fill some of these gaps. These developments include theoretical formalism[98-100] and its subsequent implementation in the quantum mechanical programs within the density functional framework for VCD. Additionally, following the first quantum mechanical prediction of optical rotation[25], remarkable advances have taken place in the prediction of ORD using density functional and coupled cluster theories[4,101]. Around the same time, density functional theoretical methods for ECD predictions[102-109] have appeared. These density functional theoretical predictions of VCD, ECD and ORD for biphenanthryl compounds have not been reported.

In this chapter we report structural investigations on one of the chiral biphenanthryl compounds, namely 2,2'-diphenyl-[3,3'-biphenanthrene]-4,4'-diol and known as VAPOL, using VCD, ECD and ORD. The absolute configuration of VAPOL was previously suggested[67] as (+)-(a*S*) based on the X-ray diffraction structure of its phosphoric amide derivative, rather than of VAPOL itself. An independent verification of this assignment is reported here. In addition it is useful to know the predominant conformation of VAPOL in solution phase, which may or may not be same as that in crystalline phase.

Experimental Section

VCD, ECD, and ORD Spectra: Both enantiomers of VAPOL have been purchased from Strem Chemicals and used as received. The absorption and VCD spectra were recorded on a commercial Fourier Transform VCD spectrometer, Chiralir, in the 2000-900 cm^{-1} region. The VCD spectra were recorded with one-hour data collection time at 4 cm^{-1} resolution. Spectra were measured in CH_2Cl_2 solvent at 0.136M concentration for (–)- and (+)-enantiomers respectively. The sample was held in a demountable cell with BaF_2 windows and a path length of 100 μm. In the absorption spectrum presented (Figure 4-2), the solvent absorption was subtracted out and the region ~1294-1248 cm^{-1} has been removed from experimental traces due to interference from strong solvent absorption. The VCD spectrum presented here (Figure 4-2) is obtained as the difference between the VCD spectra of enantiomers and the result multiplied by 0.5.

The ECD spectra (Figure 4-3) were recorded on a Jasco J720 instrument, using 0.01 cm pathlength quartz cell. The optical rotations at five discrete wavelengths (633, 589, 546, 436, 405 nm) have been measured (Figure 4-4) with a 1 dm cell using an Autopol IV polarimeter. ECD and ORD measurements were done at the respective concentrations of 9.28×10^{-4} M and 9.76×10^{-4} g/ml in CH_2Cl_2 solvent.

Calculations: All calculation were undertaken with Gaussian 03[35] program using B3LYP functional and 6-31G* basis set. For biphenanthryl molecules with axial chirality, the structure is regarded as an elongated tetrahedron[18] and either one of the two pairs of ortho-carbons is assigned the first two priorities using Cahn and Ingold rules. These priorities are shown in Figure 4-1. Keeping the lowest priority atom (#4) away from the observer, the sequence from high priority (#1) to lower priority atom (#3) shown in Figure 4-1 depicts a counter-clockwise rotation and hence (a*S*) configuration. Starting from the coordinates of crystal structure[110], the C_2 symmetric conformation shown in Figure 4-1, with (a*S*)-configuration, was used for geometry optimization, and for predicting VCD, ECD and ORD properties. Selected parameters of the B3LYP/6-31G* optimized and crystal structures are summarized in Table 4-1. To obtain VCD, ECD and ORD properties for (a*R*) configuration, those obtained for (a*S*) configuration were multiplied by (–1). From the calculated vibrational frequencies, the C_2 symmetric conformation considered was found to represent the minima on the potential energy surface, as there are no imaginary frequencies.

The theoretical absorption and VCD spectra (Figure 4-2) were simulated with Lorentzian band shapes and 5 cm^{-1} half-width at half-peak height. The predicted vibrational band positions (Table 4-2) are normally higher than the experimental vibrational band positions and therefore the calculated frequencies have been scaled by a factor of 0.9613. The theoretical ECD spectra (Figure 4-3) were simulated from the first 20 singlet → singlet electronic transitions using Lorentzian band shapes and 10 nm half-width at half-peak height. The predicted electronic transition wavelengths (Table 4-3) are reported as such without any scaling. The electronic absorption spectra (Figure 4-3) are presented as molar extinction coefficient (in $L \cdot mol^{-1} \cdot cm^{-1}$), derived from dimensionless oscillator strength. The peak extinction coefficient of i^{th} band, ε_i^0, is related to oscillator strength, f_i, as $\varepsilon_i^o = 7.369 f_i \frac{\lambda_i^2}{\Delta_i}$ where Δ_i is the half-width at 1/2 of Lorentzian band.

Results and Discussion

Referring to the structural parameters in Table 4-1, and atom numbering in Figure 4-1, it can be noted that the O-H, C-O and C-C bond lengths are not significantly different among isolated VAPOL (B3LYP/6-31G* optimized) and crystal structures. The O-H bonds are coplanar with the phenanthryl groups in isolated VAPOL molecule, while in crystal structure, the O-H groups deviate from coplanarity by about 5° (compare the dihedral angle 2-1-9-3). The phenyl groups are oriented at ~57° (the dihedral angle, 3-6-14-15) relative to the phenanthryl

groups in isolated molecule, while crystal structure indicates this relative orientation to be ~53°. The phenanthryl groups in isolated molecule are oriented at ~84° (the dihedral angle, 9-3-35-43) which is different from ~73° obtained from crystal structure. This comparison illustrates the influence of packing interactions in the crystal structure, because of which the crystal structure can deviate[111] from that of isolated molecule.

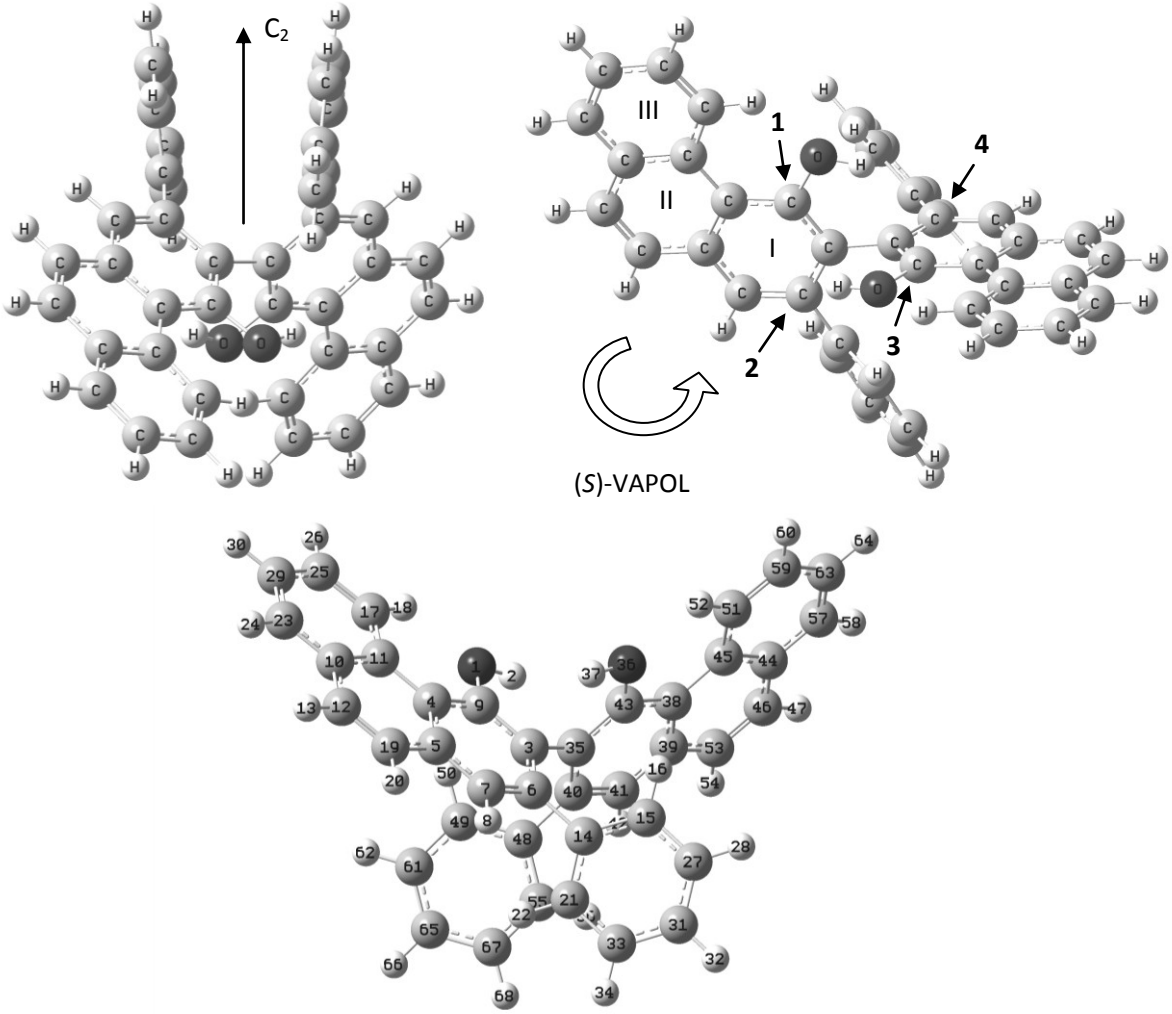

Figure 4-1: Chemical structure of 2,2'-diphenyl-[3,3'-biphenanthrene]-4,4'-diol (VAPOL) displaying C_2-symmetry (top left), numerical priority designations (top right) aiding the configurational assignment of the theoretical model and atomic numbering (bottom) for identifying the bond lengths and angles.

Table 4-1: Comparison between selected parameters of B3LYP/6-31G* optimized and crystal structure of (a*S*)-VAPOL.

Parameter[a]		B3LYP/6-31G* optimized structure	crystal structure
Bond/angle	Atom #		
H-O-C-C	D(2,1,9,3) = D(37,36,43,35)	-0.341	5.855
C-C-C-C	D(3,6,14,15) = D(35,40,48,49)	56.927	52.657
C-C-C-C	D(9,3,35,43)	84.319	73.061
H-O-C	A(2,1,9) = A(37,36,43)	107.396	109.419
O-H	B(2,1) = B(37,36)	0.977	0.838
C-O	B(1,9) = B(36,43)	1.366	1.372
C-C	B(3,35)	1.504	1.502

[a] D: dihedral angle (deg); A: angle (deg); B: bond length (Å). See Figure 4-1 for atom numbers.

The experimental vibrational absorption spectrum in the 1700-900 cm^{-1} region is compared to the corresponding predicted spectrum in Figure 4-2. This mid infrared region is dense with numerous vibrational bands, just as noted for phenathrene[87]. There are 25, either individual or groups of, absorption bands that exhibit one-to-one correspondence between experimental and theoretical absorption spectra. Although there are differences in relative-intensities among experimental and predicted absorption bands, the overall qualitative correlation is remarkably good. As the absorption spectra are sensitive to the conformation, the qualitatively satisfactory agreement seen among experimental and predicted vibrational absorption spectra can be used to suggest that the conformation used for the calculations is probably close to that adopted by VAPOL in CH_2Cl_2 solvent.

The assignment of absolute configuration depends on satisfactory comparison between experimental and calculated VCD spectra. The predicted

VCD spectrum for (a*R*)-VAPOL is compared to the experimental VCD spectrum of (-)-VAPOL in Figure 4-2. There are 24, either individual or groups of, VCD bands that display one-to-one sign correspondence and good paralleling of relative intensities between the experimental and theoretical VCD traces. This satisfactory correlation among the VCD signals in experimental and predicted spectra leads to an unambiguous assignment that the (a*R*)-configuration corresponds to the (–)-enantiomer of VAPOL.

The vibrational assignments for molecules containing biphenanthryl groups have not been reported before. Therefore the origins for the B3LYP/6-31G* predicted fundamental vibrational transitions, as deduced from GaussView program, are presented in Table 4-2. The fused-rings of phenanthryl groups have been designated as I, II, and III in order to facilitate the description of vibrational motions. Referring to Table 4-2 and Figure 4-2, the vibrational origins of dominant VCD bands can be deduced as follows. The large positive VCD band (#18) seen for (–)-VAPOL at 1493 cm^{-1} corresponds to two predicted vibrational modes at 1481 and 1472 cm^{-1}. Of these two, the former (originating from C-C stretching between the phenanthryl groups) has larger VCD intensity than the latter (originates from antisymmetric C-O-H bending). The large negative VCD band (#16) at 1444 cm^{-1} corresponds to two predicted vibrational modes both at ~1432 cm^{-1}, but one belonging to “A” symmetry representation and the other to “B” representation. They both originate from the C-C stretching and C-C-H bending motions of phenyl rings. The positive VCD band (#14) at 1390 cm^{-1} corresponds also to two predicted vibrational modes at 1364 cm^{-1} and 1360 cm^{-1}

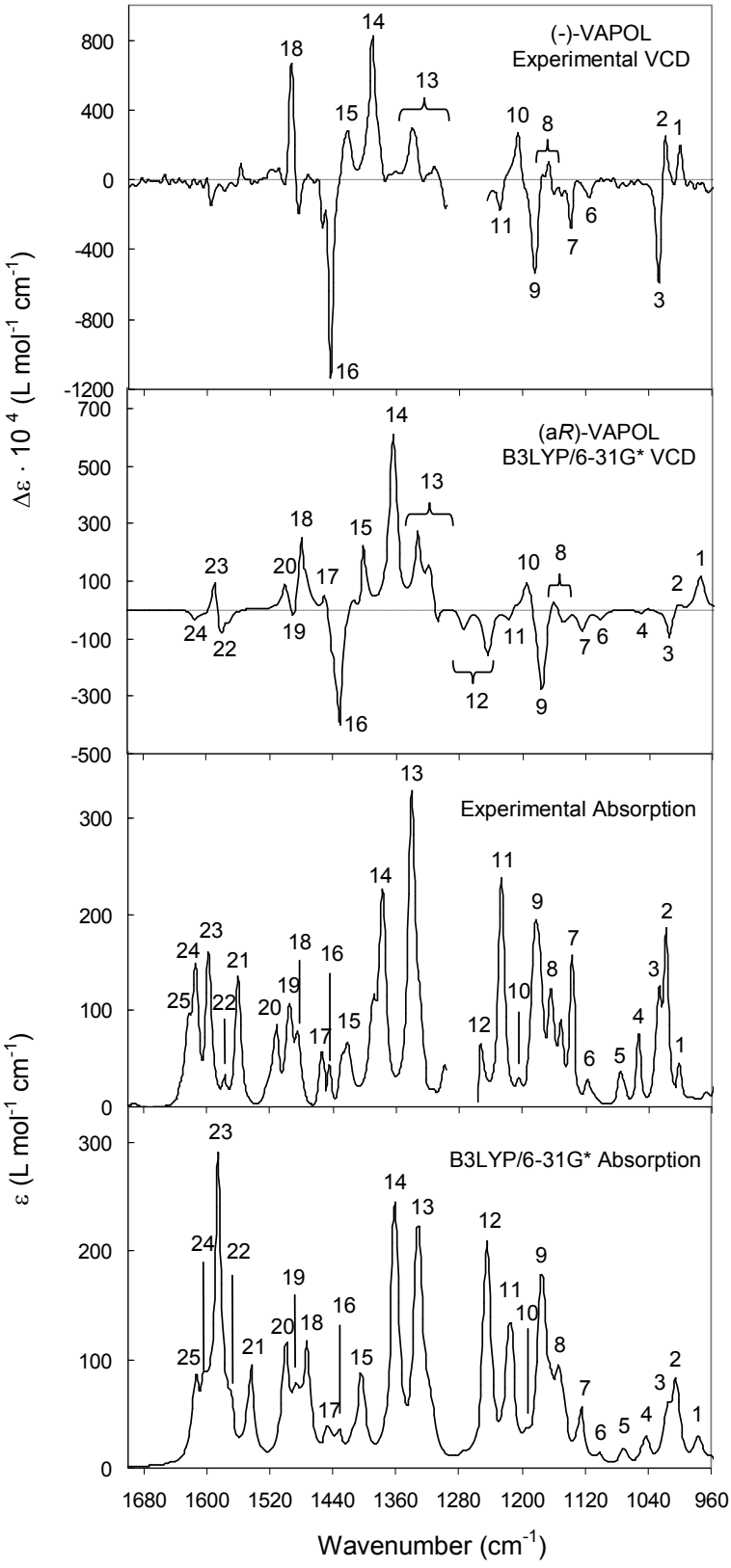

Figure 4-2: Comparison of theoretical and experimental absorption spectra (bottom two traces) and theoretical and experimental VCD spectra (top two traces) for VAPOL.

Table 4-2: Vibrational frequencies, intensities and assignments for (a*R*)-(–)-VAPOL.

(a*R*)-VAPOL (–)-VAPOL

No[a]	Sym[b]	ν^{c}_{scal}	IR[d]	R[e]	ν^{f}_{abs}	ν^{g}_{vcd}	Vibrational Assignments
1	B	974.8	5.494	35.264	1000.9	(+),999.05	antisymmetric breathing modes of rings I and III.
	A	978.4	2.807	9.357			symmetric breathing modes of phenyl rings.
	B	979.0	1.700	4.268			antisymmetric breathing modes phenyl rings.
2	A	1003.8	26.088	12.306	1018.3	(+),1018.3	symmetric breathing modes and C-O-H bending of phenanthryl groups.
3	B	1014.4	16.544	-40.564	1026.0	(-),1026.0	antisymmetric breathing modes and C-O-H bending of phenanthryl groups.
	A	1019.2	0.045	0.267			symmetric breathing mode and C-H bending of phenyl rings.
	B	1020.0	3.255	2.652			antisymmetric breathing mode and C-H bending of phenyl rings.
4	B	1042.8	9.075	3.184	1053.0		antisymmetric breathing mode and C-H bending of rings III.
	A	1042.9	0.012	0.651			symmetric breathing mode and C-H bending of rings III.
	A	1049.5	0.449	-4.522			symmetric breathing modes of phenanthryl groups and C-C stretch between phenanthryl groups.
5	B	1070.2	2.665	2.909	1076.2		antisymmetric C-C stretching and C-H bending of phenyl rings.
	A	1070.9	2.692	-2.078			symmetric C-C stretching and C-H bending of phenyl rings.
6	B	1101.5	3.213	-9.816	1116.7	(-),1116.7	antisymmetric C-O-H bending; C-H bending of phenanthryl groups.
7	B	1125.0	14.766	-52.608	1137.9	(-),1137.9	antisymmetric C-O stretching; C-H bending of phenanthryl groups.
	A	1125.3	3.363	29.554			symmetric C-O stretching; C-H bending modes of phenanthryl groups.
8	A	1145.7	0.059	-2.374	1162.9	(-),1159.1, (+),1166.8	symmetric C-O stretching; C-H bending of phenanthryl groups.
	B	1146.6	6.516	-5.967			antisymmetric C-O stretching; C-H bending of phenanthryl groups.
	A	1147.1	0.052	-0.253			symmetric C-H bending of phenyl rings.
	B	1147.4	2.038	1.137			antisymmetric C-H bending of phenyl rings.
	A	1152.0	9.191	-23.417			symmetric C-H bending of rings III .
	B	1153.9	14.739	22.013			antisymmetric C-H bending of rings II and III.
9	A	1163.0	16.596	19.896	1182.2	(-),1184.2	symmetric C-O-H bending; C-H bending of phenanthryl groups.
	B	1171.2	0.456	0.894			antisymmetric C-H bending of phenyl rings.
	A	1171.8	3.504	8.162			symmetric C-H bending of phenyl rings.
	B	1175.1	62.759	-102.264			antisymmetric C-O-H bending; C-C stretching and C-C-H bending of rings I; C-H bending of rings III.
10	A	1194.4	4.509	31.845	1205.4	(+),1205.4	symmetric C-C stretching, C-H bending of rings II and III.
	B	1199.5	0.199	3.859			antisymmetric C-C stretching, C-H bending of rings II and III.
11	A	1212.3	10.130	12.066	1226.6	(-),1228.5	symmetric C-H bending of phenanthryl groups.
	B	1216.2	41.801	-15.880			antisymmetric C-O-H bending; antisymmetric C-H bending of rings I and III.
12	A	1242.4	21.229	-15.955	1251.7		C-C stretching between phenanthryl groups; symmetric C-O stretching.
	B	1244.9	50.307	-2.257			antisymmetric C-O-H bending.
	A	1245.1	4.905	-30.172			symmetric C-O-H bending.

Table 4-2, cont.:

	B	1263.7	0.567	0.310			antisymmetric C-O-H bending; C-C stretching and C-C-H bending of rings III.
	A	1273.7	1.734	-18.043			C-C stretching between phenanthryl groups; symmetric C-O-H bending.
	B	1279.1	0.161	-3.116			antisymmetric Kekule stretching[h] of phenyl rings.
	A	1282.5	0.011	1.813			symmetric Kekule stretching[h] of phenyl rings.
13	A	1310.1	0.843	-33.562	1340.4	(+),1311.5 , (+),1340.4	symmetric C-O stretching and C-O-H bending.
	B	1314.1	5.809	17.262			antisymmetric C-C stretching and C-C-H bending of phenyl rings.
	A	1315.9	0.265	-5.563			symmetric C-C stretching and C-C-H bending of phenyl rings.
	B	1317.5	11.533	36.666			antisymmetric C-O stretching and C-O-H bending.
	A	1323.7	1.034	3.684			symmetric Kekule stretching[h] of rings III.
	B	1323.9	7.762	-2.356			antisymmetric Kekule stretching[h] of rings III.
	A	1331.8	18.822	-70.615			symmetric C-O-H bending; symmetric Kekule stretching[h] of rings I.
	B	1332.1	63.572	143.271			antisymmetric C-O-H bending; antisymmetric Kekule stretching[h] of rings I
14	B	1360.1	66.299	3.829	1377.0	(+),1390.5	antisymmetric C-O stretching; C-C(O)-C bending of rings I.
	A	1364.1	29.087	157.425			symmetric C-O stretching; C-C(O)-C bending of rings I.
15	B	1402.2	15.406	94.313	1421.4	(+),1423.3	antisymmetric C-O-H bending; antisymmetric Kekule stretching[h] of rings II.
	A	1404.8	15.815	-52.865			symmetric C-O-H bending; symmetric Kekule stretching[h] of rings II.
	B	1415.0	5.758	17.114			antisymmetric C-C stretching and C-C-H bending of phenanthryl groups.
	A	1415.3	0.026	-3.522			symmetric C-C stretching and C-C-H bending of phenanthryl groups.
16	B	1431.9	4.780	-67.121	1444.5	(-),1444.5	antisymmetric C-C stretching and C-C-H bending of phenyl rings.
	A	1432.4	3.387	-37.905			symmetric C-C stretching and C-C-H bending of phenyl rings.
17	B	1442.4	4.292	-29.959	1454.2		antisymmetric C-O-H bending; C-H bending of phenanthryl groups.
	A	1447.6	7.196	31.491			C-C stretching between phenanthryl groups; symmetric C-O-H bending; C-H bending of phenanthryl groups.
18	B	1472.3	35.951	13.298	1485.0	(+),1492.7	antisymmetric C-O-H; C-C stretching and C-C-H bending of rings I and II; C-H bending of rings III and phenyl rings.
	A	1480.8	8.529	68.538			C-C stretching between phenanthryl groups; symmetric C-O-H bending; C-C stretching and C-C-H bending of rings I and II; C-H bending of rings III and phenyl rings.
19	B	1486.9	10.390	-17.103	1494.7		antisymmetric C-C stretching between phenanthryl and phenyl groups; antisymmetric C-O-H bending; C=C stretching and C-C-H bending of phenyl rings.
	A	1489.1	5.323	-14.714			symmetric C-C stretching between phenanthryl and phenyl groups; symmetric C-O-H bending; C=C stretching and C-C-H bending of phenyl rings.
20	A	1497.7	0.000	-0.057	1512.0		symmetric C-C stretching between phenanthryl and phenyl groups; C=C stretching of phenanthryl groups and C-C-H bending of rings III.
	B	1500.3	40.147	23.609			antisymmetric C-C stretching between phenanthryl and phenyl groups; C=C stretching of phenanthryl groups and C-C-H bending of rings III.
21	B	1544.1	15.380	-5.374	1560.2		antisymmetric C=C stretching of phenanthryl groups and C-C-H bending of rings III.
	A	1544.3	16.487	6.729			symmetric C=C stretching of phenanthryl group and C-C-H bending of rings III.

Table 4-2, cont.:

22	A	1570.5	1.530	7.455	1577.6		symmetric C=C stretching and C-C-H bending of phenyl rings.
	B	1570.8	11.619	-15.997			antisymmetric C=C stretching and C-C-H bending of phenyl rings.
23	B	1585.0	62.454	-109.079	1598.8		antisymmetric C=C stretching and C-C-H bending of rings I.
	A	1586.4	43.015	110.592			symmetric C=C stretching and C-C-H bending of rings I.
24	B	1597.8	3.729	-14.331	1614.3		antisymmetric C=C stretching and C-C-H bending of phenyl rings.
	A	1597.8	2.749	12.711			symmetric C=C stretching and C-C-H bending of phenyl rings.
	A	1603.0	2.512	16.667			symmetric C=C stretching and C-C-H bending of rings III.
	B	1603.1	14.069	-19.212			antisymmetric C=C stretching and C-C-H bending of rings III.
25	B	1614.2	19.350	-8.934	1622.0		antisymmetric C=C stretching and C-C-H bending of rings II.
	A	1614.5	4.958	1.714			symmetric C=C stretching and C-C-H bending of rings II.

a: Numbers for individual or group of bands as given in Figure 4-2.
b: Symmetry representation.
c: B3LYP/6-31G* predicted frequencies scaled with 0.9613 in cm^{-1}
d: B3LYP/6-31G* predicted IR intensities in km/mol.
e: B3LYP/6-31G* predicted Rotational strengths in 10^{-44} esu^2cm^2.
f: Experimental frequencies of absorption bands in cm^{-1}
g: Experimental signs and frequencies (in cm^{-1}) of VCD bands.
h: Kekule mode: alternative bond stretching in a ring.

with the former originating from the symmetric C-O stretching vibration and latter from antisymmetric C-O stretching vibration. Even though simple conceptual models predict bisignate VCD associated with symmetric and antisymmetric C-O stretching vibrations, because of their coupling with other vibrational motions, the symmetric and antisymmetric C-O stretching vibrations here are predicted to have the same sign and to appear at nearly the same frequency, although the symmetric C-O stretching mode is predicted to have much larger VCD than its antisymmetric counterpart. The larger negative VCD bands (#9, #3) seen at 1184 and 1026 cm^{-1} for (–)-VAPOL appear to arise from the overlap of modes from

phenanthryl and phenyl rings. In general it is difficult to assign a given observed VA or VCD band to only one particular vibrational mode, as several vibrations can contribute to the same region of the observed VCD band.

The experimental electronic absorption spectrum exhibits two resolved components with strong absorption intensity at ~270 nm. These components are not resolved in the predicted electronic absorption spectrum where one broad strong intensity band is present. Similarly the two resolved weak electronic absorption bands seen in the experimental spectrum between 330 and 380 nm appear as one broad weak unresolved absorption band at 330 nm in predicted spectrum. However, examination of Table 4-3 and Figure 4-3 indicates that the strong predicted absorption at ~270 nm has contributions from several transitions, although transitions 15 and 16 are the dominant ones; the weak absorption band at ~330 nm has contributions from transitions 1 and 2. Except for the minor differences pertaining to resolution in the simulated spectra, the predicted electronic absorption spectrum compares favorably with the experimental electronic absorption spectrum (Figure 4-3). This favorable comparison can be used to suggest that the conformation used for calculations is probably close to that adopted by VAPOL in CH_2Cl_2 solvent.

ECD has been widely used in the literature, with exciton chirality model, for assigning absolute configuration. However, as mentioned in the introduction, this empirical method does not give unambiguous conclusion when multiple bisignate ECD couplets are present in the ECD spectra. This turns out to be the situation for VAPOL, where the ECD spectrum of (–)-VAPOL (Figure 4-3) exhibits

a negative band at 316 nm (which is very broad covering from 290-370 nm), a strong positive band at 271 nm, a weak negative band at 259 nm and a strong positive band at 239 nm. In the absence of additional experimental information, one could interpret the experimental ECD spectrum to contain a negative couplet (316 (–)/271 (+)), a positive couplet (271 (+)/259 (–)) and a negative couplet (259 (–)/239 (+)). Depending on the way these couplets are construed, the empirical exciton model can yield contradictory conclusions about absolute configuration. On the contrary, the B3LYP/6-31G* predicted ECD spectrum for (a*R*)-VAPOL faithfully reproduced the experimental ECD spectrum for (–)-VAPOL, as can be seen in Figure 4-3 where the correlation between band signs and positions is indicated by the dotted lines. Note that the electronic transitions predicted with the B3LYP/6-31G* basis set are known to appear[64] at longer wavelengths than those in the experimental spectra, and no attempt has been made to correct the predicted transition wavelengths. In the predicted ECD spectrum the positive band at 259 nm has contributions (see the inset in Figure 4-3) from transitions 16 and 20 and the negative band at 272 nm has contribution from transition 15. Considerable cancellation occurs between positive and negative contributions from transitions 16 and 15, because of small wavelength difference between these transitions. Similar cancellation occurs between the ECD intensities associated with transitions 11 and 12 and with transitions 1 and 2. Some contribution to the negative band at 272 nm also comes from transition 12. Transition 11 contributes to the positive band at 286 nm. The pleasing correspondence seen between the ECD spectra of (a*R*)-VAPOL and (–)-VAPOL

verifies, independent of conclusions from VCD spectra, that the absolute configuration is (–)-(a*R*).

Table 4-3: Symmetry, transition wavelengths, oscillator strengths and rotational strengths of (*a*R)-VAPOL predicted with B3LYP/6-31G* for 20 electronic transitions.

No.	Symmetry Representation	Wavelength (nm)	Oscillator Strength	Rotational strength[a] (10^{-40} erg·esu·cm/Gauss)
1	A	329.4	0.0343	88.1
2	B	329.3	0.1411	-142.5
3	B	315.9	0.0061	-8.9
4	A	313.4	0.0023	8.9
5	A	306.3	0.0051	37.6
6	B	304.4	0.0133	-24.8
7	B	298.4	0.108	-8.9
8	A	296.0	0.0001	-0.1
9	A	289.2	0.0009	1.9
10	B	289.1	0.0831	11.3
11	A	281.2	0.1674	435.1
12	B	277.7	0.1069	-287.3
13	B	277.4	0.4494	11.5
14	A	272.9	0.0442	18.0
15	B	268.6	0.9184	-1336.6
16	A	264.6	0.5739	1239.6
17	B	258.4	0.0114	-23.3
18	A	255.1	0.0005	1.9
19	B	253.4	0.0339	-67.1
20	A	253.0	0.1002	199.9

[a]velocity representation

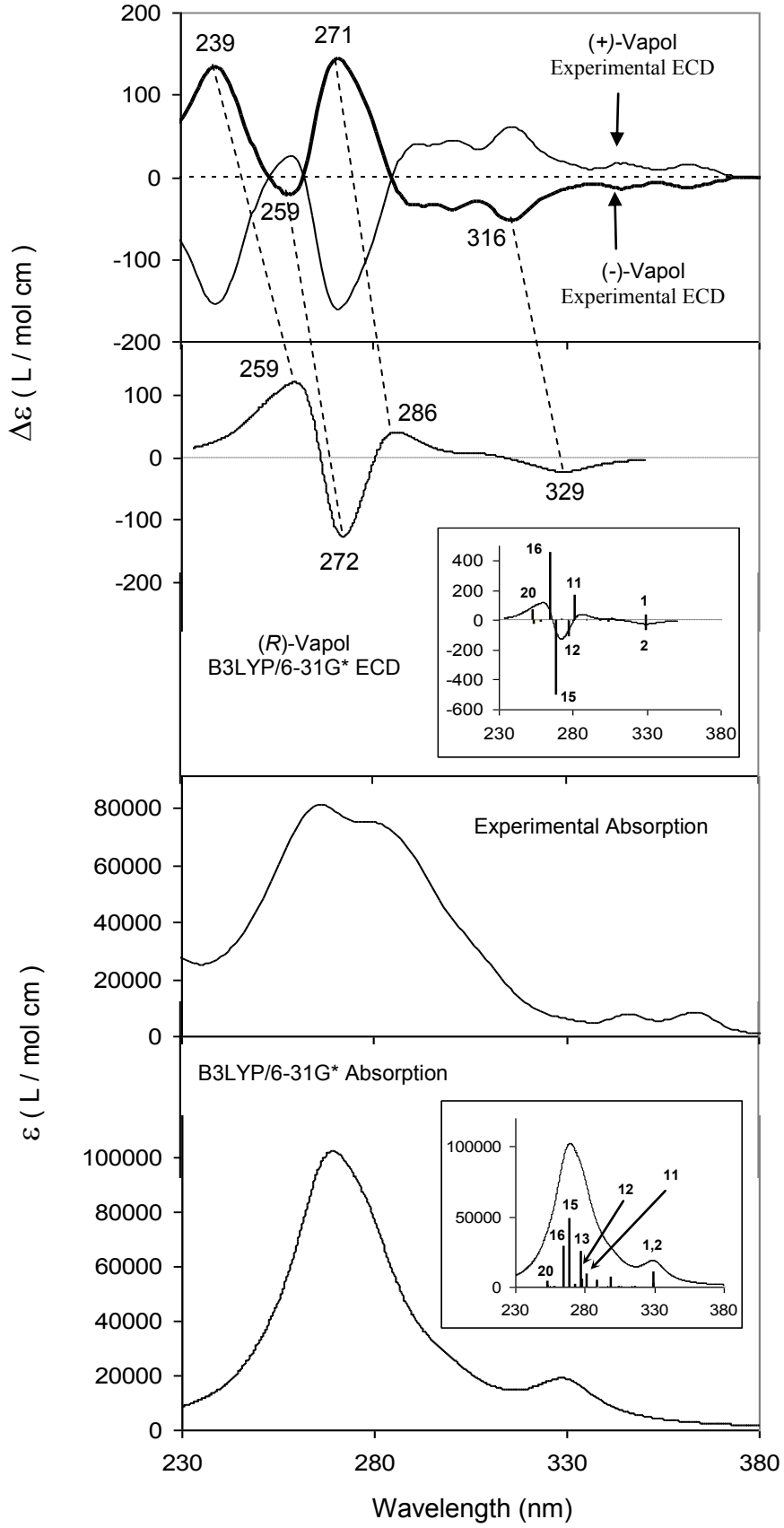

Figure 4-3: Comparison of theoretical and experimental electronic absorption spectra (bottom two traces) and theoretical and experimental ECD spectra (top two traces) for VAPOL.

As a third independent verification of the configurational assignment, the experimental ORD data of (–)-VAPOL have been compared to the predicted ORD of (a*R*)-VAPOL in Figure 4-4. In principle, the wavelengths used for ORD predictions should be shifted[29] from those used for experimental ORD measurements because the B3LYP/6-31G* predicted electronic transition wavelengths appear at higher wavelengths[64] than those experimentally observed. However, no attempt has been made here to correct for the transition wavelength differences as these differences between predicted and observed transition wavelengths do not influence the conclusions here. This is because, the predicted ORD for (a*R*)-VAPOL and experimental ORD of (–)-VAPOL, are both monosignate at all wavelengths investigated and these ORD spectra can be shifted along wavelength scale as a whole relative to each other without influencing any conclusions derived here. The experimentally obtained values of specific rotation are –78.6 at 633, –142.4 at 589, –177.6 at 546, –820.0 at 436, and –1681.0 at 405 nm. The predicted specific rotation values for (a*R*)-VAPOL are –36.9 at 633, –46.8 at 589, –62.7 at 546, –240.4 at 436, and –477.3 at 405 nm. There is a qualitatively satisfactory agreement between the experimental specific rotations for (–)-enantiomer and the corresponding values for (a*R*)-VAPOL. This agreement in signs of optical rotation, and the trend in ORD spectra (increasingly negative at shorter wavelengths), support the conclusions about absolute configuration derived from VCD and ECD data. Thus all three chiroptical spectroscopic methods independently suggest that the absolute configuration of

VAPOL is (–)-(a*R*), which is in agreement with that derived from X-ray diffraction data of its phosphoric amide derivative[67].

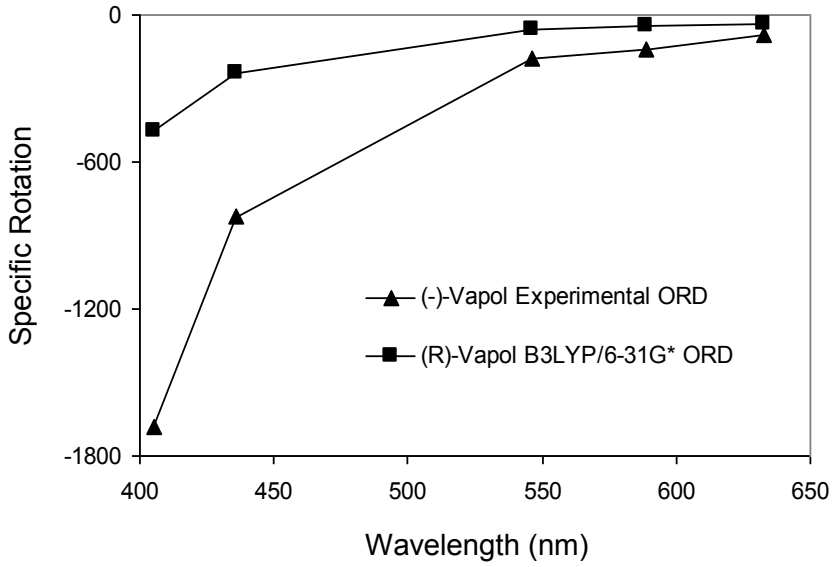

Figure 4-4: Comparison of ORD predicted for (a*R*)-VAPOL with experimental ORD data of (-)-VAPOL.

Conclusion

The comparison between experimental and predicted data associated with VCD, ECD and ORD have indicated that one dominant conformation is present in solution and that the (a*R*)-configuration belongs to (–)-enantiomer of VAPOL. Both VCD and ECD spectra are rich in observed bands, thereby providing multiple bands for comparison between experimental and theoretical data. These multiple band comparisons increase the confidence of the configurational assignment. ORD independently confirmed this assignment. The vibrational origins of the observed bands in VAPOL have also been deduced for the first time from the predicted vibrational modes.

CHAPTER V

ABSOLUTE CONFIGURATION AND CONFORMATIONS OF SULFOXIDE-CONTAINING CHIRAL MOECULES

Introduction

Chiral sulfoxides[112,113] are of considerable importance as bioactive compounds and synthetic intermediates in enantioselective asymmetric syntheses. There are numerous examples in which chiral sulfoxides play a major role in preparing a final chiral product. Satoh and Kuramochi have reported[114] the synthesis of chiral allenes by first coupling alkenyl aryl sulfoxides with aldehydes, followed by alkyl anion induced elimination of the sulfur. Toru and coworkers have reported[115] the enantioselective addition of Grignard reagents to 1-(arylsulfinyl)-2-naphthaldehyde, where a chiral sulfoxide conformer controls stereoselectivity of the addition. The same group has reported[116] the use of a chiral sulfoxide to synthesize an insecticidal chiral chrysanthamate. Ellman and coworkers[117-119] and Yuste *et al.*[120] have independently described the use of sulfoxides in asymmetric synthesis of β-amino alcohols, which, in turn, are synthetically useful chiral building blocks. Colobert *et al.*[121] and Bravo *et al.*[122] have demonstrated the use of chiral sulfoxides in the synthesis of myo-inositol, pyrrolidine and tetrahydroisoquinoline alkaloids.

Within the rich family of sulfoxides, chiral sulfinamides are also notable for their versatile utility as chiral building blocks. Sulfinamides have proven to be efficient chiral auxiliaries[123-126] and catalysts[127,128] in the enantioselective asymmetric synthesis of many organic compounds that are important for the

development of active pharmaceutical ingredients and intermediates. Specifically, sulfinamides have been applied in the synthesis of enantiopure sulfinimines[112,124,129,130] as precursors for α- and β-amino acids[130-132], α- and β-aminophosphonates[133,134] and chiral amines[135,136]. Oxidation of sulfinamides yields[137] sulfonamides, which have been suggested[138] to have applications in medicinal chemistry. Sulfinamide derivative, peptidosulfinamide, has found application[139] for the development of HIV protease inhibitors.

Over the years, chiral sulfoxides and sulfinamides have clearly demonstrated wide versatility as chiral auxiliaries in stereoselective and asymmetric synthesis. However, the applicability of these compounds necessitates a reliable determination of their absolute stereochemistry. In this chapter, chiroptical spectroscopic methods are used for assigning stereochemistry of 1,1-dimethyl-2-phenylethyl phenyl sulfoxide **1** (Figure 5-1), t-butanesulfinamide[128,140-145] **2** (Figure 5-2) and N-phenylethyl-t-butylsulfinamide **3** (Figure 5-3).

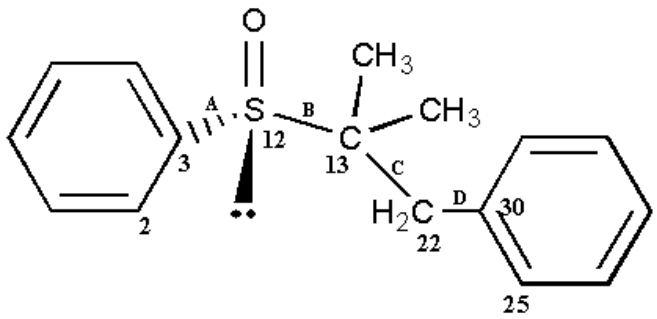

Figure 5-1: The chemical structure of (*R*)-1,1-dimethyl-2-phenylethyl phenyl sulfoxide (**1**).

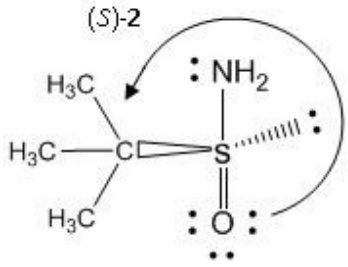

Figure 5-2: The chemical structure of (*S*)-t-butanesulfinamide (**2**)**.**

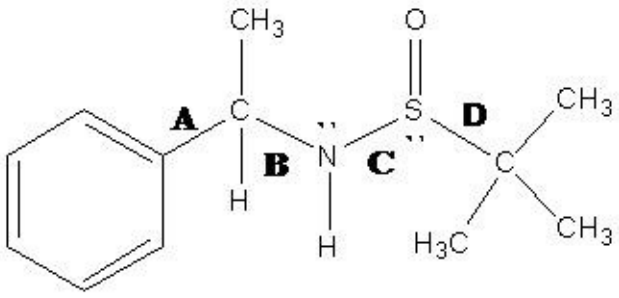

Figure 5-3: The chemical structure of N-phenylethyl-t-butylsulfinamide (**3**).

It should be noted that the absolute configuration of **1** has been incorrectly assigned in prior literature[146] and the stereochemical assignment is reestablished through the present investigation with a high degree of confidence. The absolute configuration of **2** has been suggested[117] before using the synthetic scheme as (*R*)-(+), but no prior reports indicate the predominant conformation(s). The absolute configuration and predominant conformations of **3** are established here for the first time.

Experimental Section

The chiral sulfoxide **1** was synthesized and provided to us by Armstrong *et al.*[147]. Both enantiomers of sulfinamide **2** have been purchased from Strem Chemicals and used as received. Both diastereomers of chiral sulfinamide **3** were synthesized and provided to us by Drabowicz *et al*.

VCD Spectra: The vibrational absorbance (VA) and VCD of **1**, **2** and **3** were recorded on a commercial Fourier transform VCD spectrometer Chiralir, modified[15] to reduce the level of artifacts. The spectral measurement of **1** was made at concentration of 0.1355 M in CCl_4 solvent in a fixed-pathlength cell with BaF_2 windows and 200 μm spacer. The spectra of **1** were recorded with 90 min data collection time at 4 cm^{-1} resolution. It should be noted that the experimental VCD of **1** is not displayed in two regions (1136–1211 cm^{-1} and 1066–1035 cm^{-1}). The first region has been eliminated due to the presence of an artifact, and the second region has been eliminated because of the interference from solvent absorption.

The spectra of **2** were measured in CH_2Cl_2 solvent at 0.413 M concentration, in a variable pathlength cell with BaF_2 windows and 135 μm pathlength. The data collection time was 1 hr at 4 cm^{-1} resolution. The region ~1300-1250 cm^{-1} has been excluded due to interference from strong solvent absorption. The concentration dependent VA spectra of **2** have been recorded in the 50-10 mg/mL (0.413-0.0825 M) range in CH_2Cl_2 solvent to examine presence of dimers, but the evidence for dimer formation was not apparent.

The spectra of (+)-diasteromer (*pSNA*) and (–)-diastereomer (*mSNA*) of **3** were obtained with 3 hr data collection time, at 4 cm^{-1} resolution, in a variable pathlength cell with BaF_2 windows. Measurements were done in CCl_4 solvent. A combination of two pathlengths and two concentrations has been used in order to optimize the absorption signal in the entire region of the VCD measurement. For *pSNA,* 140 μm pathlength and 0.175 M concentration have been used to optimize a high-intensity absorption and VCD signals in the ~ 1043-1103 cm^{-1} region, while signals in the remaining region have been optimized with 300 μm pathlength and 0.189 M concentration. For *mSNA,* 170 μm pathlength and 0.138 M concentration have been used to optimize a high-intensity absorption and VCD signals in the ~ 1028-1103 cm^{-1} region, while signals in the remaining region have been optimized with 200 μm pathlength and 0.343 M concentration. Signal optimization implies obtaining absorption intensity between 0.2 and 1. The concentration dependent VA spectra of **3** have also been recorded in the ~ 77-15 mg/mL (0.343-0.067 M) range in CCl_4 solvent to examine presence of dimers, but no evidence of dimer formation was apparent for either diastereomer.

ECD Spectra: ECD of all three samples was measured on a Jasco J720 spectrometer. The ECD of **1** was recorded using 0.1 cm pathlength cell and sample concentration of 0.00465 M in hexane. To aid a comparison with predicted data, experimental ECD intensity of **1** was scaled-up by a factor of six. The ECD of **2** was recorded using 0.01 cm pathlength cell and 0.0825 M concentration in CH_2Cl_2. The electronic absorption (EA) of **2** was recorded under same conditions on a Cary-4E UV-VIS spectrometer. ECD spectra of **3** were

recorded using 0.01 cm pathlength cell with 0.0195 M *pSNA* and 0.0213 M *mSNA* in hexane.

ORD Spectra: The optical rotations at six discrete wavelengths (633, 589, 546, 436, 405, 365 nm) have been measured with a 1 dm cell using an Autopol IV polarimeter. Solutions of **1** were measured at concentrations in the range 0.00465–0.000581 M in CCl_4. ORD measurements of **2** were obtained at a 0.0825 M concentration in CH_2Cl_2. The concentration-dependent ORD measurements of **3** have been recorded at concentration-ranges $38.6 \cdot 10^{-3}$ – $3.0 \cdot 10^{-4}$ g/mL (0.0865 – 0.0006 M) for *pSNA* and $19.5 \cdot 10^{-3}$ – $1.5 \cdot 10^{-4}$ g/mL (0.1713 – 0.0013 M) for *mSNA*. Intrinsic rotations were deduced for generating the experimental ORD traces.

Calculations: Geometry optimizations and chiroptical predictions of **1**, **2** and **3** were undertaken with Gaussian 98[34] and Gaussian 03[35]. All of the calculations have been based on the density functional theory (DFT) and have utilized B3LYP functional. The optimizations of **1** involving simultaneous rotations around bonds A and D (Figure 5-1) have been performed with ModRedundant option using Gaussian 98. The basis sets used in the calculations were 6-31G* and/or aug-cc-pVDZ. The study of **2** examines the suitability of these two basis sets for reliably predicting the chiroptical spectroscopic properties of sulfinamides.

The theoretical absorption and VCD spectra were simulated with Lorentzian band shapes and 5 cm^{-1} half-width at 1/2 of peak height. The frequencies calculated with 6-31G* basis set were scaled by a factor[148] of

0.9613. The theoretical ECD spectra of **1** were simulated from the first 25 singlet→singlet electronic transitions using Gaussian band shapes and 20 nm half-width at 1/e of peak height. The theoretical ECD spectra of **2** and **3** were simulated from the first 30 singlet→singlet electronic transitions using Lorentzian band shapes and 20 nm half-width at 1/2 of peak height. Rotational strength values, calculated with velocity representation, have been used for the ECD spectral simulations. The predicted ECD intensities of **3** have been scaled-up by a factor of six in order to facilitate a qualitative comparison with the experimental traces.

The EA spectral intensities were derived from dimensionless oscillator strengths. The peak extinction coefficient of i^{th} band, ε_i^o (in L·mol^{-1}·cm^{-1}), is related to oscillator strength, f_i, as $\varepsilon_i^o = 7.369 f_i \frac{\lambda_i^2}{\Delta_i}$ where Δ_i is the half-width at 1/2 of Lorentzian band.

Results and Discussion

1,1-dimethyl-2-phenylethyl phenyl sulfoxide (1):

A consideration of the rotation around four bonds (labeled as A, B, C and D in Figure 5-1), indicating four dihedral angles that can be varied, suggests 3^4 = 81 possible conformations for **1**. Each of the four dihedral angles can be rotated in increments of 120° giving: plus *gauche*, minus *gauche*, and *anti* conformations around each of the four bonds. The rotation around bonds labeled as B and C, which involves varying dihedral angles D(3,12,13,22) and D(12,13,22,30),

respectively (Figure 5-1), is considered first. The three conformations obtained by the variation of each of these dihedral angles are labeled as T, G^+ and G^- (Figure 5-4) depending on the relative orientation of the two largest end-groups defining the dihedral angle. Combination of T, G^+ and G^- conformations associated with the two dihedral angles has resulted in nine distinct conformations: TT, TG^+, TG^-, G^+T, G^+G^+, G^+G^-, G^-T, G^-G^+, G^-G^-. The geometry optimizations of these nine conformations have yielded eight stable conformations since the conformation G^-G^+ has converged into G^-T. A comparison of the electronic energies of the eight sulfoxide conformers has led to the identification of four low energy conformers (G^+T, TG^+, TT and G^-T) that would have significant population. The electronic energies of these eight conformers are given in Table 5-1.

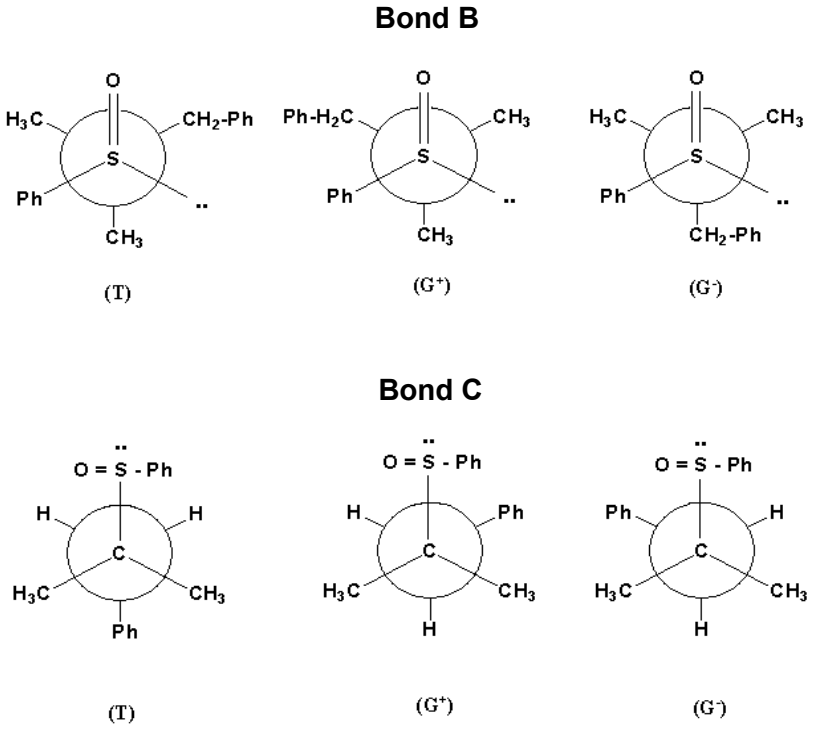

Figure 5-4: Newman projections around bonds B and C for **1**. For bonds B and C see Figure 5-1.

Table 5-1: B3LYP/6-31G* predictions of electronic energies for eight optimized conformers of **1**.

Conformer [a]	Electronic Energies (Hartrees)
TT	–1093.91582442
TG^+	–1093.91629803
TG^-	–1093.91088328
G^+T	–1093.91612233
G^+G^+	–1093.91103237
G^+G^-	–1093.90955477
G^-T	–1093.91534617
G^-G^-	–1093.91194699

[a] T, G+ and G– represent *anti*, plus *gauche* and minus *gauche* conformers. The first letter represents the conformation around bond B and the second letter around bond C.

The four low energy conformers have been subjected to further geometry optimization by incrementally rotating the phenyl groups at the end of bonds A and D. Since the phenyl ring is planar, four rotations of 45° are sufficient. Rotations around bonds A and D correspond to changes in dihedral angles D(2,3,12,13) and D(13,22,30,25), respectively. A comparison of the energies as a function of phenyl ring rotation indicated that four conformations, as summarized in Table 5-2 and displayed in Figure 5-5, are the most stable. Since the magnitudes of optimized dihedral angles D(2,3,12,13) and D(13,22,30,25) are close to 90°, the conformation around Ph–S and Ph–C bonds cannot be classified as *gauche* or *anti*.

These four conformations have been used for calculating chiroptical properties. From the calculated vibrational frequencies, the four conformations are found to represent minima on the potential energy surface, as there are no imaginary frequencies. The theoretically predicted absorbance and VCD spectra have been obtained by scaling the absorption and VCD intensities of each of the

four conformers by their corresponding populations, which are determined using the Gibbs free energies obtained in the VCD calculation. The values of converged dihedral angles discussed above as well as the populations determined from Gibbs free energies are given in Table 5-2.

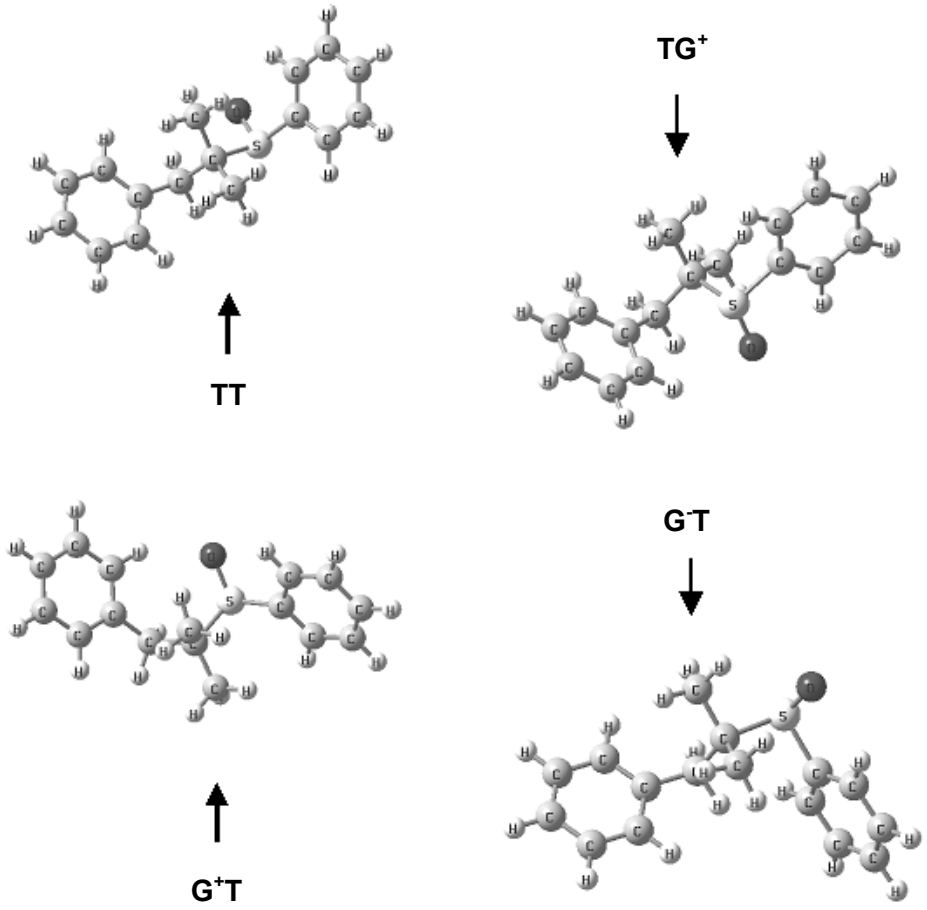

Figure 5-5: B3LYP/6-31G* optimized structures for four conformers of (*R*)-**1**.

Table 5-2: B3LYP/6-31G* predictions of converged dihedral angles, energies and fractional populations of the four minimum-energy conformers of **1**.

Conformers [a]	D [b] (2,3,12,13)	D [b] (3,12,13,22)	D [b] (12,13,22,30)	D [b] (13,22,30,25)	Gibbs energies (Hartrees)	Fractional population
G^+T	85.2	61.3	169.4	–93.6	–1093.661842	0.47
TG^+	85.1	168.3	62.5	–91.9	–1093.661097	0.21
TT	86	178.1	–178.5	–90.4	–1093.660858	0.17
G^-T	87	–64.6	–172.0	–88.2	–1093.660744	0.15

[a] T, G+ and G– represent *anti*, plus *gauche* and minus *gauche* conformers.
[b] D stands for dihedral angle in degrees. The numbers inside the parentheses indicate atom-numbers, as shown in Figure 5-1.

The calculated vibrational absorption spectra for individual conformers and population-weighted predicted vibrational absorption spectrum are compared to the experimental absorption spectrum of **1** in Figure 5-6. The absorption band with largest intensity at 1011 cm^{-1} in the predicted spectrum corresponds to the band at 1047 cm^{-1} in the experimental spectrum. Based on relative intensities and proximity in their positions, the remaining bands in the predicted spectrum at 1048, 1061, 1116, 1370, 1389 cm^{-1} and in the 1500–1450 cm^{-1} region are considered to correspond to the bands in the experimental spectrum at 1072, 1082, 1124, 1364, 1383 cm^{-1} and in the 1500–1400 cm^{-1} region, respectively. In the predicted spectrum, relative intensities of the two bands at 1048 and 1061 cm^{-1} are interchanged and the bands in the 1500–1400 cm^{-1} region are poorly resolved compared to the corresponding experimental bands. The predicted vibrational band positions and corresponding experimental band positions differ

by a significant amount in some cases even after scaling the calculated frequencies. Larger basis sets would be required to eliminate these differences.

The calculated VCD spectra for individual conformers and the population-weighted predicted VCD spectrum for (*R*)-**1** are compared to the experimental VCD spectrum of (+)-**1** in Figure 5-7. As can be seen in these spectra, only a few and weak VCD bands are seen in the experimental VCD spectrum of (+)-**1** and in the predicted spectrum of (*R*)-**1**. The only characterizing VCD signature for this molecule is a negative–positive VCD couplet seen in the experimental spectrum at 1466–1454 cm^{-1}, which is reproduced in the predicted spectrum at 1480–1461 cm^{-1}.

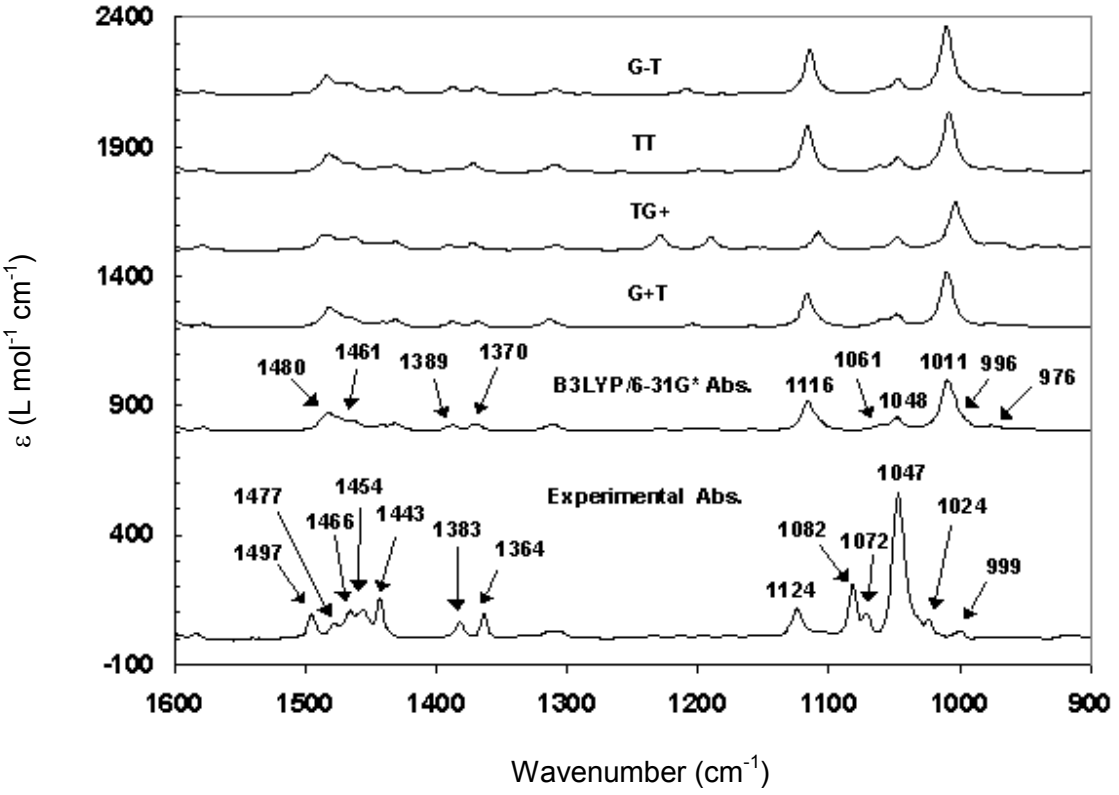

Figure 5-6: B3LYP/6-31G* calculated vibrational absorption spectra for four conformers (top four traces), population-weighted predicted absorption spectrum, and experimental absorption spectrum (bottom trace) of **1**.

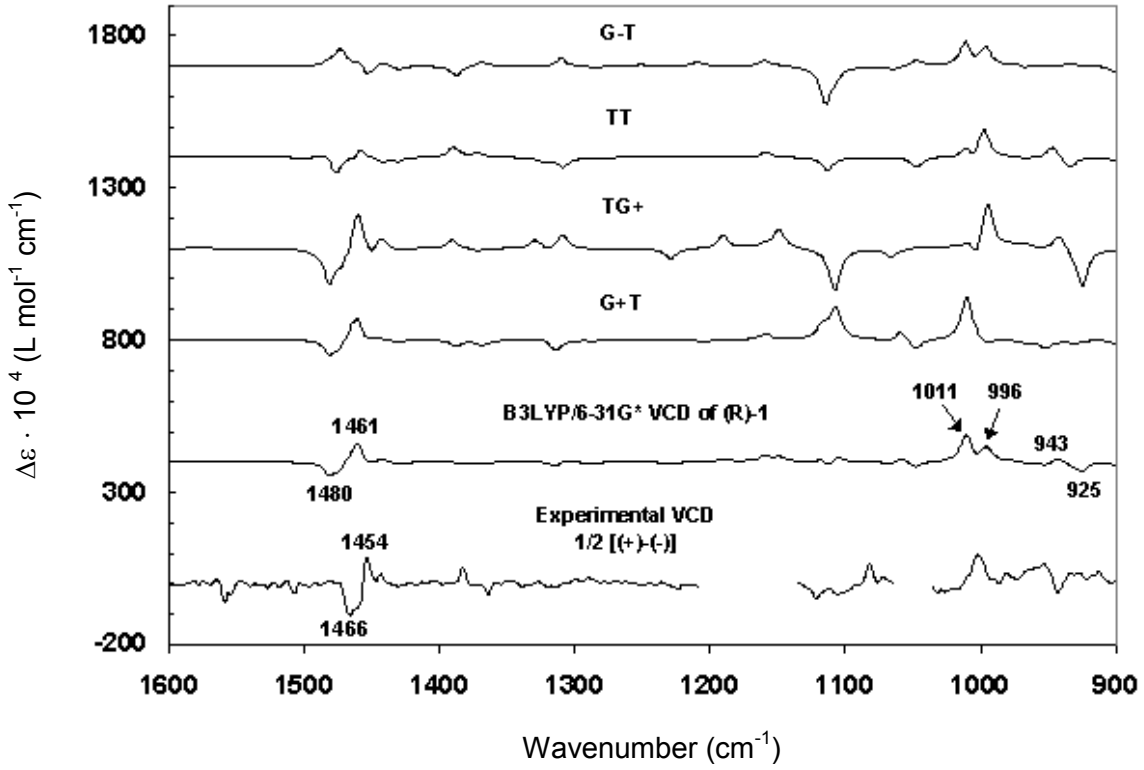

Figure 5-7: B3LYP/6-31G* calculated VCD spectra for four conformers (top four traces), population-weighted predicted VCD spectrum of (*R*)-**1**, and experimental VCD spectrum (bottom trace) of (+)-**1**.

The agreement seen between predicted and experimental VCD (Figure 5-7) bands suggests that the absolute configuration of **1** is (+)-(*R*) or (–)-(*S*). However, because of the limited number of weak VCD bands associated with this molecule it is prudent to verify this conclusion with other chiroptical spectroscopic methods, optical rotation (OR) and ECD.

The experimental optical rotations and specific rotations for (+)-**1** as a function of concentration are shown at 589 and 365 nm in Figure 5-8. The experimental value of intrinsic rotation (specific rotation at infinite dilution) is +79 ± 4 at 589 nm and (+5.7 ± 0.1) × 10^2 at 365 nm. The specific rotations were

predicted for the four optimized conformers with (*R*)-configuration. The population-weighted specific rotation, obtained with populations given in Table 5-2, are +148 at 589 nm and +858 at 365 nm. Even though the magnitudes of predicted specific rotation are 2 times larger than those of observed intrinsic rotation, the sign of rotation predicted for (*R*)-**1** supports the absolute configuration (+)-(*R*) assigned to **1** from VCD data. For a quantitative agreement between observed and predicted rotations, one has to consider the additional factors such as higher level basis sets and solvent influence.

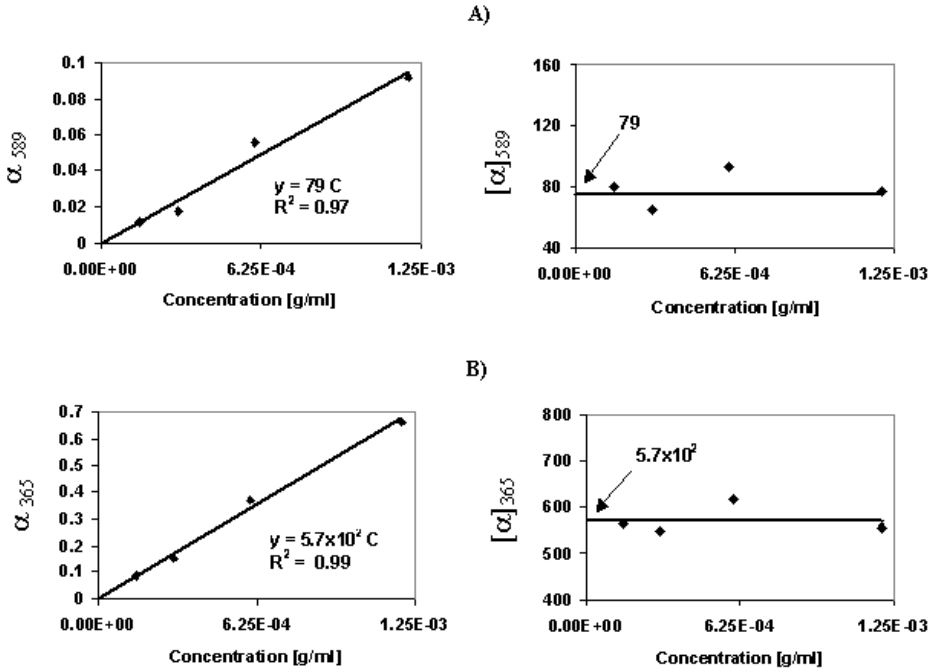

Figure 5-8: The experimental optical rotation (left panels), *α*, and specific rotation (right panels), [*α*], of (+)-**1** as a function of concentration at 589 nm (top panels) and 365 nm (bottom panels).

The ECD spectra calculated for individual conformers along with the population-weighted ECD spectrum are compared to the experimental ECD

spectrum of (+)-**1** in Figure 5-9. In the experimental spectrum presented, ECD intensities were scaled up by a factor of 6. The experimental ECD spectrum shows a broad positive ECD band in the long wavelength region and a negative ECD band in the shorter wavelength region. The same features are seen in the population-weighted predicted spectrum, thus confirming the (+)-(*R*)-**1** assignment derived from VCD and OR data.

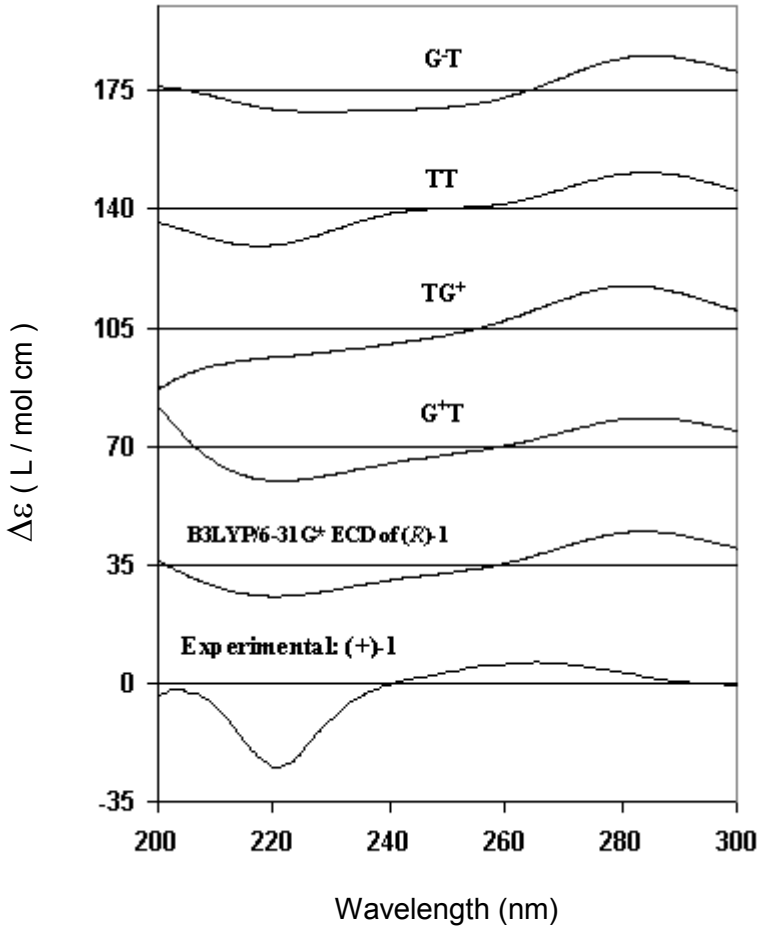

Figure 5-9: B3LYP/6-31G* calculated ECD spectra for four conformers (top four traces), population-weighted predicted ECD spectrum of (*R*)-**1**, and experimental ECD spectrum (bottom trace) of (+)-**1**.

t-butanesulfinamide (2):

The conformational search has been performed on (*S*)-configuration of **2** (Figure 5-2) by starting with staggered and eclipsed forms (Figure 5-10). The set of initial conformations has been generated by incremental 60° rotation of the amine group for both staggered and eclipsed forms. As a result of optimization, two stable conformations of **2** have been identified, both in the staggered form (Figure 5-11). These conformations have been further optimized with aug-cc-pVDZ basis set.

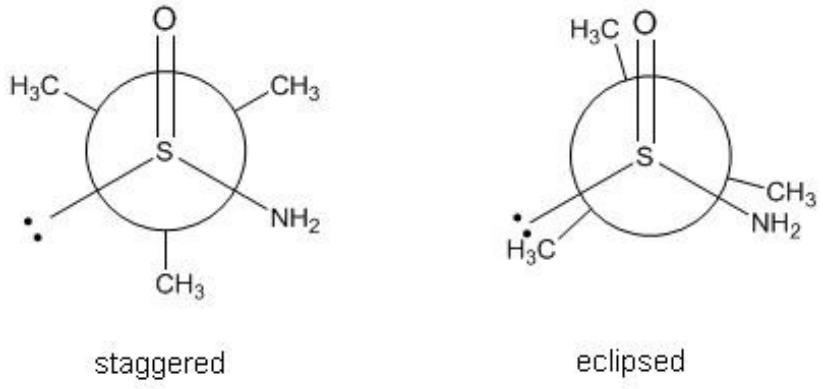

Figure 5-10: Newman projections of staggered and eclipsed forms of **2** used for conformational search.

Comparison of the Gibbs free energies of two stable conformers (Table 5-3) indicates that conformation 1 has lower energy and is significantly more populated than conformation 2. The main difference among these two conformers is in the orientation of amine hydrogens with respect to S=O group. Both amine hydrogens are gauche to S=O in conformer 1, while one amine

hydrogen is trans to S=O in conformer 2. Structural parameters of the optimized conformers (Figure 5-11) are summarized in Table 5-3.

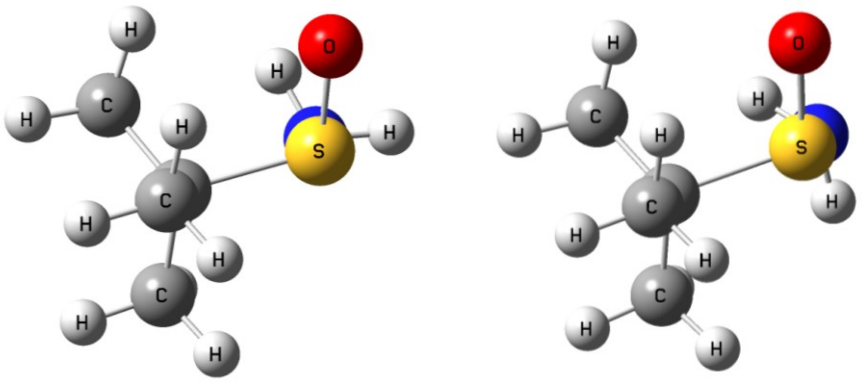

Figure 5-11: Structures of the two converged conformers of **2**.

Table 5-3: Dihedral angles, bond lengths, Gibbs free energies and relative populations of two optimized conformers of **2.**

parameter[a]	Conformer 1		Conformer 2	
	6-31G*	aug-cc-pVDZ	6-31G*	aug-cc-pVDZ
D(O-S-N-H)	-34.08	-31.37	169.49	171.49
D(N-S-C-C)	-59.25	-57.51	-61.76	-59.61
D(O-S-C-C)	54.75	55.23	49.64	50.61
R(O….H(N))	2.74	2.70	3.47	3.48
R(O….H(N))	3.04	3.05	2.88	2.87
G	-687.050044	-687.117780	-687.043572	-687.112372
Relative Populations	0.999	0.997	0.001	0.003

[a]D = dihedral angle (deg); R = distance (Å); G=Gibbs energy in Hartrees.

The comparison between experimental and theoretical VA and VCD spectra of **2** in the 900-1800 cm^{-1} range is given in Figure 5-12. Panel A displays the comparison between experimental VA spectrum and theoretical VA spectra

for both conformers of **2**. A highly satisfactory qualitative agreement between the predicted VA spectrum of conformer 1 and the experimental VA spectrum can be seen, at both basis-set levels. Specifically, the ten labeled bands in Figure 5-12A correlate qualitatively well both in frequency positions and relative intensities. The agreement is much less satisfactory when the experimental VA spectrum is compared with the theoretical VA spectrum predicted for conformer 2. This observation can be used to suggest that the negligible population predicted for conformer 2 in vacuum may not have been changed by the solvent used for experimental measurements. Based on the predicted vibrational displacements for conformer 1, the vibrational origins of ten bands in the mid infrared regions are summarized in Table 5-4.

Table 5-4: Vibrational origins of mid-infrared bands predicted with B3LYP functional and 6-31G* and aug-cc-pVDZ basis sets for conformer 1 of (S)-(–)-**2**.

Frequency (cm^{-1})				
Experimental	6-31G*	aug-cc-Pvdz	VCD sign	Vibrational Origin
939	916	944		C–C–C bending modes.
1047	1043	1036	(–)	S=O bond stretching coupled with some NH_2 twisting.
1090	1082	1094	(+)	NH_2 twisting coupled with some S=O bond stretching.
1188	1171	1186		S–C bond stretching.
1227	1224	1255		C–C–C bending modes coupled with C–C bond stretching.
1366	1369	1383		methyl group bending modes.
1393	1397	1412		
1485	1475	1482		
1475	1493	1504		
1560	1585	1584	(–)	NH_2 scissoring.

[a] vibrational frequencies predicted with 6-31G* basis set were scaled with 0.9613.

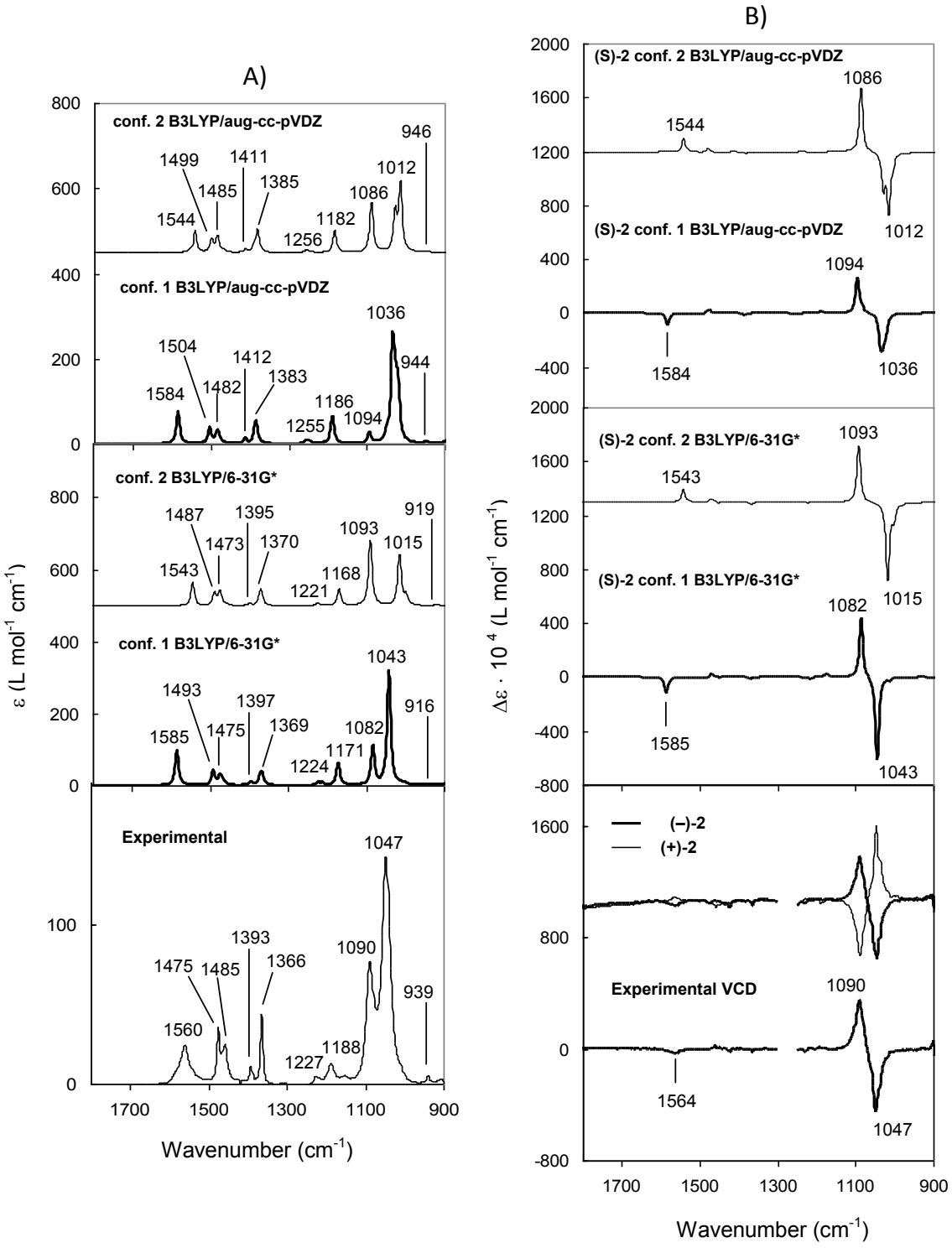

Figure 5-12: Comparison of VA (panel A) and VCD (panel B) spectra between (–)-**2** and both conformers of (S)-**2** at 6-31G* and aug-cc-pVDZ basis sets.

The experimental VCD spectra, displayed in panel B of Figure 5-12, indicate three VCD bands with expected mirror images for the two enantiomers of **2**: a negative VCD couplet (negative VCD at 1047 cm^{-1} and positive VCD at 1090 cm^{-1}) and a negative VCD band at 1564 cm^{-1} for (–)-**2**. The configurational assignment relies on the agreement of these three VCD bands between experimental and predicted VCD spectra. In the predictions obtained with aug-cc-pVDZ basis set, the VCD couplet at (–)1036/(+)1094 cm^{-1} and a weak negative VCD band at 1584 cm^{-1} for conformer 1 of (*S*)-**2** correlate well with the couplet at (–)1047/(+)1090 cm^{-1} and a weak band at (–)1564 cm^{-1} in the observed VCD spectrum of the (–)-**2**. The vibrational origin (Table 5-4) of the predicted VCD couplet is S=O bond stretching coupled with NH_2 twisting, while that of the higher-frequency negative VCD band is NH_2 scissoring. The qualitative agreement with experimental VCD spectra is equally good for predictions with 6-31G* basis set, as it is with aug-cc-pVDZ basis set for conformer 1 of (S)-**2**. Quantitatively, the aug-cc-pVDZ basis set predictions provide a slightly better intensity reproduction of the dominant low-frequency couplet. Although the experimental VCD signs of the dominant couplet are also reproduced in the calculated spectrum for conformer 2, the sign of high frequency experimental VCD band is not reproduced in the calculated spectrum for conformer 2. In the higher frequency region where (–)-**2** exhibits a negative VCD signal, positive VCD signal at 1544 cm^{-1} is predicted for conformer 2 of (*S*)-**2**. This predicted VCD signal also originates from NH_2 scissoring and its mismatch in sign with the experimental observation indicates that conformer 2 is not dominant. Overall, the

VCD spectra predicted with both basis sets provide evidence for the assignment of absolute configuration as (*S*)-(–)-**2**, with conformer 1 being dominant.

Larger discrepancies are noted in the theoretical results obtained with two chosen basis sets for ECD and ORD spectra, unlike in VA and VCD spectra. Figure 5-13 displays the correlation between experimental and predicted EA and ECD spectra. In panel A, the observed EA band at ~ 212 nm seems to correspond to the predicted band for conformer 1 at ~ 215 nm with 6-31G* basis set, and predicted shoulder band at ~ 245 nm with aug-cc-pVDZ basis set. The EA spectrum predicted with 6-31G* basis set for conformer 2 does not show well defined maximum, while that with aug-cc-pVDZ basis set shows a shoulder at ~ 245 nm, as for conformer 1.

Both conformers of (*S*)-**2** display at 6-31G* basis set (Figure 5-13B) a negative ECD band at ~ 199 nm, which qualitatively matches the observed negative ECD band of (–)-**2** at ~ 212 nm. The ECD spectra predicted with aug-cc-pVDZ basis set for both conformers of (*S*)-**2,** contain a negative band at 245 nm which correlates with the negative experimental ECD band at 212 nm of (–)-**2**. The aug-cc-pVDZ predicted ECD spectra also show a positive-going ECD band at shorter wavelength, but a corresponding band in the experimental spectrum is not seen. The correlation between experimental and theoretical ECD spectra seems at first glance to be less optimal with aug-cc-pVDZ basis set, than with 6-31G* basis set. However, it should be noted that the electronic transitions predicted with B3LYP functional appear[61,64] usually at longer wavelengths than the experimentally observed transitions. As a result, the B3LYP/aug-cc-pVDZ

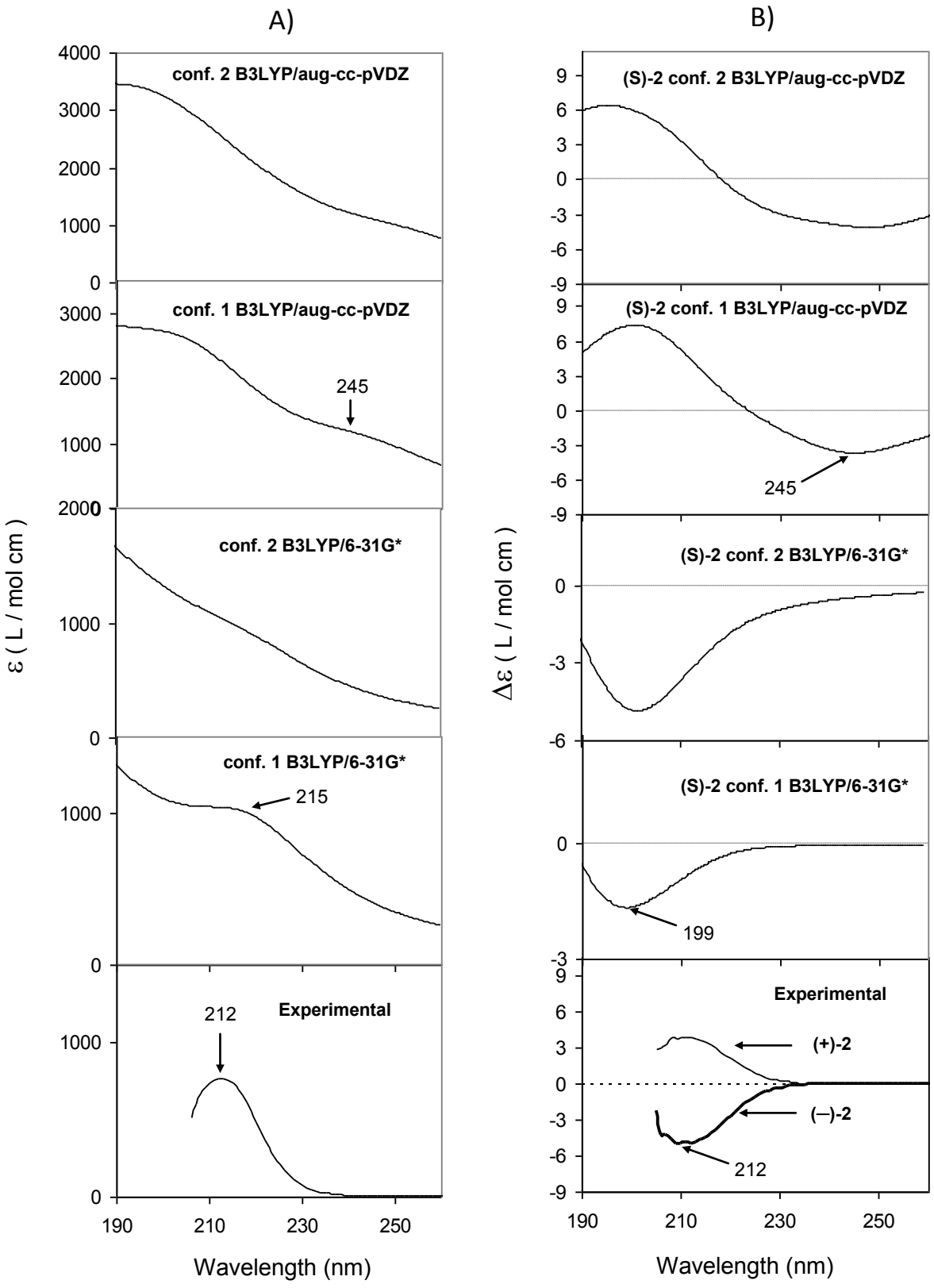

Figure 5-13: Comparison of EA (panel A) and ECD (panel B) spectra between (–)-**2** and both conformers of (S)-**2** at 6-31G* and aug-cc-pVDZ basis sets.

predicted EA and ECD spectra need to be blue shifted. Such blue shift does not appear to be necessary for predictions obtained with the lower-level 6-31G* basis set, which is probably fortuitous. When such blue shift is incorporated for aug-cc-pVDZ predictions, the predicted negative ECD band at 245 nm for (*S*)-**2** matches the experimental ECD band at 212 nm for (–)-**2**. Then the predicted positive ECD band at shorter wavelength will appear below the wavelength range where experimental measurements can be performed. Examination of the predicted molecular orbital coefficients indicate that that the electronic transition giving rise to the negative ECD band predicted with both basis sets originates from S=O group and has n → π* character.

The correlations between experimental ORD observations and theoretical ORD predictions with the 6-31G* and aug-cc-pVDZ basis sets are shown in Figure 5-14, panel A and B respectively. The discrepancy among the ORD theoretical predictions obtained with two basis sets is large to the extent that the conclusions regarding structural elucidation can vary depending on which basis set is considered. This is because, the ORD predictions for two conformers of (*S*)-**2** with lower level 6-31G* basis set have opposite signs. The ORD sign predicted for conformer 2 of (*S*)-**2** matches the experimental ORD of (–)-**2**, while that for conformer 1 of (*S*)-**2** is opposite. This observation would lead to one of the two possible conclusions: either conformer 2 of (*S*)-**2** should be more populated in solution or (–)-**2** should correspond to (*R*)-configuration. On the other hand, the ORD predictions with higher level aug-cc-pVDZ basis set for both conformers of (*S*)-**2** have the same sign as ORD of (–)-**2**, although the

magnitudes of predicted ORD values for conformer 1 are in better agreement with experimental ORD magnitudes. Based on the previously concluded configurational assignment from VCD and ECD spectra, it can be concluded that predictions of ORD with 6-31G* basis set are not reliable for **2**. Therefore this basis set may not do well for ORD calculations on other sulfonamides.

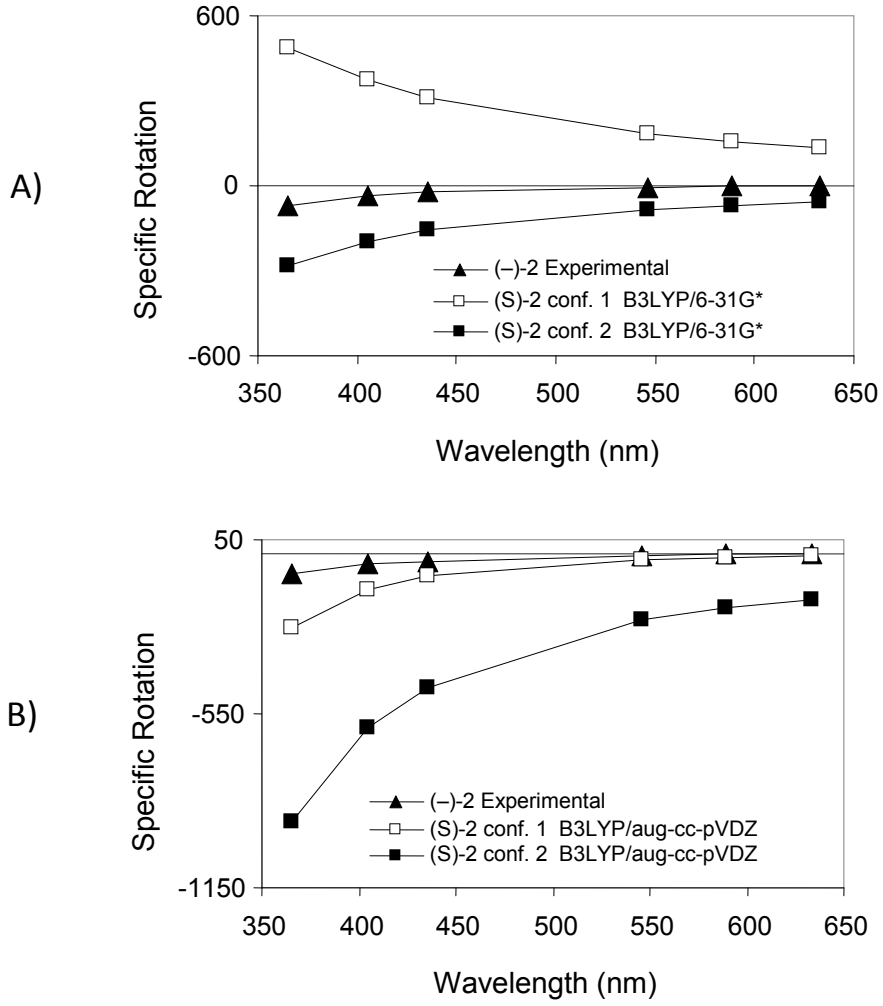

Figure 5-14: Comparison of ORD spectra between (–)-**2** and both conformers of (S)-**2** at 6-31G* (panel A) and aug-cc-pVDZ (panel B) basis sets.

The ORD observations on (*S*)-(–)-**2** also point out the incorrectness of some conclusions reported in the literature. Rosini and coworkers[149] hypothesized that for molecules that exhibit the same sign for longest wavelength ECD band and non-resonant long wavelength optical rotation, optical rotation calculations with smaller 6-31G* basis set should provide correct predictions. The first longest wavelength ECD band for (–)-**2** at 212 nm has negative sign (Figure 5-13B), as does the ORD (Figure 5-14) in the non-resonant long wavelength region (350-650 nm). Yet calculations of ORD for (*S*)-**2** with 6-31G* basis set gave incorrect signs, directly contradicting the conclusion of Rosini and coworkers. Since ECD and ORD data are interrelated[29,32] via Kramers-Kronig transformation, ORD in the long wavelength region can be influenced by several ECD bands in the short wavelength region. Therefore emphasis, or undue confidence, should not be placed on the correlation between the signs of longest wavelength ECD band and non-resonant long wavelength ORD.

The present observations on (*S*)-(–)-**2** also point out that it is important[16] to use multiple chiroptical spectroscopic methods simultaneously for any given molecule. Unless multiple spectroscopic methods lead to the same conclusion, there must be some inadequacy in one or more of these methods. Since ECD and ORD are interrelated[29,32], one cannot be certain of predicted results unless the conclusions reached from ECD and ORD are consistent. While ECD predictions obtained with 6-31G* basis support the assignment of (*S*)-(–)-**2**, the same basis set predictions of ORD concluded the opposite. This discrepancy points to the inadequacy of 6-31G* basis set for ECD and ORD predictions for **2**.

Thus the need for simultaneous investigation of ECD and ORD for a given molecule, as pointed out recently[27], is an important issue that should not be overlooked. Since the conclusions reached from VCD predictions with both 6-31G* and aug-cc-pVDZ basis set about the absolute configuration and conformation of **2** are the same, VCD spectral predictions provide a benchmark against which the predictions of ECD and ORD can be compared. This observation reflects on the advantages of using multiple spectroscopic methods in arriving at unambiguous conclusions on molecular structure.

N-phenylethyl-t-butylsulfinamide (3):

Sulfinamide **3** is a more challenging system for determining molecular stereochemistry. This is because conformational flexibility resulting from four rotatable bonds (Figure 5-3) leads, at least in principle, to 3^4= 81 conformers. Furthermore three stereogenic centers (C, N, S) of **3** lead to 2^3=8 possible diastereomers. As a result one has to consider 81·8 possibilities for establishing the absolute configuration and predominant conformations of **3**. However, since four of the diastereomers are mirror images of the other four, only one set of non-enantiomeric diastereomers need to be investigated. This is because chiroptical spectra of the second set of diasteromers are obtained by multiplying those of the first set by (–1). The four diastereomers selected as theoretical models for geometry optimization and chiroptical predictions are *SSS, SRS, SSR* and *SRR*. The three letter designations represent configurational assignment at the stereogenic atoms C, N and S respectively.

Exploration of the conformational space for each diastereomer was achieved by varying the dihedral angles corresponding to four rotatable bonds (A-D in Figure 5-3). The conformational search was initiated with incremental 120° rotations around B and C bonds in order to obtain *trans* (T), plus *gauche* (G+), and minus *gauche* (G-) conformations. Newman projections of these conformations are given in Figure 5-15. The combination of T, G+ and G- conformations associated with the two dihedral angles has resulted in nine distinct conformations (TT, TG+, TG-, G+T, G+G+, G+G-, G-T, G-G+, G-G-). For each diasteromer, conformers with the relative population greater than 0 % have been subjected to further geometry optimization. This further optimization has involved varying dihedral angles corresponding to bonds A and D. Since the bond A is associated with a planar phenyl ring, a 90° rotation was sufficient for conformational exploration. On the other hand, t-butyl group associated with the bond D is C_3-symmetric, hence requiring only a 60° rotation for the conformational search.

Special attention was given to monitoring the configurational preference of nitrogen during the geometry optimization process because this chiral center is prone[2,150] to configurational inversion. As a result of nitrogen inversion during the optimization, some of the initial structures of *SRS*-**3** have converged into one of the stable conformations of *SSS*-**3**, and likewise some of the initial structures of *SSR*-**3** have converged into the stable conformations of *SRR*-**3**.

The geometry optimization using B3LYP functional and 6-31G* basis set has resulted in six stable conformations for *SSS*-**3**, two for *SRS*-**3**, three for *SSR*-

3, and four for *SRR*-**3** diastereomers. The relative populations of the conformers of each diastereomer, determined from Gibbs free energies, are given in Table 5-5. For each of the four considered diastereomers, the most stable conformer (labeled, C_1), is shown in Figure 5-16. All conformations identified as stable represent minima on the potential energy surface, as no imaginary frequencies have been predicted.

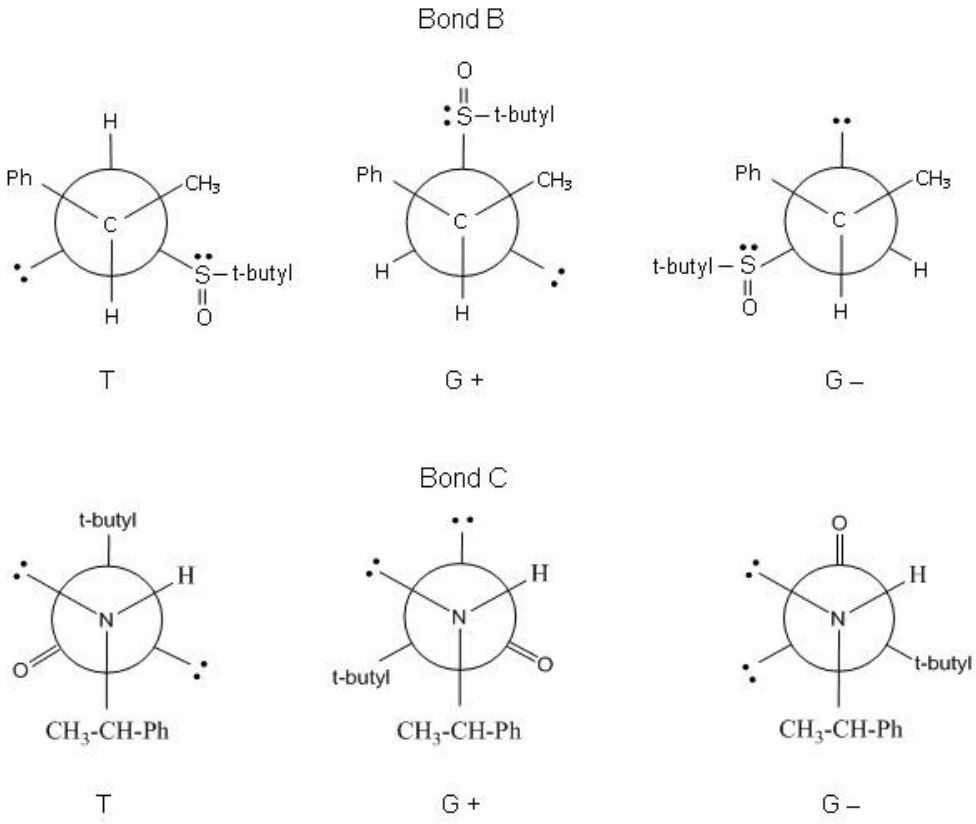

Figure 5-15: Newman projection view of *trans* (T), plus *gauche* (G+), and minus *gauche* (G-) conformations along B and C bonds of **3**.

Figure 5-16: Structures of the most stable 6-31G* conformers (C_1) for each of the four theoretically considered configurations (*SSS, SRR, SRS, SSR*) of **3**.

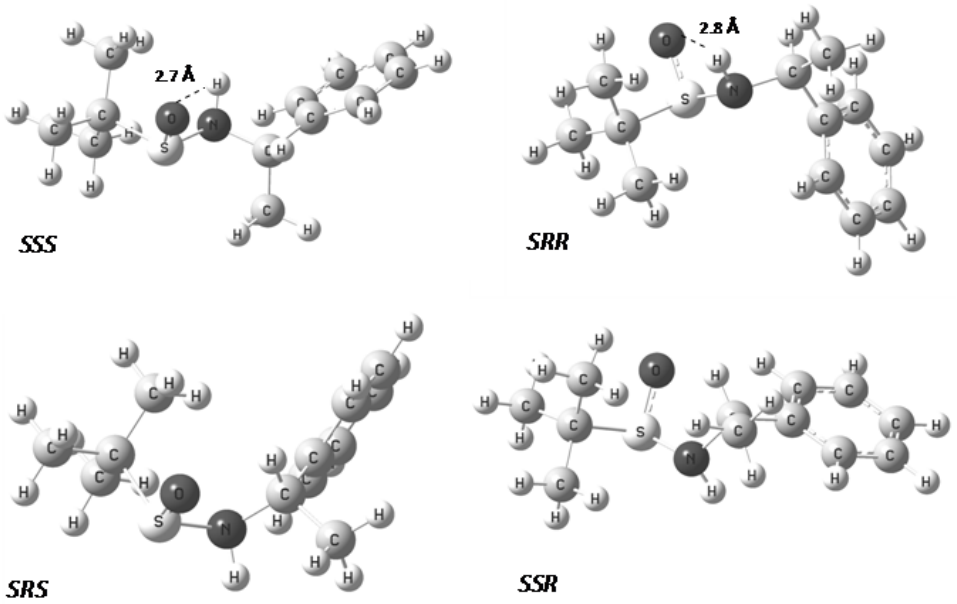

Table 5-5: Fractional populations for stable conformations of the four diasteromers of **3**. The populations are based on Gibbs free energies obtained from VCD calculation via B3LYP/6-31G*.

Fractional Populations		Configurations			
		SSS	*SRR*	*SRS*	*SSR*
Conformations	C_1	0.769	0.671	0.984	0.892
	C_2	0.094	0.145	0.016	0.074
	C_3	0.077	0.141	–	0.034
	C_4	0.040	0.043	–	–
	C_5	0.012	–	–	–
	C_6	0.008	–	–	–

Table 5-6: Fractional populations for stable conformations of the SSS and SRR diasteromers of **3**. The populations are based on Gibbs free energies obtained from VCD calculation via B3LYP/aug-cc-pVDZ.

Fractional Populations		Configurations	
		SSS	***SRR***
Conformations	**C_1'**	0.908	0.650
	C_2'	0.043	0.173
	C_3'	0.036	0.168
	C_4'	0.014	0.009

Theoretical VCD, ECD and ORD spectra for the stable conformations have been obtained using the same B3LYP functional and 6-31G* basis set. The comparison of population-weighted VCD, ECD and ORD spectra for each of the eight diastereomers with the corresponding experimental data for the two diastereomers, has indicated that *pSNA*-**3** corresponds to *SSS* configuration with six dominant conformations (C_1-C_6) and *mSNA*-**3** corresponds to *SRR* configuration with four dominant conformations (C_1-C_4).

These dominant conformers of *SSS*-**3** and *SRR*-**3** were further examined by reoptimizing their geometries with aug-cc-pVDZ basis set. These reoptimizations have resulted in the convergence of four conformations (C_1'-C_4') each for *SSS*-**3** and *SRR*-**3**. To determine the relative populations based on Gibbs free energies, VCD calculations were undertaken for all newly converged conformers. The relative populations of the conformers determined with aug-cc-pVDZ basis set are given in Table 5-6. The conformers with relative populations greater than 10 %, based on Gibbs energies, have been used for ECD and ORD predictions with aug-cc-pVDZ basis set.

Figure 5-17 displays experimental VA, VCD and noise traces for *pSNA*-**3** and *mSNA*-**3**, as optimized in the frequency region exhibiting lower intensity absorption signals. As indicated in the experimental section, VA and VCD traces in the associated with a high absorption signal, has been accounted for with a different set of pathlengths and concentrations used for each diastereomer. The traces from the two optimized frequency regions have been combined to provide

an overall experimental trace in the entire region of measurement that can be compared with the predicted traces.

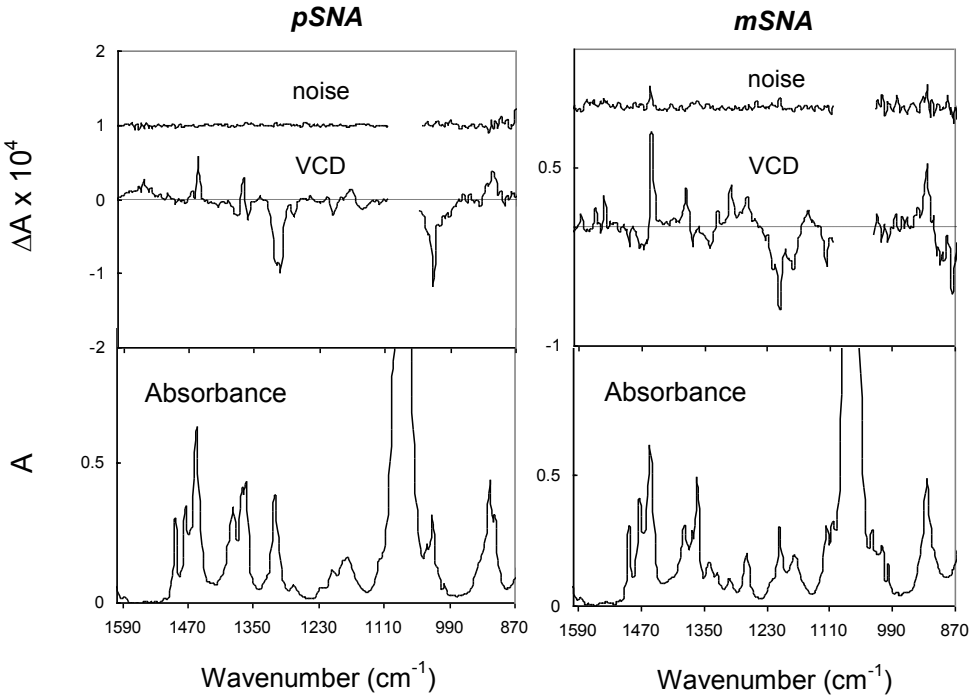

Figure 5-17: Experimental VA, VCD and noise traces for the two diastereomers of **3**. VCD and noise traces have been omitted in a region where the corresponding absorption band becomes too high for obtaining reliable signals.

The calculated VA and VCD spectra of individual conformers along with the population-weighted spectra for *SSS*-**3** have been compared to the experimental spectra of *pSNA*-**3** in Figure 5-18. An analogous spectral comparison between *mSNA*-**3** and *SRR*-**3** is given in Figure 5-19. Panels A and B in these figures pertain to lower level 6-31G* and higher level aug-cc-pVDZ basis sets, respectively. For both basis sets considered, these figures show that the population weighted absorption and VCD spectra reproduce the dominant features of experimental spectra.

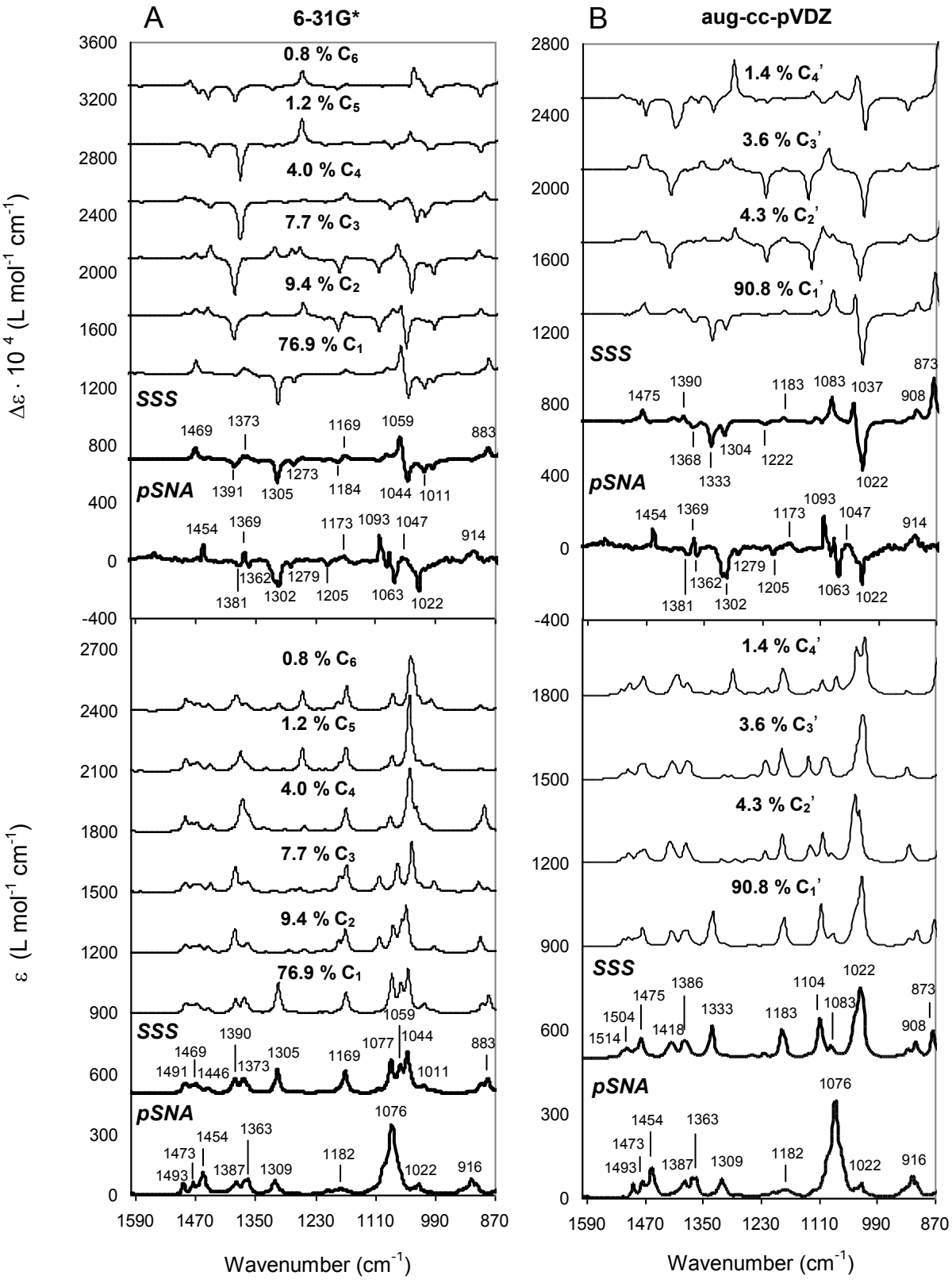

Figure 5-18: Comparison of experimental and theoretical VA and VCD traces between *pSNA* and *SSS* of **3** at two basis sets.

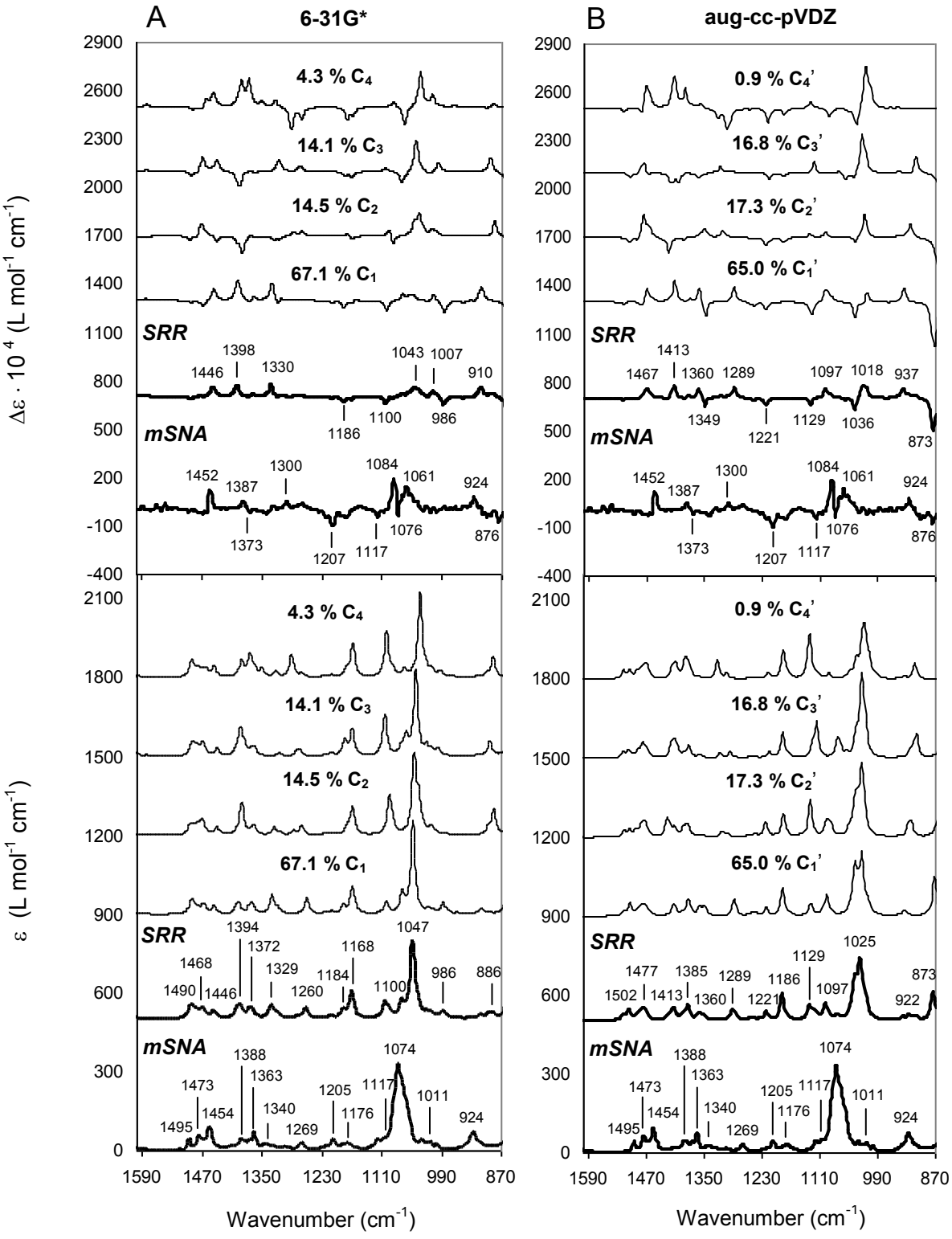

Figure 5-19: Comparison of experimental and theoretical VA and VCD traces between *mSNA* and *SRR* of **3** at two basis sets.

At 6-31G* level basis set, eleven VCD signals can be correlated (Figure 5-18A) between experimental spectra (for *pSNA*-**3**) and the theoretical spectra (for *SSS*-**3**). Specifically, the experimental bands at (+)914, (–)1022, (–)1063, (+)1093, (+)1173/(–)1205, (–)1279, (–)1302, (+)1369/(–)1381, and (+)1454 cm^{-1} correspond respectively to the predicted bands at (+)883, (–)1011, (–)1044, (+)1059, (+)1169/(–)1184, (–)1273, (–)1305, (+)1373/(–)1391, and (+)1469 cm^{-1}. Two experimental VCD bands remain uncorrelated at the lower level basis set, namely at (+)1047 and (–)1362 cm^{-1}. Eleven VCD bands can also be correlated between experimental and the theoretical (aug-cc-pVDZ) spectra in Figure 5-18B. Specifically, the experimental bands at (+)914, (–)1022, (+)1047, (+)1093, (+)1173/(–)1205, (–)1279, (–)1302, (–)1362/(+)1369, and (+)1454 cm^{-1} correspond respectively to the predicted bands at (+)908, (–)1022, (+)1037, (+)1083, (+)1183/(–)1222, (–)1304, (–)1333, (–)1368/(+)1390, and (+)1475 cm^{-1}. At the aug-cc-pVDZ basis set, also two experimental VCD signals at (–)1063 and (–)1381 cm^{-1} remain uncorrelated. However, the overall satisfactory correlation among multiple VCD bands at both basis sets leads to the conclusion that *pSNA*-**3** has the *SSS* configuration.

Vibrational origins of the most pronounced predicted VCD bands for *SSS*-**3** at aug-cc-pVDZ level are as follows: C-$CH_{3(\text{non t-butyl})}$ stretching, S-N stretching, and N-H bending give rise to the band at (+)873 cm^{-1}; C-N stretching is associated with the band at (+)908 cm^{-1}; S=O stretching coupled to some C-C stretching within t-butyl give rise to the band at (+)908 cm^{-1}; S=O stretching coupled to some C-C stretching within t-butyl gives rise to the band at (–)1022

cm^{-1}; S=O stretching coupled to some C-H bending within all CH_3 groups are associated with the band at (+)1037 cm^{-1}; C-$CH_{3(non\ t\text{-}butyl)}$ stretching coupled with some C-H bending within phenyl give rise to the band at (+)1083 cm^{-1}; C-S stretching and C-H bending within t-butyl account for the band at (+)1183 cm^{-1}; C-$C_{(phenyl)}$ stretching coupled to C-C stretching within phenyl (phenyl breathing) give rise to the band at (–)1222 cm^{-1}; C-C-C asymmetric stretching within phenyl gives rise to the band at (–)1304 cm^{-1}; C-N stretching coupled to N-H and $C_{(N)}$-H bending accounts for the band at (–)1333 cm^{-1}; Kekule mode (alternate bond stretching) of phenyl ring coupled with N-H and $C_{(N)}$-H bending give rise to the band at (–)1368 cm^{-1}; C-H bending (non t-butyl CH_3) gives rise to bands at (+)1390 and (+)1475 cm^{-1}.

The correlation among eight 6-31G* VCD bands and eleven aug-cc-pVDZ VCD bands with the experimental VCD bands in Figure 5-19 indicates that *mSNA*-**3** has the *SRR* configuration. The experimental bands at (+)924, (+)1061, (+)1084, (–)1117, (–)1207, (+)1300, (+)1387, and (+)1452 cm^{-1} are correlated with the 6-31G* predicted bands at (+)910, (+)1007, (+)1043, (–)1100, (–)1186, (+)1330, (+)1398, and (+)1446 cm^{-1}. At the 6-31G* basis set, three experimental VCD signals remain uncorrelated, namely at (–)876, (–)1076, and (–)1373 cm^{-1}.

Some differences in the VCD band intensities among population weighted and experimental spectra could be result from different sources: a) The predicted relative intensities need not be accurate enough at the theoretical level used; b) relative populations of conformers in solution environment used for experimental measurement can be different from that for an isolated molecule considered by

the theoretical model. For example, one could speculate that *SRR* conformers C_3 and C_4 could be more populated because relative intensities in their spectra provide more satisfactory agreement with those of the experimental VCD spectra of *mSNA*-**3** at 1061 and 1084 cm^{-1}. The same type of argument can be provided by the negative predicted VCD band at 986 cm^{-1}, which is present in the population-weighted spectrum, but not in the predicted VCD spectra of conformers C_3 and C_4 of *SRR*-**3** and in the experimental spectrum of *mSNA*-**3**.

In terms of aug-cc-pVDZ basis set, the predicted bands for *SRR*-**3** at (–) 873, (+)937, (+)1018, (–)1036, (+)1097, (–)1129, (–)1221, (+)1289, (–)1349/(+)1360, and (+)1413 cm^{-1} can be correlated to the experimental bands for *mSNA*-**3** at (–)876, (+)924, (+)1061, (–)1076, (+)1084, (–)1117, (–)1207, (+)1300, (–)1373/(+)1387, and (+)1452 cm^{-1}. Only one predicted VCD band at (+)1467 cm^{-1} remains uncorrelated. The overall satisfactory correspondence of VCD bands, between experimental and predicted (with both basis sets) spectra leads to the conclusion that *mSNA*-**3** has the *SRR* configuration.

Vibrational origins of the most pronounced predicted VCD bands for *SRR*-**3** at aug-cc-pVDZ level are as follows: asymmetric C-N-S stretching coupled with N-H bending give rise to the band at (–)873 cm^{-1}; C-N stretching accounts for the band at (+)937 cm^{-1}; S=O stretching, asymmetric CH_3-C-N stretching, and C-C-C bending within phenyl give rise to the band at (+)1018 cm^{-1}; S=O stretching coupled with C-C stretching within t-butyl give rise to the band at (–)1036 cm^{-1}; asymmetric CH_3-C-N stretching accounts for the band at (+)1097 cm^{-1}; C-N stretching, C-C stretching within the phenyl, some C-H bending (non t-bytyl CH_3)

give rise to the band at (–)1129 cm^{-1}; C-$C_{(phenyl)}$ stretching coupled with C-C stretching within phenyl (phenyl breathing) contribute to the band at (–)1221 cm^{-1}; C-C-C asymmetric stretching within phenyl is associated with the band at (+)1289 cm^{-1}; $C_{(N)}$-H bending and C-H bending within phenyl give rise to the band at (–)1349 cm^{-1}; Kekule mode of the phenyl ring is associated with the band at 1360 cm^{-1}; C-$C_{(phenyl)}$ stretching, N-H bending, and C-H bending within all CH_3 groups give rise to the band at (+)1413 cm^{-1}; finally, C-H bending (non t-butyl CH_3) corresponds to the band at (+)1467 cm^{-1}.

As an additional independent verification of configurational assignments for the two diasteromers, ECD and ORD spectra have been considered. The spectral comparisons associated with ECD data are displayed in Figure 5-20 and ORD data in Figure 5-21. In terms of the ECD spectra, *pSNA*-**3** displays an overall satisfactory qualitative agreement with the population-weighted spectra of *SSS*-**3** at both basis set levels. The negative ECD signal at 209 nm for *pSNA*-**3** corresponds to the 6-31G*-predicted negative ECD band at 213 nm (Figure 5-20A) and aug-cc-pVDZ-predicted negative ECD band at 234 nm (Figure 5-20B) for *SSS*-**3**. In terms of *mSNA*-**3**, its positive ECD signal at 221 nm corresponds to the 6-31G*-predicted positive ECD band at 242 nm (Figure 5-20A) and aug-cc-pVDZ-predicted positive ECD band at 245 nm (Figure 5-20B) for *SRR*-**3**. As noted in the study of smaller sulfinamide **2**, it is not unusual for the electronic transitions predicted with B3LYP functional to appear at longer wavelengths than the experimentally observed transitions. With some blue shift of the predicted ECD bands, correlation between the positive ECD band of *mSNA*-**3** and the

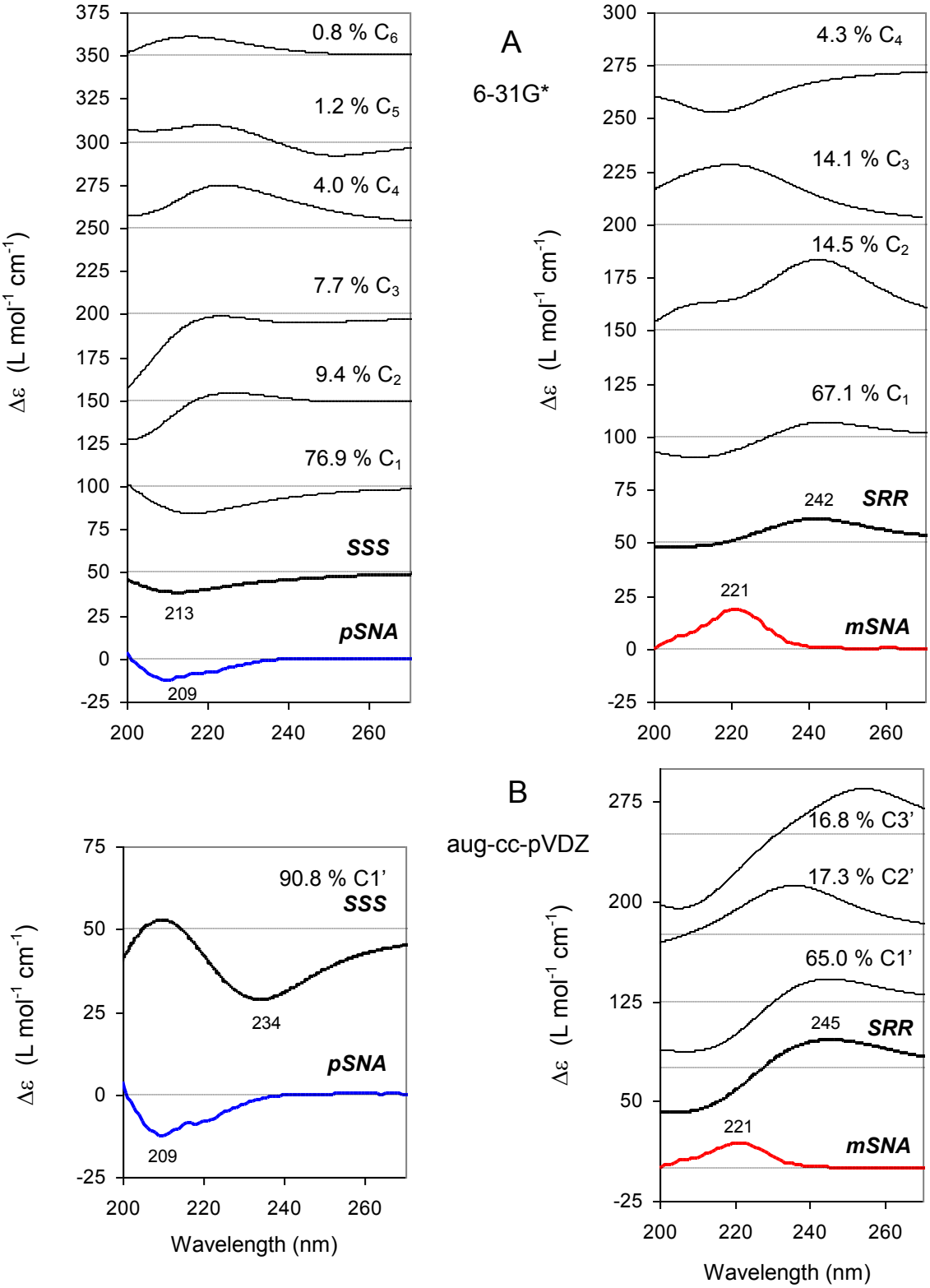

Figure 5-20: Comparison of experimental and theoretical ECD traces of **3** at two basis sets.

positive ECD band *SRR*-**3,** at both basis set levels, can be justified. Similarly, the correlation between the negative ECD band of *pSNA*-**3** and the negative ECD band of *SSS*-**3** at aug-cc-pVDZ basis set level can be justified. The close positioning of 6-31G* predicted ECD band at 213 nm for *SSS*-**3** with that of *pSNA*-**3** is most likely fortuitous.

The absolute configurations suggested by VCD and ECD are supported by a good qualitative agreement of ORD between experimental and predicted ORD spectra (Figure 5-21). The experimentally obtained intrinsic rotation values for *pSNA*-**3** are +35.5(±0.9) at 633, +40.1(±0.8) at 589, +47.8(±1.0) at 546, +68.5(±1.0) at 436, +74.7(±1.4) at 405, and +77.9(±1.7) at 365 nm; those obtained for *mSNA*-**3** are –139.1(±2.2) at 633, –161.7(±3.1) at 589, –190.5(±3.5) at 546, –309.8(±6.1) at 436, –358.0(±5.4) at 405, and –446.4(±8.3) at 365 nm. The population-weighted optical rotation values for *SSS*-**3** at 6-31G* basis set (Figure 5-21A) are +88.4 at 633, +103.2 at 589, +121.7 at 546, +200.8 at 436, +237.8 at 405, and +302.8 at 365 nm; those predicted at aug-cc-pVDZ basis set (Figure 5-21B) are +100.5 at 633, +117.1 at 589, +137.8 at 546, +223.8 at 436, +261.9 at 405, and +323.6 at 365 nm. The population-weighted optical rotation values for *SRR*-**3** at 6-31G* basis set (Figure 5-21A) are –138.1 at 633, –160.1 at 589, –187.1 at 546, –295.7 at 436, –341.7 at 405, and –412.6 at 365 nm; those predicted at aug-cc-pVDZ basis set (Figure 5-21B) are –107.2 at 633, –123.4 at 589, –142.7 at 546, –211.1 at 436, –232.4 at 405, and –244.0 at 365 nm. The specific rotation signs for the population-weighted *SSS*-**3** remain positive at each of the six wavelengths considered, which is in agreement with the *pSNA*-**3**.

Likewise, specific rotation signs at all wavelengths considered for the population-weighted *SRR*-**3** remain negative as is the case for *mSNA*-**3**.

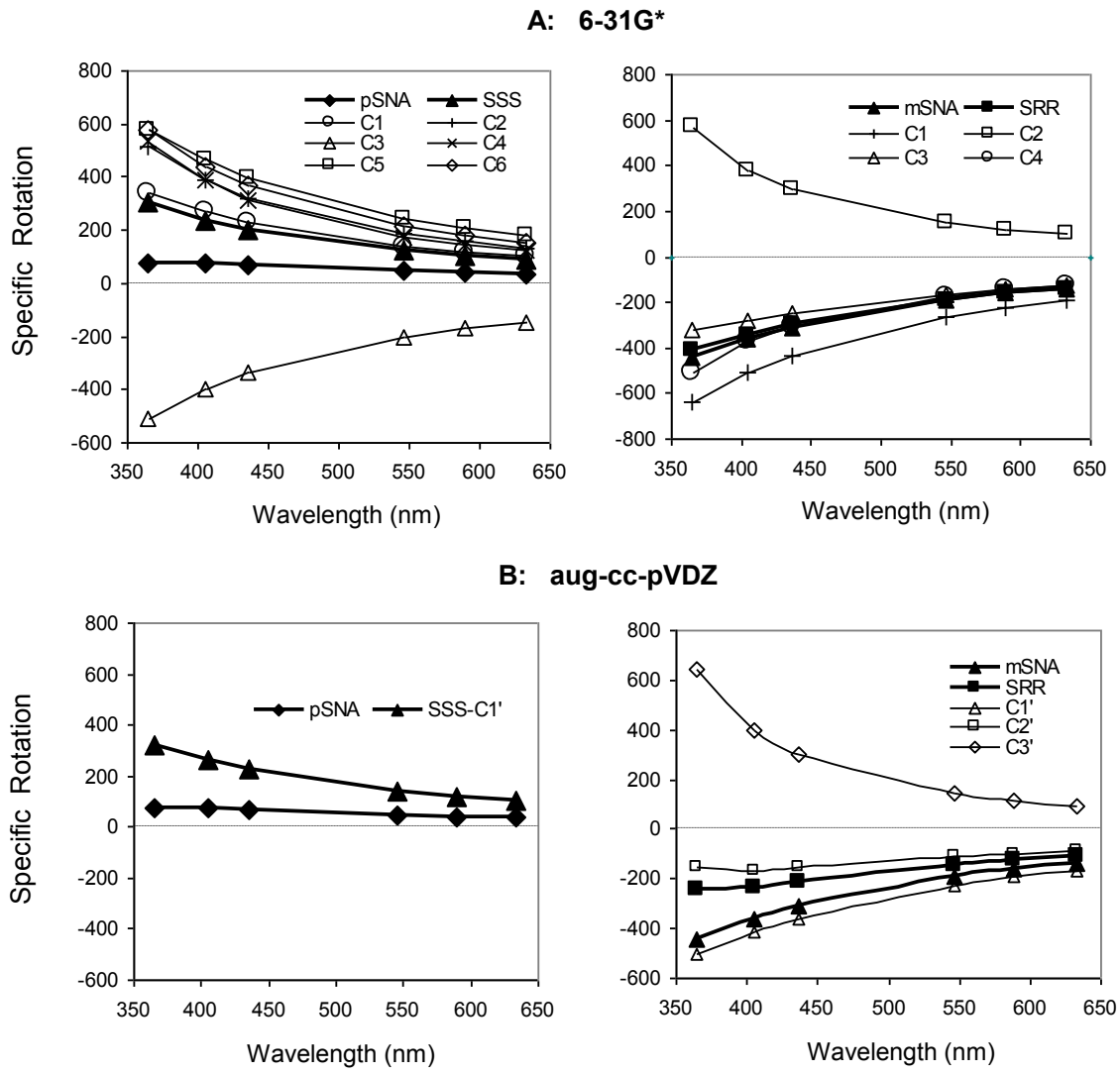

Figure 5-21: Comparison of experimental and theoretical ORD traces of **3** at two basis sets.

Satisfactory correlations between experimental and predicted spectra independently derived from each of the three chiroptical spectroscopic methods, at both basis set levels, as well as a univocal consensus in the stereochemical

assignment among the three methods provide confidence to the conclusions established about the stereochemistry of diasteromeres of **3**.

Conclusion

Conclusions derived from a combined chiroptical study of 1,1-dimethyl-2-phenylethyl phenyl sulfoxide (**1**) are that the conformations labeled as $G^{+}T$, TG^{+}, TT, and $G^{-}T$ are predominant in solution and that the absolute configuration of (+)-**1** is (*R*) and, hence of (–)-**1** is (*S*).

The absolute configuration of (–)-t-buanesulfinamide (**2**) has been determined as (–)-(*S*). Furthermore the predominant conformation of this molecule is determined to have S=O and NH_2 groups staggered with respect to the three methyl groups and to have amine hydrogens in gauche orientation with respect to S=O. The quality of predictions obtained for vibrational properties, namely VA and VCD, is found to be satisfactory with B3LYP functional and 6-31G* basis set. However, this basis set is found to be inadequate for obtaining reliable predictions of electronic properties, as reflected by ORD, but a larger aug-cc-pVDZ basis is found to provide satisfactory prediction of electronic properties. The study of sulfinamide **2** emphasizes the importance of simultaneous investigation of ECD and ORD, and the use of multiple chiroptical spectroscopic methods, for reliable determination of stereochemistry.

Collaborative implementation of the three chiroptical methods gives a high-degree of confidence in elucidating the absolute configurations and dominant conformations for two diastereomers of N-phenylethyl-t-

butylsulfinamide (**3**). One diastereomer, *pSNA*-**3** has *SSS* configuration with one predominant conformation, while the second diastereomer *mSNA*-**3** has the *SRR* configuration with three predominant conformations.

CHAPTER VI

ABSOLUTE CONFIGURATION, CONFORMATION AND MONOMER-DIMER EQUILIBRIUM OF T-BUTYL-PHENYL-PHOSPHINOAMIDATE

Introduction

Over the last decade a diverse assortment of chiral phosphorous reagents has been identified[151-159], which subsequently resulted in a substantial progress in application of these reagents in a variety of stoichiometric and catalytic versions of asymmetric and stereoselective syntheses. Within the rich family of phosphorous compounds, phosphinoamidates (or phosphinic amides, phosphinamides) have been identified as particularly useful reagents. A series of phosphinoamidates have been reported[155,156] as novel catalysts for asymmetric reductions of ketones by borane. These studies have indicated that phosphinoamidates act as Lewis bases which activate borane, and through donation of electron density effectively accelerate the reduction. Li and coworkers have reported[157,158] a similar class of phosphinoamidates, derived from L-amino acids, which facilitate synthesis of chiral secondary alcohols in excellent chemical yields and moderate to high enantiomeric excess. Further, Sorensen *et al.* have recently reported[160] design and synthesis of novel cyclic phosphinoamidate derivatives, which act as potent matrix metalloproteinase inhibitors, thus could be considered as possible drug candidates for treatment of diseases such as multiple sclerosis, osteoarthritis, psoriasis, as well as tumor growth and metastasis. Chan *et al*.[161] suggested the use of phosphinoamidates to modulate the activity of endothelin family of peptides, responsible for causing

vasoconstriction. This modulation potentially allows treatment of endothelin-mediated disorders. Lin *et al.* have described[162] the synthesis of bis(aziridinyl)phosphinoamidate derivatives of thymidine and have suggested their potential application as anticancer agents. The recognition of phosphinoamidates as compounds of importance as synthetic auxiliaries and bioactive reagents has attracted attention to synthesis and characterization of these compounds.

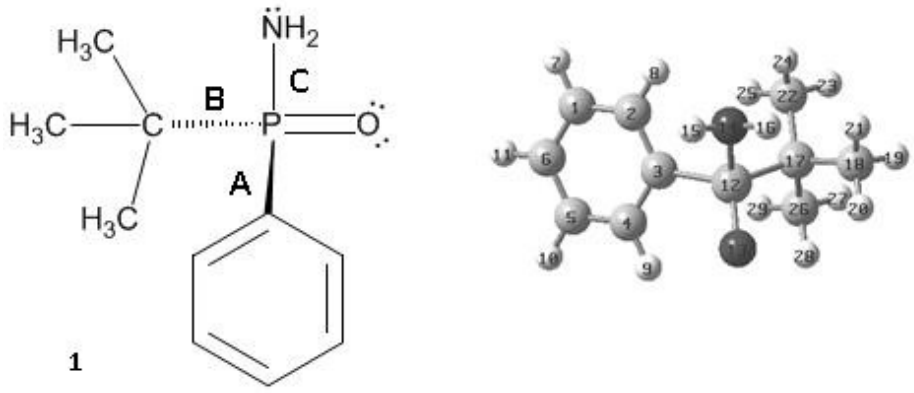

Figure 6-1: The chemical structures of t-butylphenylphosphinoamidate, **1**.

From the literature cited in the previous paragraph, it is evident that chiral phosphinoamidates have demonstrated a potential for versatile applications as synthetic reagents as well as compounds of interest for biologically relevant use. The effectiveness in application of any chiral compound can be to a significant extent determined by its absolute configuration and conformations. In this manuscript we report on the determination of the absolute configuration and conformations of (–)-t-butylphenylphosphinoamidate **1**, (Figure 6-1) via

thenchiroptical spectroscopic methods, namely, VCD, ECD and ORD. The monomer-dimer equilibrium and conformations of **1** in solution state are also investigated.

Experimental Section

VCD, ECD, and ORD Spectra: The synthesis of racemic and enantiomeric t-butylphenylphosphinoamidate **1** will be reported elsewhere[163]. The concentration dependent infrared vibrational absorption spectra, was measured at five concentrations between 0.84 - 0.05 M in $CHCl_3$ by using a demountable cell with 100 μm pathlength spacer. For VCD measurements, the vibrational absorption and VCD spectra of (–)-**1** and (±)-**1** were obtained with 3 hr data collection time at 4 cm^{-1} resolution, using a commercial Fourier transform VCD spectrometer Chiralir, modified with dual polarization modulation[15]. These spectra were measured in $CDCl_3$ solvent at a concentration of ~ 0.17 M using two different pathlengths of 320 and 220 μm for both samples. The lower pathlength has been used for optimizing the high absorbance and VCD signals in the region between ~ 1132 and 1248 cm^{-1}. Measurable VCD bands are seen only in the region below ~ 1250 cm^{-1}. The samples were held in a variable pathlength cell with BaF_2 windows. In the presented absorption spectrum, the solvent absorption was subtracted out. In the presented VCD spectrum, the VCD spectra of the (±)-**1** has been subtracted from that of (–)-**1**, in order to establish the zero-baseline. For experimental ECD spectra, one ECD spectrum was recorded for (–)-**1** at ~ 0.284 M in $CHCl_3$ solvent in the 240 to 490 nm region, using 0.01 cm

pathlength cell. Another ECD spectrum of (–)-**1** was obtained at ~ 0.027 M in hexane in the 200 to 280 nm region, again using 0.01 cm path length cell. Both ECD spectra were measured on a Jasco J720 spectrometer. For intrinsic rotations, solutions of (–)-**1** in $CHCl_3$ solvent were prepared by successive dilutions from the parent stock solution. These concentration-dependent studies have resulted in five data points, ranging in concentrations from 0.013 to 0.002 g/ml. The intrinsic rotation, which represents specific rotation at infinite dilution, was extracted from the optical rotations at different concentrations as described before[22]. These measurements were made at six wavelengths 633, 589, 546, 436, 405, 365 nm, using an Autopol IV polarimeter, to obtain optical rotatory dispersion (ORD).

Calculations: Geometry optimizations as well as the calculation of vibrational frequencies, vibrational absorption (VA), and VCD intensities were undertaken with either Gaussian 98[34] or Gaussian 03[35] programs. The specific rotation and ECD calculations for isolated molecule were performed using Gaussian 03. The calculations used the density functional theory (DFT) with B3LYP hybrid functional and 6-31G*, 6-311G(2d,2p) as well as aug-cc-pVDZ basis sets. The theoretical VA and VCD spectra were simulated with Lorentzian band shapes and 5 cm^{-1} half-width at half-peak height. Since the predicted band positions are normally higher than the experimental band positions, the calculated monomer frequencies have been scaled by a factor of 0.9613 for 6-31G* basis set and 0.9678 for 6-311G(2d,2p) basis set. This kind of scaling was not used for the monomer frequencies predicted with aug-cc-pVDZ basis set or

for the dimer frequencies. The theoretical ECD spectra were simulated from the first 30 singlet → singlet electronic transitions using Gaussian band shapes and 20 nm half-width at 1/e of peak height.

Results and Discussion

Monomer-Dimer Equilibrium in Solution: In order to determine the absolute configuration of a chiral molecule using chiroptical spectroscopic methods, it is necessary first to determine its predominant conformations. In addition for molecules that favor dimer formation, the conformations of dimer[164] and monomer-dimer equilibrium[165-167] should also be investigated. Intermolecular hydrogen bonding for **1** can occur through its oxygen atom and hydrogen atoms of the primary amine group. The X-ray structure[163] indicated that the structure of **1** has two-dimensional network with hydrogen bonding facilitated through water. The solvent used for chiroptical spectroscopic studies is not capable of facilitating hydrogen bonding with **1**, but intermolecular hydrogen bonding can take place between two different molecules of **1,** leading to the formation of dimers. Thus the monomer-dimer equilibrium for **1** in solution needs to be considered.

For equilibrium between monomer, A, and the dimer, A_2, the following relations apply[165-167]:

$$A + A \leftrightarrow A_2 \qquad (6-1)$$

$$C_m + 2C_d = C_o \qquad (6-2)$$

$$K = \frac{C_d}{C_m^2} \qquad (6-3)$$

where C_m and C_d represent the equilibrium concentrations of monomer and dimer, respectively. C_o represents the concentration of the sample and *K* stands for monomer-dimer equilibrium constant. Using the above three equations, the integrated absorbance of i^{th} band of monomer, $A_{m,i} = C_m l \int \varepsilon_{m,i}(\nu) d\nu$, becomes:

$$A_{m,i} = P_m C_o \varepsilon_{m,i} l \qquad (6-4)$$

where $\varepsilon_{m,i} = \int \varepsilon_{m,i}(\nu) d\nu$ represents the integrated molar absorptivity of i^{th} band of monomer, l is the pathlength used and P_m is the fractional population of monomer, given as:

$$P_m = \frac{2}{(1 + 8 \cdot K \cdot C_o)^{1/2} + 1} \qquad (6-5)$$

Non-linear least square fitting of the integrated absorbance of individual bands of monomer, $A_{m,i}$, with C_o provides the equilibrium constant K, and hence the fractional population of monomer at a given concentration C_o. The dimer population is then obtained as $P_d = 1 - P_m$.

To investigate the monomer-dimer equilibrium of **1**, the infrared absorption spectra were measured (Figure 6-2) at five different concentrations in the 0.84 - 0.05 M range. In Figure 6-2, a shoulder at 1570 cm^{-1} (labeled as VII) appears to indicate dimer formation as the concentration is increased. However, the bands I-V are better resolved and appear to be associated with the monomer. The concentration dependent integrated area of each of the five bands are determined by fitting the spectra to individual bands with the PeakFit[168] program and these areas are fit to the equation non-linear in C_o (Equation 6-4) using

KaleidaGraph[169]. The average K value obtained from these five monomer bands (bands I-V) is 0.44 (±0.11). However, to avoid the uncertainties resulting from spectral fitting process used in the PeakFit program, one can consider the area of a larger region that contains only the monomer bands. By summing Equation 6-4 over monomer bands one obtains:

$$A_m = \sum_i A_{m,i} = P_m C_o l \sum_i \varepsilon_{m,i} = P_m C_o l \varepsilon_m = \frac{2C_o l \varepsilon_m}{(1 + 8 \cdot K \cdot C_o)^{1/2} + 1} \qquad (6-6)$$

where the summation runs over monomer bands.

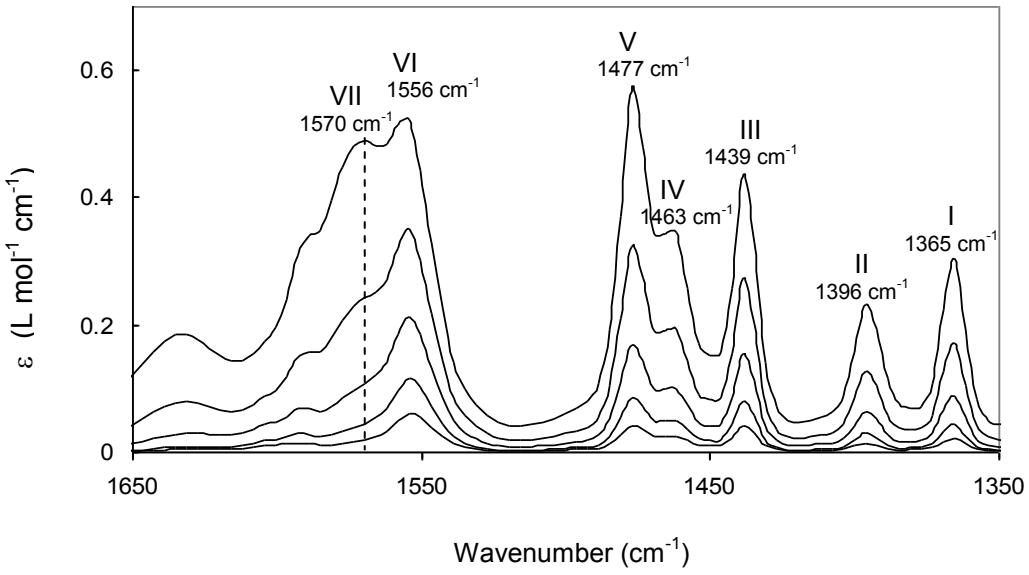

Figure 6-2: Concentration dependent (0.84 - 0.05 M) vibrational absorption spectra of **1**.

The area in the 1518-1348 cm^{-1} frequency range is obtained in this manner with the Grams software supplied with Chiralir instrument and fit to C_o using Equation 6-6 (see Figure 6-3). The K value is determined to be 0.34

(±0.05). At the concentration used for VCD studies (0.17 M), the K value of 0.34 corresponds to 90% monomer and 10% dimer populations. At the lower concentrations used for ECD (0.027M) the dimer population (~ 2%) is negligible. For ORD studies, specific rotation was extrapolated to zero concentration, where the dimer population can be considered to be absent.

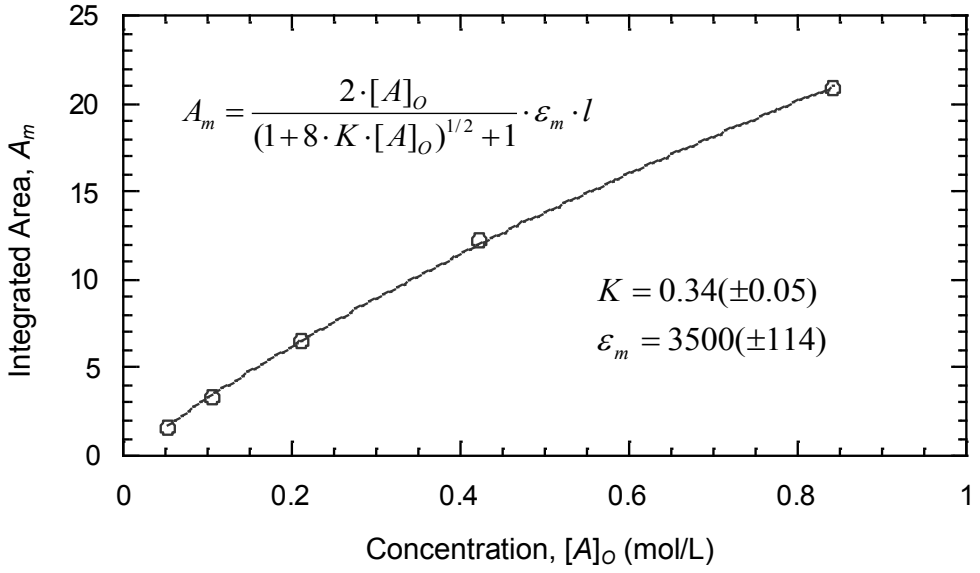

Figure 6-3: Non-linear least square fitting of the total area underneath bands I-V as function of concentration using Equation 6-6.

Conformations of Monomer: Monomer conformations of **1** were explored by considering three rotatable bonds (A, B, and C in Figure 6-1), indicating three dihedral angles that can be varied**.** Each dihedral angle is composed of atoms numerically labeled as given in Figure 6-1. The bond A corresponds to dihedral angle D(4,3,12,13) and is associated with the orientation of phenyl group. Potential energy scan (PES) was performed by varying D(4,3,12,13) in 30°

increments. The bond B corresponds to dihedral angle D(18,17,12,13) and is associated with the orientation of t-butyl group. Since t-butyl group has three equivalent methyl groups, a single 60° rotation was sufficient for exploring the conformational mobility around the bond B. The bond C is associated with the primary amine group and dihedral angle D(15,14,12,13). This dihedral angle was incrementally varied five times, 60° at a time. The geometry optimization carried out using a B3LYP functional with the 6-31G* basis set has resulted in two distinct conformations given in Figure 6-4. The electronic energy difference between these two optimized conformers is approximately 3 kcal/mol, with conformation 1 being significantly more stable than conformation 2. The minimum energy conformation obtained with 6-31G* basis set was also optimized with 6-311G(2d,2p) and aug-cc-pVDZ basis sets. A comparison of the converged values for the three relevant dihedral angles, and electronic energies are displayed in Table 6-1.

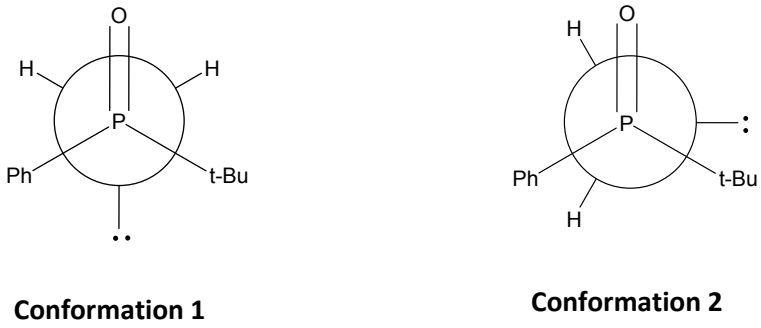

Figure 6-4: Structures of the two stable monomer conformations of **1.** Conformation 1 is significantly more stable than conformation 2.

Table 6-1: B3LYP optimized dihedral angles and electronic energies for(*S*)-**1a.**

Basis set		Converged Dihedral Angles[a] (deg.)			
		D(4,3,12,13)	D(18,17,12,13)	D(15,14,12,13)	Electronic Energies (Hartrees)
6-31G*	Conformation 1	-19.5	-63.1	-64.3	-862.0747606
	Conformation 2	158.3	-175.3	-34.8	-862.0700732
6-311G(2d,2p)	Conformation 1	-19.4	-61	-64.5	-862.2817658
aug-cc-pVDZ	Conformation 1	-19	-62.5	-64	-862.1527717

[a]the atom labels are given in Figure 6-1.

The equilibrium between two tautomeric structures, **1a** and **1b**, (Figure 6-5) is also considered, as was done for phophine oxide[151], phosphinothioic acid[152] and phsophites[170]. In addition to the possible conformations of tautomer **1a,** discussed earlier, the conformations of **1b** have also been investigated by varying the dihedral angles associated with phenyl and t-butyl groups. Tautomer **1b** also exhibits two minimum energy conformations, one of which is considerably more stable than the other. The comparison of electronic energies obtained for the minimum energy conformers of **1a** and **1b** indicates that **1a** is significantly more stable than **1b**. In fact, even the less stable of the two conformations of **1a** ($E_{electronic}$ = -862.0701 Hartrees) is significantly more stable than the most stable conformation of **1b** ($E_{electronic}$ = -862.0384 Hartrees). The analysis of the two tautomers clearly shows that equilibrium is shifted towards the tautomer **1a**, as depicted in Figure 6-5.

The lowest energy conformation of tautomer **1a** with (*S*)-configuration has been used for calculating VA, VCD, ECD and ORD using the B3LYP functional with 6-31G*, 6-311G(2d,2p) as well as aug-cc-pVDZ basis sets. From the

calculated vibrational frequencies, the conformation considered was found to represent the minima on the potential energy surface, as there are no imaginary frequencies. To obtain the theoretical data for (*R*)-**1a**, the magnitudes of calculated VCD, ECD and ORD values for (*S*)-1a were multiplied by (–1).

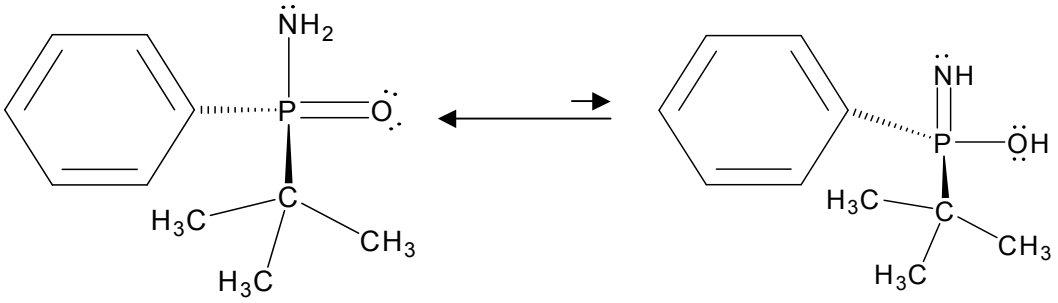

1a **1b**

Figure 6-5: The equilibrium between the two possible tautomers of **1**.

Conformations of Dimer: Dimer conformations of **1a** were explored by considering all possible orientations of two monomer units between which intermolecular hydrogen bonding can occur. As displayed in Figure 6-6, the amine hydrogen spatially closer to phenyl ring has been designated as “ph” and the amine hydrogen spatially closer to t-butyl group as “t-b”. The two monomeric units have been oriented in three different ways towards each other to produce three different dimer forms. The B3LYP/6-31G* energies of optimized geometries of these three forms indicate that the populations of dimers given in panel A, B, and C of Figure 6-6 are, respectively, 21%, 26% and 53%. These values have been used for obtaining the population-weighted VA and VCD spectra of the

dimer. The predicted dimer spectra have been overlaid with the monomer spectra at the B3LYP/6-31G* level for comparison with the experimental trace in Figures 6-7 and 6-8.

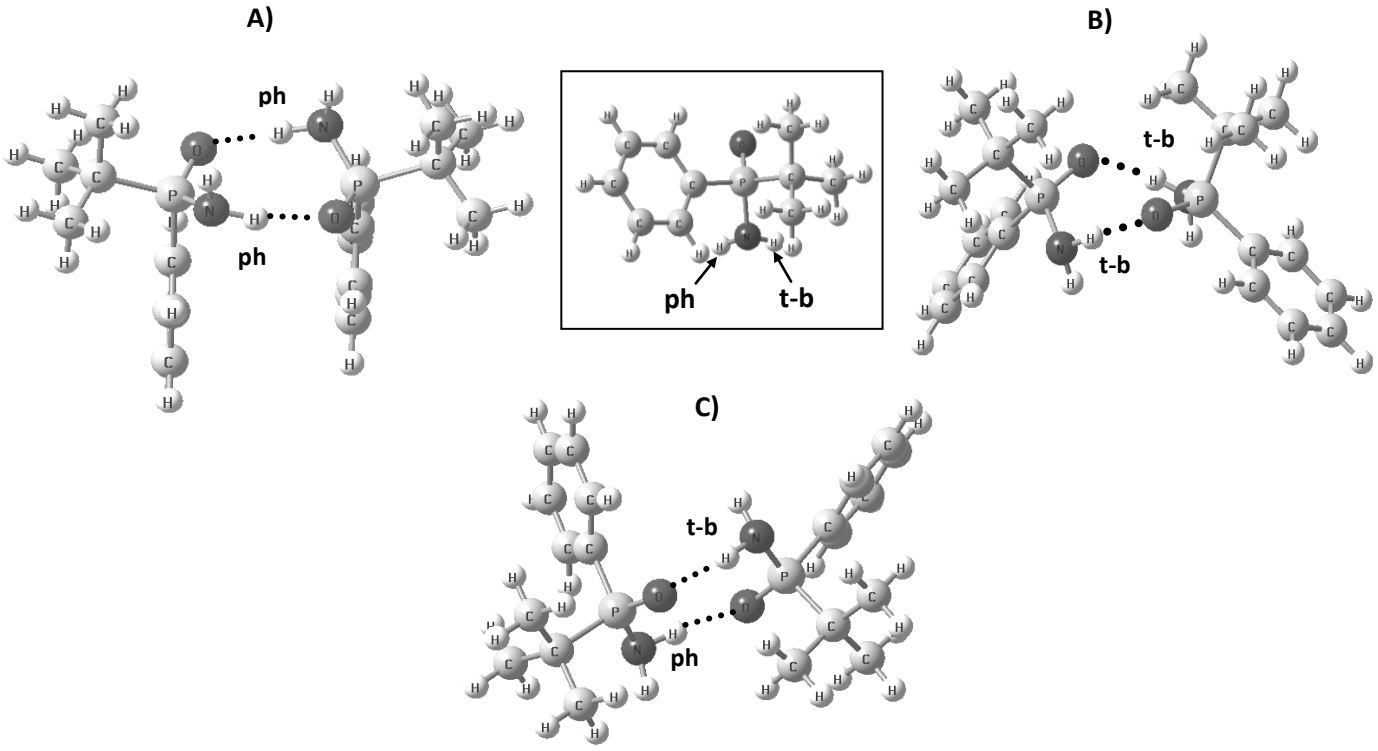

Figure 6-6: Structures of the three stable dimer conformations (A, B, C) of **1**. The populations of conformers in panels A, B, and C are 21%, 26%, 53%, respectively.

Comparison of experimental and predicted spectra: The comparison between experimental and predicted absorbance spectra is shown in Figure 6-7, while the comparison of corresponding VCD spectra is shown in Figure 6-8. The theoretical VCD spectra displayed in Figure 6-8 correspond to (*R*)-**1a**, while the experimental spectrum is given for (–)-**1** enantiomer. In both figures, the

theoretical spectrum at the B3LYP/6-31G* level is given as an overlaid monomer (90%) and dimer (10%) traces. As it can be seen from Figure 6-7, the experimental absorption band with the largest intensity at 1171 cm^{-1} corresponds to a theoretical band at 1166 cm^{-1} in the 6-31G*, at 1176 cm^{-1} in the 6-311G(2d,2p), and at 1159 cm^{-1} in the aug-cc-pVDZ predicted spectrum. In the frequency region below the highest intensity band, three absorption bands are correlated between the theoretical and experimental spectrum. The experimental band at 1117 cm^{-1} corresponds to the predicted modes at 1087 cm^{-1}, 1093 cm^{-1}, and 1116 cm^{-1}, respectively, with 6-31G*, 6-311G(2d,2p) and aug-cc-pVDZ basis sets. The experimental band at 1072 cm^{-1} corresponds to the predicted modes at 1065 cm^{-1}, 1063 cm^{-1}, and 1093 cm^{-1} respectively with 6-31G*, 6-311G(2d,2p), and aug-cc-pVDZ basis sets. Finally, the experimental band at 1014 cm^{-1} corresponds to theoretical bands at 1011 cm^{-1}, 1010 cm^{-1} and 1035 cm^{-1} obtained with 6-31G*, 6-311G(2d,2p) and aug-cc-pVDZ basis sets. In the frequency region between ~ 1200 and 1700 cm^{-1}, seven bands exhibit correspondence between the experimental and theoretical spectra. Specifically, experimental bands at 1217, 1365, 1396, 1439, 1463, 1477, and 1556 with shoulder at 1603 cm^{-1}, respectively correspond to 6-31G* predicted bands at 1205, 1371, 1400, 1426, 1474, 1492, 1580 cm^{-1}, 6-311G(2d,2p) predicted bands at 1204, 1362, 1390, 1428, 1464, 1483, 1557 cm^{-1}, and aug-cc-pVDZ predicted bands at 1222, 1388, 1418, 1454, 1488, 1506, 1586 cm^{-1}. Figure 6-7 indicates a fairly good reproduction of the relative intensities of the correlated bands, especially in the ~1200-1000 cm^{-1} region. Even though positions of the predicted

and corresponding experimental vibrational bands differ quantitatively, an overall satisfactory one-to-one qualitative agreement reinforces the conclusion that the theoretically considered monomer conformation is the predominant solution conformation.

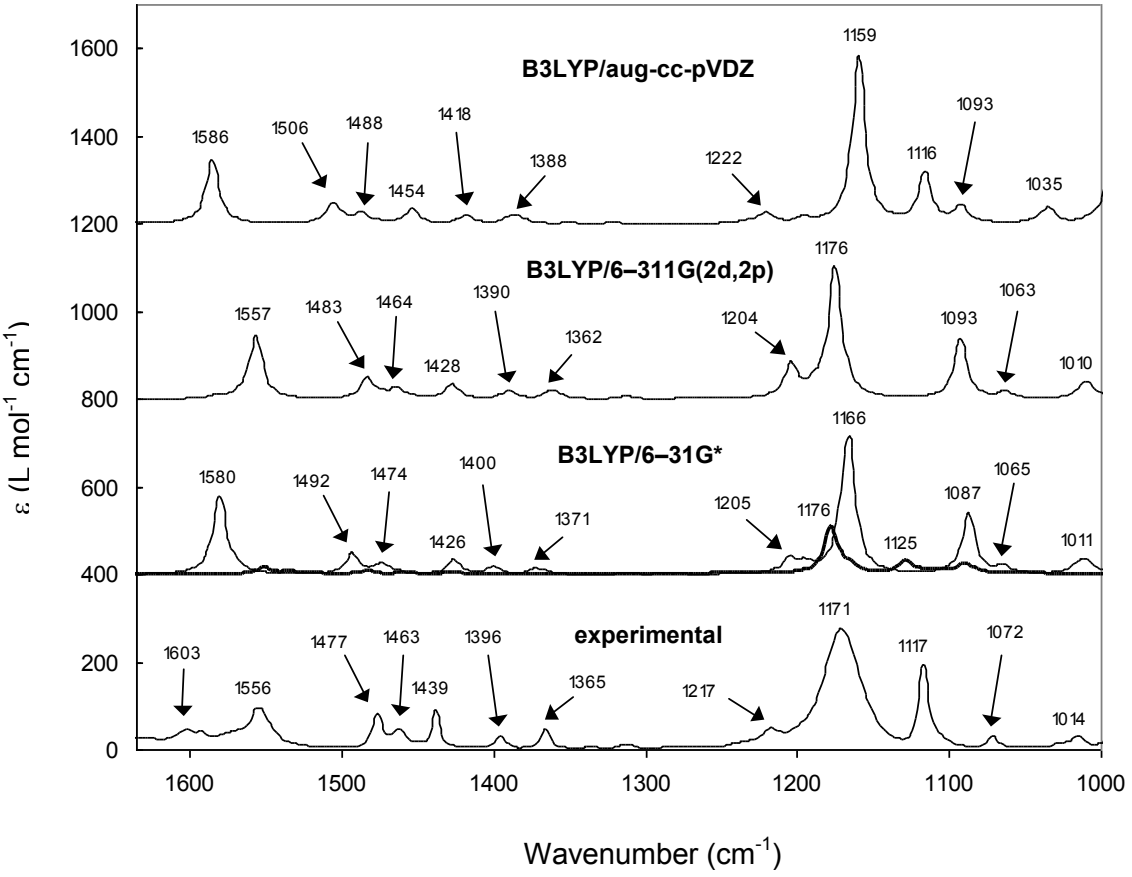

Figure 6-7: Comparison of experimental absorption spectrum with predicted absorption spectra of **1**. At 6-31G* level, two traces are overlaid: a thin line corresponds to the monomer spectrum (90%) and a thick line to the dimer spectrum (10%).

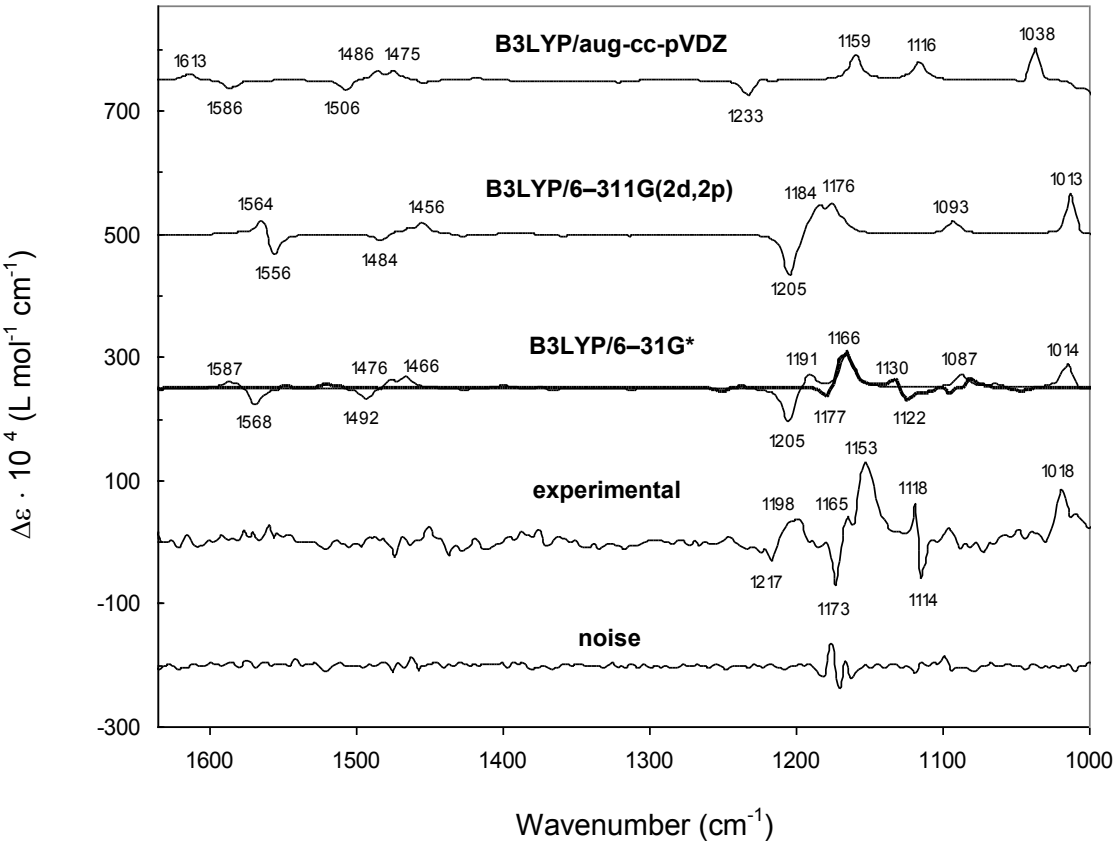

Figure 6-8: Comparison of experimental VCD spectrum of (–)-**1** with the predicted VCD spectra of (*R*)-**1.** At 6-31G* level, two traces are overlaid: a thin line corresponds to the monomer spectrum (90%) and a thick line to the dimer spectrum (10%).

Three notable VCD signals can be correlated between the experimental and the monomer theoretical traces. The positive experimental band at 1018 cm^{-1} corresponds to the positive band at 1014 cm^{-1}, 1013 cm^{-1} and 1038 cm^{-1}, predicted respectively with 6-31G*, 6-311G(2d,2p), and aug-cc-pVDZ basis sets. Another positive experimental band at 1153 cm^{-1} appears to correspond to the positive band predicted at 1166 cm^{-1}, 1176 cm^{-1}, and 1159 cm^{-1}, respectively with 6-31G*, 6-311G(2d,2p) and aug-cc-pVDZ basis sets. A bisignate couplet at (+)1198/(–)1217 cm^{-1} in the experimental spectrum corresponds to that at

(+)1191/(–)1205 cm^{-1} and at (+)1184/(–)1205 cm^{-1} in 6-31G* and 6-311G(2d,2p) predicted spectra. The aug-cc-pVDZ basis set doesn't display such couplet, but here the negative peak at 1233 cm^{-1} likely corresponds to the negative experimental peak occurring at 1217 cm^{-1}. Overall, the predicted absorbance and VCD spectra with aug-cc-pVDZ basis set appear to be in poorer agreement with the experimental spectra than those predicted with 6-31G* and 6-311G(2d,2p) basis sets.

The vibrational origins of the most pronounced 6-31G* predicted monomer VCD bands are as follows: benzene ring breathing modes and methyl group bending modes at 1014 cm^{-1}; phosphorus–carbon(benzene) bond stretching at 1087 cm^{-1}; phosphorus-oxygen bond stretching at 1166 cm^{-1}; asymmetric bond stretching among t-butyl carbons at 1191 cm^{-1}; phosphorus-carbon(t-butyl) bond stretching at 1205 cm^{-1}; methyl group bending modes at 1466, 1476, and 1492 cm^{-1}; bending (scissoring) modes of the amine group and carbon-carbon(benzene) stretching at 1568 and 1587 cm^{-1}.

Among the VCD bands, the missing correlations between the experimental and predicted monomer spectra are found in the dimer spectrum. Specifically, a bisignate couplet at (–)1114/(+)1118 cm^{-1} in the experimental spectrum corresponds to a couplet at (–)1122/(+)1130 cm^{-1} in the B3LYP/6-31G* predicted spectrum of the dimer. Also the negative experimental band at 1173 cm^{-1} is correlated to the B3LYP/6-31G* predicted negative band at 1177 cm^{-1}. It should be noted that the noise (bottom most trace in Figure 6-8) associated with the experimental VCD band at 1173 cm^{-1} makes the intensity associated with this

band less certain. The phosphorus-oxygen bond stretching and amine group bending modes are the predominant sources for these bands. Overall, the mixture of monomer and dimer theoretical spectra gives satisfactory correlation with all of the major experimental VCD bands, which leads to the conclusion that both monomer and dimer spices are present at the concentration used and that the absolute configuration of **1** is (–)-(*R*) or (+)-(*S*).

The ECD spectra calculated for (*R*)-**1a** with 6-31G*, 6-311G(2d,2p) and aug-cc-pVDZ basis sets are compared to the experimental ECD spectrum of (–)-**1** in Figure 6-9. The experimental ECD spectrum exhibits a pronounced positive peak and a partially measured negative ECD signal near ~ 200 nm. In order to facilitate the inspection of the short wavelength negative ECD signal, the spectrum in the 200-210 nm region is shown on an expanded scale in Figure 6-9E. The positive experimental ECD signal is reproduced in all three predicted spectra, although at a longer wavelength than that seen in the experimental spectrum. The negative experimental ECD signal is also reproduced in all three predicted ECD spectra, as can be seen in Figures 6-9A, B, and C. Furthermore, the experimental ECD intensity magnitude of ~ 0.7 for the pronounced positive peak matches well the predicted ECD intensity magnitude of ~ 0.6 in 6-31G* and 6-311G(2d,2p) calculations. The agreement is not as good between experimental and aug-cc-pVDZ predicted ECD magnitudes, since the predicted magnitude is ~ 2.4. Nevertheless, aug-cc-pVDZ basis set provides better correlation between the experimental and predicted wavelength position of the dominant positive ECD band. The qualitative correlation of the overall positive ECD signal in the

higher wavelength region and appearance of a negative ECD signal in the lower wavelength region confirms the (–)-(*R*)-**1** assignment derived from VCD data.

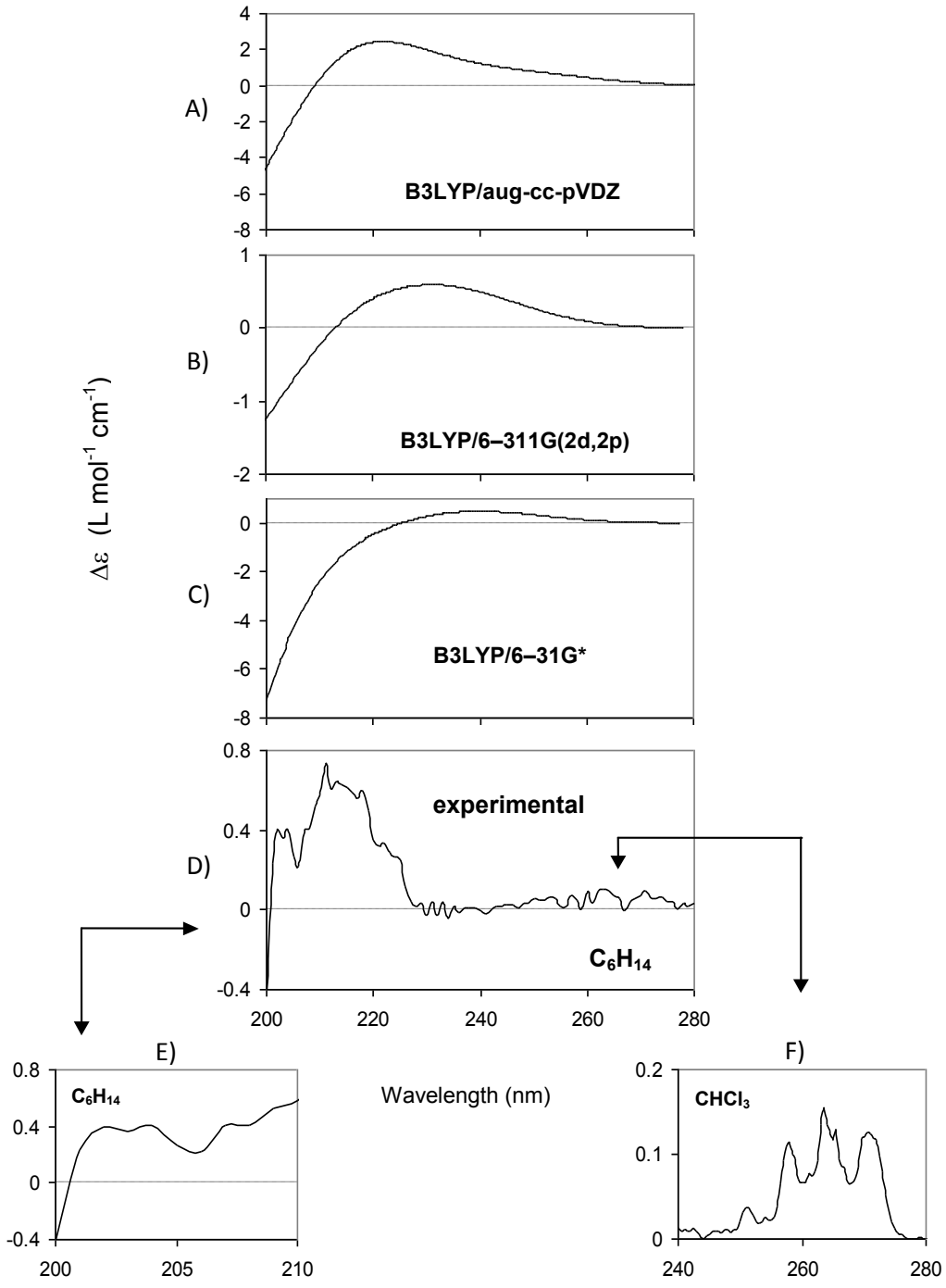

Figure 6-9: Predicted ECD spectrum for (*R*)-**1** (A,B,C) and experimental (D,E,F) ECD spectra of (–)-**1**.

The ECD spectra shown in Figure 6-9F contain weak positive bands experimentally obtained for (–)-**1** in $CHCl_3$ solvent. Although weaker in intensity due to the concentration used, these positive bands are also present in the experimental spectrum of (–)-**1** in hexane (Figure 6-9D). These weak positive ECD bands show three distinct maxima. It is well known[93,94,171] that these bands are characteristic of vibrational fine structure associated with π → π* electronic transition of phenyl chromophore, which is forbidden but appears due to vibronic interactions[93,94,171-173]. Such bands cannot be seen in the predicted spectra unless vibronic coupling is included[174] in the theoretical predictions of ECD.

As an additional independent verification of the configurational assignment of **1**, ORD data have been used (Figure 6-10). The experimentally obtained values of intrinsic rotation are –10.8(±0.3) at 633, –13.0(±0.4) at 589, –15.5(±0.9) at 546, –26.0(±0.9) at 436, –31.8(±1.8) at 405, and –40.0(±1.5) at 365 nm. The predicted optical rotation values for (*R*)-**1** obtained with 6-31G* basis set are –5.95 at 633, –7.21 at 589, –8.88 at 546, –17.26 at 436, –21.80 at 405, –30.65 and at 365 nm; those obtained with 6-311G(2d,2p) basis set for (*R*)-**1** are: –9.61 at 633, –11.26 at 589, –13.34 at 546, –22.34 at 436, –26.53 at 405, and –33.64 at 365 nm. As can be seen from these ORD data displayed in Figure 6-6, there is a satisfactory agreement of the overall trends between experimental data for (–)-**1** and predicted data for (*R*)-**1** via 6-31G* and 6-311G(2d,2p) basis sets. The agreement in signs of optical rotation support the absolute configuration assigned for **1** from VCD and ECD data.

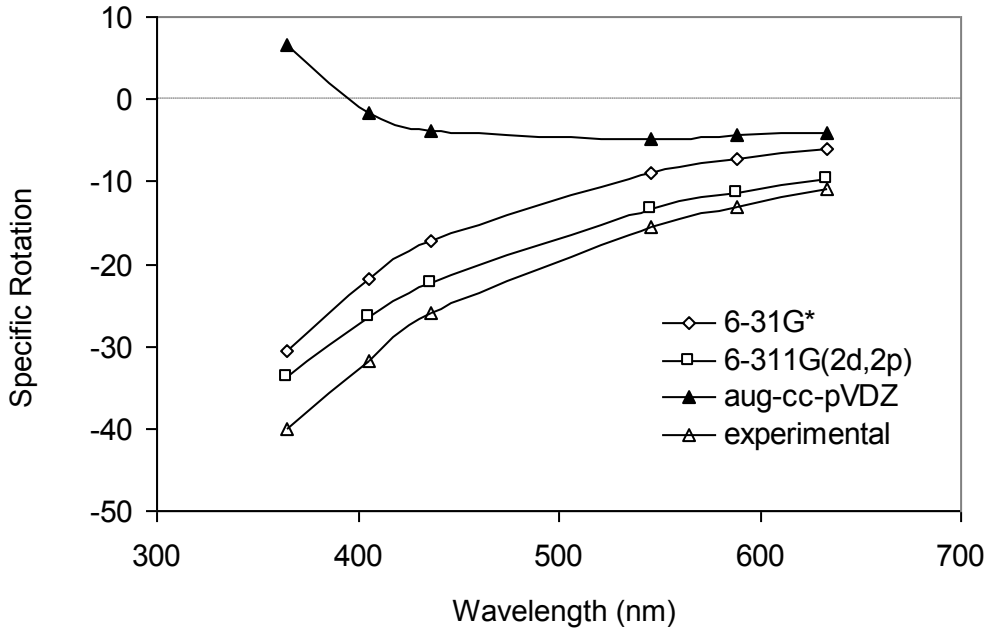

Figure 6-10: Comparison of ORD predicted for (*R*)-**1** with experimental ORD of (–)-**1**.

Unlike the 6-31G* and 6-311G(2d,2p) basis sets whose absolute magnitudes of calculated specific rotation increase with the decreasing wavelength, aug-cc-pVDZ basis set predicts a different trend for specific rotation and a change in its sign from negative to positive as wavelength decreases. The predicted optical rotation values for (*R*)-**1** associated with aug-cc-pVDZ basis set are: –4.00 at 633, –4.39 at 589, –4.72 at 546, –3.79 at 436, –1.56 at 405, and +6.59 at 365 nm. The predicted ORD with aug-cc-pVDZ basis set is bisignate which might result from two or more ECD bands of opposite sign at wavelengths below 200 nm. Thus, it appears that the aug-cc-pVDZ basis set may have incorrect ECD predictions at wavelengths shorter than 200 nm.

Conclusion

The comparison between experimental and predicted data associated with VCD, ECD and ORD have indicated that: a) only one tautomeric structure and one conformation is predominant for t-butylphenylphosphinoamidate; b) all three chiroptical methods suggest the assignment of (*R*)-configuration to (–)-t-butylphenylphosphinoamidate, which confirms the assignment by X-ray diffraction[163] c) at the concentration used for the VCD measurements, both monomer (90%) and dimer (10%) forms are present in the solution. For VCD, ECD and ORD predictions the aug-cc-pVDZ basis set gave poorer agreement with the experimental data, than the 6-31G* and 6-311G(2d,2p) basis sets. Our results indicate that aug-cc-pVDZ basis set might not be the most optimally parameterized for chiroptical predictions of phosphinoamidates.

CHAPTER VII

KRAMERS-KRONIG TRANSFORMATION OF EXPERIMENTAL ECD: APPLICATION TO THE ANALYSIS OF OPTICAL ROTATORY DISPERSION IN DIMETHYL-L-TARTRATE

Introduction

It is well known that electronic circular dichroism (ECD) and optical rotatory dispersion (ORD) are related via Kramers-Kronig (KK) transform[175,176]. Thus if one of these two properties is measured as a function of wavelength then the second can be obtained via KK transform. However, such transformation between experimental ECD and ORD has been undertaken[177-181] rarely, in practice. This is because, the instruments for measuring ECD and ORD are widely available and they can be measured independent of each other. The issue of converting ECD into ORD or vice versa does not arise in the routine use of ECD or ORD for chemical analysis. However, latest developments in independent quantum mechanical predictions of ECD[104-107] and ORD[4,101] brought these two areas to prominence for molecular structural determination. The conversion from quantum mechanically predicted ECD to ORD, using either KK or sum-over-states (SOS) transform, has been reported[27,29] recently. In the course of these investigations, it became apparent[27] that ECD must also be investigated for the analysis of ORD and that they should not be investigated in isolation from one another.

In this chapter, the utility of experimental ECD for the analysis of ORD is demonstrated with dimethyl tartrate as an example. Although dimethyl tartrate

can exhibit intramolecular and intermolecular hydrogen bonding, depending on the nature of solvent used, the focus of this work is not on finding systematic dependence on solvent, but is to explain the observed solvent dependent variations in ORD using the corresponding experimental ECD spectra. The experimental ECD spectra of tartartes[182-185] have been discussed before in the literature, but we could not find any literature reports on the experimental ORD of dimethyl tartrate. We are also not aware of experimental ECD investigations of dimethyl tartrate in different solvents. The experimental ECD spectra, as well as the experimental ORD spectra at discrete wavelengths, are presented here for dimethyl-L-tartrate in different solvents. The experimental ECD spectra do not show striking differences in different solvents, but the experimental ORD spectra show marked solvent dependence. These observations are analyzed by undertaking the KK transform of experimental ECD spectra. Quantum mechanical predictions of ECD and ORD for (*R,R*)-dimethyl tartrate obtained at the B3LYP/aug-cc-pVDZ level are also presented here for the first time.

Experimental Section

ECD and ORD Spectra: All ECD spectra have been recorded on a Jasco (J-720) spectrometer at room temperature using a scan speed of 100nm/min and 1 nm resolution and presented as averages of 20 scans. The short wavelength instrumental cutoff is at ~180 nm. A 0.1 cm path length quartz cell has been used for all ECD measurements. The ECD spectrum of ammonium d-camphor-10-sulfonate has been obtained in the 180-350 nm region. Survey scans indicated

that there are no ECD bands in the region above 350 nm for ammonium d-camphor-10-sulfonate. For dimethyl-L-tartrate, ECD spectra are obtained in the 180 to 275 nm region. Here again survey scans indicated no ECD bands in the region above 275 nm for dimethyl-L-tartrate. An Autopol III polarimeter with a resolution of 0.001° (reproducibility of 0.002°) has been used for optical rotation measurements. ORD spectra are obtained at discrete wavelengths by measuring the optical rotation at six different wavelengths, namely 633, 589, 546, 436, 405, 365 nm. The solutions are held in a cylindrical cell with 1 dm path length and optical rotation was measured several times (by removing the cell from, and reinserting the cell into, the sample compartment) to check for consistency. The averages of these measurements are used to calculate specific rotation. This procedure ensured that no unusual data scatter was present in the measurements. The same solutions of a given concentration have been used for both ECD and ORD studies. The concentration used for ammonium d-camphor-10-sulfonate (d-CSA) in H_2O is 1.2 mg/mL. The concentrations used for dimethyl tartate are 1 mg/mL for H_2O, acetonitrile (CH_3CN) and dimethylsulfoxide (C_2H_6SO) solutions. Dimethyl tartrate has limited solubility in carbon tetrachloride (CCl_4) and cyclohexane (C_6H_{12}). For this reason a concentration of 0.25 mg/mL was used for CCl_4 and saturated solution was used for C_6H_{12}. For these two cases, dissolution was facilitated by agitating the solutions in a sonicator. The absolute intensities displayed for C_6H_{12} solution are not accurate because of uncertainty in the concentration, but since the same solution was used for ECD and ORD, both measurements would have the same common error.

Calculations: We are not aware of any literature reports on quantum mechanical predictions of ECD or ORD for dimethyl tartrate, except for quantum mechanical predictions[25,186] of optical rotation at 589 nm. Three principle conformations of (*S,S*)-dimethyl tartrate, classified as trans-$COOCH_3$, trans-OH and trans-H, are defined with respect to rotation around the C^*-C^* bond. Within each of these principle conformers several possibilities exist[187] for intramolecular hydrogen bonding making the exploration of the conformational space of isolated dimethyl tartrate a tedious task. Rychlewska *et al.*[188] and Buffeteau *et al.*[189] have previously investigated the conformations of isolated dimethyl tartrate using 6-31G* basis set at either[188,189] RHF or B3LYP level. In the present study calculations have been done using a much larger aug-cc-PVDZ basis set. A total of 22 different conformations, including nine trans-$COOCH_3$ conformations, eight trans-OH conformations and five trans-H conformations have been optimized first at the B3LYP/6-31G* level. The five lowest energy conformations, that included two trans-$COOCH_3$ conformations and three trans-OH conformations have been further optimized at B3LYP/aug-cc-pVDZ level. The two lowest energy conformers (see Figure 7-1) optimized at B3LYP/aug-cc-pVDZ level are trans-$COOCH_3$-1 and trans-$COOCH_3$-2 with relative populations of 92% and 8% respectively. Gibbs energies were used to calculate the populations. The lowest energy conformer, trans-$COOCH_3$-1, with two internal hydrogen bonds between the hydrogen atoms of OH groups and their nearest C=O groups. The second lowest energy conformer, trans-$COOCH_3$-2 has one internal hydrogen bond between hydrogen atom of one OH group and its nearest C=O; the hydrogen

atom of second O-H group is approximately in between the oxygen atom of first OH group and the nearest ester oxygen atom (see Figure 7-1). These two lowest energy conformers of isolated molecule are similar to those found in previous studies[188,189]. The geometry optimizations were also undertaken in CCl_4 solvent using the PCM model implemented in Gaussian program, but the relative populations of the two lowest energy conformers remained approximately the same.

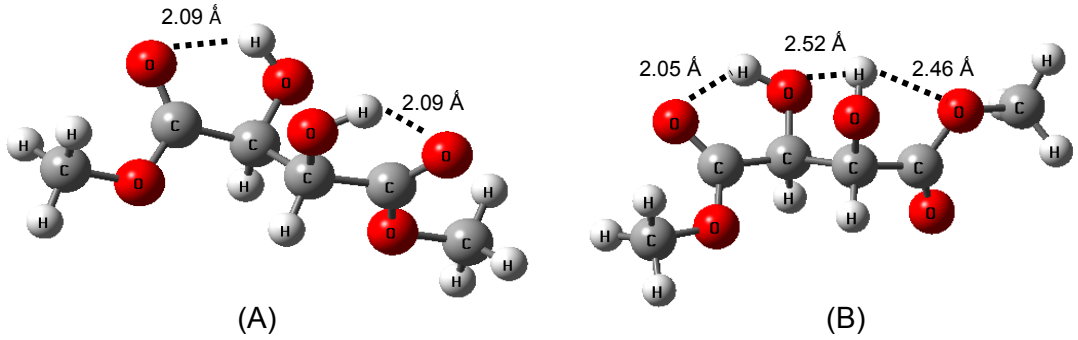

Figure 7-1: Two lowest energy conformers of (*S,S*)-dimethyl tartrate: (A) Trans-$COOCH_3$-1 and (B) trans-$COOCH_3$-2. Listed numbers are the distances between hydrogen atoms of hydroxyl groups and the nearest non-bonded oxygen atom(s).

ECD and OR predictions for the two lowest energy conformers, trans-$COOCH_3$-1 and trans-$COOCH_3$-2, of isolated dimethyl (*S,S*)-tartrate have been obtained using Gaussian 03 program[35] at B3LYP/aug-cc-pVDZ level. ECD and OR data for (*R,R*)-dimethyl tartrate are obtained by multiplying those obtained for (*S,S*)-dimethyl tartrate with (–1).

Conversion of experimental ECD into ORD: As it was explained in Chapter I, the KK transformation from molar ellipticity $[\theta(\mu)]$ (as a function of wavelength

μ) to the molar rotation $[\varphi(\lambda)]$ (both in the same units, deg·cm^2 ·dmol^{-1}) at wavelength λ is given as[190]:

$$[\varphi(\lambda)] = \frac{2}{\pi}\int_0^{\infty}[\theta(\mu)]\frac{\mu}{(\lambda^2-\mu^2)}\,d\mu \qquad (7-1)$$

The integration in Equation 7-1 is normally truncated to a limited region, because it is not practical to integrate from zero to infinity. The integral on the right hand side of Equation 7-1 has singularity at $\lambda = \mu$. To overcome singularity and convert experimental ECD into ORD, the method suggested by Ohta and Ishida[31] has been adopted here. With this method raw experimental ECD data can be used as such without need for any spectral simulations. When the experimental ECD spectrum is available at constant intervals of h and the wavelengths and spectral intensities at these intervals are labeled, respectively, as μ_j and $[\theta(\mu_j)]$ with j = 1,2 ..N, Equation 7-1 can be approximated, following Ohta and Ishida[31], as:

$$[\varphi(\lambda)] = \frac{2}{\pi}\int_0^{\infty}[\theta(\mu)]\frac{\mu}{(\lambda^2-\mu^2)}\,d\mu \approx \left(\frac{2}{\pi}\right)(2h)\left(\frac{1}{2}\right)\sum_j{}^{\#}\left[\frac{[\theta(\mu_j)]}{\lambda-\mu_j} - \frac{[\theta(\mu_j)]}{\lambda+\mu_j}\right] \qquad (7-2)$$

As indicated in Chapter I, the summation $\sum^{\#}$ signifies that the summation uses alternate data points to avoid singularity at $\lambda = \mu$. To evaluate this method for converting experimental ECD into ORD, the experimental ECD and ORD have been measured (see Figure 7-2) for ammonium d-camphor-10-sulfonate in water, which is commonly used as the standard for these measurements. The experimentally measured ORD and that obtained as the KK transform of ECD are in excellent agreement (Figure 7-2).

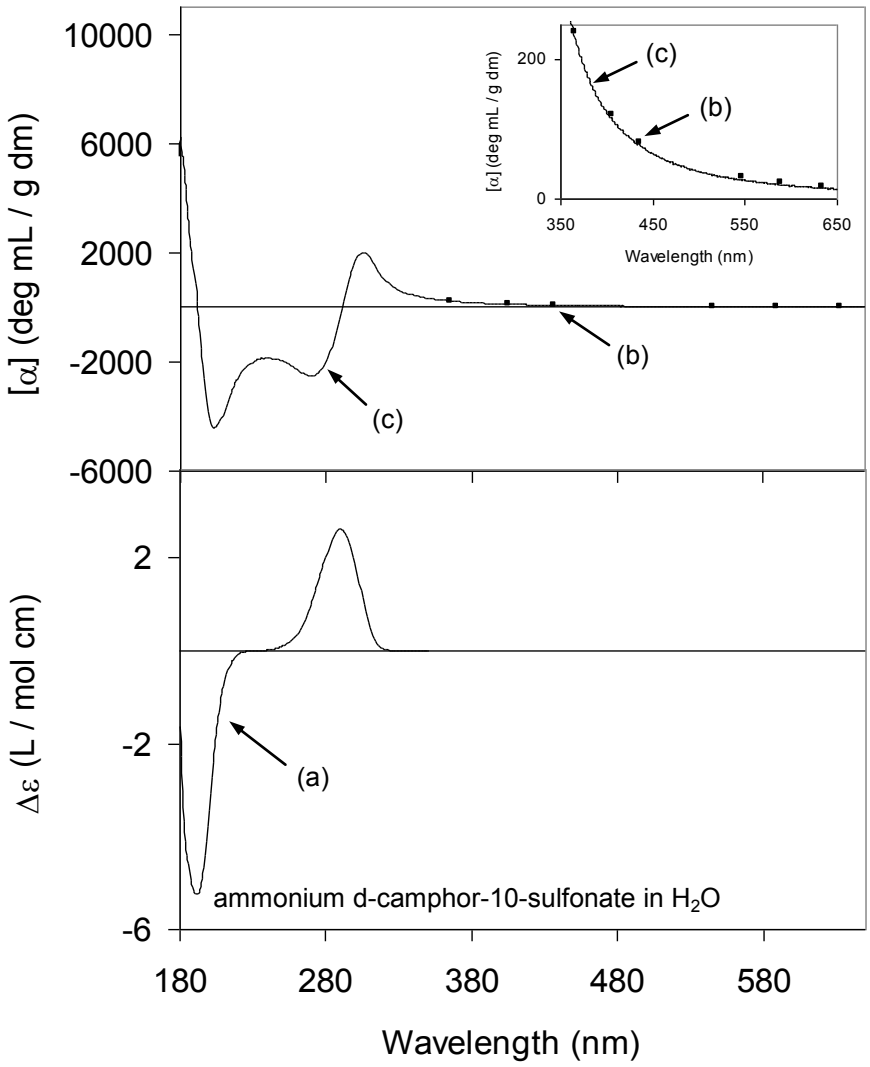

Figure 7-2: ECD and ORD spectra of ammonium d-camphor-10-sulfonate (d-CSA) in water. Trace (a) is experimental ECD spectrum, data points (b) represent experimental ORD, and trace (c) is ORD obtained as KK transform of experimental ECD.

An alternative method for converting experimental ECD to ORD, also indicated in Chapter I, uses the sum-over-states (SOS) expression for ORD that is applicable in both non-resonant and resonant regions[27].

$$[\varphi(\lambda)] = \frac{0.915 \cdot 10^{42}}{2} \sum_n \lambda_n \left[\frac{(\lambda - \lambda_n)}{(\lambda - \lambda_n)^2 + \sigma_n^2} - \frac{(\lambda + \lambda_n)}{(\lambda + \lambda_n)^2 + \sigma_n^2} \right] R_n \qquad (7-3)$$

In Equation 7-3, λ_n is the wavelength of the band center of n^{th} band and σ_n is the *half-width* at half the maximum height of that band. The use of rotational strengths (which represent the integrated ECD band intensities) in Equation 7-3 requires that the experimental ECD spectra be subjected to curve fitting. This extra labor is avoided by using the raw experimental ECD data with Equation 7-2. As indicated in Chapter I, specific rotation (in deg·mL·dm^{-1}·g^{-1}) is obtained from molar rotation as $[\alpha(\lambda)] = \frac{100}{M}[\varphi(\lambda)]$.

Results and Discussion

The experimental ORD data for dimethyl-L-tartrate in different solvents are displayed in Figure 7-3. The lowest energy ECD band for dimethyl tartrate (*vide infra*) appears at ~215 nm, so the ORD region displayed in Figure 7-3 is the non-resonant region. In this region it can be seen clearly that both sign pattern and magnitude of ORD of dimethyl-L-tartrate vary with the solvent. In inert solvents CCl_4 and C_6H_{12}, dimethyl-L-tartrate exhibits monosignate negative ORD in the long wavelength non-resonant region. In polar solvents CH_3CN and C_2H_6SO, ORD in the long wavelength non-resonant region is bisignate with weak positive values at longer wavelengths and a change of sign near 546 nm in C_2H_6SO and between 405 and 365 nm in CH_3CN. Such bisignate ORD in the non-resonant long wavelength region is an indication[29] of oppositely signed ECD contributions from two or more different transitions at shorter wavelengths. In H_2O, ORD in the long wavelength non-resonant region is positive which is opposite to that observed in CCl_4 and C_6H_{12}.

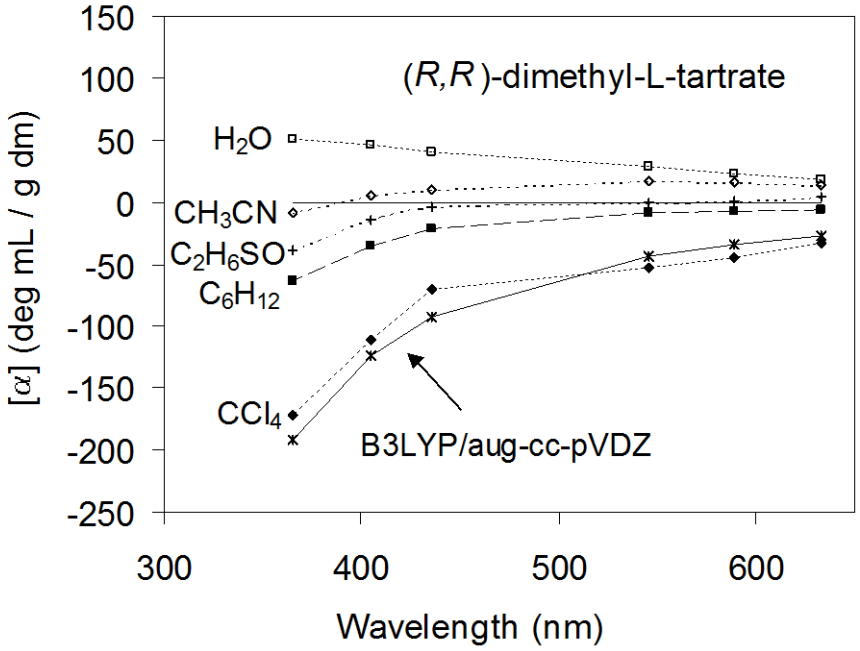

Figure 7-3: ORD spectra of dimethyl tartrate. Experimental ORD was measured for dimethyl-L-tartrate in five solvents. Theoretical ORD was obtained for (*R,R*)-dimethyl tartrate at B3LYP/aug-cc-pVDZ level for the two lowest energy trans-$COOCH_3$ conformers and presented as population weighted data.

To understand the variation of ORD with solvent, the experimental ECD spectra are investigated. Solvent interference prevented ECD measurements in CCl_4 and C_2H_6SO. The ECD spectra of dimethyl-L-tartrate in H_2O, CH_3CN and C_6H_{12} are displayed in Figures 7-4 to 7-6. In all three solvents, ECD spectra show a negative band at 214 nm in H_2O, at 216 nm in CH_3CN and at 214 nm in C_6H_{12}. These spectra also hint a positive ECD band at ~180 nm, which is not measured fully because of the instrumental cut off at 180 nm. The experimentally measured ORD and that obtained as the KK transform of experimentally measured ECD are also compared in Figures 7-4 to 7-6. In H_2O, ORD in the non-resonant long wavelength region obtained as KK transformed ECD is negative and opposite in sign to the experimentally measured ORD. In CH_3CN, ORD in

the non-resonant long wavelength region obtained as KK transformed ECD is also negative but the experimentally measured ORD is weak positive in the ~633-400 nm and changes sign to negative below ~400 nm. In C_6H_{12}, ORD in the non-resonant long wavelength region obtained as KK transformed ECD and experimentally measured ORD are both negative, but the former has larger magnitude. Since the KK transform of experimental ECD is not in agreement with the experimentally measured ORD, in all three solutions, there must be one or more ECD bands at shorter wavelengths that are not fully included in the KK transform of experimental ECD. To determine these missing ECD bands, the following approach has been used. Equation 7-1 can be written for the experimentally measured ORD as:

$$[\varphi(\lambda)]^{\exp} = \frac{2}{\pi}\int_{0}^{\mu_S}[\theta(\mu)]^{mis}\frac{\mu}{(\lambda^2-\mu^2)}\,d\mu + \frac{2}{\pi}\int_{\mu_S}^{\mu_L}[\theta(\mu)]^{\exp}\frac{\mu}{(\lambda^2-\mu^2)}\,d\mu \qquad (7-4)$$

where μ_S and μ_L are the shortest and longest wavelengths where the experimental ECD measurements terminated; superscript “exp” indicates experimentally measured data and “mis” represents the missing experimental data that could not be measured. The wavelengths longer than μ_L need not be included in the above equation provided ECD is zero at wavelengths longer than μ_L. The second term on the right hand side of Equation 7-4 represents the actual KK transform undertaken. The major contribution to $[\theta(\mu)]^{mis}$ in the first term on the right hand side of Equation 7-4 comes from ECD bands in the wavelength range 0 to μ_S that could not be measured. Therefore the first term on the right

hand side of Equation 7-4 can be approximated by the SOS expression, leading to:

$$[\varphi(\lambda)]^{\exp} \approx \frac{0.915\cdot 10^{42}}{2} \sum_{n}^{\#} \lambda_n^{mis} \left[\frac{\left(\lambda - \lambda_n^{mis}\right)}{(\lambda - \lambda_n^{mis})^2 + \sigma_n^2} - \frac{\left(\lambda + \lambda_n^{mis}\right)}{(\lambda + \lambda_n^{mis})^2 + \sigma_n^2} \right] R_n^{mis} + [\varphi(\lambda)]^{KK} \quad (7-5)$$

where the # sign on the summation indicates that this summation is restricted to the transitions that appear at wavelengths shorter than μ_S and $[\varphi(\lambda)]^{KK} = \frac{2}{\pi} \int_{\mu_S}^{\mu_L} [\theta(\mu)]^{\exp} \frac{\mu}{(\lambda^2 - \mu^2)} d\mu$. The approximate sign in Equation 7-5 results from the fact that, since each ECD band has a certain band profile, a portion of the contribution from the first term on the right side of Equation 7-5 may already be present in the experimentally measured $[\theta(\mu)]^{\exp}$. For the same reason, a portion of $[\theta(\mu)]^{mis}$ may have contributions from ECD bands in the range μ_S to μ_L. The difference between experimentally measured ORD, $[\varphi(\lambda)]^{\exp}$, and KK transformed ECD, $[\varphi(\lambda)]^{KK}$, is then approximated as:

$$[\varphi(\lambda)]^{\exp} - [\varphi(\lambda)]^{KK} \approx \frac{0.915\cdot 10^{42}}{2} \sum_{n}^{\#} \lambda_n^{mis} \left[\frac{\left(\lambda - \lambda_n^{mis}\right)}{(\lambda - \lambda_n^{mis})^2 + \sigma_n^2} - \frac{\left(\lambda + \lambda_n^{mis}\right)}{(\lambda + \lambda_n^{mis})^2 + \sigma_n^2} \right] R_n^{mis} \quad (7-6)$$

On the right hand side of Equation 7-6 there are three unknowns, namely the band center λ_n^{mis}, rotational strength R_n^{mis} and *half-width* at half the maximum height of the band σ_n for each missing ECD band. If the experimental ORD is measured continuously at constant wavelength intervals, in the entire region as for ECD, then there will be enough data points for subjecting Equation 7-6 to

least square fitting with sufficient accuracy. It should be noted that if several missing ECD bands contribute to the observed ORD and their band positions are not known, then the least square analysis of Equation 7-6 may only provide some *averages* of missing band centers and rotational strengths. Therefore one should not expect to extract the precise number of missing ECD bands, their band positions and intensities from Equation 7-6.

In the present case, we do not have access to a continuous scan ORD instrument and therefore the experimental ORD was measured only at six discrete wavelengths in the non-resonant long wavelength region. Six data points are not sufficient enough to determine multiple missing bands with three unknown parameters for each band. For this reason, we limit Equation 7-6 to one missing ECD band and write it as:

$$[\varphi(\lambda)]^{\exp} - [\varphi(\lambda)]^{KK} \approx \frac{0.915 \cdot 10^{42}}{2} \lambda_n^{mis} \left[\frac{\left(\lambda - \lambda_n^{mis}\right)}{(\lambda - \lambda_n^{mis})^2 + \sigma_n^2} - \frac{\left(\lambda + \lambda_n^{mis}\right)}{(\lambda + \lambda_n^{mis})^2 + \sigma_n^2} \right] R_n^{mis} \qquad (7-7)$$

Since the positive ECD band at ~180 nm in the experimental ECD spectrum was not fully measured, the KK transform of experimental ECD was restricted to the region of 193-275 nm in the analysis of Equation 7-7. Assuming σ_n =16.65 nm (which equals 20 nm at 1/e of peak height for Gaussian bands), a non-linear least square fitting of Equation 7-7 was undertaken to determine the unknown parameters λ_n^{mis} and R_n^{mis}. It should be emphasized that the present analysis amounts to assuming that a single ECD band in the experimentally inaccessible region is responsible for observed variations in the experimental

ORD. The results obtained in this analysis are presented in Table 7-1. The two parameters λ_n^{mis} and R_n^{mis} are strongly correlated, with the magnitude of R_n^{mis} increasing as λ_n^{mis} decreases.

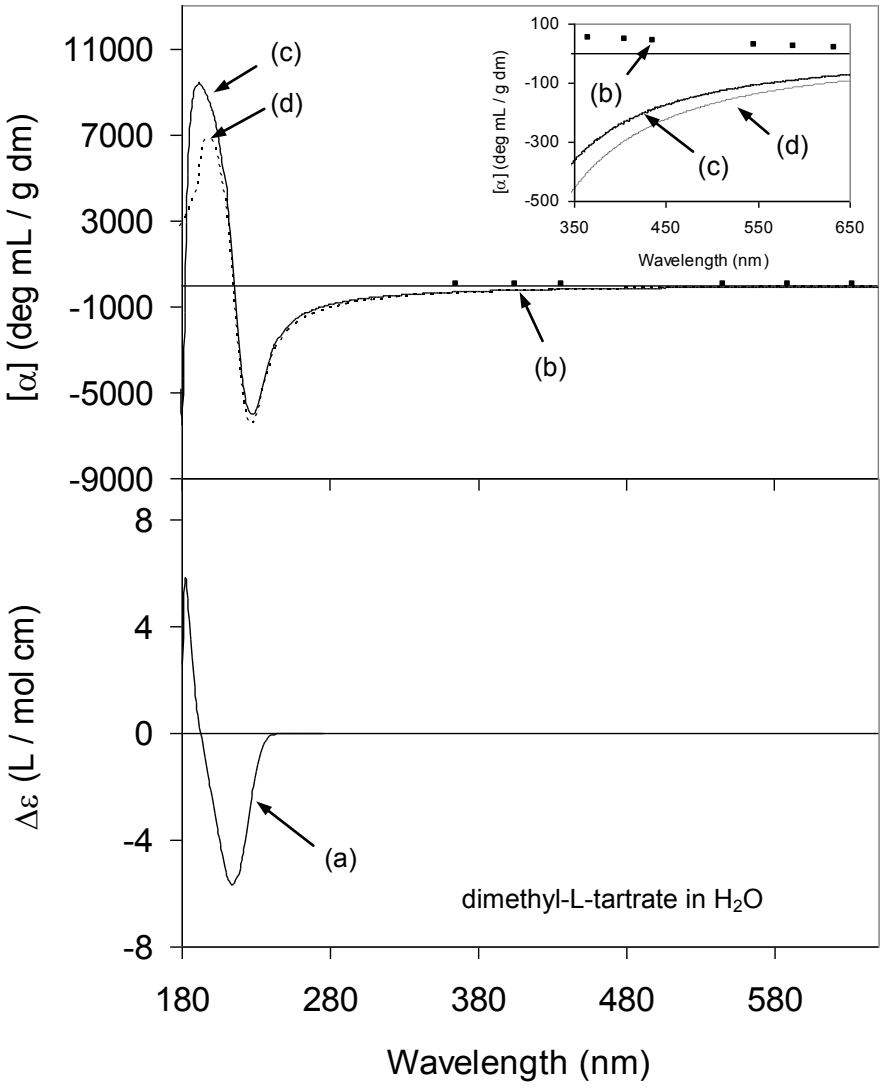

Figure 7-4: ECD and ORD spectra of dimethyl L-tartrate in water. Trace (a) is experimental ECD spectrum, trace (b) represent experimental ORD, trace (c) represents the ORD obtained as KK transform of experimental ECD in the 180-275 nm range, while trace (d) represents the ORD obtained as KK transform of experimental ECD in the 193-275 nm range.

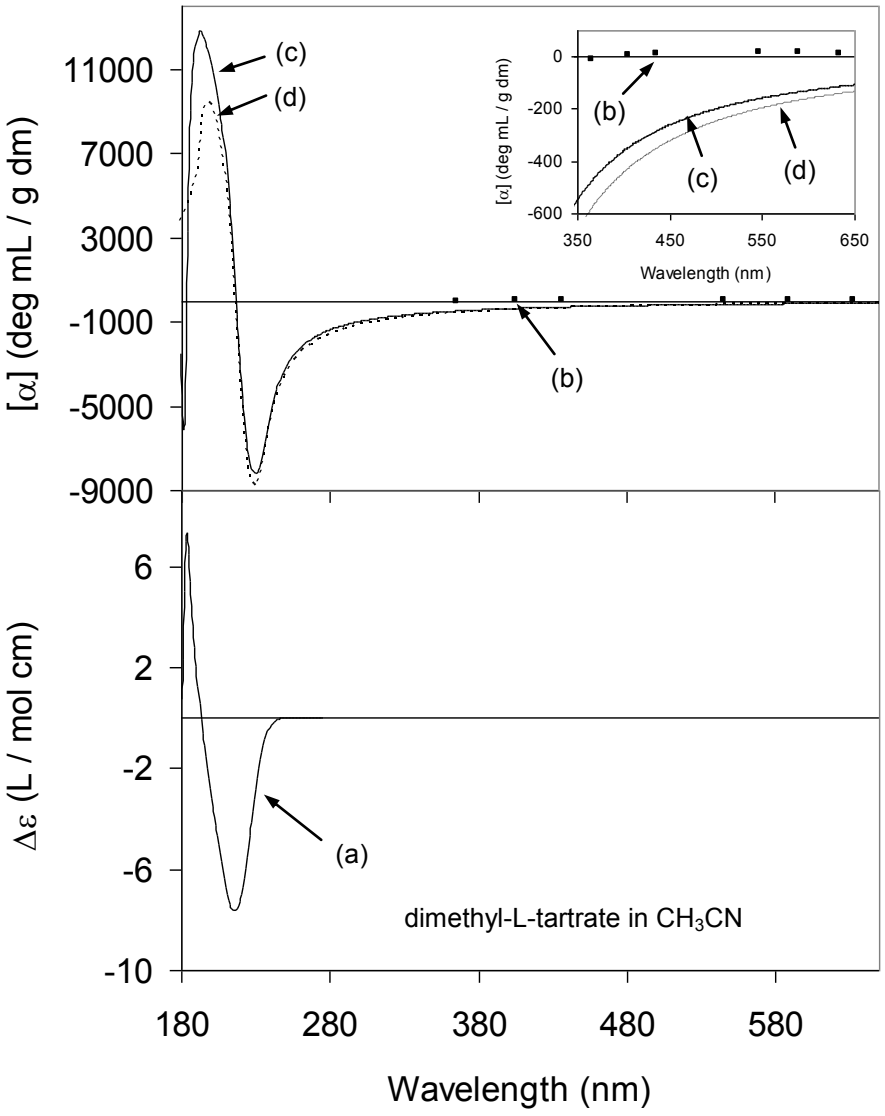

Figure 7-5: ECD and ORD spectra of dimethyl L-tartrate in CH_3CN. Trace (a) is experimental ECD spectrum, trace (b) represent experimental ORD, trace (c) represents the ORD obtained as KK transform of experimental ECD in the 180-275 nm range, while trace (d) represents the ORD obtained as KK transform of experimental ECD in the 193-275 nm range.

Table 7-1: ECD bands of dimethyl-L-tartrate.

	Observed low energy band		High energy band estimated from Eq.7-7	
solvent	Wavelength (nm)	Peak intensity[b]	Wavelength (nm)	Peak intensity[a,b]
H_2O	214	-5.67	198 ± 2	$+6.2 \pm 0.1$
CH_3CN	216	-7.62	188 ± 4	$+8.6 \pm 0.4$
C_6H_{12}	214	-6.10	183 ± 5	$+5.9 \pm 0.4$

[a] Gaussian band profile with 16.65 nm half width at 1/e of peak height was assumed; experimental ECD data in the 193-275 nm was used for the KK transform.
[b] L/(mol cm)

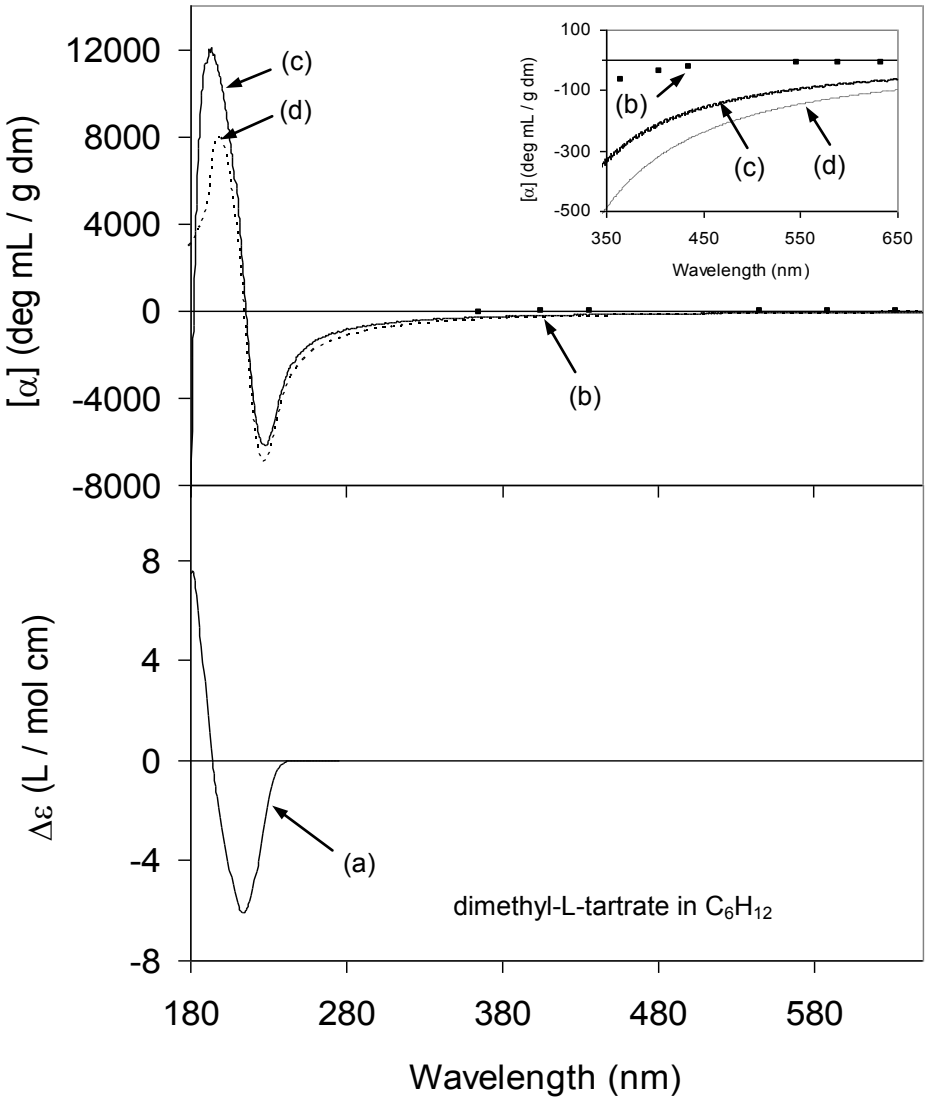

Figure 7-6: ECD and ORD spectra of dimethyl L-tartrate in C_6H_{12}. Trace (a) is experimental ECD spectrum, trace (b) represent experimental ORD, trace (c) represents the ORD obtained as KK transform of experimental ECD in the 180-275 nm range, while trace (d) represents the ORD obtained as KK transform of experimental ECD in the 193-275 nm range.

The estimated values for missing ECD bands in Table 7-1 serve to identify that the experimental ECD spectrum must have at least one strong positive ECD band in each of the three solvents. This positive ECD band determines the sign behavior of ORD in the long wavelength resonance region. The band center of positive ECD band was predicted to be 198, 188 and 183 nm, respectively in

H_2O, CH_3CN and C_6H_{12} solutions. However, based on the experimental ECD spectra measured (Figures 7-4 to 7-6), the band center of positive ECD band appears to be at or below ~180 nm. Thus it should be emphasized that the precision of the numbers listed in Table 7-1 is less than desired because of the limited amount (six data points) of experimental optical rotation data used in deriving them. The measurement of full ORD spectrum in the entire region as was done for ECD, rather than measuring optical rotation values at six discrete wavelengths, is necessary to provide correct estimates of band positions and intensities for the missing experimental ECD bands at shorter wavelengths. It is expected that when full ORD spectrum is used the band position of missing positive ECD band would have been located at a shorter wavelength and its intensity would have been higher (especially in water and CH_3CN) than those listed in Table 7-1.

Despite the uncertainties in the band positions and intensities of missing ECD bands mentioned above, the reason for different ORD patterns for dimethyl-L-tartrate in different solvents can be explained as follows. From the limited experimental ORD data for dimethyl-L-tartrate, and KK transform of experimental ECD, it is certain that at least one positive ECD band around 180 nm contributes significantly to ORD in the non-resonant long wavelength (365-633 nm) region. However, the present data does not allow us to ascertain if there is more than one positive ECD band. The ORD of dimethyl-L-tartrate has mutually counteracting contributions from low energy negative ECD band at ~214 nm and high energy positive ECD band around 180 nm. In water solvent, the contribution

from positive ECD band dominates that from negative ECD band resulting in positive ORD in the non-resonant long wavelength region. In CH_3CN solvent also the contribution from positive ECD band dominates that from negative ECD band resulting in positive ORD in the non-resonant long wavelength region but the opposing contributions from these two ECD bands cancel each other between 365 and 405 nm resulting in a sign change for ORD. The same situation is expected to apply to ORD in C_2H_6SO. In C_6H_{12} solvent, the contribution from negative ECD band dominates that from high energy positive ECD band resulting in negative ORD in the long wavelength non-resonant region. The same situation is expected to apply in CCl_4.

While the experimental ECD spectra in the 190-275 nm range do not reflect significant solvent influence on dimethyl-L-tartrate, ORD in the non-resonant long wavelength region clearly indicates significant solvent influence. The present analysis using KK transform of experimental ECD and its comparison to experimentally measured ORD helps to understand the reason for remarkable solvent dependence of ORD for dimethyl tartrate.

Recently Vaccaro and coworkers successfully correlated[191] the solvent dependence of optical rotation of cis-pinane in the non-resonant region to the dielectric function of solvent. In the present case for dimethyl tartrate, the reason for dominant contribution to ORD in the long wavelength region from the high energy positive ECD band in some solvents (H_2O, CH_3CN, C_2H_6SO) and not others (CCl_4, C_6H_{12}), cannot be directly linked to the dielectric properties of solvents alone. This is because the structure of dimethyl-L-tartrate can be

influenced by the nature of solvent in two different ways. 1) The low energy conformations of isolated molecule may change their relative populations in different solvents. 2) Due to the differences in hydrogen bonding capabilities of solvents, conformers that are different from those of isolated molecule may be present in different solvents. To assess the feasibility of these possibilities, quantum mechanical predictions of ORD and ECD have been undertaken on the two lowest energy conformers of isolated molecule. The ORD predicted for isolated (*R*,*R*)-dimethyl tartrate (see Figure 7-2) matches closely that observed for dimethyl-L-tartrate in CCl_4 suggesting that the conformations predicted for isolated molecule could be good representations for inert solvents. This is also confirmed by the predicted ECD spectra shown in Figure 7-7, where the spectra for individual conformers and population weighted ECD spectrum are compared to the experimental ECD spectra. The population weighted ECD spectrum of (*R,R*)-dimethyl tartrate shows a negative ECD band at 220 nm, which is similar to the experimental ECD spectra of dimethyl-L-tartrate (except for a shift in relative band positions), and a positive ECD band centered at ~169 nm. The ECD spectra of individual conformers of (*R,R*)-dimethyl tartrate show oppositely signed ECD for the low energy bands in the 220-240 nm region, but higher energy bands in the 160-180 nm range have the same sign for ECD. Thus as the relative population of the second lowest energy conformer increases and that of first lowest energy conformer decreases, the low energy negative ECD band in the population weighted spectrum decreases in intensity but high energy positive ECD band will remain approximately the same. The mutual cancellation of ORD

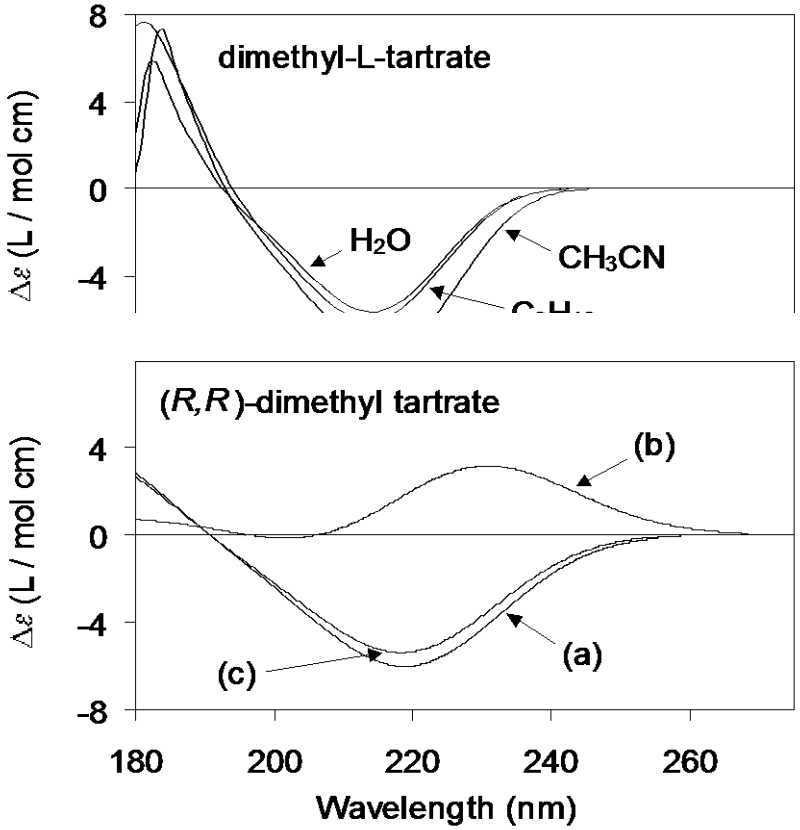

Figure 7-7: Comparison of B3LYP/aug-cc-pVDZ predicted ECD spectra of (*R,R*)-dimethyl tartrate (bottom panel) with experimental ECD spectra of dimethyl-L-tartrate (top panel). (a) ECD of the lowest energy conformer (trans-$COOCH_3$-1); (b) ECD of the second lowest energy conformer (trans-$COOCH_3$-2); (c) population weighted ECD spectrum.

contribution from these two ECD bands can then lead to a change in sign pattern for ORD in the long wavelength non-resonant region. Thus, in principle, the variation of ORD with solvent may be qualitatively explained in terms of relative population changes of the two lowest energy conformers in different solvents. However, this explanation is unlikely to be correct because the same two conformers could not explain the observed[192] vibrational circular dichroism of dimethyl tartrate in different solvents. It is very likely that the hydrogen bonding ability of solvents (especially H_2O and C_2H_6SO) may stabilize new conformations

that are not stable for isolated molecule. Then it is necessary to investigate the solvent influence on quantum mechanically optimized structures. Such investigations are not trivial because simple solvent models used for quantum mechanical calculations are far from being realistic. As a result it might be necessary to explicitly include solvent molecules in geometry optimizations, in which case the quantum mechanical predictions of chiroptical properties for dimethyl tartrate in different solvents may remain a challenging task for some time to come.

Conclusion

It is found that the ECD spectra of dimethyl tartrate in the 190-275 nm region are similar in different solvents. On the contrary, ORD of dimethyl tartrate in the 365-633 nm region varies with solvent significantly. These observations are explained by obtaining the Kramers-Kronig transform of experimental ECD and comparing it with the experimentally observed ORD. This analysis indicated that a positive ECD band at shorter wavelength, which could not be measured experimentally, has dominating contribution to ORD in the long wavelength region. The position and intensity of this positive ECD band change with solvent, resulting in the variation of ORD pattern in the long wavelength non-resonant region. This analysis demonstrates that the conversion of experimental ECD into ORD provides important insights in the analysis of ORD. The predicted ECD spectrum for (*R,R*)-dimethyl tartrate at the B3LYP/aug-cc-pVDZ level matches the experimentally observed ECD for dimethyl-L-tartrate in the wavelength region

available for comparison. The predicted ORD spectrum for (*R,R*)-dimethyl tartrate at the same level matches the experimentally observed ORD for dimethyl-L-tartrate in non-polar solvent CCl_4. However, predictions of the experimentally observed ORD of dimethyl-L-tartrate in polar solvents (H_2O, CH_3CN and C_2H_6SO) require additional careful calculations.

CHAPTER VIII

VIBRATIONAL CIRCULAR DICHROISM OF CARBOHYDRATE FILMS FORMED FROM AQUEOUS SOLUTIONS

Introduction

Carbohydrates are easily identified as one of the most important classes of chemical compounds, because they are responsible not only for sustenance of life but also for various chemical processes, such as those in chiral chromatographic separations. Furthermore, carbohydrates take an important role in modern industrial society, such as in the manufacture of drugs. As the function of a given carbohydrate depends to a large extent on its structure, a large amount of the research work is focused on developing methods that can reveal the structure of carbohydrates. Chiroptical spectroscopic methods have been explored since very early days because chirality is an important aspect of carbohydrate chemistry. In the older literature on carbohydrate structural chemistry, the use of optical rotation has found wide spread applications[193,194]. Although ECD has become a routine method[11] in biochemical laboratories, its applications to carbohydrates[100,195] have been limited due to the absence of easily accessible electronic transitions in the visible/ultraviolet region. Special instrumentation extending into vacuum ultraviolet is necessary for studying carbohydrates using ECD and some such studies have been reported[100,195] for carbohydrates in solution. Nevertheless ECD measurements for film or solid state samples are known to contain artefacts[196]. Specially designed

instruments[197] that nullify the artifacts are necessary for solid state ECD measurements and such instruments are not accessible to many researchers.

In light of the difficulties encountered for ECD studies on carbohydrates, the emergence of mid infrared VCD[198] and vibrational Raman optical activity (VROA)[199] in the early seventies was greeted with great enthusiasm, as reflected by rapid growth[200-206] in these areas. Carbohydrates, however, were considered[207-210] as difficult samples for VCD measurements, because flexible nature of carbohydrates yields smaller VCD signals compared to the signals obtained for molecules with rigid structures. In recent years, improved VCD instrumentation has overcome the problems in measuring the weak VCD signals associated with carbohydrates[211-215]. As these improvements took place, it soon became apparent that the strong infrared absorption of water at 1650 cm^{-1} overwhelms the sample absorption bands and prevents VCD measurements on carbohydrates in aqueous media. As a consequence, most VCD studies on carbohydrates were conducted[211-215] in dimethylsulfoxide (DMSO) solvent, which is not quite native to biological processes. VCD measurements on carbohydrates in DMSO were restricted to the 1600-1150 cm^{-1} region, as the strong absorption of solvent at ~1000 cm^{-1} prevented VCD measurements below ~1150 cm^{-1}. Since water does not interfere in Raman spectra, VROA spectroscopy on the other hand was found to be useful for characterizing the carbohydrates and several applications of VROA for carbohydrates have been reported by Barron and coworkers[216-222].

In the quest for finding ways to measure VCD of carbohydrates in aqueous media, studies in our laboratory demonstrated that using very high concentrations (up to 4 M in some cases) and short path length (6 μm) liquid cells, one can measure[223] VCD for aqueous carbohydrate solutions. Strong absorption bands for carbohydrates were found in the 1200-900 cm^{-1} region, so the initial measurements[223] were conducted in this region. Since the absorption bands for carbohydrates in the ~1600-1200 cm^{-1} region (where vibrational modes, such as -C-H bending, CH_2 wag, and –O-H in-plane bending appear) are weaker than those in the ~1200-900 cm^{-1} region (where C-O stretching bands appear), even higher concentrations than those already used for ~1200-900 cm^{-1} region were required for measurements in the ~1600-1200 cm^{-1} region. For this reason the previous aqueous solution investigation[223] focused in the ~1200-900 cm^{-1} region, a region which is not accessible in DMSO solvent. Despite this advance, the fact that a large amount of carbohydrate sample was required for these studies, which is a serious issue for those working in biochemical arena, has dampened the enthusiasm for VCD studies on carbohydrates.

In the present study we report a significantly improved and simplified procedure for measuring the VCD spectra of carbohydrates, where the amount of sample required for VCD measurements has been reduced by one to two orders of magnitude. Specifically, using a newly modified instrument[15,224,225] that uses dual polarization modulation method[226], we show that by depositing aqueous solution samples of carbohydrates as films, VCD spectra obtained for films are identical to those obtained for aqueous solutions. Spectra obtained in this

manner for carbohydrate films required up to two orders of magnitude smaller amounts of carbohydrate samples than those in the previous[223] aqueous solution study. Furthermore, removal of interfering water absorption resulted in higher light throughput and better signal to noise. Additionally we present data demonstrating that the VCD spectra for carbohydrate films can be obtained in the entire 2000-900 cm^{-1} region by controlling the concentration or volume of parent aqueous solution used to prepare the films. Numerous new future directions for VCD studies can result from the development presented in this chapter

Experimental Section

The carbohydrates used in this study were obtained from Sigma and used as received. In the case of allose, fucose, and glucose, the solutions were allowed to equilibrate (allowing for mutarotation) for at least 24h. The choice of carbohydrates studied was made based on the availability of aqueous solution-based VCD spectra for comparison, and also on the variety of glycosidic linkages.

Spectral measurements on films: In order to prepare the film samples a drop-cast method was used, where a certain amount of parent aqueous solution was deposited on a 2.5 cm diameter BaF_2 window and allowed to dry at room temperature for approximately 2-3 hours in a fume hood, which provided a constant airflow over the sample.

The film VCD measurements were obtained on a modified ChiralIR (Bomem-Biotools, Canada) instrument[15,224,225] using double polarization

modulation method[226], ZnSe beam splitter, BaF_2 polarizer, optical filter (transmitting below 2000 cm^{-1}) and a 2×2 mm HgCdTe detector. Both PEMs used in this instrument contained ZnSe optical elements that did not have anti-reflection coating. As a consequence the throughput of our instrument is only 50% and better signal to noise than that presented here can be obtained in principle by using antireflection coated ZnSe optical elements. VCD spectra were recorded at 4 cm^{-1} resolution, with PEM settings of 1214 cm^{-1} and 1400 cm^{-1} for the first and second PEM respectively. The spectral collection times varied from 1 to 3 hours depending on the sample. Spectra for trehalose and cyclodextrin were recorded for one hour (as these samples are known[223] to exhibit larger signals), those for allose and fucose were recorded for 2 hours and those for the rest of the samples were recorded for 3 hours. Baseline corrections were performed by subtracting the VCD spectrum of a blank BaF_2 window, obtained under the same conditions as the sample spectrum. For the absorption spectra of films neither the solvent absorbance subtraction nor a background subtraction was needed. To verify the independence of film orientation, both absorption and VCD spectral measurements were repeated by rotating the film 45º around the light beam axis.

A point that needs to be clarified is the fact the concentration in a given film is undefined because of solvent evaporation during film formation. The concentrations we refer to for film studies are those of parent solutions used to make the films.

Spectral measurements on aqueous solutions: The VCD measurements for carbohydrates in water solutions were obtained in our laboratory several years ago as described previously[223] using ChiralIR instrument with a single PEM. The aqueous solution spectra presented here for maltose, cyclodextrin, trehalose, glucose, cellobiose and gentiobiose are same as those reported earlier[223], but those for fucose and allose have not been reported before. For solution measurements, a 6 μm path length cell was used and the absorption and VCD spectra of water solvent were subtracted from their respective parent spectra.

Results and Discussion

The absorption and VCD spectra of α-D-Glucopyranosyl-(1→4)-D-glucose (maltose, Figure 8-1), cyclomaltohexaose (α-cyclodextrin, Figure 8-2), α-D-Glucopyranosyl α-D-glucopyranoside (α,α-trehalose, Figure 8-3), α-D-Glucopyranosyl-(1→6)-D-glucose (gentiobiose, Figure 8-4), α-D-Glucopyranosyl-(1→4)-D-glucose (cellobiose, Figure 8-5), and D-*gluco*-Hexose (D-glucose, Figure 8-6) are displayed in Figures 8-1−8-6. In each case absorption and VCD bands obtained from solution studies (left panels in the figures), are compared to those obtained for film samples (right panels in the figures).

The concentrations of parent solutions and the volume of solution used to deposit the films were varied to give optimal absorption (between 0.5 and 1) in the ~1200-900 cm^{-1} region. The volumes of aqueous carbohydrate solutions

deposited are 150 µl for allose and fucose and 200 µl for the rest of carbohydrates studied. Table 8-1 summarizes the concentrations of parent solutions used and the peak absorbances obtained for both solution and film studies. It should be noted that even with the high concentrations used for solution studies on α-cyclodextrin and cellobiose, peak absorption intensities obtained in solution spectra are lower than those in the corresponding film spectra. For example, while actual peak absorption intensity for α-cyclodextrin is 0.35 for solution sample, its peak absorption intensity is 0.70 for film sample. Similarly, while peak absorption intensity for cellobiose is 0.28 for solution sample, the corresponding intensity is 0.58 for film sample. This difference is not apparent in Figures because all the intensities displayed for solution based spectra are scaled in order to match the peak intensities of film based spectra. This scaling has been performed in order to provide a straightforward comparison of the spectra obtained for solution and film samples.

Table 8-1: Concentrations used and maximum peak absorbances obtained for solution and film.

	Aqueous solution Studies		**Film Studies**	
Carbohydrate	**Concentration (M)**	**Maximum Peak Absorbance[a]**	**Concentration[b] (M)**	**Maximum Peak Absorbance**
Maltose	1.8	0.88	0.036	0.84
α-cyclodextrin	0.14	0.35	0.016	0.7
α,α-trehalose	1.9	0.76	0.039	0.9
Gentiobiose	2.7	1.04	0.044	0.9
Cellobiose	0.5	0.28	0.043	0.58
D-glucose	3.8	0.79	0.078	0.76
D-fucose	3.97	1.18	0.072	1.07
D-allose	2.3	0.63	0.11	0.76

[a] these values are after subtracting the water solvent absorbance.
[b] this concentration refers to that of parent solution used for preparing the film.

It is worth noting that depending on the sample solution and its surface interaction with the IR transparent BaF_2 plate, some sample-solutions are more easily spread on the surface of BaF_2 plate than others. For instance, α-cyclodextrin solution spreads more easily than that of allose. For solutions which spread easily, films formed were thinner than for those which did not spread easily. To verify the independence of film orientation, both absorption and VCD spectral measurements were repeated by rotating the film 45º around the light beam axis. Thus each film-based spectrum contains two traces. The full line trace represents the film spectra prior to the 45º rotation, while the dashed line represents the spectra obtained upon 45º rotation. For all the absorption and VCD spectra reported here, the band positions, magnitudes and signs were found to be unaffected upon 45º rotation of the film.

An alternate way to verify the reliability of VCD spectra of films is to examine the mirror image nature of VCD signals expected for enantiomers of a given carbohydrate sample. The absorption and VCD spectra for film samples of D- and L-enantiomers of 6-Deoxygalactose (fucose), and D- and L-enantiomers of *allo*-Hexose (allose) are displayed in Figures 8-7 and 8-8, respectively. The mirror-image VCD spectra obtained for enantiomers of fucose and of allose confirm the reliability of VCD spectra for films. As an additional test, the VCD spectra for enantiomers of fucose film samples are also compared to those obtained for solution samples in Figure 8-7. The solution spectra are again in excellent agreement with those obtained for corresponding films. For allose, we measured the VCD spectrum in solution for single enantiomer D-allose, and this

spectrum (Figure 8-8) again matches well with the corresponding spectrum of D-allose film.

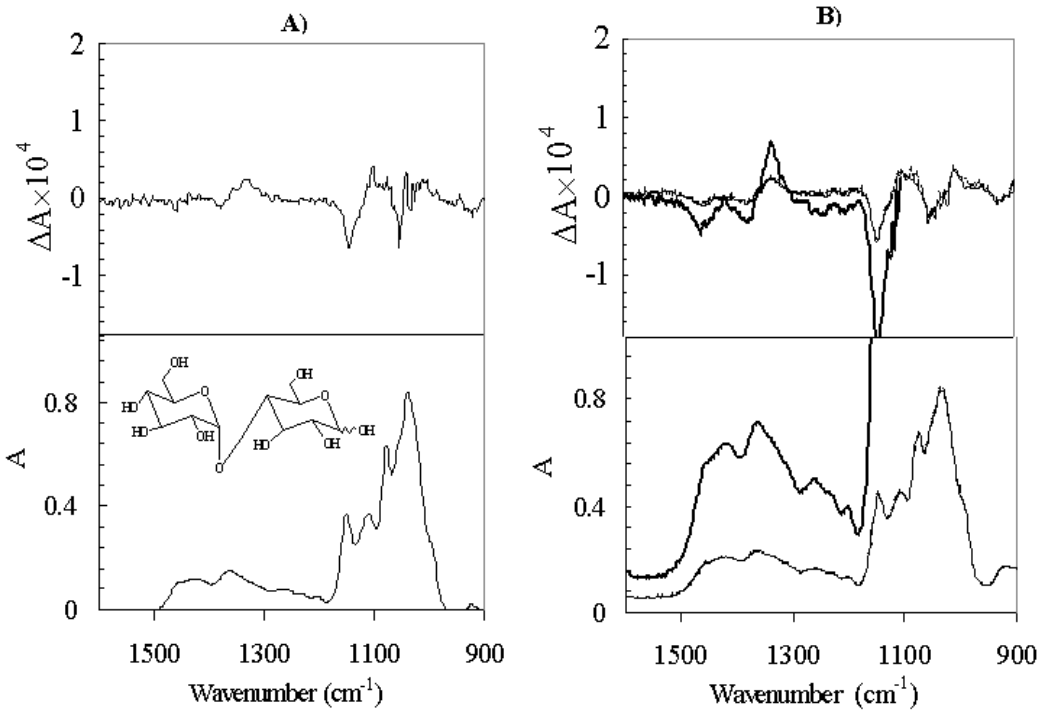

Figure 8-1: Vibrational absorption (bottom panels) and circular dichroism (top panels) of aqueous solution (left panels, A) and film (right panels, B) samples of α-D-glucopyranosyl-(1→4)-D-glucose (maltose).

Visual inspection of VCD band intensities and positions indicates a very good agreement between the spectra obtained for aqueous solution and those for films. A quantitative consideration also indicates that the solution and film VCD spectra are essentially identical. There are some minor differences in band widths, which reflect more so in absorption than in VCD spectra. In general, band widths are slightly larger for film samples than those for solution samples.

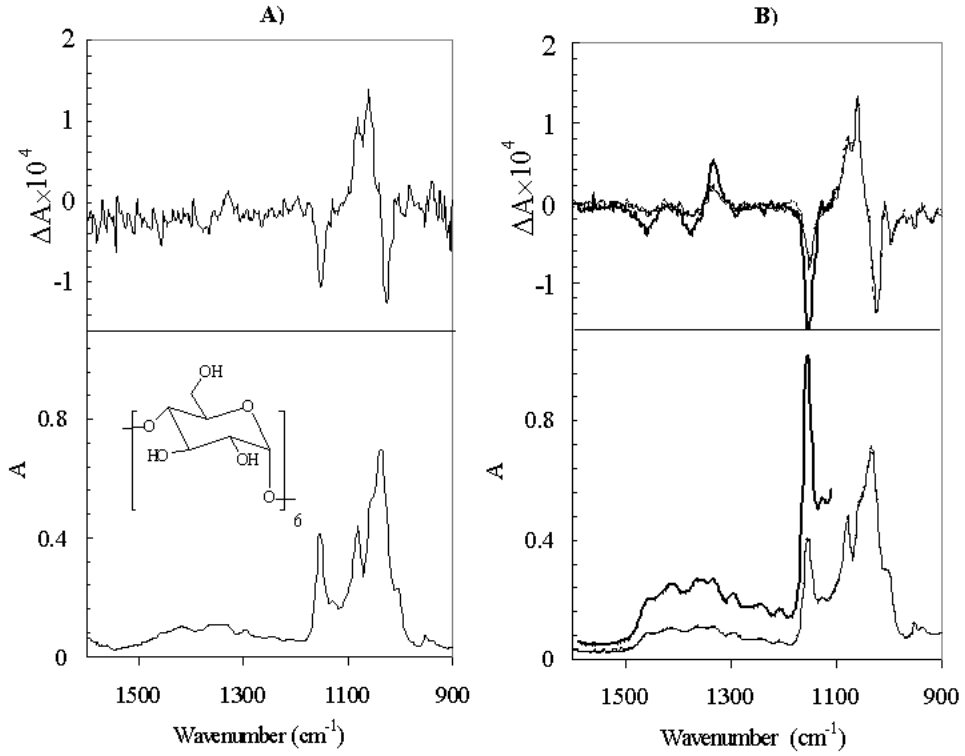

Figure 8-2: Vibrational absorption (bottom panels) and circular dichroism (top panels) of aqueous solution (left panels, A) and film (right panels, B) samples of cyclomaltohexaose (α-cyclodextrin).

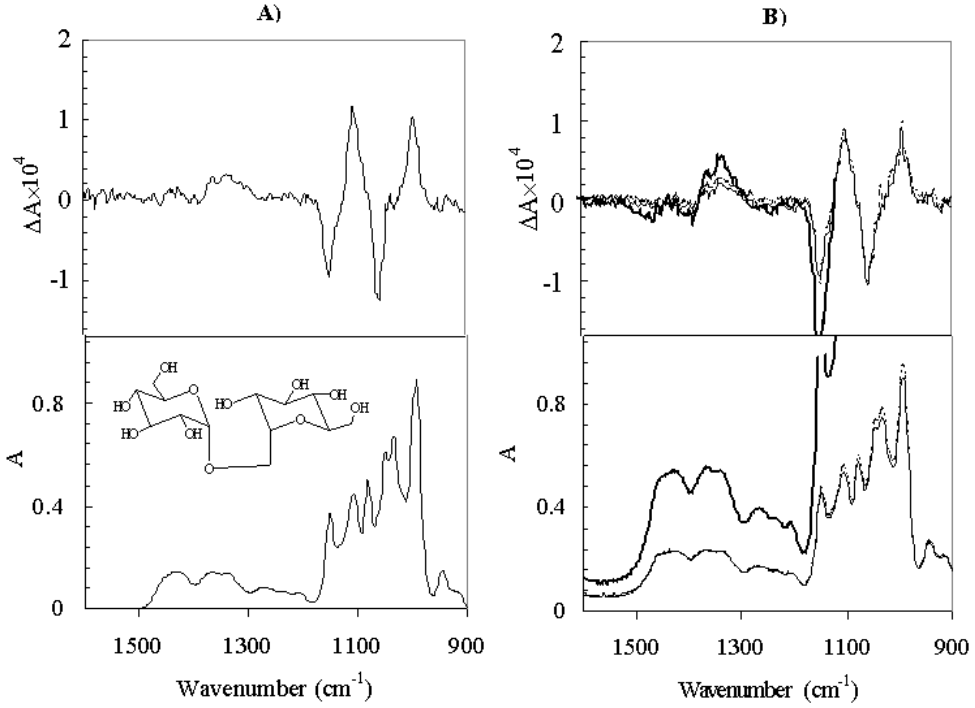

Figure 8-3: Vibrational absorption (bottom panels) and circular dichroism (top panels) of aqueous solution (left panels, A) and film (right panels, B) samples of α-D-glucopyranosyl α-D-glucopyranoside (α,α-trehalose).

The most pronounced absorption and VCD bands are found in the 1200-900 cm^{-1} region, characteristic of C-O/C-C stretching modes. For instance, maltose (Figure 8-1) is characterized by a negative VCD ($\Delta A/A = -1.8 \times 10^{-4}$ for solution, -1.4×10^{-4} for film) at ~1148 cm^{-1} and a negative VCD ($\Delta A/A = -0.6 \times 10^{-4}$ for solution, -0.5×10^{-4} for film) at ~1053 cm^{-1}. Similarly, α-cyclodextrin (Figure 8-2) shows a negative VCD signal ($\Delta A/A = -2.5 \times 10^{-4}$ for solution, -2.2×10^{-4} for film) at ~1149 cm^{-1}, a positive VCD signal ($\Delta A/A = +2.4 \times 10^{-4}$ for solution, $+1.8 \times 10^{-4}$ for film) at ~1080 cm^{-1}, a positive VCD signal ($\Delta A/A = +2.8 \times 10^{-4}$ for solution, $+2.6 \times 10^{-4}$ for film) at ~1060 cm^{-1} and a negative VCD signal ($\Delta A/A = -2.6 \times 10^{-4}$ for solution, -2.3×10^{-4} for film) at ~1027 cm^{-1}. Further, α,α-trehalose (Figure 8-4) is characterized by a negative VCD ($\Delta A /A = -2.9 \times 10^{-4}$ for solution, -2.1×10^{-4} for film) at ~1148 cm^{-1}, a positive VCD ($\Delta A /A = +2.6 \times 10^{-4}$ for solution, $+1.5 \times 10^{-4}$ for film) at ~1105 cm^{-1}, a negative VCD ($\Delta A/A = -2.6 \times 10^{-4}$ for solution, -2.1×10^{-4} for film) at ~1057 cm^{-1}, and a positive VCD ($\Delta A \backslash A = +1.1 \times 10^{-4}$ for solution, $+1.0 \times 10^{-4}$ for film) at ~995 cm^{-1}. The most pronounced VCD signals exhibited by D-fucose are a negative VCD ($\Delta A/A = -2.7 \times 10^{-4}$ for solution, -1.7×10^{-4} for film) at ~1164 cm^{-1}, a positive VCD ($\Delta A/A = +2.0 \times 10^{-4}$ for solution, $+1.3 \times 10^{-4}$ for film) at ~1001cm^{-1} and a positive VCD ($\Delta A/A = +2.0 \times 10^{-4}$ for solution, $+8.8 \times 10^{-5}$ for film) at ~964 cm^{-1}. For D-allose, the dominant signals are a positive VCD ($\Delta A/A = +1.2 \times 10^{-4}$ for solution, $+1.0 \times 10^{-4}$ for film) at ~1126 cm^{-1}, a negative VCD ($\Delta A/A = -6.6 \times 10^{-5}$ for solution, -7.3×10^{-5} for film) at ~1093 cm^{-1}, and a positive VCD ($\Delta A /A = -5.9 \times 10^{-5}$ for solution, -4.1×10^{-5} for film) at ~1026 cm^{-1}. Overall, the $\Delta A/A$ magnitudes observed for film samples are

slightly smaller than those for the solution samples, which may be partly because of larger bandwidths in the spectra of films. The ΔA/A values were determined from the peak intensities, while areas, or widths, of the bands were not taken into consideration. But the above noted differences are not large enough to cause any concern. For D-glucose, gentiobiose and cellobiose no prominent VCD signals (such as those seen for maltose, α-cyclodextrin and α,α-trehalose) are seen in the considered region. All these data present evidence for satisfactory quantitative agreement between the solution and film VCD spectra.

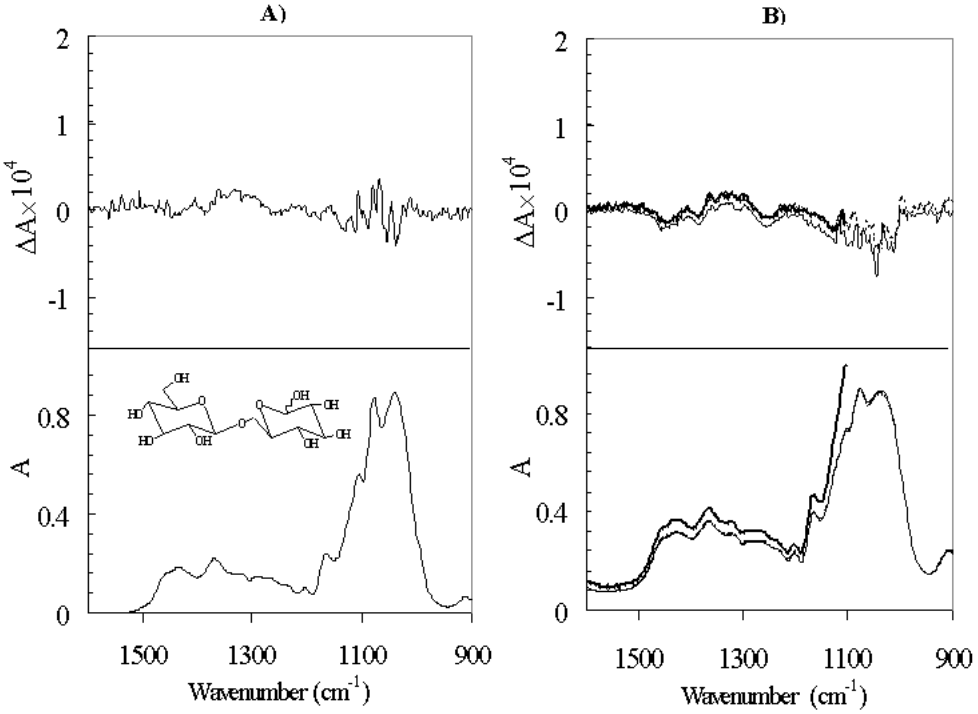

Figure 8-4: Vibrational absorption (bottom panels) and circular dichroism (top panels) of aqueous solution (left panels, A) and film (right panels, B) samples of β-D-glucopyranosyl-(1→6)-D-glucose (gentiobiose).

The fact that the amounts of samples needed for obtaining sufficient absorption and hence VCD signal in film studies are much lower than those needed for obtaining solution based spectra is a significant advantage associated with film studies. For example, to obtain nearly the same absorbance in solution and film studies on maltose, solution studies used a concentration of 1.8 M, while the film study used a parent solution concentration of only 0.036 M. This translates into approximately 50 times smaller amount of sample required for film studies than that in solution studies. However it should be noted that this advantage varies from sample to sample and depends on the surface tension of the solution on the BaF_2 window. If the solution spreads more easily, as in the case of α-cyclodextrin, thinner and wider film is formed. As a consequence, a parent solution of higher concentration or more volume is needed to prepare the film to obtain a given absorption. On the other hand for solutions that do not spread easily, thicker films are formed in a smaller region of the window, yielding higher absorbance. Inspite of the varying thicknesses for different sample films we did not notice any significant differences between solution and film VCD spectra. We also did not notice any artifacts in the film VCD spectra. This favorable observation for VCD spectra on films is attributed to the longer wavelengths of incident light in the infrared region.

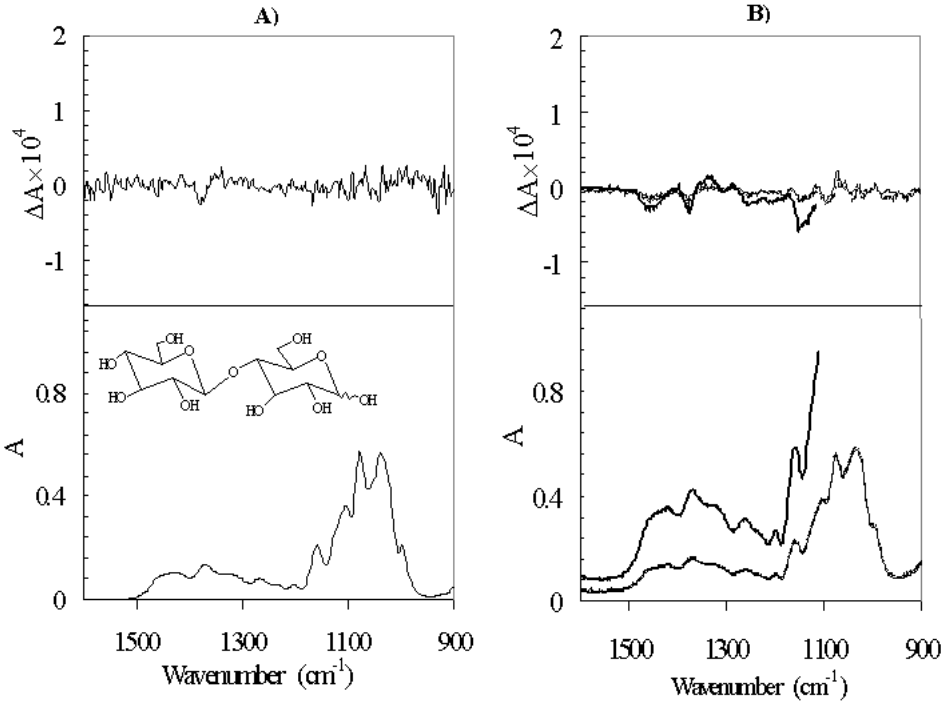

Figure 8-5: Vibrational absorption (bottom panels) and circular dichroism (top panels) of aqueous solution (left panels, A) and film (right panels, B) samples of β-D-glucopyranosyl-(1→4)-D-glucose (cellobiose).

In order to measure VCD in the ~1600-1200 cm^{-1} region with sufficient signal to noise, the intensities of absorption bands in this region are to be increased. For solution-based studies, higher concentration solution would be needed for this purpose, but the restrictions imposed by solubility of some carbohydrates limits the concentrations that one can use. Considering α-cyclodextrin as an example, for obtaining the VCD spectra in aqueous solutions a concentration of 0.14 M has been used. This is a nearly saturated solution because the solubility[227] for α-cyclodextrin in water is 0.15 M. Thus there is not much freedom to increase the concentration of α-cyclodextrin for solution study, and to enhance the weak absorption bands in the ~1600-1200 cm^{-1} region. This

restriction is removed from film studies because a parent solution of 0.016 M was sufficient for preparing films with higher absorption in the ~1200-900 cm^{-1} region and a parent solution of higher concentration can be used to enhance the absorption of weak bands in the ~1600-1200 cm^{-1} region. To demonstrate the ability to increase the absorption of films and measure VCD signals in the ~1600-1200 cm^{-1} region, an additional parent solution concentration of 0.035M has been used for α-cyclodextrin sample (see Figure 8-2). The thick line traces in Figure 8-2 represent the spectra of film prepared from higher concentration solution. The VCD features in the ~1600-1200 cm^{-1} region are now clearly seen.

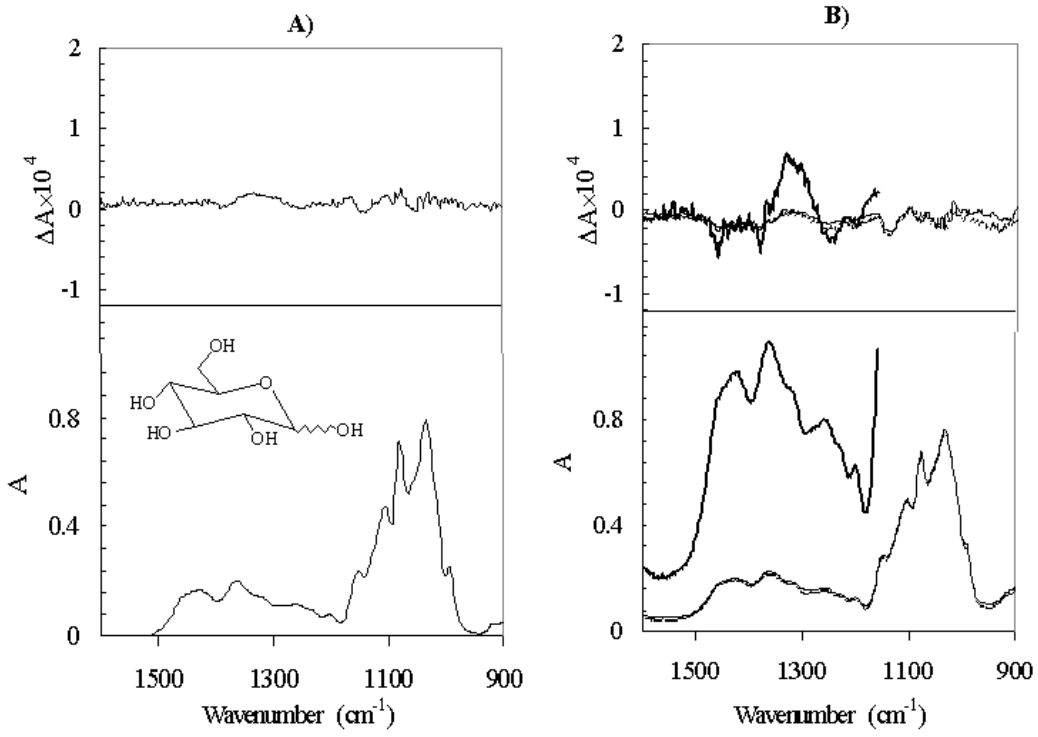

Figure 8-6: Vibrational absorption (bottom panels) and circular dichroism (top panels) of aqueous solution (left panels, A) and film (right panels, B) samples of D-glucose.

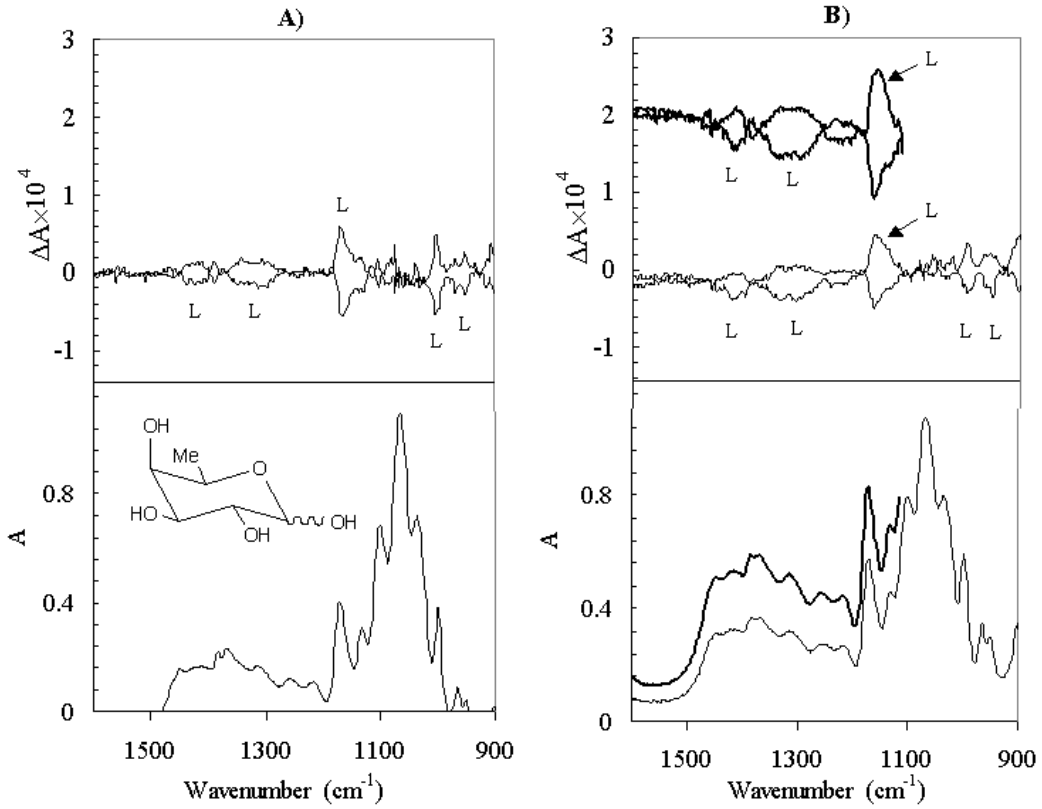

Figure 8-7: Vibrational absorption (bottom panels) and circular dichroism (top panels) of aqueous solution (left panels, A) and film (right panels, B) samples of both enantiomers of 6-deoxygalactose (fucose).

For all of the samples studied, the 1600-1200 cm^{-1} region has been remeasured by preparing films from higher concentration parent solution, as displayed in Figures 8-1−8-8 as thick traces. The concentrations of parent solutions used for preparing films were 0.093 M for maltose, 0.035 M for α-cyclodextrin, 0.10 M for α,α-trehalose, 0.065 M for gentiobiose, 0.11 M for cellobiose, 0.19 M for glucose, 0.14 M for fucose, and 0.18 M for allose. The VCD spectra of carbohydrates connected via α-linkage (α(1→4) for maltose and α-cyclodextrin and α(1→1) for α,α-trehalose) have revealed the existence of three distinct bands, two negative and one positive, in the 1600-1200 cm^{-1} region. In the case of maltose, the first negative VCD band ($\Delta A/A = -9.1 \times 10^{-5}$)

occurs at ~1459 cm^{-1}, the second negative VCD band ($\Delta A/A = -4.7 \times 10^{-5}$) occurs at ~1375 cm^{-1}, and the positive VCD band ($\Delta A/A = +1.1 \times 10^{-4}$) occurs at ~1333 cm^{-1}. The pronounced peaks characteristic of α-cyclodextrin are a negative VCD ($\Delta A/A = -2.2 \times 10^{-4}$) at ~1458 cm^{-1}, a negative VCD ($\Delta A/A = -1.8 \times 10^{-4}$) at ~1374 cm^{-1}, and the positive VCD band ($\Delta A/A = +1.9 \times 10^{-4}$) at ~1332 cm^{-1}. The peaks exhibited by α,α-trehalose are a negative VCD ($\Delta A/A = -7.4 \times 10^{-5}$) at ~1465 cm^{-1}, a negative VCD ($\Delta A/A = -7.3 \times 10^{-5}$) at ~1386 cm^{-1}, and the positive VCD band ($\Delta A/A = +9.4 \times 10^{-5}$) at ~1340 cm^{-1}. The three bands found in the 1600-1200 cm^{-1} region, for maltose, α-cyclodextrin and α,α-trehalose, are also found for other α-linked oligosaccharides (not shown here), but they are not as prominent for α-linked oligosaccharides (gentiobiose and cellobiose). The film prepared from higher concentration parent solution of D-glucose exhibits a weak negative VCD band at ~1458 cm^{-1}, a weak negative VCD band at ~1379 cm^{-1}, a positive VCD band ($\Delta A/A = +7.6 \times 10^{-5}$) at ~1329 cm^{-1}, and a negative VCD band ($\Delta A/A = -5.3 \times 10^{-5}$) at ~1241 cm^{-1}. VCD bands of D-fucose film, obtained from higher-concentration parent solution, are a positive VCD ($\Delta A/A = +6.1 \times 10^{-5}$) at ~1413 cm^{-1} and a positive VCD ($\Delta A/A = +7.2 \times 10^{-5}$) at ~1313 cm^{-1}.

The spectra obtained for films of maltopentaose, maltohexaose and maltoheptaose are similar (not shown here) to those of maltose (Figure 8-1). However, the VCD spectrum of cyclomaltohexaose (α-cyclodextrin, Figure 8-2) shows strong VCD bands at 1080, 1060 and 1027 cm^{-1} that are not seen for non-cyclic maltose or its higher oligomers. Enhancement in the intensity of VROA couplet at around 915 cm^{-1} in cyclodextrin, compared to that in maltose, and its

higher oligomers, was attributed[228] to the constrained conformation of cyclodextrin.

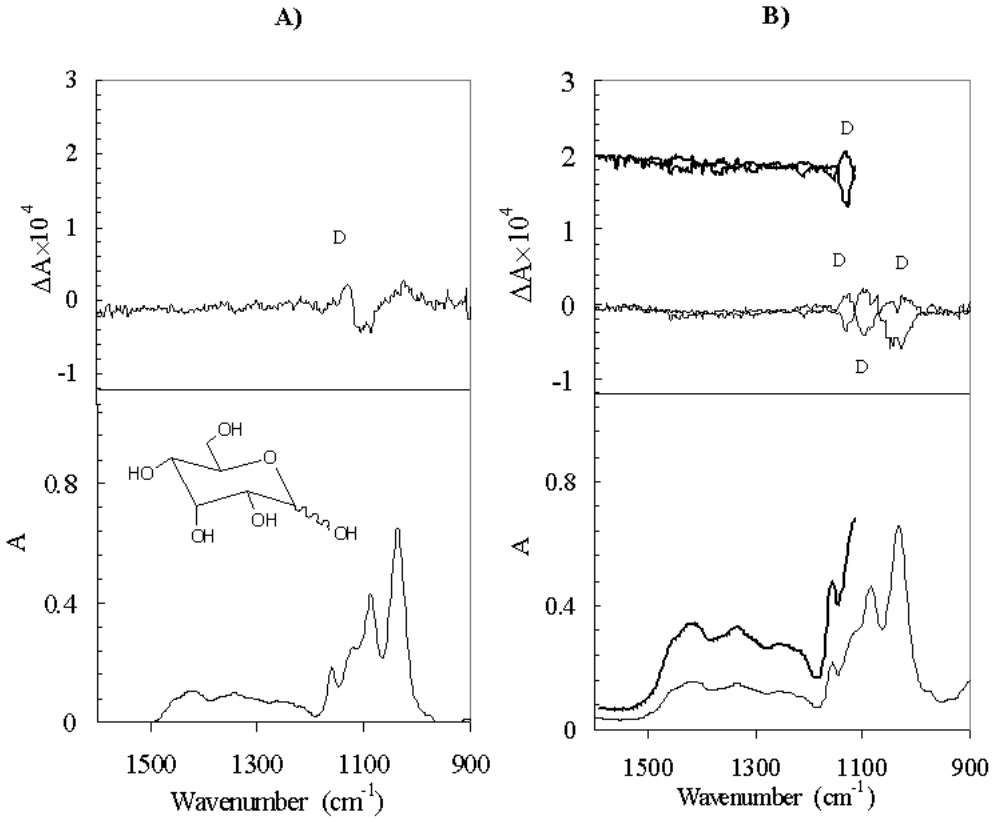

Figure 8-8: Vibrational absorption (bottom panels) and circular dichroism (top panels) of aqueous solution (left panels, A) and film (right panels, B) samples of enantiomers of allose. The raw VCD spectra obtained for both D and L enantiomers are shown for film samples.

The 2000-1600 cm^{-1} region is not shown in the spectra presented here because the unsubstituted carbohydrates do not exhibit fundamental absorption bands in this region. When it becomes necessary to investigate substituted carbohydrates that exhibit absorption bands in this region, films prepared from aqueous solutions do not pose any additional limitations. Recent studies in our

laboratory indicated that good quality VCD spectra can be obtained in the 2000-1600 cm^{-1} region for protein films[15,224,225].

The fact that the measured VCD spectra are identical for solution and film samples indicates that the molecular structure in films is not significantly different from that in concentrated solutions, at least as "seen" by VCD. This observation is significant for VCD spectroscopy because in the past VCD researchers had to avoid the chemical/biological problems that involved water solutions or substitute either D_2O or unnatural organic solvents for water. But now the measurements on aqueous solutions can be undertaken by using films that are conveniently prepared from aqueous solutions.

Based on our experience, we believe that VCD studies on carbohydrate films is a general approach applicable for any carbohydrate solution that can form a film (without microcrystalline deposits) upon solvent evaporation. Thus a wide variety of problems in carbohydrate chemistry can now be tackled using VCD spectroscopy that was not possible before.

Conclusion

The present work demonstrates that VCD spectra for carbohydrates in aqueous solutions can be obtained in entire 2000-900 cm^{-1} region, by depositing the aqueous solutions as films. VCD measurements on films are advantageous over solution state measurements because, the amount of carbohydrate sample required for VCD film study is approximately one to two orders of magnitude smaller that that for corresponding aqueous solution studies. The VCD spectra

obtained for films derived from aqueous solutions are found to be identical to those obtained for aqueous solutions. The spectral regions that are not easily accessible in aqueous solution studies can be accessed using films, because the water interference has been removed in film studies, which also results in higher throughput and better signal to noise. These observations open up many new applications for VCD in carbohydrate chemistry that could not be attempted before.

CHAPTER IX

VIBRATIONAL CIRCULAR DICHROISM INVESTIGATION OF HOMOPOLYNUCLEOTIDES

Polyriboadenylic Acid (polyA):

Introduction

PolyA (Figure 9-1) is a constituent of mRNA of all living organisms, and it has been established that it participates in several processes[229] including mRNA transportation from nucleus to cytoplasm, degradation, and translation initiation.

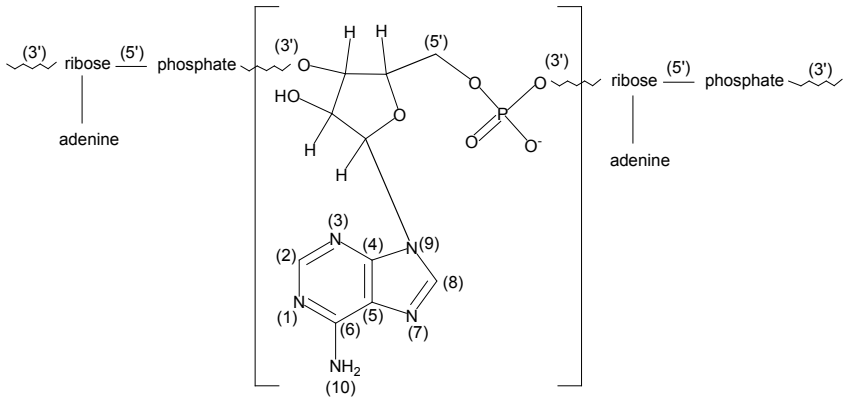

Figure 9-1: The chemical structure of a monomer unit of the polyadenylic acid (polyA).

Early work on the structural elucidation of polyA included X-ray diffraction studies,[230,231] ultraviolet (UV) spectroscopy,[232-235] optical rotatory dispersion (ORD)[236-240] electronic circular dichroism (ECD)[232,241-243], and nuclear magnetic resonance (NMR)[244-246]. On the basis of the previous studies it has been concluded that polyA exhibits two secondary structures depending on the pH. On

the basis of sedimentation constants and viscosities, Fresco and Doty[247] noted that polyA undergoes structural changes when going from neutral to acidic conditions. The structure of polyA at alkaline and neutral pH was suggested to be a right-handed single-stranded helix, stabilized by the stacked array of bases with their planes nearly perpendicular to the helix axis.[236,241,243] There is no evidence[248] for internucleotide hydrogen bonding in the neutral, single-helical form. In support of this structure, NMR data[249] of the adenine protons showed chemical shifts that are analogous to those found in other systems of stacked aromatic rings. UV-ECD[250,251] and ORD data[236] displayed the behavior expected for stacked chromophores with transition moments perpendicular to the helix axis. At acidic pH, however, polyA exhibits a right-handed double-stranded helical structure with parallel chains and stacked protonated bases.[230,234,247] The bases are tilted[230,236] with respect to the helical axis. Each nucleotide is held in place by stacking interaction with adjacent bases as well as by hydrogen bonds to the other chain. The double-stranded form contains eight nucleotide pairs per helix turn.[242,252] Several observations have been cited in support of the double helix. On the basis of the X-ray diffraction studies, Rich *et al.*[230] have proposed that the double-stranded structure is stabilized by the electrostatic attraction between the positively charged protons at the $N_{(1)}$ atoms of the adenines and the negatively charged phosphate groups (Figure 9-2). On the basis of correlations between hydrogen-ion titration data and thermal denaturation curves, Holcomb and Timasheff[253] later reconfirmed the idea of the double-helix stabilization through electrostatic interactions. As depicted in Figure 9-2, two parallel strands

are held together by four hydrogen bonds per base pair, two of which are between $N_{(10)}H_2$ and $N_{(7)}$ and the other two are between $N_{(10)}H_2$ and a phosphate oxygen.[236] Furthermore, small-angle X-ray scattering measurements[231] showed that the mass per unit length of the neutral structure is one-half of that in the acidic structure, which represents a convincing evidence concerning single- versus double-helix structural differences associated with changes in pH.

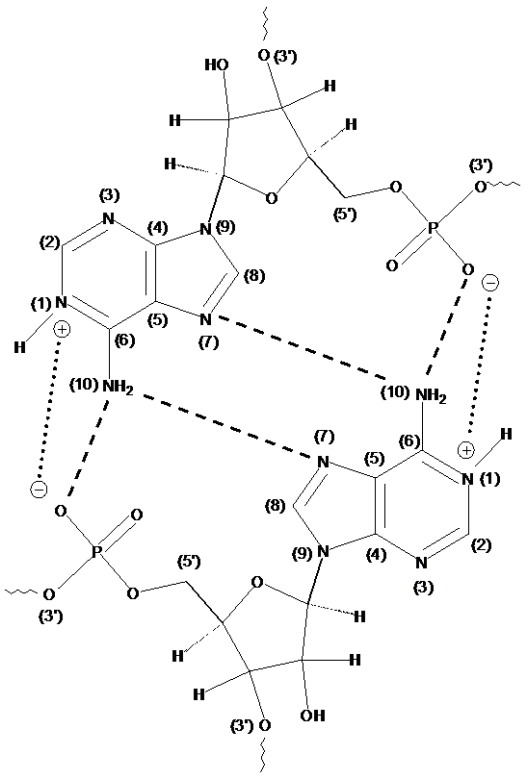

Figure 9-2: The interaction of two monomer units belonging to complementary chains of polyA, when found in an acidic environment. Hydrogen bonds are designated with broken-lines, while electrostatic interactions are given by dotted lines.

A structural transition from the neutral, single-strand structure to the acidic, double-strand structure was reported to occur at a pH near the pK_a of 5.87 for polyA, as inferred from UV absorption, ORD, and ECD.[254] Interestingly, as originally determined from the X-ray data by Rich *et al*.[236], full protonation is not a structural requirement for the acidic structure of polyA. Namely, depending on the extent of protonation of the molecule, three different acidic conformations are found for polyA: B form, A form, and "frozen" form. [255-257] The least acidic of the three forms (at higher pH) is designated as the B form, also known as an "intermediate"[256] form, which is considered to be stable near half-protonation. Form B is the only structure present at a pH just below pK_a, associated with the partial protonation of adenine moieties. At pH 5.81, ORD[254] of polyA indicates the B form. As the pH is further lowered, there is a gradual conversion of form B into form A. Form A, also known as the "tightly packed" form, is stable at complete protonation of adenine constituents. At pH 4.00, ORD[254] of polyA indicates the pure A form. Finally, the third and the most acidic form, known as the "frozen" form, is created from neutral polyA at low pH (<3.8).[256] According to previous studies,[255-257] the frozen form represents a gridlike aggregate consisting of alternating, variably sized, single-stranded regions linked with short double-stranded regions. The prevention[255] of formation of the frozen form can be accomplished by a slow dialysis of single-strand solution against an acidic solvent. Additionally, the frozen form of aggregated polyA can be destroyed[256,257] by heating, which promotes the process of separation of strands and their recombination in a more ordered manner.

In this section of the chapter we report the pH-dependent IR and VCD spectra of polyA, in both solution and film states, to deduce the structural/conformational changes from these spectra.

Experimental Section

The polyA potassium salt (P9403), and D-(+)-trehalose were obtained from Sigma Chemical Co. and have been used as received. D_2O was obtained from Cambridge Isotope Laboratories, Inc.

Liquid solution samples, at a final concentration of ~18 mg/mL, were prepared by dissolving polyA in 0.1 M NaCl solution, containing 10 mM citrate buffer (for pH ~3.5-6.0) or Tris buffer (for pH ~8.0) in D_2O. A glass-body liquid-filled microcombination pH electrode was used for all pH readings. No corrections were made for the differences between pH and pD. The 10 mM concentration of citric acid is low enough for the absorption associated with its carbonyl group not to interfere with the base vibrational bands. PolyA is prone to gel formation at higher concentrations, in acidic environment. For the concentration used here, polyA solution became increasingly more viscous as the pH was lowered. At pH 4.0, it was considerably viscous but could be drawn out with a pipet. At pH 3.5, the polyA solution had a gellike appearance and was transparent.

For each of the pH values considered, IR and VCD spectra of polyA solution have been measured at room temperature (~ 22°C), at an elevated temperature (~ 70°C), and back at room temperature (after allowing for 1 hr of

cooling time). This thermal cycling was used to establish whether the conformational change during heating is reversible upon cooling. Heating was accomplished by holding the sample in a variable temperature cell. The temperatures were read with a thermocouple embedded in the cell. The aggregated sample solution at pH 3.5 was additionally heated to ~ 110°C for approximately 5 min, and the spectra were taken after allowing the sample to equilibrate back to room temperature.

For preparation of the film samples a drop-cast method was used, where ~ 200 µL of parent aqueous solution, at a concentration of ~ 6 mg/mL, was deposited on a 2.5 cm diameter CaF_2 window and allowed to dry at room temperature for approximately 2-3 hr in a fume hood, which provided a constant airflow over the sample. Trehalose was added to the polyA solution at a mass ratio of 2:1 (trehalose/polyA). The pH of the parent solutions was adjusted in the same manner as for the solution study. The difference in preparation of the solution and film state samples was that for film samples the solution buffer concentration was ~ 5 mM and no NaCl was included to avoid its precipitation on the surface of the film. Films were tested for orientational dependence by taking the spectra at two positions: an arbitrarily chosen 0° position and a position corresponding to 45° rotation around the light beam axis.

IR and VCD measurements for both solution and film state samples were obtained on a modified ChiralIR instrument. All VCD spectra were recorded for 1 hr of data collection time at 8 cm^{-1} resolution. The solution sample was held in a demountable cell with CaF_2 windows and a 50 µm Teflon spacer. Baseline

corrections for all solution-based absorption (or VCD) spectra were done by subtracting the absorption (or VCD) of the buffered D_2O solvent, containing NaCl.

Results and Discussion

Solution-State Measurements: The pH-dependent IR absorption (A) and VCD (B) spectra in the 1800 and 1300 cm^{-1} region measured at room temperature (22 °C) and at a higher temperature (70 °C) are shown in Figure 9-3. The region below 1300 cm^{-1} is not displayed due to strong interference from D_2O. Figure 9-3 indicates that lowering of the pH from 8.0 to 3.5 leads to continuous changes in the spectral features.

There are four absorption bands, labeled as I-IV in Figure 9-3A, that exhibit notable changes as a function of pH. The most pronounced changes are seen for band I at ~1665 cm^{-1}, which undergoes a considerable increase in intensity as the pH is lowered. Band I is of particular interest here because this band was not recognized[204,258] in the literature theoretical analyses, perhaps due to its absence in some measurements under apparently similar experimental conditions. The reasons for the appearance/disappearance of band I and its vibrational origin were not discussed, and this band was excluded[204,258] from the spectral analysis.

As the acidity of the solution increases, the following structural changes were reported[230] to take place: atom $N_{(1)}$ of the adenine ring becomes protonated (with D in place of H in D_2O), thus resulting in the development of a positive charge that can form favorable electrostatic interactions with the phosphate

moiety; atom $N_{(7)}$ of one polyA chain begins hydrogen bonding with $N_{(10)}H_2$ of another polyA chain (Figure 9-2), which gives rise to intertwining of the two chains and stabilization of the double-helical structure; $N_{(10)}H_2$ additionally stabilizes the double-helical structure by participating in the hydrogen bonding with oxygen belonging to the phosphate moiety of the complementary polyA chain. These changes become reinforced as the environment becomes increasingly more acidic.

On the basis of the tabulated correlations[201,259] between various types of vibrational modes and typical frequency ranges where these modes occur, the origin of band I can be associated with C=N ($C_{(2)}=N_{(3)}$, $C_{(6)}=N_{(1)}$, $C_{(8)}=N_{(7)}$; see Figure 9-1) stretching vibrations with contributions from $N_{(10)}H_2$ bending vibrations. Since the origin of band I is associated with vibrations of atoms undergoing the above-mentioned modifications, it is not surprising that this band undergoes a considerable change in its intensity as the pH is lowered. The magnitude of band I becomes intensified with the formation of a double helix in the acidic environment. The intensity of band I represents a direct measure of the degree of adenine ring protonation and, hence, double-helix formation. The observation that the IR spectrum at pH 8.0 does not exhibit band I and that at pH 6.0 this band starts to grow can be taken as the diagnostic marker for the double-stranded helical structures of polyA. This identification was not reported to date.

It should be noted that among the previously reported studies, aside from band I, the remaining bands for polyA were reproduced. For instance, good reproducibility is displayed for band II, which is located at ~1628 cm^{-1} and

previously received much attention because it gives the rise to a strong, sharp, positive VCD couplet at neutral pH. Some literature studies of polyA in a neutral aqueous environment have assigned[260-263] the origin of band II to $C_{(4)}=C_{(5)}/C_{(5)}-C_{(6)}$ stretching motions. Nevertheless, in a recent study[204] Andrushchenko *et al.* correlated the ab initio calculated normal vibrational modes of an octamer $(rA)_8$ with experimental IR bands of polyA in D_2O and indicated that the band at ~1628 cm^{-1} originates from adenine ring C=N stretches coupled to N-D vibrational deformations. Furthermore, the ab initio predicted[204] theoretical absorption and VCD spectra of $(rA)_8$, with properties transferred from adenine surrounded by five D_2O molecules, are in good agreement with the D_2O-based experimental spectral features of poly A reported here at basic pH.

In terms of the pH-dependent changes, band II undergoes a twofold change. First, its intensity gradually decreases as the pH is lowered, but this decrease is not as pronounced as the increase in intensity of band I. Second, while band II remains centered at ~1628 cm^{-1} over the pH range of 5.5-8.0, its position gradually shifts to ~1627 cm^{-1} at pH 5.0, to ~1624 cm^{-1} at pH 4.5 and 4.0, and finally, to ~1621 cm^{-1} at pH 3.5. The gradual transformation of band II in both magnitude and position reflects the transformation from the less protonated, acidic form B to the more protonated, acidic form A. It should be noted that the ability to differentiate between forms A, B, and the frozen form is easier based on the VCD spectral features (*vide infra*).

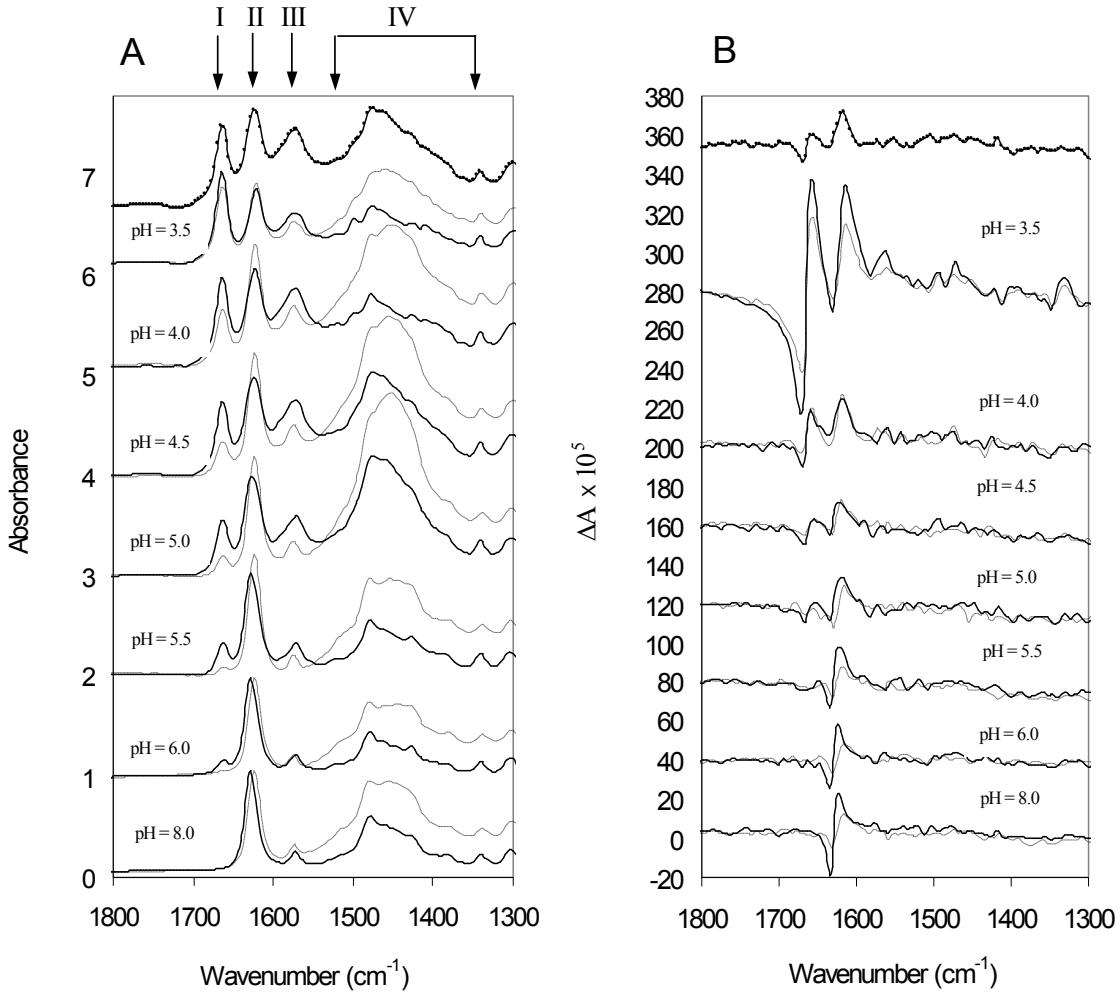

Figure 9-3: Solution-based vibrational absorption (left) and circular dichroism (right) spectra of polyA in the pH range of 8.0 to 3.5. Concentrations used for solution preparations are given in the experimental section. The traces given by the straight line correspond to spectra taken at room temperature (22°C), while the traces given by the broken-line correspond to spectra taken at elevated temperature (70°C). The top most trace corresponds to spectrum taken when the sample at pH 3.5 was heated to 110°C and then cooled back to room temperature.

Band III, located at ~1573 cm^{-1}, undergoes the least notable change. Its intensity and position remain essentially the same during pH transitions, yet the peak shape somewhat broadens as the pH decreases. On the basis of the correlation between IR spectra of the octameric $(rA)_8$ model and polyA,

Andrushchenko *et al*.[204] suggested that band III is predominantly due to C=N stretching vibration.

Unlike the three bands noted in the region between 1700 and 1550 cm^{-1}, whose changes are gradual and with a clear transition in tendencies as the pH is lowered, the frequency region labeled as IV, between 1550 and 1350 cm^{-1}, is not very useful for structural interpretation because the broad unresolvable features here may arise from D_2O or HDO. The two spectra at pH 6.0 and 5.5 resemble each other, as do those at pH 5.0 and 4.5, and those at pH 4.0 and 3.5. The spectral features at pH 8.0 seem to best resemble those at pH 6.0 and 5.5.

More transparent evidence for the existence of three distinguishable conformations can be seen in the pH-dependent VCD spectra displayed in Figure 9-3B. At pH 8.0 and 6.0, absorption band II, observed at ~1628 cm^{-1}, gives rise to a sharp, positive VCD couplet of equal intensities for negative and positive lobes. As the pH is lowered to 5.5, the positive couplet centered at ~1628 cm^{-1} remains but with a slight decrease in intensity and a shift of the positive lobe from ~1624 to ~1622 cm^{-1}. In addition, band I at ~1665 cm^{-1} begins to develop a negative VCD contribution at pH 5.5. As the pH is further lowered to 5.0, not only does this negative VCD band become well-defined, but also a positive VCD contribution is developed at a slightly lower frequency. These two VCD contributions appear to form another conservative, positive VCD couplet at ~1665 cm^{-1}. At pH 4.5 and especially 4.0, the newly developed positive couplet becomes dominant, while the positive couplet at ~1628 cm^{-1} is diminished in intensity, giving the appearance of a positive band centered at ~1618 cm^{-1}. The noticeably different

VCD spectrum at pH 3.5, especially in terms of intensity of the signal, is the result of the formation of an aggregated frozen conformation. As mentioned in the Experimental Section, at pH 3.5, the solution becomes extremely viscous, essentially gellike, which may be taken as physical evidence for the formation of the frozen form. Figure 9-3 also includes the VCD spectrum at pH 3.5 to show the discernible difference between the spectra of the frozen form versus other acidic forms. The VCD spectral features associated with pH 3.5 reflect the ability of the VCD technique to differentiate the frozen from other acidic forms, which cannot be achieved with ordinary IR absorption spectra. A large increase in VCD intensity with aggregation has been observed[264] for DNA, where the aggregation was due to the formation of large dense particles in the presence of Cr^{3+} ions. An increase in ECD intensity was also reported[265] for DNA in the presence of poly(ethylene glycol), where aggregation led to compactization of DNA structure.

Since the major VCD features associated with pH values 8.0 and 6.0 appear essentially the same, the transition from single-helical structure to double-helical structure is more evident from the changes in absorption spectra associated with the appearance of band I. On the other hand, VCD features are more indicative of the pH-dependent transitions among the three acidic forms. The appearance of negative VCD contribution at ~1668 cm^{-1} at pH 5.5 and 5.0 indicates the formation of the half-protonated B form. The emergence of the well-defined positive couplet at ~1665 cm^{-1} as well as the disappearance of the positive couplet at ~ 1628 cm^{-1} reflect the stabilization of a fully protonated A form, at pH 4.5 and 4.0. The high-intensity VCD couplet centered at ~1665 cm^{-1},

along with the positive band at ~1614 cm^{-1}, is indicative of the frozen form of polyA at pH 3.5. To find out if the temperature-dependent conformational changes are reversible, solution-based spectra were taken at an elevated temperature of ~70°C for each of the pH values considered and also upon cooling the sample back to room temperature. The aggregated sample, at pH 3.5, was additionally heated to ~110°C, and its spectra were also measured upon cooling the sample back to room temperature.

To facilitate the comparison of the temperature-dependent spectral differences in the pH range 8.0-3.5, the absorption and VCD spectra at elevated temperature (dotted lines) are collected in Figure 9-3 along with those at room temperature (solid lines). The temperature-induced change when going from 22 to 70°C that is common to all absorption traces is associated with frequency region IV and is manifested through an increase in the relative intensity as well as through a slight modification in the overall band-shape appearance. As mentioned earlier, the broad unresolved features in region IV may arise from D_2O or HDO, so these changes are probably associated with increased H-D exchange at higher temperature. In the pH range of 6.0-3.5, both bands I and III undergo a decrease in intensity with increasing temperature. Since band I was identified with the double-helix structure, the decrease in intensity of this band with increasing temperature indicates heat-induced partial unfolding of a double helix. Band II undergoes a twofold change as the result of increase in temperature: an increase in its relative intensity at essentially all pH values studied and a shift in its band position to a slightly lower frequency region in the

pH range of 8.0-5.0. The VCD couplet associated with absorption band II is also shifted to a slightly lower frequency, but its magnitude is diminished, unlike the associated absorption intensity, in the pH range of 8.0-5.0. At pH 4.5 and below, the shift of band II to a lower frequency region does not occur, and the attenuation of VCD intensity is not as pronounced. The VCD intensity changes for band II suggest that some unfolding of the single helix also takes place as the temperature is increased to 70°C.

The temperature-dependent spectral features seen at 70°C are reversible because, upon cooling the samples to room temperature, the peaks observed originally at room temperature are restored. It was reported[230,242] that the melting temperature (T_m) of a solution of polyA at pH 4.25 is about 90°C. On the basis of this observation, the frozen form at pH 3.5 was also studied at 70 and 110°C. Although heating of the frozen form to ~ 70°C also leads to reversible changes, this compact form is irreversibly disrupted at ~ 110°C. The observable transition from a viscous, essentially gellike sample at pH 3.5 and room temperature to a much more fluidlike sample at 110°C represents clear physical evidence of a conformational transformation at ~110°C. Cooling back to room temperature does not revert the sample back to gellike appearance, so the disruption of the aggregate form at ~110°C is an irreversible process. The spectra obtained after heating the aggregated polyA to 110°C, followed by cooling to room temperature, are also displayed in Figure 9-3 (topmost traces). A comparison of these spectra with those at initial room temperature at all pH values indicates that these spectra closely resemble those at pH ~4.5, suggesting that the frozen form upon heating

to 110 °C converts to the A form. Heating the sample to ~110 °C promotes the separation of aggregated strands and their subsequent recombination into the A form. A smaller influence may also arise from the temperature dependence[266] of pH, because upon heating the buffer for 5 min at ~110 °C, the pH of the buffer solution increased from 3.5 to 3.6.

Film State Measurements: Rich *et al*. have performed the X-ray diffraction study on solid state polyA fibers at a variety of relative humidities to "determine the influence of water on the structure".[230] They found that the diffraction pattern remains essentially completely intact between 100% and 0% relative humidity, suggesting that water has no influence on the fiber structure. To monitor the influence of drying, the absorption spectrum obtained for H_2O solution prepared without buffer is compared to that of the film derived from the same solution in Figure 9-4. Major changes are not seen as a consequence of drying. The only significant change seen is for the high-frequency band, which shifted from 1659 cm^{-1} in solution to 1651 cm^{-1} in the film.

The absorption spectral features observed for the H_2O solution (Figure 9-4, top trace) are directly comparable to those observed for the film (Figure 9-4, bottom trace) derived from the same solution. Since VCD spectra cannot be measured for H_2O solution, because of interference from H_2O solvent absorption, one can then undertake VCD measurements for films derived from H_2O solution. Such film spectra have not been reported to date for polyA. For this reason we investigated the absorption and VCD spectra for films prepared from buffered

parent solutions at the same selection of pH values as explored in the D_2O solution-state study.

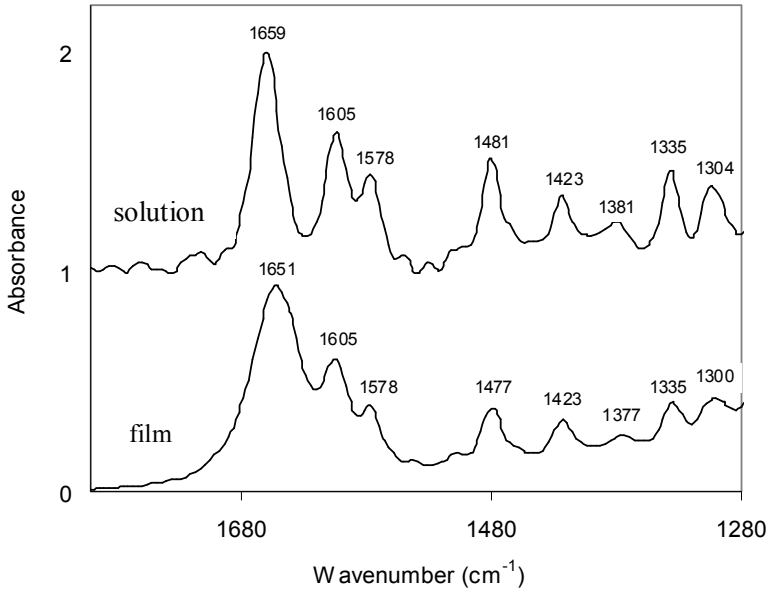

Figure 9-4: Changes in absorption features of polyA in going from H_2O solution to a film state.

The VCD spectra in the film state were reported[15,267,268] previously for proteins and carbohydrates where spectra were found to be independent of rotational orientation of the film around the light beam, but polyA films did not exhibit such rotational independence for VCD spectra, as shown for a representative example at pH 5.5 in Figure 9-5C' (*vide infra*). Although the rotational dependence is not always as pronounced as in Figure 9-5C', the conditions affecting the degree of the rotational dependence are unpredictable, which makes the measurement of VCD spectra of these films unreliable.

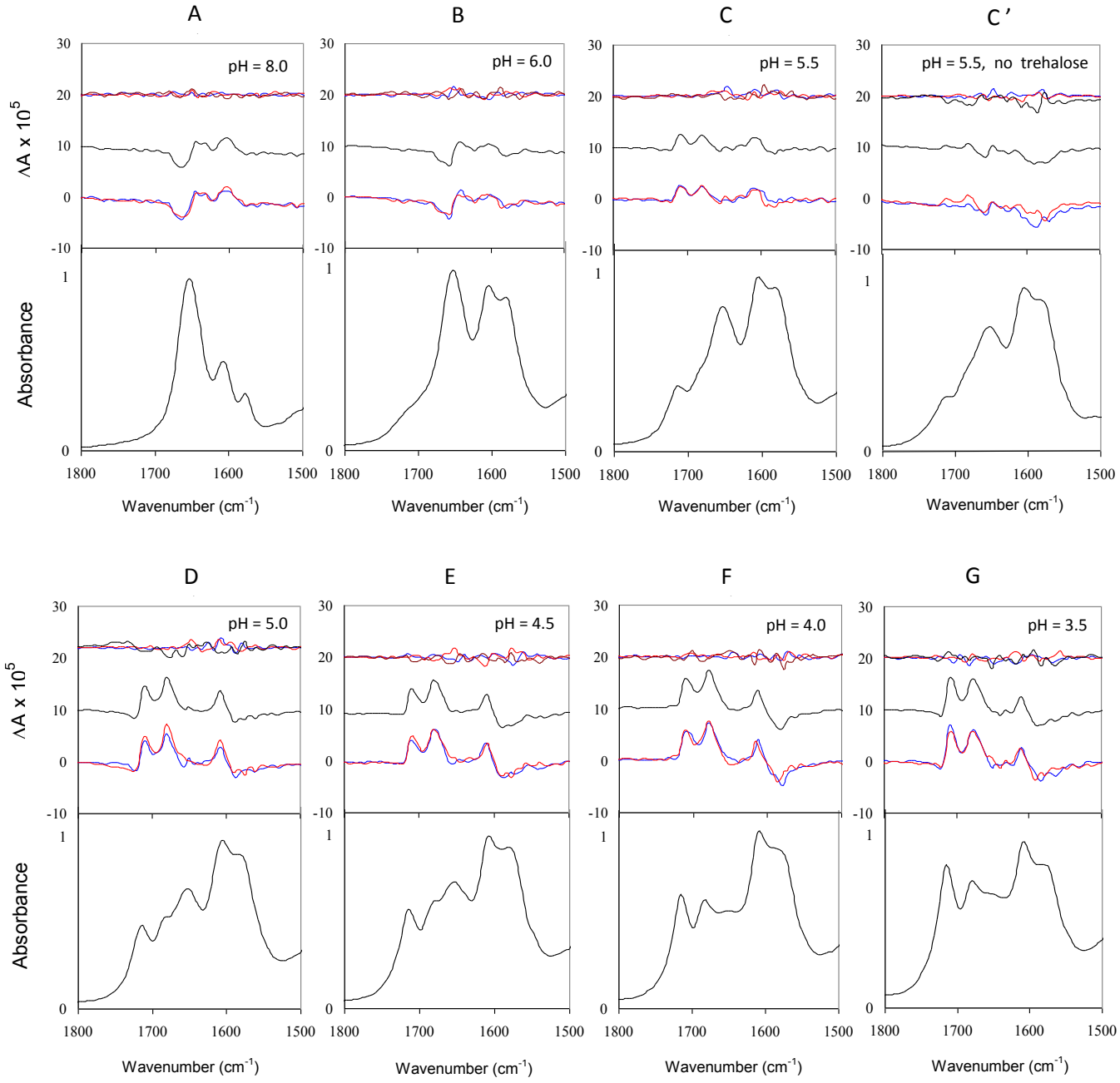

Figure 9-5: Film-based vibrational absorption (bottom panel) and circular dichroism (top panel) spectra of polyA in the pH range of 8.0 to 3.5. The top panel displays three sets of traces. The bottom set in the top panel represents traces for VCD spectra obtained at arbitrarily chosen 0° position (red trace) and at position obtained via 45° rotation (blue trace) of the film around the light beam axis. The spectra displayed in the middle of the top panel (black trace) represents an average of 0° and 45° VCD spectra. The spectra displayed at the top of top panel represent traces associated with 0° noise spectra (red trace), 45° noise spectra (blue trace) and the difference between the 0° and 45° VCD spectra (black trace). All spectra, except C’, were obtained from parent solutions containing trehalose. The spectrum C’ was obtained at pH 5.5 without trehalose.

As discussed in the literature,[196] the rotational dependence for circular dichroism in films originates from linear birefringence and linear dichroism caused by macroscopic orientation or microcrystalline sample formation. In certain cases these unwanted effects and rotational dependence for VCD can be avoided by using matrix-assisted film formation.[268] The studies in our laboratory have indicated[15,267,268] that carbohydrates are capable of forming transparent films that can yield rotationally independent VCD spectra. In addition, some literature reports[269,270] indicated that carbohydrates can act as stabilizing carriers for nucleic acids. Carbohydrates such as lactose, sucrose, dextran, etc. are widely used in the pharmaceutical industry for storage and protection of biochemicals, especially during drying. There are suggestions[271] that stabilization of solute molecules most likely comes from hydrogen bonding with the matrix.

When polyA is in an aqueous environment, the hydrogen bonding potential associated with hydroxyl groups as well as with nitrogen atoms of polyA is fulfilled via their interaction with hydroxyl groups of water. However, upon evaporation of water during the film formation, such intermolecular hydrogen bonding can be influenced. It is possible that introduction of a carbohydrate matrix, which is rich with hydroxyl groups, can stabilize the polyA sample via intermolecular hydrogen bonding and by minimizing the electrostatic repulsions among phosphate groups. Trehalose is considered[272] to either replace water molecules for hydrogen bonds or entrap water molecules for bioprotection. For this reason, trehalose-assisted films were prepared for polyA. The optimal ratio for obtaining rotationally independent VCD spectra was determined to be 1:2

(polyA/trehalose). The rotational independence for VCD in polyA films was achieved with a trehalose matrix, as shown in Figures 9-5A-G, where the frequency region between 1800 and 1500 cm^{-1} is shown. The region below 1500 cm^{-1} is not displayed due to interference from trehalose absorption and VCD signals. The main criteria used for assessing the trehalose-containing films is to ensure that the differences between the VCD signals obtained at 0° and 45° positions are within the noise level of the individual VCD spectra.

We believe that trehalose acts only as a stabilizing carrier and does not have chemical interaction with polyA for two reasons. First, as seen by the comparison of Figures 9-5C and 9-5C' (both at pH 5.5), the addition of trehalose has very little effect on the observed absorbance of polyA. Second, the solution-based absorption and VCD spectra obtained for polyA sample with added trehalose (not shown) are found to be identical to the spectra exhibited by polyA sample without adding trehalose.

Figure 9-6 displays the progression of absorption (A) and VCD (B) spectral features for film-based samples of polyA, as a function of pH. Absorption bands (as appearing at pH 5.5), ~1713, ~1682, ~1655, ~1605, and ~1581 cm^{-1} are labeled as V-IX, respectively. As the pH is lowered, bands V and VI increase, and band VII decreases in intensity. Absorption intensity changes for bands VIII and IX, when going from pH 8.0 to 6.0, are associated with the change of buffer at these two pH values. (The citrate buffer used for the pH range of 6.0-3.5 has absorption features in the region of bands VIII and IX causing these changes.)

There is a slight frequency shift of band VIII from 1605 to 1608 cm^{-1}, when going from pH 5.5 to 5.0.

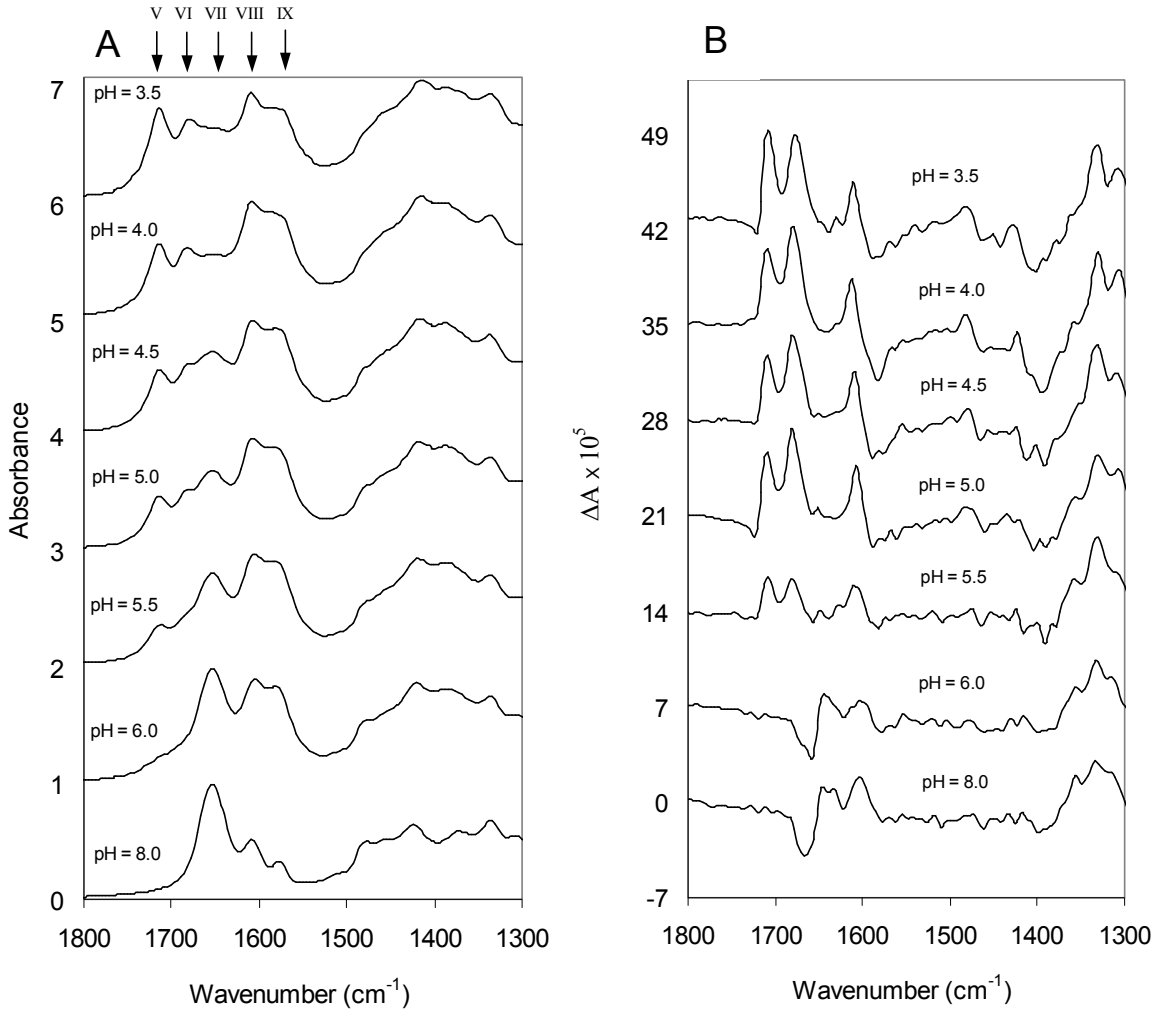

Figure 9-6: Vibrational absorption (A) and circular dichroism (B) spectra of film samples of polyA, obtained from trehalose-containing parent solutions at pH values of 8.0, 6.0, 5.5, 5.0, 4.5, 4.0, 3.5.

In the context of correlation between pH-induced changes for the spectral features of solution and film samples, the most notable resemblance is seen

(Figure 9-7) between absorption bands I and II of solution and absorption bands V and VII of films, respectively.

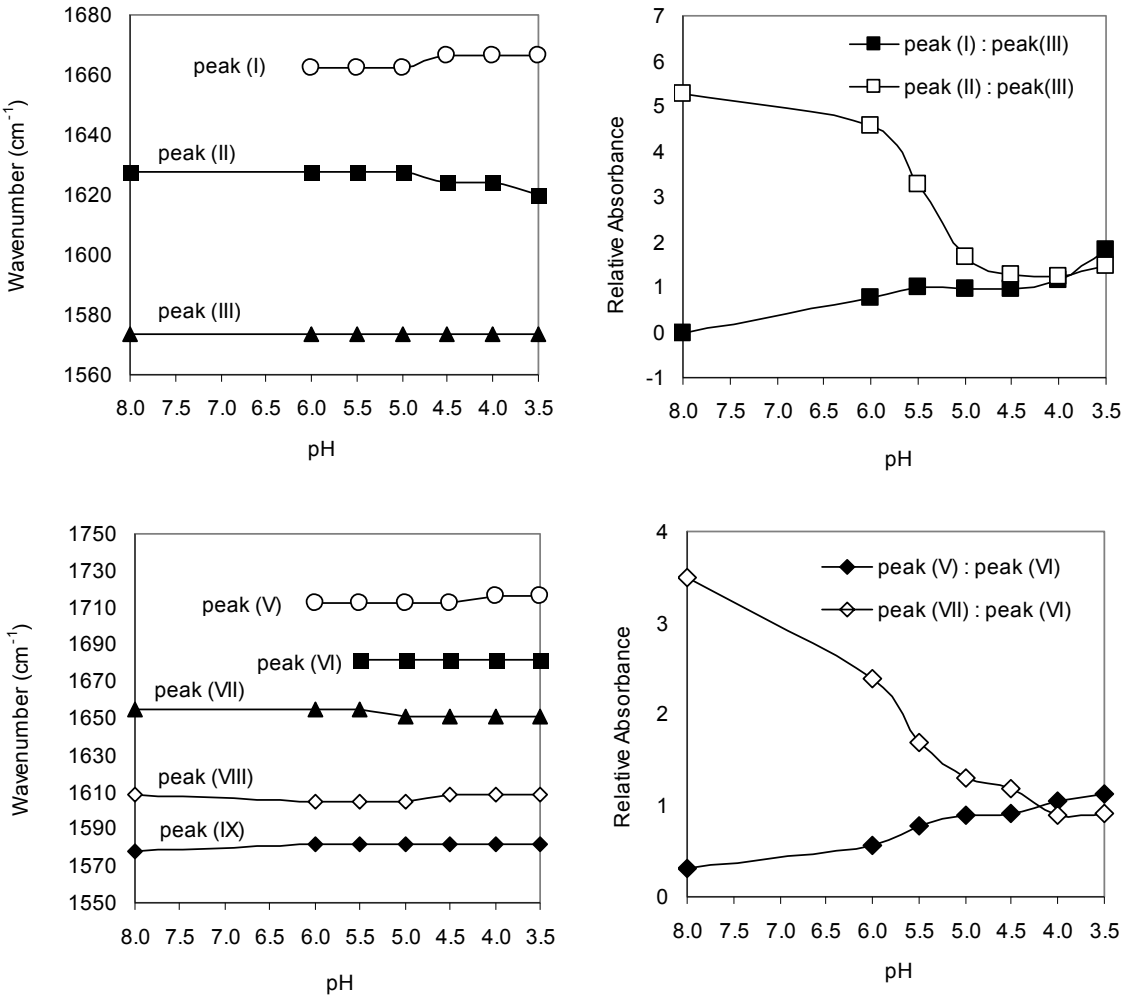

Figure 9-7: pH dependent changes in band positions (left two panels) and relative absorption intensities (right two panels) in the solution (top two panels) and film (bottom two panels) spectra.

Absorption band I appears in solution at pH 6.0 and becomes gradually intensified as the pH is lowered; similarly absorption band V in film becomes noticeable at pH 6.0 and becomes gradually intensified as the pH is lowered. The position of band I in solution shifts to a higher frequency at lower pH, as does

band V of the film. Similarly the position of band II in solution shifts to a lower frequency at lower pH, as does band VII of the film. Furthermore, just as the intensity of band II in solution is diminished as the pH of the solution is lowered, the intensity of band VII in film also diminishes as the pH of the parent solution for the film is lowered. The plots (Figure 9-7) showing dependence of band positions and relative absorption band intensities on pH support these comments. For obtaining relative intensities, band III of the solution and band VI of the film were chosen as the references as their frequencies did not change with pH. The changes in relative band intensities of bands I and II of solution correlate well (Figure 9-7) with those of bands V and VII, respectively, of the film. Since occurrence of band I has been identified as the marker of the double-helix formation in solution-based spectra, band V can be considered to indicate the formation of double helix in the film-based spectra.

The VCD features observed for films (Figure 9-6) at pH values of 8.0 and 6.0 appear to reflect a single-helix structure. As in the solution-state spectra (Figure 9-3) the film absorption spectrum hints the beginning of the formation of double helix at pH 6.0, in terms of developing a weak band V, and this development has not yet been reflected in the VCD spectrum of the film at pH 6.0. The VCD features for films in the pH range 5.5-3.5 reflect a double-helix structure. Then the single-helix structure is represented by a positive couplet originating from absorption band VII and by a positive band associated with absorption band VIII of the film. The development of the double helix is marked in the film by an abrupt occurrence of the two positive VCD signals, associated with

absorption bands V and VI, at pH 5.5 and loss of the positive couplet associated with band VII. As the pH is lowered further and the double helix is reinforced, the positive VCD signals from absorption bands V and VI become more intense, and a negative VCD couplet is formed in region VIII. However, unlike in the solution-state VCD spectra (Figure 9-3), the distinction between the three acidic forms of polyA, namely, B, A, and frozen forms, is less clear in the film VCD spectra. At pH 3.5 enhanced VCD signals are not seen for films, unlike in solution-state VCD spectra, probably because the concentration of parent solutions used to make films is ~3 times smaller than that used for solution-state VCD measurements. As a result, the extent of aggregation in the parent solutions of film samples is less than that in the solutions used for solution-state VCD measurements. For all of the pH values considered, VCD signal magnitudes exhibited by the film samples are considerably weaker than those exhibited by the solution samples.

To confirm the generality of VCD observations for film samples, it is necessary to undertake film studies on different homopolynucleotides that in the solution-state behave similarly to polyA. Since several solution-state homopolynucleotides exhibit VCD band-shape generality, it would be of interest to investigate if similar generality is also reproduced for corresponding films. If the generality turns out to be present, then film-based studies can be used advantageously for nucleic acids.

Conclusion

The present work reports the IR absorption and VCD spectral changes and their correlation to structural changes of polyA as a function of pH in both solution and film states. The analysis of the solution data as a function of pH sheds new light on the previously unrecognized absorption band I at ~1665 cm^{-1} and identifies this band as the marker of the double-helix structure of polyA. The solution spectra additionally demonstrate that the transition from a single- to a double-helical structure is more easily identified from changes in absorption spectra, while the changes in VCD features reflect more transparently the pH-dependent transitions among the three acidic forms of polyA (A form, B form, and frozen form). The solution study also included a temperature-dependent investigation that leads to the conclusion that heating the solution to ~70°C leads to a partial yet reversible unfolding of a single-helix at neutral pH and of a double helix at acidic pH. However, heating of the most acidic frozen form to ~110°C leads to irreversible disruption of the aggregated structure, promoting the separation of aggregated strands and their subsequent recombination into the A form.

Rotationally independent VCD spectra can be collected for films of polyA when a trehalose-assisted film formation technique is applied. Trehalose serves as a stabilizing carrier for polyA probably through hydrogen bonding interactions or by trapping H_2O from evaporation. Nevertheless, we believe that changes in IR absorption and VCD spectral features of the film state polyA between pH values of 6.0 and 5.5 are indicative of the transition of the secondary structure

from a single to a double helix. The spectra of polyA in the film state represent the first step toward realizing the prospect of using film-based spectra in monitoring secondary structural changes for nucleic acids. Believing that the pH-dependent film-based spectra do reflect changes in the secondary structure as observed in solution state, we foresee three instances where films could be used advantageously: 1) in cases where it is difficult to acquire solution spectra because of the limited solubility of polynucleotides, 2) in cases where the solution spectra cannot be collected due to the tendency of certain polynucleotides to form viscous gellike solutions, 3) in cases where the monitoring of polynucleotide structural changes within a natural biological environment (H_2O rather than D_2O) is desired. The present results provide a beginning for the use of the film-based spectra for monitoring the secondary structural changes of polynucleotides.

Polyribocytidylic Acid (polyC):

Introduction

PolyC has been previously investigated using a number of techniques that included X-ray diffraction,[273,274] NMR[275], UV absorption spectroscopy,[276-282] electronic circular dichroism (ECD),[276,283-285] linear dichroism (LD),[283] optical rotatory dispersion (ORD),[276,279,286] specific rotation,[287,288] IR absorption spectroscopy,[280,289-296] Raman spectroscopy,[289,291,294,297] vibrational circular dichroism (VCD),[258,263,298,299] phase diagrams,[300] and proton buffer capacity.[301] From the results obtained in the literature studies, it is established that polyC adopts three distinct structures as a function of pH. The transition among the

three structural forms takes place at pH values near the two pK_a values[280,300,302] (5.7 and 3.0) of polyC. At a pH above 5.7, polyC exhibits a single-stranded structure with an ordered, six nucleotides per turn, right-handed helical backbone.[273] It was suggested that the forces responsible for maintaining the single-stranded helix are hydrophobic in nature,[276,286] with the stability provided by the base stacking of cytidine residues. The single-stranded structure was first deduced from an X-ray diffraction study,[273] and subsequently, this assignment has been supported via other techniques. [277,278,280,282,283,285,286,293,294,297,302-304]

At a pH below 5.7, but above 3.0, protonation of the nitrogen atom $N_{(3)}$ (see Figure 9-8) of the cytosine bases induces an intertwining of the two parallel polyC strands forming a hemi-protonated, double-stranded helical structure[273,274,288] with 12 nucleotides per turn. The labeling hemi-protonated implies that alternate bases on each strand are protonated. The two strands are held together by three hydrogen bonds per pair of cytosine residues. Figure 9-9 displays the cross-sectional view of the proposed[274,288] double-helical model, indicating how a pair of cytosine residues forms hydrogen bonds. One hydrogen bond is formed by sharing a proton between the $N_{(3)}$ atoms of two cytosines across the center. This hydrogen-bonding interaction occurs between a protonated cytosine of one strand and an unprotonated cytosine of another strand. The other two hydrogen bonds are formed between the amino groups of a cytosine residue of one strand and the carbonyl oxygens of a cytosine residue belonging to the complementary strand. The structural assignment involving hydrogen bonding was deduced, independently, on the basis of investigation of

the polyC fibers via X-ray diffraction study[274] as well as on the basis of data obtained from viscosity, sedimentation and specific rotation study.[288] The existence of the double-helical form at pH below 5.7 was subsequently supported with studies involving other techniques.[283,297,302]

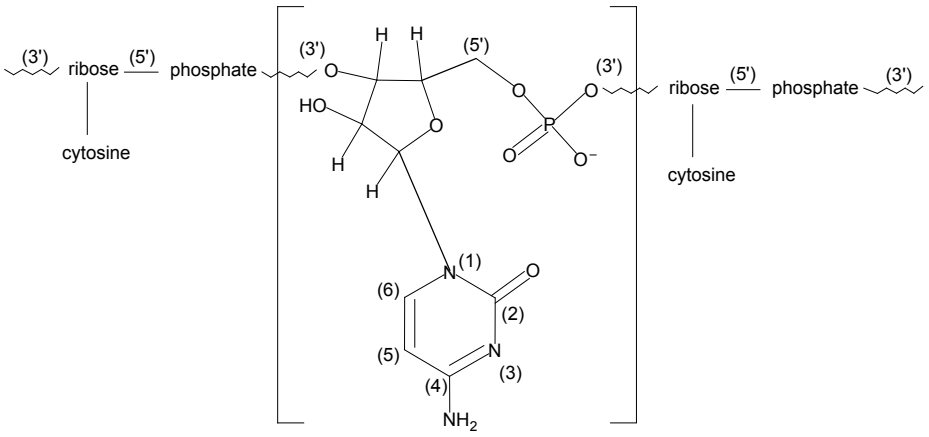

Figure 9-8: The chemical structure of a monomer unit of the polyribocytidylic acid (polyC).

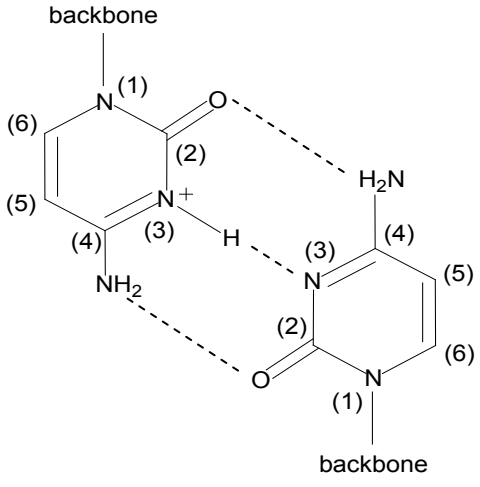

Figure 9-9: The interaction of two monomer units belonging to complementary chains of polyC, when found in an acidic environment. Hydrogen bonds are designated with broken-lines.

The dissociation of double-stranded helix into two disordered chains with protonated cytosines takes place[280,284,294,295] below pH 3.0. The double-helical form requires an uptake of only one proton per base pair, and its disruption is achieved via addition of a second proton to this base pair, which makes the hydrogen bonding across $N_{(3)}$ atoms of cytosines impossible.

The application of VCD as a probe of nucleic acid structure was first published by Keiderling and co-workers in a collective solution-based study[299] of several homopolynucleotides, including polyC in a buffered solution at pD 7.6 (or pH 7.2). It has been reported[258,263,299] that the single-stranded helical form of polyC is associated with a positive VCD couplet centered at ~1658 cm^{-1}. Although it was stated[299] that a decrease in magnitude of this positive VCD couplet with a decreasing pD from 7.6 to 6.1 (or pH from 7.2 to 5.7) can be correlated to a change from a single- to a double-helical form, the absorption or VCD bands characteristic of the double-helical form of polyC have never been presented or identified. The absorption and VCD spectra of polyC at pH 6.2 and 5 °C, reported by Tsankov *et al*.,[298] did reveal the appearance of a new band at 1694 cm^{-1} assigned to the protonated form, but their investigation focused on the similarities between the spectra of polyC and the spectra of $d(C)_{12}$. The pH-dependent changes for polyC itself were not studied. The conversion from the single- to the double-helical form of polyC is expected to occur below pH 5.8, so the potential information contained within the VCD spectra of polyC at pH below 5.8 has not yet been explored.[258,263,299] The results presented in this chapter fill this gap.

In the polyA study[305], described previously, the absorption and VCD bands characterizing the double-helical structure of polyA have been identified. Furthermore, it was suggested that both solution and film VCD spectral features can be used as independent probes of pH-dependent structural transitions. Film studies have an advantage of requiring lower sample concentrations. The polyA study has provided the impetus for investigating other homopolynucleotides. Since both polyA and polyC display[299] VCD band-shape generality for single-helical structures in the solution state, it would be interesting to examine if this kind of generality can be observed in the film state as well.

Here we present detailed changes in IR and VCD spectral features that reflect the pH-dependent structural transition from the single- to the double-helical form of polyC. The pH-dependent structural investigations are performed in both solution and film states to investigate how these results correlate with each other and also independently reflect the structural conversion. The potential advantages of using film VCD studies for investigating nucleic acids are also discussed.

Experimental Section

The polyC potassium salt (P4903) and D(+)-trehalose were obtained from Sigma Chemical Co. and have been used as received. D_2O was obtained from Cambridge Isotope Laboratories, Inc.

Liquid solution samples, at a final concentration of ~20 mg/mL, were prepared by dissolving polyC in a solution that contained 0.1 M NaCl and 10 mM

citrate buffer in D_2O. The reason for using citrate buffer is the availability of a wider pH range (2.2-7.2) with this buffer. The pH values of the citrate buffer and of the polyC solution in this buffer used for solution studies are summarized in Table 9-1. The corresponding values of solutions used for film studies are summarized in Table 9-2. From the data in these tables, it can be noted that the pH of the starting buffer solution changes significantly upon adding polyC. A glass-body liquid-filled micro-combination pH electrode was used for all pH readings. The pH meter readings are reported here as such. However, pD can be derived from the pH meter readings as[306] pD = pH(meter) + 0.4. The 10 mM concentration of citric acid is low enough for the absorption associated with its carbonyl group not to interfere with the base vibrational bands. For the concentrations used here, the polyC solutions appeared more viscous as the pH was lowered below 5.8, although there was no difficulty in drawing the solution with a pipet.

Table 9-1: pH of the buffer solutions and of polyC (~20 mg/mL) solution in that buffer, used for solution studies.

Citrate Buffer (10mM)	polyC + Citrate Buffer
7.1	6.5
5.9	6.0
5.3	5.8
3.5	5.7
2.5	5.1

Table 9-2: pH of the buffer solutions and of polyC (~6 mg/ml) solution in that buffer, used for film studies.

Citrate Buffer (10mM)	polyC + Citrate Buffer
7.0	6.9
5.5	5.7
3.5	4.5

IR and VCD spectra of polyC solutions have been measured at room temperature (~ 22°C), at an elevated temperature (~ 70°C), and back at room temperature (after allowing for 1 hr of cooling time) for each of the pH values considered. This thermal cycling was used to establish whether the conformational change during heating is reversible upon cooling. Heating was accomplished by holding the sample in a variable temperature cell. The temperatures were read with a thermocouple embedded in the cell.

For preparing the film samples, a previously described drop-cast method with ~200 µL of the parent H_2O solution containing polyC (~6 mg/mL) and trehalose (~12 mg/mL) was used. Trehalose at a mass ratio of 2:1 (trehalose/polyC) was added to obtain orientationally independent VCD spectra, as described in the polyA study. Another difference in preparation of the solution and film state samples was that for film samples, no NaCl was included to avoid its precipitation on the surface of the film. Films were tested for orientational independence by taking the spectra at two positions: an arbitrarily chosen 0° position and a position corresponding to a 45° rotation around the light beam axis.

IR and VCD measurements for both solution and film state samples were obtained on a modified ChiralIR instrument. All spectra were recorded at 8 cm^{-1} resolution. For the solution-based VCD spectra, a 1 hr data collection time was used. The data collection time for films varied from 1 to 6 hr, as films gave relatively weaker VCD signals. The solution sample was held in a demountable cell with CaF_2 windows and a 50 μm Teflon spacer. Baseline corrections for all solution-based absorption (or VCD) spectra were done by subtracting the absorption (or VCD) of the buffered D_2O solvent, containing NaCl. Baseline for the VCD spectra of films was estimated.

Results and Discussion

Solution State Measurements: The pH-dependent IR absorption and VCD spectra in the 1800-1450 cm^{-1} region measured at room temperature (22°C) and at an elevated temperature (70°C) are displayed in Figure 9-10. The 1450-1300 cm^{-1} region has been omitted as no useful bands were observed in this region, and the region below 1300 cm^{-1} had a strong interference from D_2O absorption.

The lowering of the pH from 6.5 to 5.1 led to noticeable changes in spectral features (see Figure 9-10), which parallel the expected structural changes. There are five absorption bands, labeled as I-V in Figure 9-10A, that undergo changes as a function of pH. The changes in band positions are displayed in Figure 9-11A, and those in absorption band intensities are displayed in Figure 9-11B,C. As the acidity of the solution increases, one of the most notable changes is exhibited by band I at ~1693 cm^{-1}. This band is completely

absent at pH 6.5 and 6.0 and begins to emerge at pH 5.8. At pH 5.7 and 5.1, this absorption band at 1693 cm^{-1} is clearly seen. Tsankov *et al*.[298] observed this band at pH 6.2 probably because of the differences in thermal (5°C instead of 22°C) and buffering (no buffer in place of citrate buffer) conditions used in their study. The protonation of cytosine residues at and below pH 5.8 is expected to be responsible for the growth of absorption band I. The relative intensity of the absorption band I, in relation to that of band II, increases upon further lowering of the pH, as was also observed for the corresponding band in polyA. The vibrational origin of band I in polyA was assigned to the C=N stretching vibration coupled to -N-D bending vibrations. However, the C=O stretching vibration of cytosine (which is absent in adenosine) can appear in the same wavenumber region. Thus, in accordance with previously reported IR spectral interpretations,[294,298,307] it seems reasonable to assign the origin of band I to the $C_{(2)}$=O stretching vibration. It is known[304,308] that the C=O band intensities typically change as a result of the involvement of the C=O group in hydrogen-bonding formation. In acidic environments, as can be seen from Figure 9-9, the carbonyl group ($C_{(2)}$=O) is involved in hydrogen bonding with the amine group of the opposite strand. Thus, unlike in the polyA case, the vibrational mode giving rise to band I in polyC may not directly involve the $N_{(3)}$ atom that is being protonated. Nevertheless, the absorption band I appears to be a diagnostic marker of the double-stranded helical form of polyC, which was not recognized to date.[258,263,299] An alternate interpretation of associating band I with the quadruplex form is also possible, which is discussed later in this section.

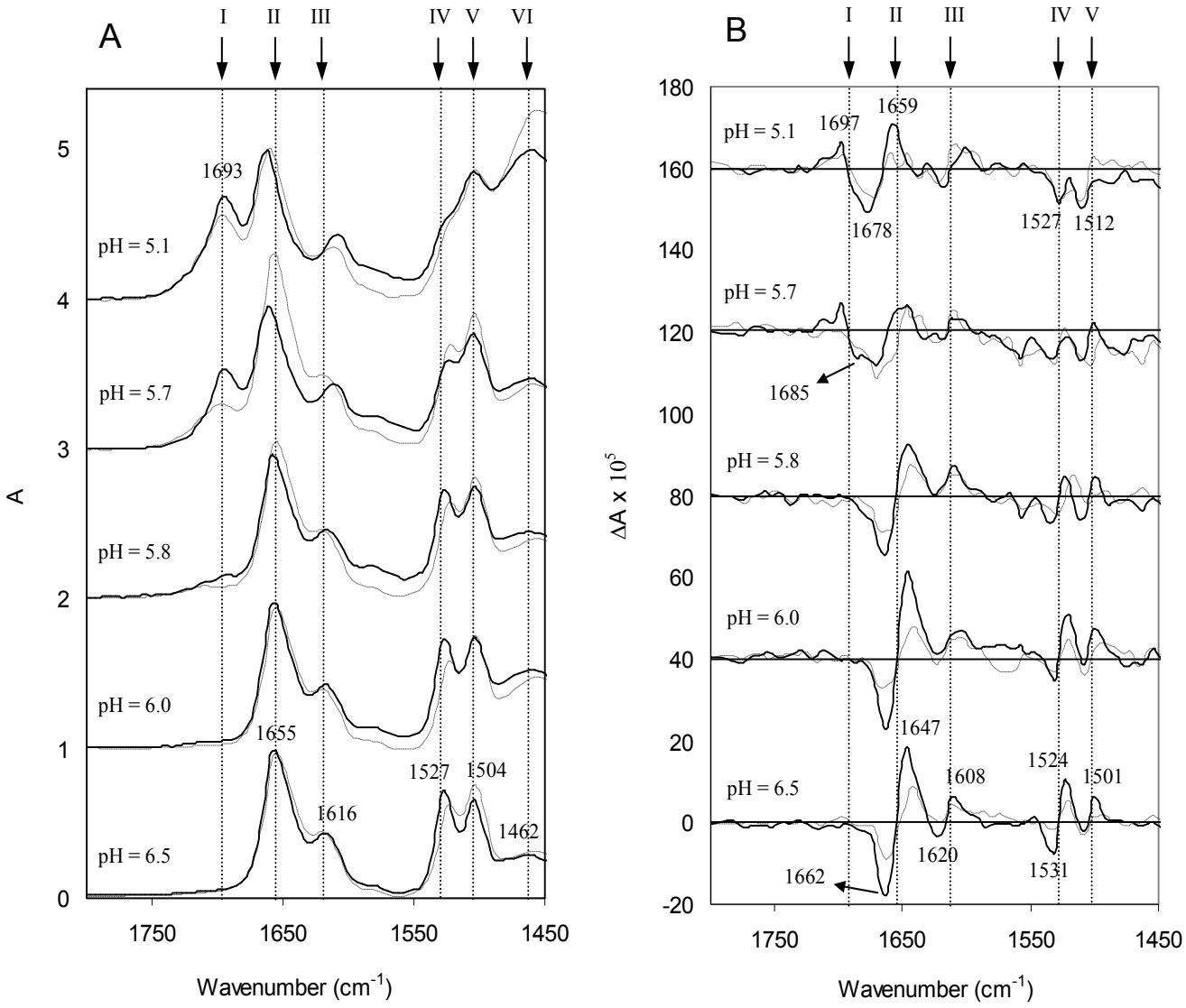

Figure 9-10: Vibrational absorption (left) and circular dichroism (right) spectra of polyC solutions in the pH range of 6.5 to 5.1. Concentrations used for solution preparations are given in the experimental section. The traces given by the solid line represent the spectra taken at room temperature (22°C), while the traces given by the broken-line represent the spectra taken at elevated temperature (70°C).

Among the five absorption bands noted in Figure 9-10, band II has the highest absorption intensity. This band undergoes a 2-fold change as a function of pH. First, the wavenumber position of band II increases as the pH is lowered: from ~1655 cm^{-1} at pH 6.5 and 6.0 to ~1659 cm^{-1} at pH 5.8 and to ~1663 cm^{-1} at

pH 5.7 and 5.1. Second, its relative intensity, in relation to that of band I, decreases as the pH is lowered. While a majority of the previously conducted theoretical and experimental studies[263,289,292-294,298] assign the origin of band II to the $C_{(2)}$=O vibrational motion of unprotonated cytosine, the discussion of Shimanouchi *et al*.[296,307] suggested that delocalization of π-electrons, among C=O, C=N, and C=C bonds, occurs at neutral pH thus leading to the mixed stretching vibrations of these groups. Thus, band II has been assigned[296,307] to mixed stretching vibrations of C=O, C=N, and C=C bonds. The corresponding band in polyA was assigned to the C=N stretching vibration coupled to the -N-D bending vibration by Andruschenko *et al*.[204]

The wavenumber position of band III gradually decreases as the pH is lowered: from ~1616 cm^{-1} in the pH range of 6.5-5.8 to ~1612 cm^{-1} at pH 5.7 and to ~1608 cm^{-1} at pH 5.1. This band originates[263,289,293,294] from the coupled stretching vibrations of groups $C_{(6)}$=$C_{(5)}$ and $C_{(4)}$=$N_{(3)}$ or C-C. For this band, the decrease in frequency continues even below pH ~5.7, reflecting continual protonation with increased acidity of the environment. Additionally, the decrease in band frequency follows the expected behavior[289,308] arising from hydrogen-bond formation between the added hydrogen of the $N^{+}_{(3)}$-H group and the $N_{(3)}$ atom on the opposite strand.

Band IV is located at ~1527 cm^{-1} at pH values 6.5-5.8, and then it shifts to ~1524 cm^{-1} at pH 5.7 and 5.1. On the other hand, the wavenumber position of band V remains at ~1504 cm^{-1} as the pH is decreased. The identification of the vibrational origin of these bands is challenging because of the considerable

vibrational coupling[289,291,297] among several groups, such as C=C/C-C, C=N, and C=O stretching vibrations. The NH_2 bending deformations are not expected to be contributing here because in D_2O solvent, the NH_2 groups become ND_2. Nevertheless, bands IV and V do seem to give some insight into the pH-induced structural changes. The lowering of pH results in a change in the relative absorption intensities of bands IV and V (see Figure 9-11C). At pH 6.5, where the single-helical form dominates, the absorption intensity of band IV is slightly larger than that of band V. At pH values 6.0 and 5.8, the absorption intensities of these two bands are essentially equal. At pH values of 5.7 and 5.1, where the double-helical form is expected to dominate, it is easily seen that band IV has a lower absorption intensity than band V. This implies that the change in relative absorption intensities of bands IV and V is also correlated with single-to-double-helix transitions. A single helix is present when band IV is more intense than band V, and the double helix is the dominant form when these relative band intensities are reversed. These observations are in agreement with the previously reported[302] suggestion that band IV is characteristic of unprotonated cytosine, and it decreases in intensity with increasing protonation. Nevertheless, among the five absorption bands, band I seems to undergo the most notable change as a function of lowering the pH and hence can be identified as the most sensitive marker of the transition from the single- to the double-helical form of polyC.

The major VCD features seen in Figure 9-10B arise from absorption bands I and II. At pH 6.5, the positive VCD couplet associated with absorption band II is the signature[258,263,298,299] of the single-helical structure of polyC.

Analogous to absorption band II, which shifts toward a higher frequency as the pH is lowered, the associated positive VCD couplet also shifts in the same direction. Specifically, the positive lobe of this VCD couplet remains at 1647 cm^{-1} in the pH range from 6.5 to 5.7 and then shifts to 1659 cm^{-1} at pH 5.1. The negative lobe, on the other hand, is located at 1662 cm^{-1} in the pH range from 6.5 to 5.8, after which it shifts to 1670 cm^{-1} at pH 5.7 and then to 1678 cm^{-1} at pH 5.1. Additionally, as the pH is lowered, the magnitude of this positive VCD couplet decreases. It should be noted, nevertheless, that the shifted couplet slightly intensifies at pH 5.1 as compared to that at pH 5.7.

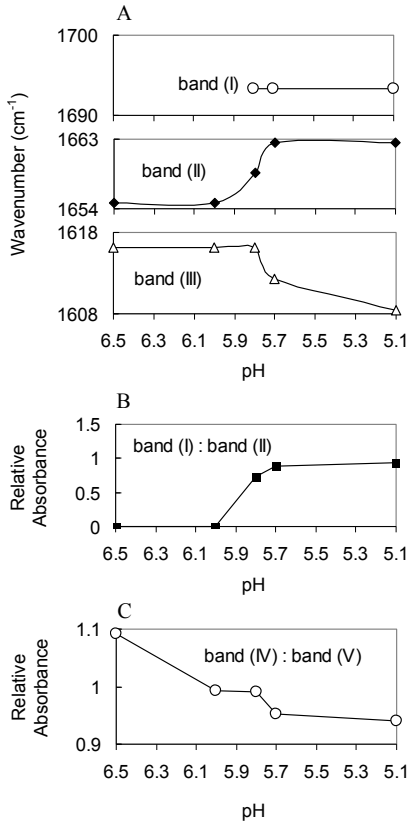

Figure 9-11: pH dependent changes in band positions (A) and relative absorption intensities (B and C) in the solution spectra.

As the pH is lowered, a negative VCD couplet at ~1692 cm^{-1} is developed beginning at pH 5.7. This negative couplet, with a positive lobe at 1697 cm^{-1} and a negative lobe at 1685 cm^{-1}, is associated with absorption band I. The negative lobe of this couplet is located adjacent to the negative lobe belonging to the positive VCD couplet associated with absorption band II. These two negative lobes (one coming from the positive VCD couplet and the other from the negative VCD couplet) appear to combine together to give one negative VCD lobe at 1678 cm^{-1} at pH 5.1. In a previous VCD study,[299] the VCD spectrum of polyC at a pH lower than 7.2 has not been presented, but it was mentioned that at pH 5.7, the drop in magnitude of positive VCD couplet, associated with band II, can be correlated to a change from the single- to the double-helical form. The negative VCD couplet, centered at ~1692 cm^{-1}, and associated absorption band I are clearly seen in the present work as is also seen in the study of Tsankov *et al*.[298]

The VCD bands associated with absorption bands III, IV, and V also undergo changes as a function of pH, but these changes seem less revealing from the perspective of the structural interpretation. Specifically, the positive VCD couplet at 1620(–)/1608(+) cm^{-1}, associated with absorption band III, seems to decrease in intensity and is not well-defined as the pH is lowered. The positive VCD couplet at 1531(–)/1524(+) cm^{-1}, arising from absorption band IV, and a positive VCD couplet at 1512(–)/1501(+) cm^{-1}, arising from absorption band V, at pH 6.5 transform into two negative bands at ~1527 and ~1512 cm^{-1} at pH 5.1.

It should be pointed out that although absorption band I and associated VCD represent diagnostic markers for double-helix formation for both polyA and

polyC, the vibrational origin and frequency position of these bands are different for the two homopolynucleotides. The band positions associated with the single- and double-helical forms of polyA and polyC are summarized in Table 9-3. Band I in polyA involves the vibration of protonated $N_{(1)}=C_{(6)}$, while in polyC, the $C_{(2)}=O$ group is involved. Not only does the vibrational origin of band I in these two polynucleotides differ, but also the number and type of hydrogen bonds involved in double-helix formation are different between polyA and polyC. For these reasons, it is not surprising that the VCD markers for the double-helical form of polyA and polyC are of opposite sign (Table 9-3), the positive couplet in the former and the negative couplet in the later. Nevertheless, the VCD marker for the single-helical form, a positive couplet, is the same for the two homopolynucleotides.

In addition to pH-dependent spectral features at a room temperature of 22°C (solid lines), the absorption and VCD spectra at 70°C (dashed line) are also shown in Figure 9-10. At pH 5.8, the weak absorption band I becomes weaker upon increasing the temperature. The same trend is observed for absorption band I upon heating the solutions at pH values 5.7 and 5.1, but the intensity decrease is more pronounced at pH 5.7. Since absorption band I has been identified as a marker of the double-helical form of polyC, the decrease in its intensity with increasing temperature reflects the thermal disruption of the double-helical form, potentially via partial unwinding of the two strands. The observation that the absorption band I and its corresponding VCD couplet are less prone to the temperature-induced intensity lowering at pH 5.1, as compared

to that at 5.7, could be interpreted as reflecting a greater stability of the double-helical form at the lower pH.

Table 9-3: Absorption and VCD bands of helical forms of polyC and polyA in solution.

	Single helix		Double helix	
	Absorption	VCD	Absorption	VCD
polyC	1655	1662(−)/1647(+)	1693	1697(+)/1678(−)
polyA	1628	1636(−)/1623(+)	1665	1670(−)/1659(+)

When the temperature is increased, the absorption band II undergoes a 2-fold change that is evidenced at pH 5.8 and especially pronounced at 5.7. First, it undergoes an increase in its relative intensity, and second, its position shifts to a slightly lower wavenumber. Both of these heat-induced modifications seem to counteract the pH-induced spectral changes of absorption band II at room temperature. As mentioned earlier, absorption band II also reflects the single-to-double-helix conversion by decreasing in intensity and shifting its position from 1655 cm^{-1} at pH 6.5 to 1663 cm^{-1} at pH 5.7. Upon increasing the temperature at pH 5.7, not only does the intensity of band II increase, but also its frequency shifts from 1663 cm^{-1} at room temperature to 1655 cm^{-1} at elevated temperature. This heat-induced frequency shift is essentially reverting the position of band II to that at higher pH and room temperature. At pH 5.1, on the other hand, band II is much less prone to the heat-induced changes. All this implies that at pH values of 5.8 and 5.7, the just-formed double-helix is not as stable and resistive to the heat-induced disruptions as is the double-helix at pH 5.1. The VCD couplet

associated with absorption band II begins to display a notable heat-induced change even at pH values 6.5 and 6.0. As compared to absorption, VCD generally displays a greater sensitivity to different conformations available to a molecule. Therefore, the decrease in intensity of the VCD couplet at the elevated temperature most likely signifies a conformational change due to some degree of heat-induced unfolding of the single helix. As the acidity of the environment increases and the double-helical form becomes stabilized, VCD undergoes a relatively smaller change at elevated temperature. It has been verified that the heat-induced structural modifications are reversible since, upon cooling, the bands observed originally at room temperature were restored in both absorption and VCD spectra.

Finally, it is important to point out a possible alternate interpretation for pH-dependent spectral changes in polyC. It is known that[309,310] at lower pH, oligonucleotides with deoxy-cytosine residues, $d(C)_4$, $d(TC_5)$, and $d(C_3T)$, etc., fold into a quadruplex structure. This quadruplex structure is composed of two parallel duplexes with protonated cytosine-cytosine pairing. The two parallel duplexes are integrated through base pair intercalation and noncovalent interactions of backbones in antiparallel arrangements. The antiparallel assembly is stabilized via a nonstandard short C-H$\cdots$O hydrogen-bonding network between $O_{4'}$ and $C_{1'}$-$H_{1'}$ as well as $C_{4'}$-$H_{4'}$ moieties of deoxyriboses. This nonstandard hydrogen bonding has been identified for several complexes.[44,45] However, the studies that have identified the nonstandard hydrogen bonding are based on X-ray crystallographic methods, which leads one to speculate that the

quadruplex structure might dominate in the crystalline state where molecules exist in a more ordered, compact form. According to Berger *et al*.,[311] backbone-associated hydrogen-bonding interactions provide a stabilization motif not only in DNA but also in RNA type molecules, so the hydrogen-bonding network of the proposed quadruplex model in deoxyribocytidines is also possible for ribocytidines. For these reasons, one cannot exclude the possibility that what we have identified for polyC as diagnostic marker of a double-helix formation can also be interpreted as a signature of quadruplex formation. But, the literature studies on polyC did not provide any evidence for such a structure.

Tsankov *et al*. suggested[298] that for $d(C)_{12}$, the appearance of band I (~1693 cm^{-1}) and its corresponding negative VCD couplet are markers of a quadruplex formation. The pH-dependent behavior of band I appears similar for $d(C)_{12}$ and polyC, but there are several differences in the pH-dependent behavior of other bands. As the pH is lowered, the positive VCD couplet associated with band II is poorly defined in $d(C)_{12}$, but this couplet remains well-defined in polyC. The frequency of absorption band IV increases in $d(C)_{12}$, from 1523 to 1527 cm^{-1}, as opposed to a decrease from 1527 to 1524 cm^{-1} in polyC, as the pH is lowered. The relative intensity of absorption band IV is lower than that of band V in $d(C)_{12}$ at all three pH values[298] of 7.2, 5.6, and 3.8, while in polyC, the relative intensity of absorption band IV is greater than that of V at pH 6.5 and then decreases as the pH is lowered. The VCD features associated with absorption bands IV and V and their pH-dependent behavior are also different in polyC and $d(C)_{12}$. It is possible that polyC does not have a strong propensity for nonstandard hydrogen-

bonding formation required for quadruplex formation in solution. Thus, we preferred to interpret the pH-dependent structural changes of polyC in terms of the structural transition from the single- to the double-helical form.

The VCD couplet associated with band II in polyC was reproduced[258,263,299] by coupled oscillator and Devoe theory model calculations for a single-stranded helical structure. However, no attempt has yet been made to predict the VCD features associated with duplex or quadruplex structures for polyC. Given the limitations[258,263,299] of these model calculations, it is unlikely that they will be able to resolve the question of the duplex versus quadruplex structure for polyC. Quantum mechanical calculations on these structures might be useful to resolve this issue, although such calculations are time consuming. It is known that polyG forms a parallel quadruplex structure, and therefore, experimental VCD investigations on polyG might also provide additional information on this issue. These investigations are presented in the next section of this chapter.

Film State Measurements: In addition to establishing how solution spectra reflect structures of single- and double-helical forms of polyC, it is also of interest to explore the same for film spectra.

As in the polyA study, the trehalose matrix was used to obtain orientationally independent VCD spectra. The main criteria used for assessing and confirming the quality of trehalose-assisted films was to ensure that the differences between the VCD signals obtained at the 0 and 45° positions are within the noise level of the individual VCD spectra.

Figure 9-12 displays the progression of absorption (panel A) and VCD (panel B) spectral features for polyC films as a function of pH in the range of 6.9-4.5. The region below 1500 cm^{-1} is not displayed due to interference from trehalose absorption and VCD signals. To provide a convenient monitoring of how absorption bands change as a function of pH, band wavenumbers and relative intensities are displayed in Figure 9-13A,B.

A compelling correlation between solution and film-based spectral features can be seen from the comparison of spectra in Figures 9-10 and 9-12. The absorption spectra (Figure 9-12A) display three main bands that are labeled as I, II, and III. Analogous to the absorption band I in solution spectra, the absorption band I in film spectra is absent at pH 6.9 but then begins to develop at 1720 cm^{-1} as the pH is reduced to 5.7. At pH 4.5, the absorption band I gains considerable intensity. The spectral behavior of this band in film spectra is essentially identical to that of 1693 cm^{-1} band in solution, although the wavenumber positions of these bands in solution and film spectra are different. Therefore, the development of band I in the film spectra, as the pH is reduced, reflects the formation and stabilization of the double-helical form of polyC.

As the pH is lowered, the absorption band II in film spectra undergoes two changes that are also analogous to those of band II in the solution spectra. First, the relative intensity of band II, in relation to that of band I, decreases (Figure 9-12A); in addition, the wavenumber position shifts from ~1651 cm^{-1} at pH 6.9 and 5.7 to ~1666 cm^{-1} at pH 4.5. Unlike in the solution spectra, the absorption band III in film spectra is very broad.

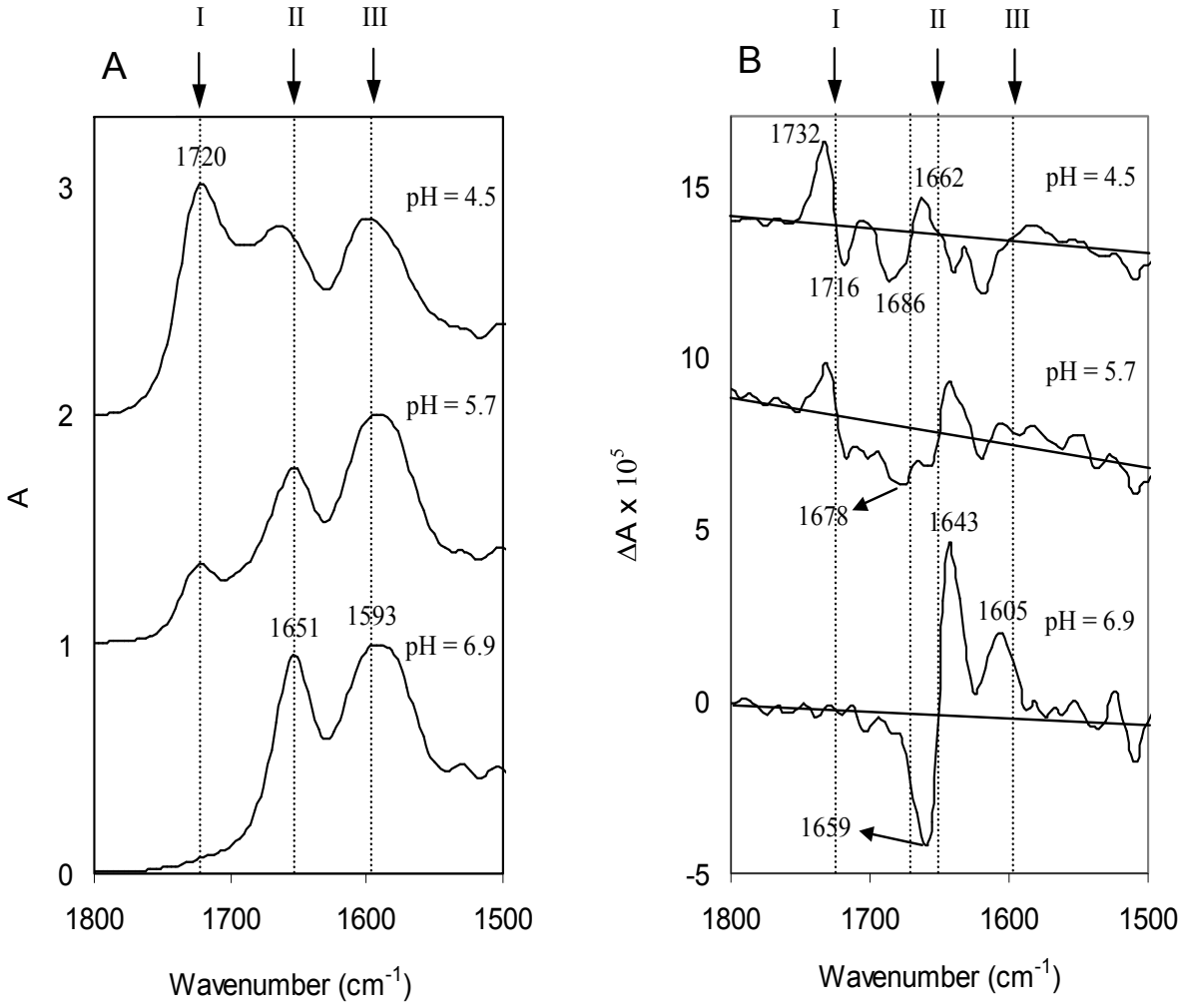

Figure 9-12: Vibrational absorption (A) and circular dichroism (B) spectra of film samples of polyC, obtained from trehalose-containing parent solutions at pH values of 6.9, 5.7, and 4.5. Concentrations used for parent-solution preparations are given in the experimental section.

A similar correlation is also found among VCD bands (Figure 9-12B) in the film and solution spectra. At pH 6.9, the film spectra display a positive VCD couplet, with a negative lobe at ~1659 cm^{-1} and a positive lobe at ~1643 cm^{-1}, associated with absorption band II. These VCD bands represent the characterizing signature of a single-helical form. This single-helix VCD signature is similar for the film and solution-based studies, as was the case also for polyA.

As mentioned earlier, polyA and polyC display VCD band-shape generality at neutral pH in solution state, which raises the question if the same type of spectral mimicking exists in the film state as well. The generality of the positive VCD couplet associated with the single-helical form of polyC and polyA is, in fact, also seen in the film VCD spectra.

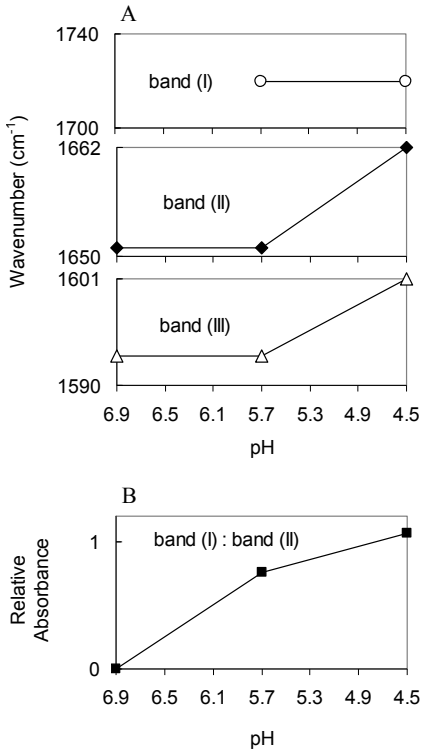

Figure 9-13: pH dependent changes in band positions (A) and relative absorption intensities (B) in the film spectra.

Comparable to the solution spectra, the film VCD spectrum characterizing the double helix of polyC exhibits a negative couplet associated with band I at pH 5.7, although the VCD baseline is not flat in the film spectra. The positive lobe of this couplet is located at ~1732 cm^{-1}, while the negative lobe is located at ~1716

cm^{-1}. The intensity of this negative couplet increases as the double-helical form of polyC becomes stabilized at pH 4.5. The positive VCD couplet originating from band II decreases in intensity upon double-helix formation and shifts to a slightly higher wavenumber. Specifically, at pH 5.7, the negative lobe of positive couplet remains at ~1659 cm^{-1} but only as a shoulder of a newly developing negative band at ~1678 cm^{-1}. At pH 4.5, the negative lobe of the positive couplet is located at 1686 cm^{-1}. Likewise, the corresponding positive lobe shifts from ~1643 cm^{-1} at pH 5.7 to ~1662 cm^{-1} at pH 4.5. Overall, it can be concluded that the main VCD signals arising from bands I and II, in both solution and film spectra, reflect in the same manner the pH-induced structural conversion of polyC.

The existence of parallel behavior in film and solution spectral features highlights the advantages for film studies. First, the concentration of parent solutions used for making films is approximately 3 times lower than that used for solution studies. Lower sample concentrations are certainly useful, and sometimes essential, in cases where concentration-dependent aggregation occurs. Second, lower sample concentrations lead to smaller pH changes when the sample is added to a given buffer solution. Evidence for this point can be seen in Tables 9-1 and 9-2. The disadvantages of film studies, at least for now, are that a suitable matrix is needed in some cases to obtain orientationally independent VCD spectra. This results in a narrower useful wavenumber region because of overlap from bands arising from the matrix. Additionally, to ensure orientational independence, at least two different VCD measurements are required as opposed to a single VCD measurement for the solution spectra.

Nevertheless, the practical conveniences in handling films, and other advantages mentioned previously, are the attractive factors for pursuing film VCD spectra.

For the double-helical form, the VCD spectral correspondence is not found between polyC and polyA either in solution or in film spectra. A negative VCD couplet is associated with the double-helical form of polyC, while a positive VCD couplet is associated with double-helical form of polyA. This difference is not surprising if one reflects on the fact that polyC has a C=O group that is absent in polyA. As a result, the nature of vibrations responsible for these couplets in polyC and polyA is different. In addition, the manner in which the two homopolynucleotides form double helices is also different. For instance, the hydrogen bond N^+-H···N seen for the double-helical form of polyC in Figure 9-9 is not present in the double-helical form of polyA, where N^+-H is involved in electrostatic interaction with the phosphate group.

Conclusion

The infrared absorption and VCD spectral changes and their correlation to structural changes of polyC as a function of pH in both solution and film states are presented. Analysis of the solution data led us to establish the appearance of a negative VCD couplet associated with an absorption band at 1693 cm^{-1} as the most transparent diagnostic marker of the double-helix formation. An alternate interpretation suggesting quadruplex formation for polyC was also discussed. The solution study also included a temperature-dependent investigation that led to the conclusion that heating the solution to ~70°C leads to partial, yet reversible

unfolding of single helix at a pH above 5.8 and of double helix at a pH below 5.8. An elevated-temperature study also reveals that at pH 5.1, the double-helical form becomes stabilized and is slightly less prone to a heat-induced disruption, as compared to that at pH 5.7.

We additionally report that orientationally independent VCD spectra can be obtained for films of polyC using a trehalose-assisted film formation technique. The spectral changes observed in the film spectra correlate with those in the solution spectra and are equally informative in monitoring the pH-induced structural changes of polyC. Thus, the film VCD spectra represent an alternative to the solution VCD spectra and carry a potential for being advantageous in cases when: 1) lower concentrations are to be used and 2) spectral data in a wider pH range, with standard buffer concentrations, are desired.

Polyriboguanylic Acid (polyG):

Introduction

The number of hydrogen-bonding donor and acceptor sites differs among nucleic acid bases. Due to these differences, some homopolynucleotides adopt single or double helix structures, while polyG adopts quadruplex structure. The ability to form four inter-residue hydrogen bonds per guanine facilitates the formation of a quadruplex structure, referred to as G-quartet (Figure 9-14), as first suggested[312] by Davies *et al.* in 1962. The cyclic inter-residue hydrogen bonding pattern stabilizing the G-quartet is achieved from interactions between

$N_{(1)}H$ and $C_{(2)}$-N-H of one residue with $C_{(6)}$=O and $N_{(7)}$ respectively of another residue.

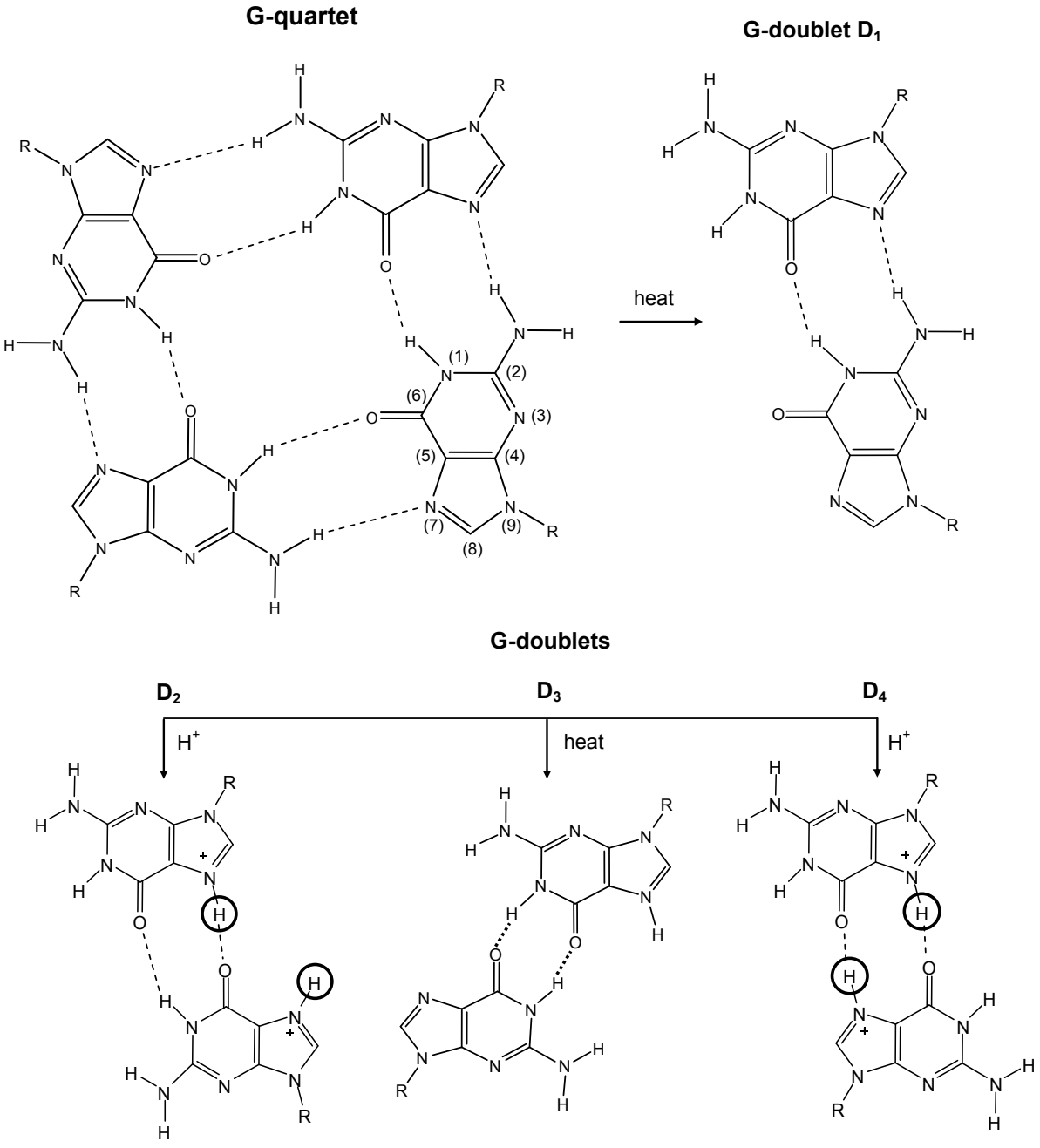

Figure 9-14: The structure and hydrogen-bonding pattern of the G-quartet and G-doublets (D_1-D_4). The doublets result from disruption of hydrogen bonding within the G-quartet either via heating or protonation.

The quartet layer formed from the four guanine residues leads to the presence of a cavity in the center of quartet. On the basis of X-ray fiber diffraction data, Zimmerman *et al.*[313] have proposed a four-stranded helical structure for polyG with twisting of backbone in the stacked G-quartet layers. Another X-ray study done by Arnott *et al.*[314] has revealed a slight tilt, 8.9°, of hydrogen-bonded bases relative to the helix axis. Later additional investigations including X-ray analysis[315,316], electronic circular dichroism (ECD)[317-319], infrared (IR)[307,320-322], Raman[323,324], NMR[325], and fluorescence[326] have lead to the consensus that polyG exists as a parallel four-stranded right-handed helix in the neutral pH range and at ambient temperature. Molecular dynamics studies[327] have indicated that G-quadruplex structure is further stabilized by cations (Na^+) present in the cavity area of the G-quartets.

The increased interest in G-quadruplex structure results from the observations that G-rich nucleic acids forming quadruplex structure assume important functions with chromosomal telomeres[328], immunoglobulin switch regions[329], and human immunodeficiency virus genome[330]. Further, polyG has been reported[331] to inhibit the replication of murine leukemia virus in cultured cells. It was also reported[332] that G-quadruplex motif selectively increases the cellular uptake of certain oligonucleotides in the brain cortex, which could prove to be useful in the application of therapeutic oligonucleotides in neurological diseases. The G-quadruplex has been additionally implicated[333,334] in the field of anticancer drug design, since it appears to induce selective apoptosis of certain tumor cells. Expression of several tumor cell oncogenes, such as *c-Myc*[335] and *c-*

Kit[336], can be suppressed via stabilization of G-quadruplex structure. G-quadruplex has also been proposed[337,338] as a building block for molecular nanowires in nanoelectronics. The recognition of potential for these versatile applications has instigated many structural investigations in an effort towards establishing the structure-function relationship.

It is of interest to note that the literature measurements on physico-chemical properties of polyG have displayed some inconsistencies. Howard *et al*.[320] recognized that this homopolynucleotide undergoes a slow transition from metastable to stable state. The duration[318,320] of the transition at ambient temperature was reported to be several days. The inconsistencies in the literature observations result, to some extent, from not realizing this transition and carrying-out studies at different time points during the transition process. According to Howard *et al*., commercially available lyophilized polyG is received in a metastable form.

The conversion from a metastable to stable form was deduced[9] from IR spectral studies. Three time dependent IR spectral changes have been noted for polyG. a) First the carbonyl IR absorption band, initially observed at higher frequency (~1695-1686 cm^{-1}), representing a metastable form, becomes shifted to a lower frequency (~ 1674-1667 cm^{-1}), representing the stable form. b) Second, a weak IR absorption band at ~1610 cm^{-1} disappears at a more rapid rate than the changes associated with the above mentioned carbonyl IR absorption band. c) Third, the IR absorption band at ~ 1585 cm^{-1} shifts to higher frequency of ~ 1591 cm^{-1} and increases in intensity, over the same period of time

as changes observed for the carbonyl band. The last two spectral modifications are deemed less pronounced when compared to the first one.

Using electron micrographs, Lesnik *et al*.[317] have concluded that the metastable structure represents a globular state while the stable structure represents a linearized state of polyG. Then transition from metastable to stable states involves untwisting and elongation from globular to a linear form, but both states have four-stranded helical conformation. Based on their studies Lesnik *et al.*[317] also concluded that there are a number of defective quadruplex-fibers with loops and separated end-sections resulting in single, double and triple stranded tails. It was also suggested that presence of Na^+ counterions is essential for avoiding significant defects in the quadruplex structure.

When the sample was heated to 90°C, Howard *et al*.[9] noted a shift of the carbonyl IR absorption band to 1670 cm^{-1}, after which cooling to 30°C has brought back this band position to 1672 cm^{-1}. Although the consequence of heating the sample is thought to result in a more rapid frequency shift in the direction designating the stable form, it is not clear if heating to such a high temperature will not result in some irreversible disruptions of the four stranded helix. Reports[317,318] by Lesnik *et al.* seem to put at question the statement[320] that the function of heating is merely to accelerate a very slow process of conversion from metastable to stable form. Based on the evidence provided by electron micrographs[317], heating for 30 minutes at 80°C in D_2O leads to the formation of extended double-stranded segments. Thus heating may result in mixture of both duplex and quadruplex polyG structures. From hydrogen-tritium exchange

investigation[318], there is an indication that even in the temperature range from 40 to 55°C polyG is converted into another structural form, possibly a double-stranded helix.

Literature reports indicate that structural transition of polyG from quadruplex to duplex occurs not only upon increase of temperature but also upon decrease of pH below 4.2. Based on ECD[317] and spectrophotometric titration curves[326], polyG was suggested to be in the protonated double-stranded form at pH < 3.5. Protonation of bases occurs at atom $N_{(7)}$. The ECD spectra suggested that the different duplex forms obtained by different mechanisms (temperature vs. pH) may be characterized by different hydrogen bonding arrangements between bases. The effect of pH on conversion from metastable to stable form is such[320] that this conversion at higher pH of 8.5 seems to be slower than at lower pH of 4.5. Since the pK_a of polyG is 4.2, the more rapid conversion at lower pH could be associated with protonation-induced conversion of a four-stranded helix into a two-stranded structure. Nevertheless, polyG should exist in the quadruplex form at pH > 5. In highly alkaline solution (pK_a = 11.2), polyG was suggested[339] to exist in a disordered single-stranded form.

Despite the existence of abundant IR and ECD spectral data on polyG, vibrational circular dichroism (VCD) spectroscopic investigations[258,263,299] on this homopolynucleotide have not been systematic and complete. Although literature VCD reports on polyG have appeared after the reported[9] conversion from metastable-to-stable form, the reported VCD spectra appeared to have been measured either before the stable form has been achieved or during the initial

stages of conversion process. This is because, the carbonyl absorption band is displayed[299] to center at 1684 cm^{-1}, which is closer to the frequency-range of metastable state. The time and temperature dependent VCD studies and systematic VCD studies at different pH values, probing structural transitions in polyG, have not been reported before. The VCD spectra representing the stable state of polyG have not been reported either.

Previously we have reported IR and VCD spectral studies on polyA[305] and polyC[340], where spectra have been monitored systematically as a function of pH and temperature. From these studies we have identified the key IR and VCD signatures for single and double helical structures of these two homopolynucleotides. In this manuscript we report the first systematic time, temperature and pH dependent VCD spectral studies on polyG to understand the structural transitions of polyG.

Experimental Section

Measurements: The polyriboguanylic acid (polyG) potassium salt (P4404) and D-(+)-trehalose were obtained from Sigma Chemical Co. and have been used as received. D_2O was obtained from Cambridge Isotope Laboratories, Inc.

Solution samples, at a final concentration of ~ 30 mg/mL in D_2O, were prepared by dissolving polyG in buffered solutions containing 0.1 M NaCl. The 50mM cacodylate buffer was used for obtaining pH ~ 6.4, while the 50mM citrate buffer was used for obtaining pH ~ 3.1. A glass-body liquid-filled micro-combination pH electrode was used for all pH readings. The pH readings

reported here are not those of buffers, but are those of final polyG solutions in appropriate buffer. The cacodylate buffer was prepared at pH ~ 8.0 and when polyG was added to this buffer, solution with a final pH ~ 6.4 was obtained. The citrate buffer was prepared at pH ~ 3.0 and when polyG was added to this buffer, solution with a final pH ~ 3.1 was obtained. These pH readings have not been corrected for deuterium effect [pD = pH(meter) + 0.4][306].

IR and VCD spectra of polyG solutions have been measured as a function of time and temperature. Time periods at which measurements have been conducted were 0, 5 and 10 days. During the waiting period, sample was held in a desiccator in order to minimize hydrogen-deuterium exchange with atmospheric H_2O. Temperature dependent measurements have been conducted at 22°C, 40°C, 60°C and 80°C. Heating was accomplished by holding the sample in a variable temperature cell. The temperatures were read with a thermocouple embedded in the cell. After the heating process, the heater was turned off and sample was allowed to cool back to 22°C. Spectral measurements conducted after cooling have been used to establish if the heat-induced spectral changes are reversible.

IR and VCD measurements were obtained on a modified[15] ChiralIR (Bomem-Biotools, Canada) instrument. All VCD spectra were recorded at 8 cm^{-1} resolution with 1 hr data collection time. The sample was held in a demountable cell with CaF_2 windows and a 50 μm Teflon spacer. Baseline corrections for all absorption (or VCD) spectra were done by subtracting the absorption (or VCD) of the buffered D_2O solvent, containing NaCl. VCD spectra were also obtained for

the polyG film samples following the procedures of polyA and polyC studies conducted previously[305,340] in our lab, but they are not reported due to the poor-quality of the VCD spectra obtained for polyG films.

Calculations: Calculations of vibrational frequencies, absorption and VCD intensities have been performed on three theoretical models: one quadruplex and two duplex models of polyG (Figure 9-15). The models were obtained by taking a high resolution X-ray crystal structure data[316] and truncating the helix into two G-quartet layers for the quadruplex model and four G-doublet layers for the duplex models. Additionally, the ribose-phosphate backbone has been removed, and hydrogen atoms added to satisfy the valence of carbon atoms where backbone was removed. The amine hydrogen atoms have been replaced by deuterium atoms to reflect the experimental measurements in D_2O. Thus the coupling between C=O stretching and C-N-H bending deformations is not present in the theoretical calculations, as is also the case for experimental measurements in D_2O.

All theoretical calculations have been performed at B3LYP/6-31G* level of theory. With 1400 basis functions, these calculations are among the largest VCD calculations[341] ever reported. The computed vibrational frequencies have been scaled with 0.9613 as recommended[148] for 6-31G* basis set. The theoretical spectra were simulated with Lorentzian band shapes and 20 cm^{-1} half-width at one-half of the peak height.

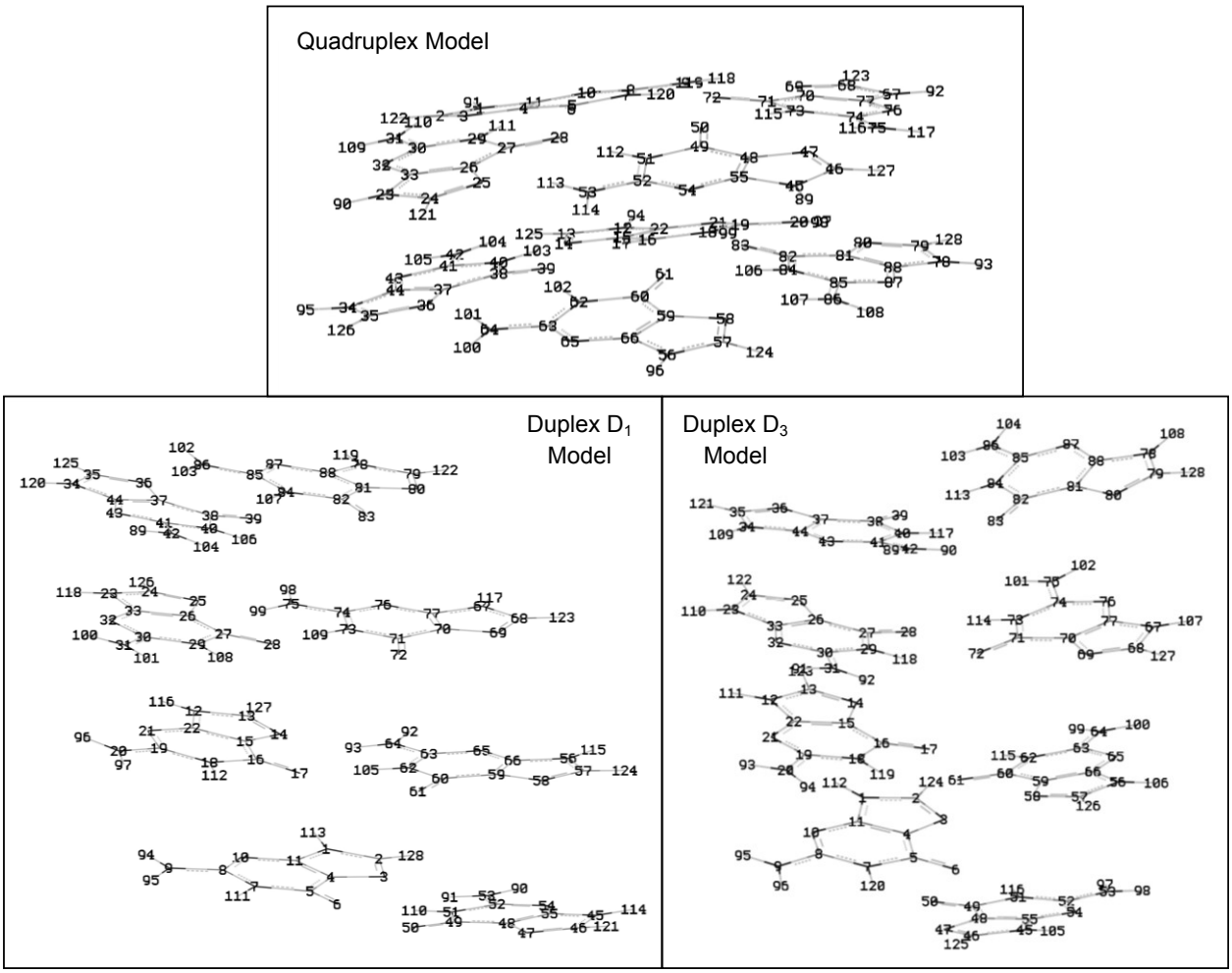

Figure 9-15: Quadruplex model (top panel) composed of two layers of G-quartets and two duplex models (bottom panels) composed of four-layers of G-doublets with conformations D_1 and D_3.

Results and Discussion

The experimental vibrational infrared absorption and VCD spectra as a function of waiting-time at different pH values and as a function of temperature are shown in Figures 9-16 to 9-18. Figure 9-16 displays time-propagated spectral features, while Figures 9-17 and 9-18 display temperature-propagated spectra at a specified waiting time and pH. In all cases, the absorption spectra exhibit four main bands, labeled as I-IV. Bands I, II and III undergo both time and

temperature dependent modifications while band IV does not. The spectral modifications induced in two different ways (time vs. temperature) appear in many ways similar when absorption spectra are considered, but some differences are apparent when VCD spectra are considered.

Based on[307] the normal mode assignments for guanine, the absorption band I is believed to originate from C=O bond stretching, while bands II, III, and IV arise from coupled vibrational motions predominantly involving groups C=C/C-C and C=N/C-N. At pH 6.4, band I propagates from 1689 cm^{-1} to 1682 cm^{-1} during the 5 day waiting period (Figure 9-16A). No additional modifications were found in the spectra obtained after 10 days. Based on a previous report[320], it takes approximately a week for polyG quadruplex to convert spontaneously from metastable to stable form. Since the present results show no noticeable spectral differences between 5 and 10 days, it is possible that at pH 6.4 and at polyG concentration used here the conversion is completed within 5 days or less. As mentioned in the introduction, the conversion process can be viewed as linearization of the initially globular polyG quadruplex form. Frequency-downshift of band I can be regarded as the marker of this conversion. A positive VCD couplet, at 1689 cm^{-1}(–)/1674 cm^{-1}(+), with positive VCD on the lower frequency side and negative VCD on the higher frequency side of absorption band, associated with absorption band I accordingly follows the frequency downshift of band I as the stabilization process takes place. There seems to be an indication of an additional weak VCD couplet associated with band II at 1612 cm^{-1} in 0 day measurement. This couplet diminishes as the stabilization proceeds to 5^{th} and

10^{th} day. Band III also undergoes a noticeable change with respect to time that can be correlated to stabilization and linearization of polyG. This change is evidenced by the frequency up-shift from 1581 to 1585 cm^{-1}. The absorption band III at pH 6.4 is not associated with any discernable VCD signal at any time during the stabilization process.

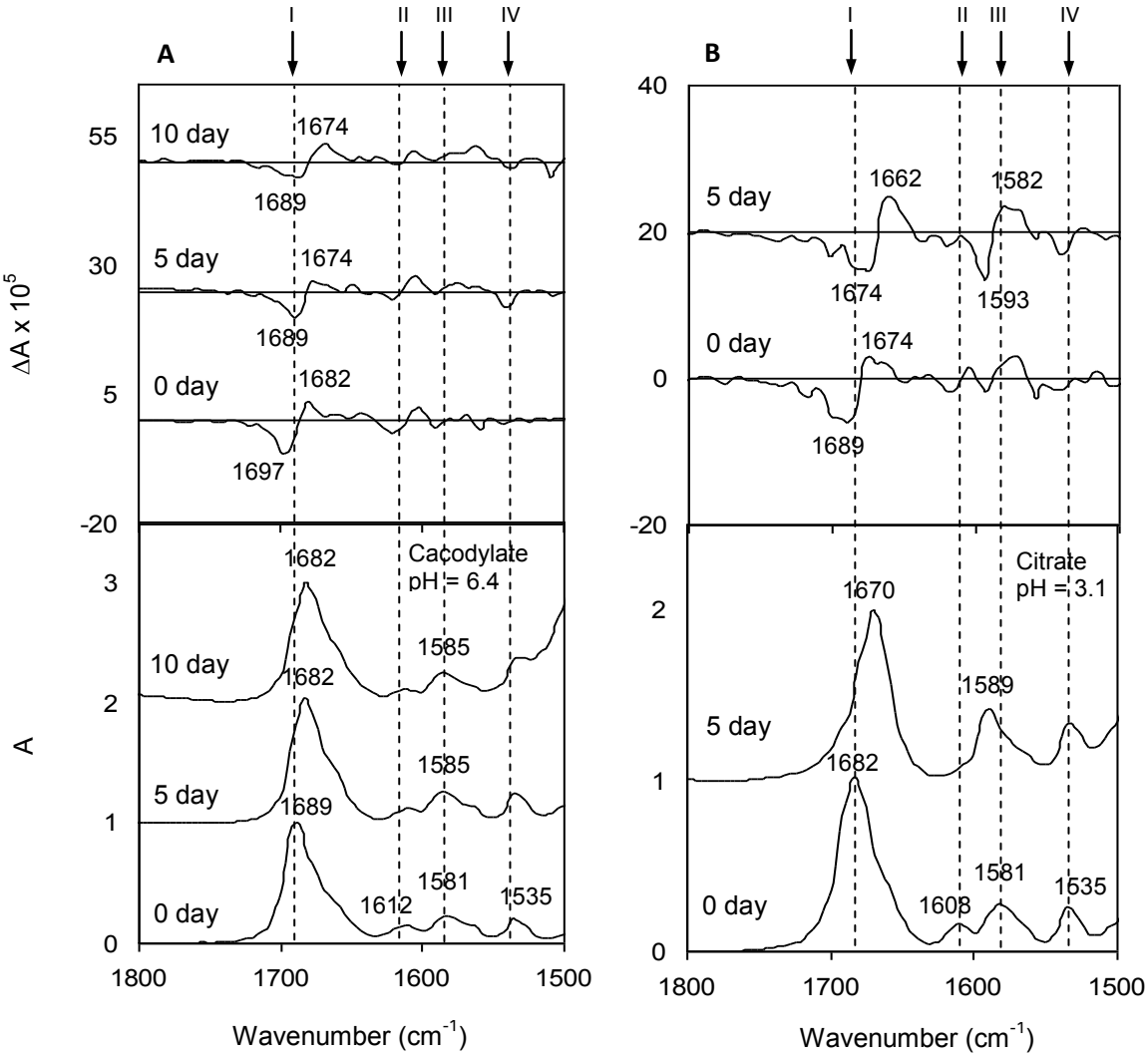

Figure 9-16: Time-propagated absorption (bottom) and VCD (top) spectra, of polyG at pH = 6.4 and pH = 3.1 given in panels A and B respectively.

Time-dependent spectral changes seen at pH 3.1 differ from those at pH 6.4, especially when VCD feature associated with band III (Figure 9-16B) is considered. The most noteworthy spectral behavior at pH 3.1 is associated with band III. Similar to what happens at pH 6.4, band III becomes up-shifted in frequency (from 1581 to 1589 cm^{-1}) in acidic environment. However, unlike the absence of VCD signal associated with band III at pH 6.4, band III develops a discernable positive VCD couplet, at 1593 cm^{-1}(–)/1582 cm^{-1}(+), within 5 days at pH 3.1. Since pH 3.1 favors the $N_{(7)}$-protonated double-helical form of polyG, we believe that the development of an additional VCD couplet at band III marks the disassembly of quadruplex into a duplex form. Therefore, the spectra of polyG at pH 3.1 obtained on 5^{th} day may reflect all duplex structure. Although the absorption band I at 1682 cm^{-1} and its corresponding VCD couplet, at 1689 cm^{-1}(–)/1674 cm^{-1}(+), become downshifted in frequency with passage of time, this shift spans wider frequency range at pH 3.1, (absorption band from 1682 to 1670 cm^{-1} and VCD couplet from 1689(–)/1674(+) to 1674(–)/1662(+)).The intensity of absorption band II decreases as polyG at acidic pH becomes stabilized in time. In comparison, this band doesn't undergo any noticeable change at pH 6.4.

Thus, while spectral changes with passage of time at pH 6.4 reflect conversion from metastable to stable quadruplex form, those at pH 3.1 reflect conversion from quadruplex to duplex form. At pH 3.1 and 0^{th} day, the positive VCD couplet of absorption band I at 1682 cm^{-1} is associated with the quadruplex structure. At pH 3.1 and fifth day, the positive VCD couplets of absorption bands I and III, at 1670 and 1589 cm^{-1}, are associated with duplex structure. This means

that both quadruplex and duplex structures yield positive VCD couplets for band I, while the duplex also yields an additional positive couplet for band III. This difference may be used to distinguish between quadruplex and duplex structures of polyG.

Based on normal mode vibrational assignments[307] of the guanine residue, band III originates from predominantly $N_{(3)}$-$C_{(4)}$ as well as $C_{(4)}$-$C_{(5)}$ bond stretching. Since the origin of band III involves stretching of an N-C bond, it is likely that this vibrational motion also involves $N_{(7)}$-$C_{(5)}$ and $N_{(7)}$=$C_{(8)}$ bond stretching. This vibrational origin assignment may explain how spectral changes associated with band III parallel structural conversion from quadruplex to duplex polyG form. Specifically, protonation of $N_{(7)}$ in an acidic environment disrupts hydrogen bonding established between $N_{(7)}$ and NH_2 group in quadruplex. As a result of the absence of the hydrogen bonding, force constants associated with bonds between $N_{(7)}$-$C_{(5)}$ and $N_{(7)}$=$C_{(8)}$ increase, causing the frequency position of corresponding band III to increase with passage of time.

Figure 9-17 displays progression of spectral features at pH 6.4 with respect to temperature increase. Here three different solutions were prepared and one was investigated right away (0 day), the second was investigated during fifth day (5 day) and the third was investigated during tenth day (10 day). Designations A, B, and C reflect 0, 5 and 10 day waiting periods, respectively. When comparing the spectra obtained initially at 22°C with those obtained at the same temperature after heating cycle, irreversible spectral changes can be seen. Regardless of the time allowed to elapse (0, 5 or 10 days) before making the first

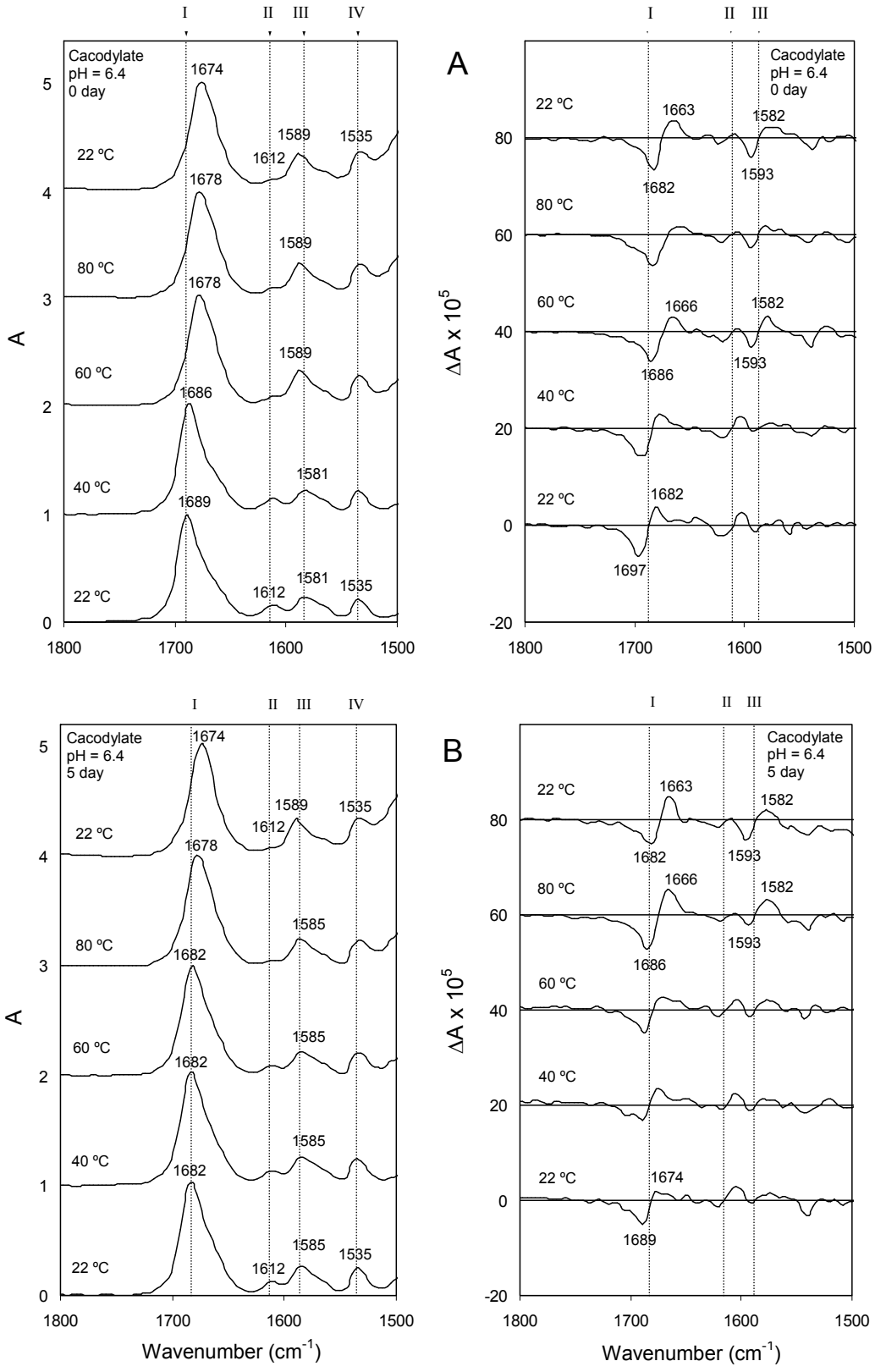

Figure 9-17: Temperature-propagated absorption (left panels) and VCD (right panels) spectra, of polyG at pH = 6.4. Panels labeled A, B, and C are for 0, 5, and 10 day waiting period.

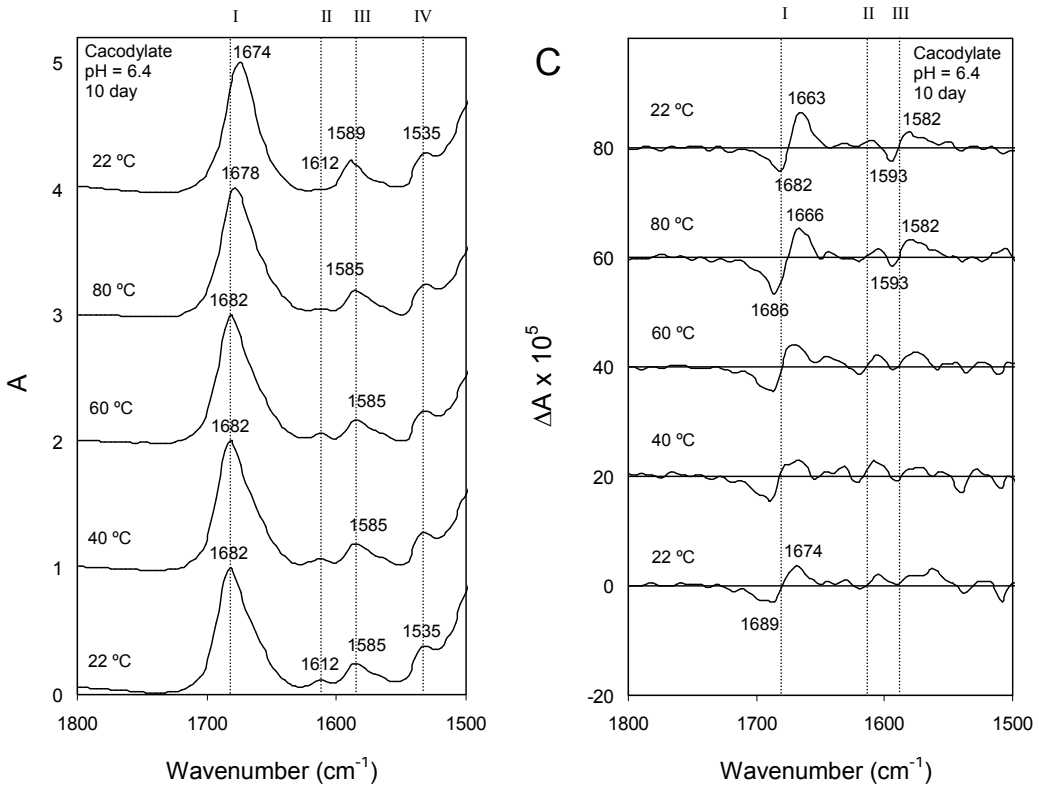

Figure 9-17, cont.

spectral measurement, the manner in which the heat-induced modifications appear is similar. As the temperature is increased, absorption band I (and associated VCD couplet) down-shifts in frequency, band II slightly decreases in intensity, and band III up-shifts in frequency. The only differences in the spectra of the three time passage conditions are the initial frequency positions of I and III. For the absorption spectra, heat induced modifications are similar to the ones induced by time passage. However, VCD features disclose that the changes resulting from heating and time passage are not entirely the same.

In terms of VCD features, signals associated with bands I and II undergo the same type of changes with the aid of heating as changes observed with the passage of time at a given pH. The VCD couplet of band I becomes down-shifted

in frequency as temperature is increased and a weak couplet associated with band II looses in its intensity. However, unlike the absence of any VCD signal for absorption band III with passage of time at pH 6.4, the temperature increase influences the VCD associated with band III as it develops a weak positive VCD couplet with temperature increase. Although its intensity is weaker, the VCD couplet associated with band III is reminiscent of the one at pH 3.1 that was identified earlier as a marker of a double-helical structure. Therefore, it can be surmised that as polyG goes through the heating process its quadruplex form becomes disrupted into a duplex form, especially when it has been subjected to 80^{o}C and cooled back to room temperature. The extent of duplex generated by heating at pH 6.4 is most likely smaller than that obtained without heating at pH 3.1, because VCD couplet of band III is weaker in the former case. Time passage alone at pH 6.4 does not lead to duplex form, but heating without regard to the waiting period does result in duplex form as can be seen from the development of VCD couplet for band III in Figure 9-17A-C.

Figure 9-18 displays progression of spectral changes at pH 3.1 with respect to temperature increase. Designations A and B reflect zero and fifth day waiting periods, respectively. While spectra do undergo heat induced modifications during 0th day condition, all spectral changes cease to exist during fifth day. As a result, heating induces no further changes in the spectra taken during fifth day at pH 3.1. Specifically, both absorption and VCD spectra obtained at the end of heating cycle on 0th day are essentially identical to traces obtained

during the 5th day. Thus the structure of polyG in acidic (pH=3.1) environment stabilizes by fifth day of waiting.

We therefore conclude that when polyG is in an acidic (pH=3.1) environment, heating only accelerates the conversion to the stable acidic form (duplex structure) that could otherwise be obtained with passage of time. When polyG is near (pH=6.4) neutral environment, passage of time leads to conversion from metastable to stable quadruplex from, but heating at this pH certainly induces the formation of duplex structure which would not be obtained simply by the passage of time.

The present VCD results can be compared to those published by Annamalai *et al.*[299] and Xiang *et al.*[263]. None of these earlier studies acknowledged that the conversion from metastable to stable form has been taken into account in designing their experiments. Based on the displayed frequency positions[263,299] of band I at 1684 cm^{-1} and 1688 cm^{-1}, in the study of Annamalai *et al.* and Xiang *et al.*, we can conclude that their absorption and VCD measurements have been recorded while polyG was in a metastable form. VCD spectra by Annamalai *et al.* appear to have non-negligible noise level, making the validity of what appears as a negative VCD signal, on the lower frequency side of the positive couplet, uncertain. Our spectra do not provide evidence for the existence of this negative signal in that region. Study done by Xiang *et al.* has presented absorption and VCD spectra under two different conditions: first, at pH 3.5 and 10°C after quickly heating to 70°C; second, at pH 7.0 and 20°C. But based on the present observations, since quick heating to

70°C does not guarantee complete structural conversion and since near neutral pH it takes several days to complete structural conversion, the results of Xing *et al.* do not represent stable structure of polyG.

Xiang *et al.* have also presented calculated spectra of the polyG quadruplex with degenerate extended coupled oscillator model. However, the predicted VCD spectrum does not exhibit a satisfactory match with the experimental spectra under both conditions, thus leading to no concrete conclusions. Finally, a VCD investigation[32] by Self *et al.* presents comparison of calculated spectra obtained with DeVoe polarizability model with experimental spectra obtained by Annamalai *et al.* This study suggested that the best match with experimental spectrum is obtained when calculated spectrum is presented as a weighted average of 80% right-handed single stranded and 20% left-handed four stranded polyG forms. However, the suggestion for polyG to be predominantly in a single stranded form is disputable, since most of the published studies, regardless of the method, show evidence for polyG existing in predominantly quadruplex form.

The experimental VCD results of the present polyG investigation indicate that the key spectral-signature for the quadruplex form is a single positive VCD couplet at higher frequency, while the spectral-signature for a duplex form contains an additional positive VCD couplet at a lower frequency. These features have to be reproduced by any successful calculation. It is to be noted that for homopolyribonucleotides, the VCD spectral signature for a particular type of structure can depend on the constituent nucleic acid base (see Table 9-4).

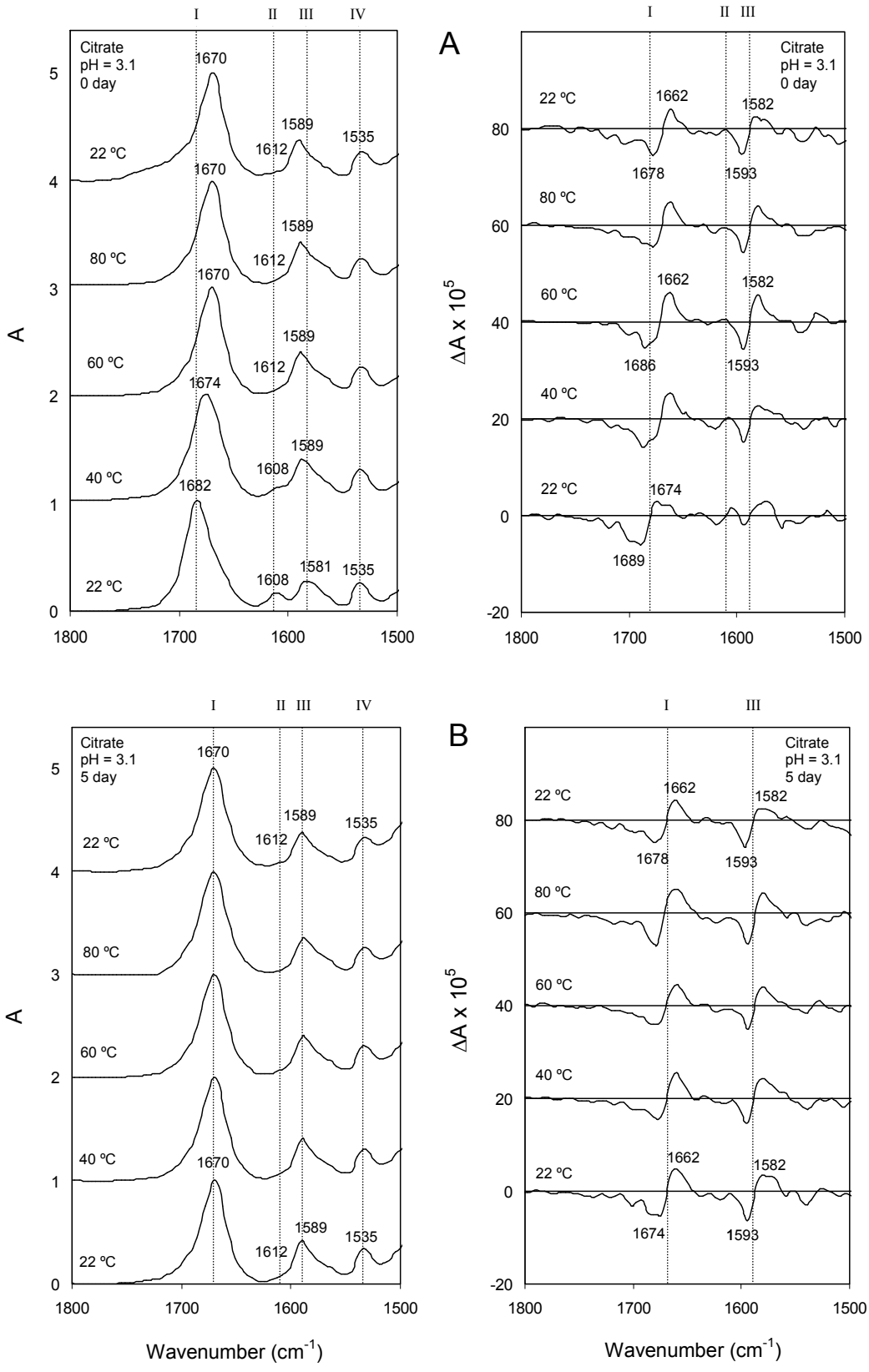

Figure 9-18: Temperature-propagated absorption (left) and VCD (right) spectra of polyG at pH = 3.1. Panels labeled A and B are for 0 and 5 day waiting period.

Table 9-4: VCD signatures of helical structures in different homopolyribonucleotides.[a]

	polyA	polyC	polyG	polyI
Single helix	1636(–)/1623(+)	1662(–)/1647(+)	N/A	N/A
Double helix	1670(–)/1659(+)	1697(+)/1678(–)	1593(–)/1582(+)	N/A
Quadruplex	N/A	N/A	1689(–)/1674(+)	1690(–)/1678(+)

[a]N/A stands for "not applicable"

In the case of polyA, double helical form is identified[33] by the development, at lower pH, of a positive VCD couplet [with negative lobe at 1670 cm^{-1} and positive lobe at 1659 cm^{-1}]. In the case of polyC, double helical form is identified[34] by the development, at lower pH, of a negative VCD couplet [with positive lobe at 1697 cm^{-1} and negative lobe at 1678 cm^{-1}]. However, the double helical form of polyG is identified by the development, at lower pH, of positive couplet [with negative lobe at 1593 cm^{-1} and positive lobe at 1582 cm^{-1}]. Positive VCD couplets are also associated with quadruplex structure of polyG [negative lobe at 1689 cm^{-1} and positive lobe at 1674 cm^{-1} for the stable form,] and of polyI[39] [negative lobe at 1690 cm^{-1} and positive lobe at 1678 cm^{-1}]. The data in Table 9-4 indicate that VCD signatures in the 1800-1500 cm^{-1} region for polyA, polyC and polyG duplexes are not all the same. This observation may not be surprising since the vibrational modes giving rise to VCD signals in the investigated region are associated with nucleic acid bases, rather than with the ribose-phosphate backbone, which is the common structural feature for homopolyribonucleotides considered.

Quantum mechanical calculations: Due to the ambiguity in the literature calculations concerning the polyG structural investigation, we have undertaken quantum mechanical predictions in order to correlate theoretical VCD spectra for quadruplex and duplex models with what we experimentally interpreted as quadruplex and duplex VCD signatures.

The models for theoretical investigation are displayed in Figure 9-15. For the quadruplex model, two G-quartet layers have been extracted from the reported X-ray crystallographic data[316]. For the two duplex models, four layers have been extracted with each layer containing two guanine bases (G-doublet). The four possible duplex conformational variations in cross-sectional layers are shown in Figure 9-14. Among these, G-doublets designated as D_1 and D_3 have been considered for modeling. These two layer-structures are the most likely ones to result from heat-induced quadruplex dissociation into a duplex. The doublet D_1 results from breaking the hydrogen bonds between two pairs of adjacent doublets in the G-quartet. Doublet D_3 results from breaking all hydrogen bonds of the G-quartet and bringing the two diagonal guanine units closer to form hydrogen bonding between these two diagonal bases. Although doublets D_2 and D_4 are plausible, they involve not only $N_{(7)}$ protonation but also reorientation of guanine bases. Since D_2 and D_4 doublets necessitate protonation, their consideration would not be appropriate for describing the duplex formed as a result of heating near neutral pH. Additionally, since the experimental VCD signatures for the duplex are the same regardless of the perturbation (temperature and pH), the computations undertaken on D_1 and D_3 are deemed

sufficient for obtaining representative theoretical VCD spectra for the polyG duplex.

It is necessary to acknowledge that the models used here are not the most optimal due to the necessity to truncate the homopolynucleotide (by removing sugar-phosphate backbone) and to consider either two or four layers only. The truncation was necessary because of high computational demand for the quantum mechanical calculations of vibrational properties. The optical activity of polyG helices arises from twisting among consecutive G-quartet or G-doublet layers. Although this twist is duplicated from crystal structure into both quadrupex and duplex theoretical models, some of the contribution to the vibrational chiroptical response from sugar-phosphate backbone has been lost as a result of the truncation. It is to be noted that the structural information obtained from crystal structure was used as such and no attempts were made to optimize the geometries. This is because any geometry optimization, in the absence of sugar-phosphate back bone, can result in planar structure for G-quartets with no helicity among the G-quartet layers, leading to unreasonable quadruplex and duplex models.

The theoretically predicted VCD spectra along with the corresponding absorption spectra are shown in Figure 9-19. The theoretical VCD signature for quadruplex is given by a single positive couplet, with a positive lobe at ~ 1545 cm^{-1} and a negative lobe at ~ 1614 cm^{-1}. On the higher frequency side of this positive couplet there is an additional positive signal at ~ 1686 cm^{-1}. The theoretical signatures for the two duplex models closely resemble each other and

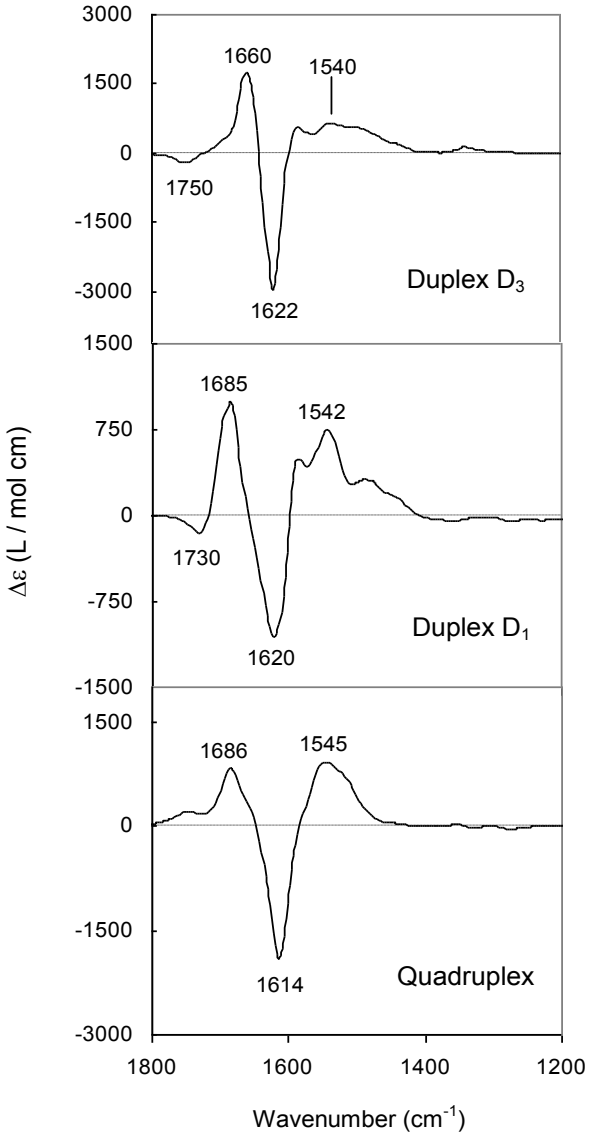

Figure 9-19: Predicted VCD spectra for the quadruplex and two duplex models of polyG, obtained via B3LYP/6-31G* level of theory.

both contain two positive couplet contributions. Based on the predicted Gibbs free energies, however, the duplex associated with D_1 conformation is ~ 21 kcal/mol more stable than the one with the D_3 conformation. For duplex with D_1 layer conformation, the lower frequency couplet has a positive lobe at ~ 1542 cm^{-1} and a negative lobe at ~ 1620 cm^{-1}, while the higher frequency couplet has a

positive lobe at ~ 1685 cm^{-1} and a negative lobe at ~ 1730 cm^{-1}. For duplex with D_3 layer conformation, the lower frequency couplet has a positive lobe at ~ 1540 cm^{-1} and a negative lobe at ~ 1622 cm^{-1}, while the higher frequency couplet has a positive lobe at ~ 1660 cm^{-1} and a negative lobe at ~ 1750 cm^{-1}. The dominant vibrational contributions giving rise to the theoretically observed VCD signals are summarized in Table 9-5 with the corresponding numerical atom designations given in Figure 9-15.

The discrepancy between the theoretical and experimental quadruplex VCD signatures is an additional positive VCD band present in the theoretical spectra. The discrepancy between the theoretical and experimental duplex VCD signatures is that the two positive couplets are not as separated as what has been observed in the experimental spectra. Also the experimental higher-frequency VCD couplet associated with band I is observed for duplex at a lower frequency position than that for quadruplex. But reverse trend is seen in the predicted VCD spectra. Two possible justifications for these discrepancies are the use of: a) truncated polyG model without sugar-phosphate backbone; b) crystal geometry, rather than optimized geometry, for vibrational property calculations. Nonetheless, the qualitative correlations between experimental and theoretical spectra for the key signatures of quadruplex and duplex patterns are present. The common features confirm that polyG quadruplex is marked by a single positive VCD couplet, while polyG duplex is marked by an additional positive VCD couplet.

Table 9-5: Listing of dominant vibrational origins for B3LYP/6-31G* predicted VCD signals of quadruplex, duplex D_1 and duplex D_2. For atom numbering see Figure 9-15.

Quadruplex	**Dominant Vibrational Origin**
(+) 1545 cm^{-1}	asymmetric stretching of: N(76)-C(74)-N(75), N(53)-C(52)-N(54), N(51)-C(49)=O(50); stretching of C(71)=O(72).
(–) 1614 cm^{-1}	asymmetric stretching of: N(76)-C(77)-C(70), N(54)-C(55)-C(48), N(32)-C(33)-C(26); stretching of C(55)-C(48), C(49)=O(50), N(86)-C(85), N(31)-C(30).
(+) 1686 cm^{-1}	asymmetric stretching of: C(81)-C(82)=O(83), C(70)-C(71)=O(72), C(37)-C(38)=O(39), C(15)-C(16)=O(17); stretching of C(37)-C(44), N(75)-C(74) .
Duplex D_1	**Dominant Vibrational Origin**
(+) 1542 cm^{-1}	asymmetric stretching of: N(32)-C(33)-C(26), N(43)-C(44)-C(37); stretching of N(42)-C(41).
(–) 1620 cm^{-1}	asymmetric stretching of: N(32)-C(33)-C(26), N(10)-C(11)-C(14), N(53)-C(52)-N(54); stretching of N(31)-C(30), N(64)-C(63), N(65)-C(66), C(49)=O(50).
(+) 1685 cm^{-1}	asymmetric stretching of C(48)-C(49)=O(50); stretching of N(54)-C(52).
(–) 1730 cm^{-1}	asymmetric stretching of C(15)-C(16)=O(17).
Duplex D_3	**Dominant Vibrational Origin**
(+) 1540 cm^{-1}	asymmetric stretching of: N(21)-C(22)-C(15), N(43)-C(44)-C(37); stretching of N(42)-C(41).
(–) 1622 cm^{-1}	asymmetric stretching of N(21)-C(22)-C(15); stretching of N(20)-C(19), N(18)-C(16).
(+) 1660 cm^{-1}	asymmetric stretching of: C(4)-C(5)=O(6), C(48)-C(49)=O(50), C(59)-C(60)=O(61); stretching of N(65)-C(63), C(49)=O(50).
(–) 1750 cm^{-1}	asymmetric stretching of C(15)-C(16)=O(17).

Conclusion

In the present work we demonstrate how vibrational infrared absorption and VCD spectral changes correlate with structural changes of polyG as a function of time, temperature and pH. The following conclusions result from the present investigation: a) From the progression of spectral features with respect to waiting time, stabilization of the quadruplex structure at pH 6.4 (near neutral

environment) takes place within 5 days and it is most clearly evidenced by a downshift of the carbonyl absorption band (band I) and the corresponding positive VCD couplet. Time-induced spectral modifications also indicate that at pH 3.1 (acidic environment) and within a 5-day waiting period, polyG develops duplex structure. An additional positive VCD couplet associated with band III at 1589 cm^{-1} is identified as a marker of a polyG duplex. b) From the progression of spectral features with respect to temperature in a near-neutral environment, heating to 80°C certainly induces structural changes that favor the formation of a duplex. This duplex structure would not form simply by the passage of time at near-neutral pH. When polyG is in an acidic environment (pH 3.1), heating accelerates the conversion to the stable acidic form (duplex) that could otherwise be obtained with passage of time at that pH. c) Based on the comparison of experimental and theoretical VCD spectra for polyG, the key spectral-signature for the quadruplex form is a single positive VCD couplet, while the spectral-signature for a duplex form contains an additional positive VCD couplet at a lower frequency. The present investigation represents the first VCD study which conclusively establishes how changes in spectral features relate to the structural modifications of polyG. This study demonstrates that VCD serves as a sensitive tool for monitoring the structural transitions of polyG, which could prove useful to understand the structure-function relationship of other polynucleotides in future investigations.

Polyriboinosinic Acid (polyI):

Introduction

Among homopolynucleotides capable of forming unusual quadruplex structures are polyriboguanylic acid (polyG) and polyinosinic acid (polyI). The common quadruplex structural feature between polyI and polyG is expected because these two homopolynucleotides are close molecular analogs, differing only in the presence (in guanine) and the absence (in inosine) of one NH_2 group. The purine base of polyI, hypoxanthine, is a deaminated guanine. The quadruplex structure of polyG, referred to as G-quartet, is stabilized by eight hydrogen bonds. However, as hypoxanthine lacks NH_2 group at the $C_{(2)}$ position, the quadruplex structure of polyI, referred to as I-quartet, (Figure 9-20) is stabilized by only four hydrogen bonds. These hydrogen bonds occur between $N_{(1)}H$ of one base residue and $C_{(6)}$=O of neighboring base residue. As a consequence of the reduced number of hydrogen bonds in the I-quartet structure, I-quartet is anticipated to be more fragile than G-quartet structure. However, I-quartet is known to gain stability when alkali metal ions are trapped in the central cavity. Thus the stability of poly I quadruplex structure to a large extent relies on the presence of alkali metal ions and hence depends on ionic strength. It has been reported[323,342-346] that the structure of polyI quadruplex is supported in the presence of 0.1M NaCl or higher. In aqueous solutions of low ionic strength, polyI is classified as a disordered, single-stranded polynucleotide chain, containing no appreciable stacking of hypoxanthine bases and no specific base-base interactions. The single-stranded disordered structure of polyI can

also be obtained upon thermal denaturation[345] as well as deprotonation[347] of $N_{(1)}H$, which disrupts the cyclic hydrogen bonding of the I-quartet. The structural characteristics of polyI summarized above represent the consensus of literature investigations which can be traced back to as early as the 1950s. The techniques that have been employed in the past include X-ray crystallography[347,348], electron microscopy[349], calorimetry[350], infrared (IR)[293,323,351,352], Raman[323,345,346,351-354], NMR[355], optical rotatory dispersion (ORD)[342], and electronic circular dichroism (ECD)[343,344,356].

I-quartet

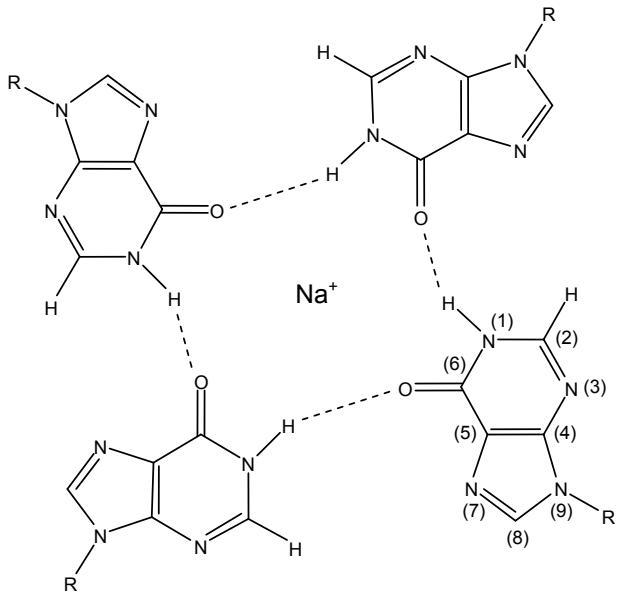

Figure 9-20: The structure and cyclic hydrogen-bonding pattern of I-quartet.

One vibrational circular dichroism (VCD) investigation[299] on polyI has been reported before by Annamalai and Keiderling. This study was however cursory in nature and detailed structural assignments or structure-related spectral interpretations were not undertaken. To fill this gap, here we report a systematic VCD investigation on polyI structure. We present, for the first time, not only VCD spectra that reflect structural changes of polyI as a function of alkali metal ion concentration, temperature and pH, but also explain how the observed changes in these spectra reflect structural changes in polyI. Spectral measurements and structural interpretations have been undertaken for both solution- and film-based samples of polyI.

Experimental Section

The polyI potassium salt (P4154) and D(+)-trehalose were obtained from Sigma Chemical Co. and have been used as received. D_2O was obtained from Cambridge Isotope Laboratories, Inc.

Solution samples, at a final concentration of ~ 20 mg/mL in D_2O, were prepared by dissolving polyI in buffered solutions containing 1.0 M, 0.1 M or no NaCl. The 10 mM citrate buffer was used for obtaining pH ~ 6.0, while the 10 mM tris buffer was used for obtaining pH ~ 8.0. The buffer concentration was chosen such that vibrational band intensities of buffer are negligible with respect to those of polyI. The reported pH values are those of appropriate polyI solutions and not those of buffers. The citrate buffer was prepared at pH ~ 7.0 and when polyI was added to this buffer the resulting pH of polyI solution was ~ 6.0. The tris buffer

was prepared at pH ~ 10.0 and when polyI was added to this buffer the resulting pH of polyI solution was ~ 8.0. A glass-body liquid-filled micro-combination pH electrode was used for all pH readings. The pH meter readings are reported as such and no corrections for deuterium effect [pD = pH(meter) + 0.4][357] have been made.

IR and VCD spectra of polyI solutions have been measured as a function of temperature in the range from 22°C to 70°C. Heating was accomplished by holding the sample in a variable temperature cell. The temperatures were read with a thermocouple embedded in the cell. Since heat-induced spectral changes were noticed between 60°C and 70°C, an additional set of measurements has also been made at 65°C. After the heating process, sample was allowed to cool back to room temperature by letting the sample solution stand at room temperature for 1 hr.

For preparing the film samples, a drop-cast method was used, where ~200 µL of the parent H_2O solution, which contained polyI (~6 mg/mL) and trehalose (~12 mg/mL) in 10mM citrate buffer, was deposited on a 2.5 cm diameter CaF_2 window and allowed to dry at room temperature for approximately 2 hr in a fume hood, which provided a constant airflow over the sample. The purpose of adding trehalose at a mass ratio of 2:1 (trehalose/polyI) was to obtain orientationally independent VCD spectra, as described in the polyA[358] and polyC[359] studies. The film sample contained no NaCl in order to avoid its crystallization on the surface of the film. Films were tested for orientational independence by taking the spectra at two positions: an arbitrarily chosen 0° position and a position corresponding to

a 45° rotation around the light beam axis. The heating of the polyI film sample to 70°C and spectral measurements at this temperature were accomplished by holding CaF_2 window with deposited polyI film in a cell equipped with heating cartridges.

Infrared vibrational absorption and VCD measurements for both solution and film state samples were obtained on a modified[360] ChiralIR (Bomem-Biotools, Canada) instrument. All VCD spectra were recorded at 8 cm^{-1} resolution with 1 hr data collection time. The solution sample was held in a demountable cell with CaF_2 windows and a 50 μm Teflon spacer. Baseline corrections for all solution-based absorption (or VCD) spectra were done by subtracting the absorption (or VCD) of the buffered D_2O solvent, containing appropriate concentration of NaCl. Baseline for the film-based VCD spectrum was estimated.

Results and Discussion

The vibrational absorption and VCD spectra displayed in Figure 9-21 reflect heat-induced spectral changes of polyI at pH ~ 6.0, with three different alkali metal ion concentrations. Panels A, B, and C present the spectra of polyI solutions with 1.0 M, 0.1 M and 0.0 M NaCl, respectively. Spectra will be discussed in the order of decreasing ionic strength. Regardless of the alkali metal ion concentrations used, the dominant absorption band present in the ~1680 cm^{-1} region originates[345,353] from $C_{(6)}$=O stretching vibration and it gives rise to a positive VCD couplet (positive VCD on the lower frequency side and negative VCD on the higher frequency side of absorption band) at room temperature.

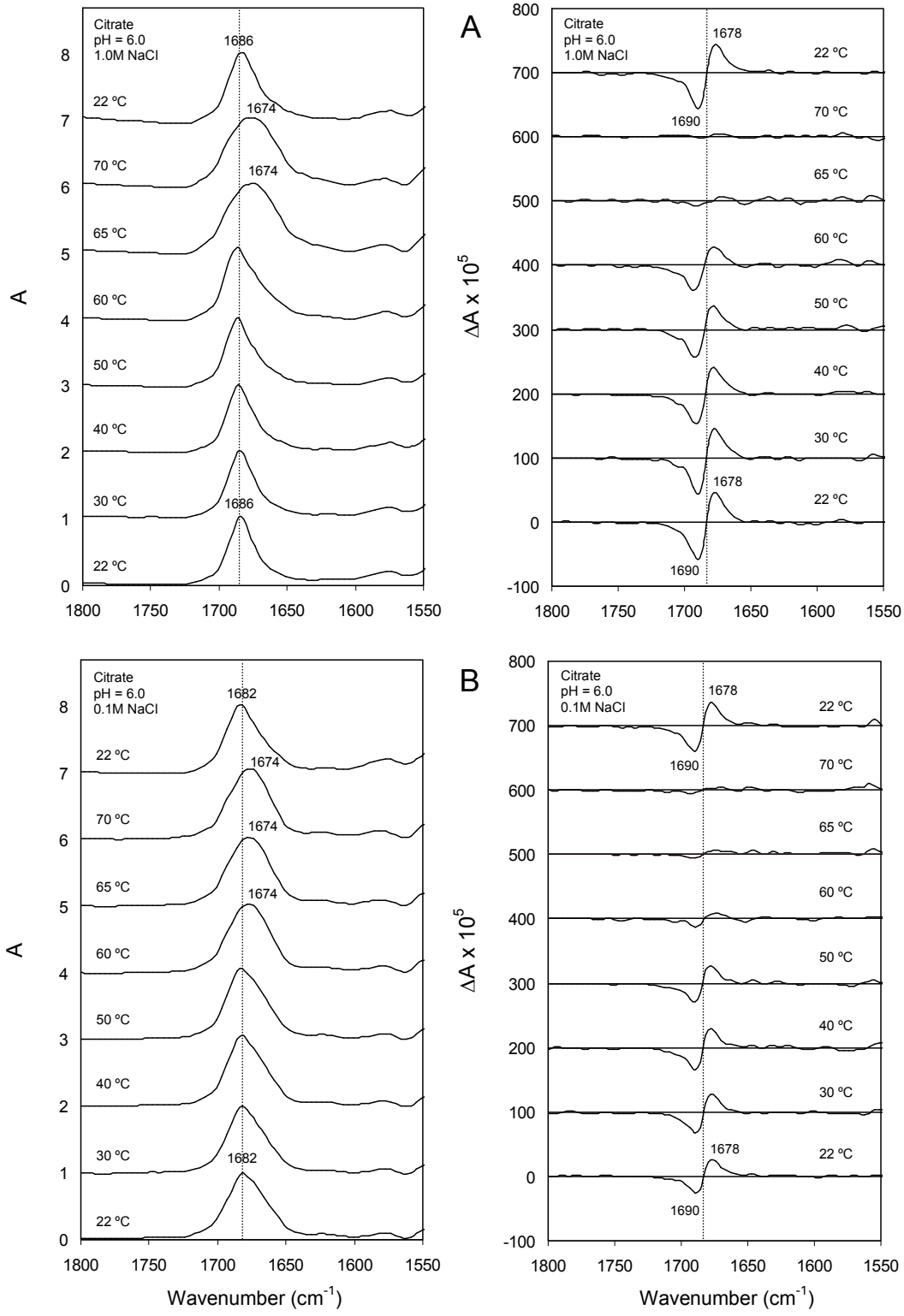

Figure 9-21: Heat-induced absorption (left) and VCD (right), spectral changes of polyl solution at pH = 6.0. NaCl concentrations associated with panels A, B, and C are 1.0M, 0.1M and 0.0M NaCl respectively.

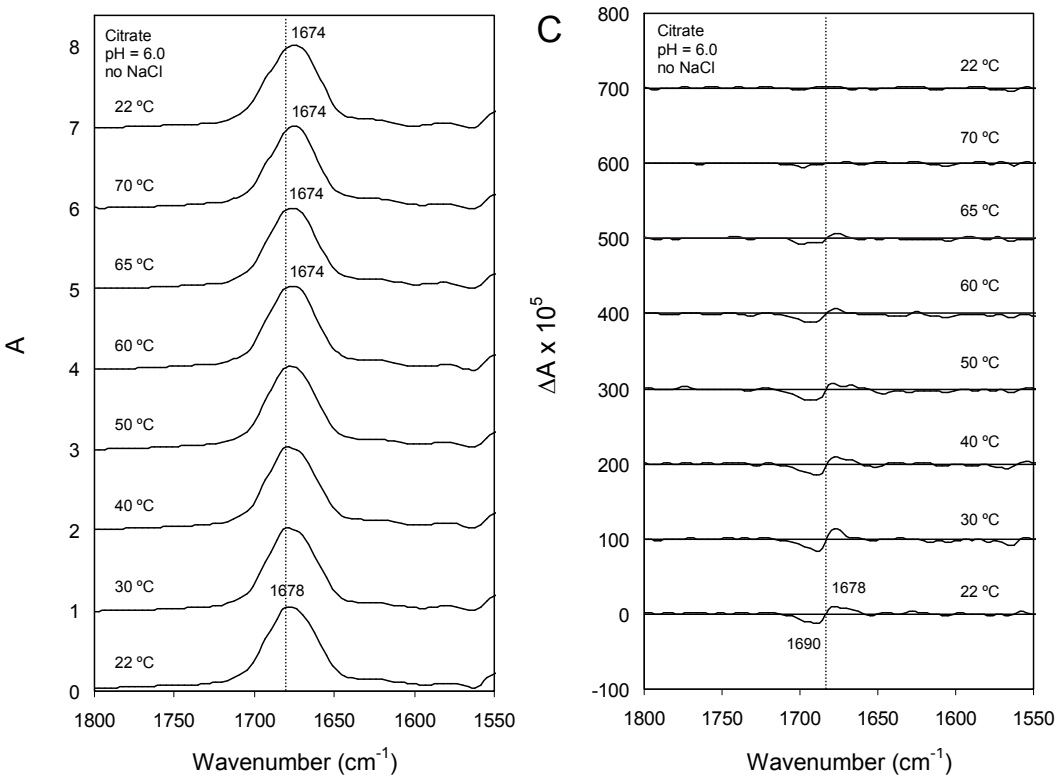

Figure 9-21, cont.

In Figure 9-21A, this absorption band undergoes a downshift in frequency from ~ 1686 cm^{-1} at 22°C to 1674 cm^{-1} at 65°C. The absorption band shape also changes with increasing temperature, as this band becomes broader at 65°C. The down shifted band position prevails as the temperature is increased to 70°C. Note that during the gradual heating the original frequency position remains unchanged up to 60°C and then undergoes a 12 cm^{-1} downshift at 65°C, indicating a fairly sudden structural change. Since heating is expected to unfold the quadrupelx via disruption of the cyclic hydrogen bonding of the I-quartet, one would expect an upshift rather than the observed downshift of the carbonyl stretching mode. However, as the qudruplex structure unwinds, the base

residues become susceptible to hydrogen bonding with the surrounding D_2O molecules and this may decrease the force constant of the $C_{(6)}$=O group.

The spectral changes observed for absorption are paralleled by those for VCD. However, VCD spectral changes display higher sensitivity to the heat-induced structural modification. The positive VCD couplet, 1690 cm^{-1}(–)/1678 cm^{-1}(+), which prevails up to 60°C, essentially vanishes at 65°C. This VCD spectral change is more striking than the downshift and broadening observed for the corresponding absorption band at 1686 cm^{-1}. The abrupt VCD intensity loss, accompanied by the downshift of the corresponding absorption band, can be associated with heat-induced disruption of polyI quadruplex. The positive VCD couplet associated with the carbonyl vibrational band is considered to be the VCD signature of the polyI quadruplex structure, as was also the case[23] for quadruplex structure of polyG. The fact that the VCD couplet marking the quadruplex structure disappears with heating indicates that once the hydrogen-bonding of the I-quartet is disrupted, the helical structure and global chirality associated with the backbone-propagated twisting of stacked bases is lost. Furthermore as no other VCD signal emerges, the newly formed structure can be considered to be fairly disordered with no helical-chirality.

The heat-induced spectral changes seen for solution containing 0.1 M NaCl (Figure 9-21B) are similar to those seen for solution containing 1 M NaCl (Figure 9-21A): the carbonyl absorption band becomes downshifted in frequency and the corresponding positive VCD couplet loses its intensity as the temperature is increased to 60°C. However, the threshold temperature at which

abrupt changes occur is 60°C for 0.1M NaCl solution (Figure 9-21B), as opposed to 65°C for 1 M NaCl solution. This spectral behavior signifies that, in the heating process, quadruplex loses its structural support sooner at lower alkali metal ion concentration than that at higher alkali metal ion concentration.

In the absence of alkali metal ions (Figure 9-21C), the position of carbonyl absorption band at room temperature is lower in frequency and it undergoes a smaller heat-induced downshift, while the corresponding positive VCD couplet is much weaker in intensity. In fact the positive VCD couplet observed at room temperature is essentially as diminished as the positive VCD couplet observed for 0.1 M NaCl solution at 60°C. In the absence of coordination with cations in solution, the quadruplex is either no longer stable or regular enough to produce noticeable chiroptical response in the mid-infrared region. The relative intensity of the VCD couplet associated with carbonyl absorption band can be used as the indicator of the proportion of polyl that takes the quadruplex structure.

At alkali metal ion concentrations of 1.0 M and 0.1 M NaCl, heating the sample to 70°C followed by cooling the sample back to room temperature completely restores the before-heating frequency position of the carbonyl band and its corresponding positive VCD couplet. However, as can be observed in Figure 9-21C, neither the frequency of the carbonyl absorption band nor the positive VCD couplet are restored upon cooling the sample back to room temperature when no NaCl is present. Instead, the spectra upon cooling the sample back to room temperature retain the heat-disrupted features seen at

70°C. Thus, in the absence of Na^+ ions, heat induced structural changes in polyI are irreversible.

The previously reported[299] VCD spectrum of polyI at 0.1 M NaCl and near neutral pH, matches the spectrum obtained in the present study at room temperature. However, at elevated temperature there are discrepancies between our results and those reported by Annamalai and Keiderling[18]. This previous work reported that the positive VCD couplet observed at room temperature suddenly changes to a single positive VCD signal of smaller magnitude above 52°C. Our observation, on the other hand, indicates an abrupt loss of intensity of the positive couplet at ~ 60°C, with no indication of the emergence of a positive VCD band or any other VCD signal. Since the VCD spectra reported by Annamalai and Keiderling were restricted to only two temperatures (room temperature and 52°C) it is difficult to establish any particular temperature dependent trend in their measurements. Nevertheless, the carbonyl absorption band displayed by Annamali and Keiderling undergoes an analogous downshift in frequency as observed in our measurements. From the perspective of structural interpretation, we believe that the heat-induced loss of the positive VCD couplet, as seen at other ionic strengths also in the current study, is easily relatable to the expected disruption of the quadurplex into a helicity-lacking structure for polyI.

Figures 9-22A and B also display the heat-induced spectral changes, at alkali metal ion concentrations of 1.0 M and 0.1 M NaCl respectively, but in basic environment with pH ~8.0. In the presence of 1.0 M NaCl, the spectra obtained at pH ~8.0 display similar heat-induced modifications as those observed at pH ~6.0.

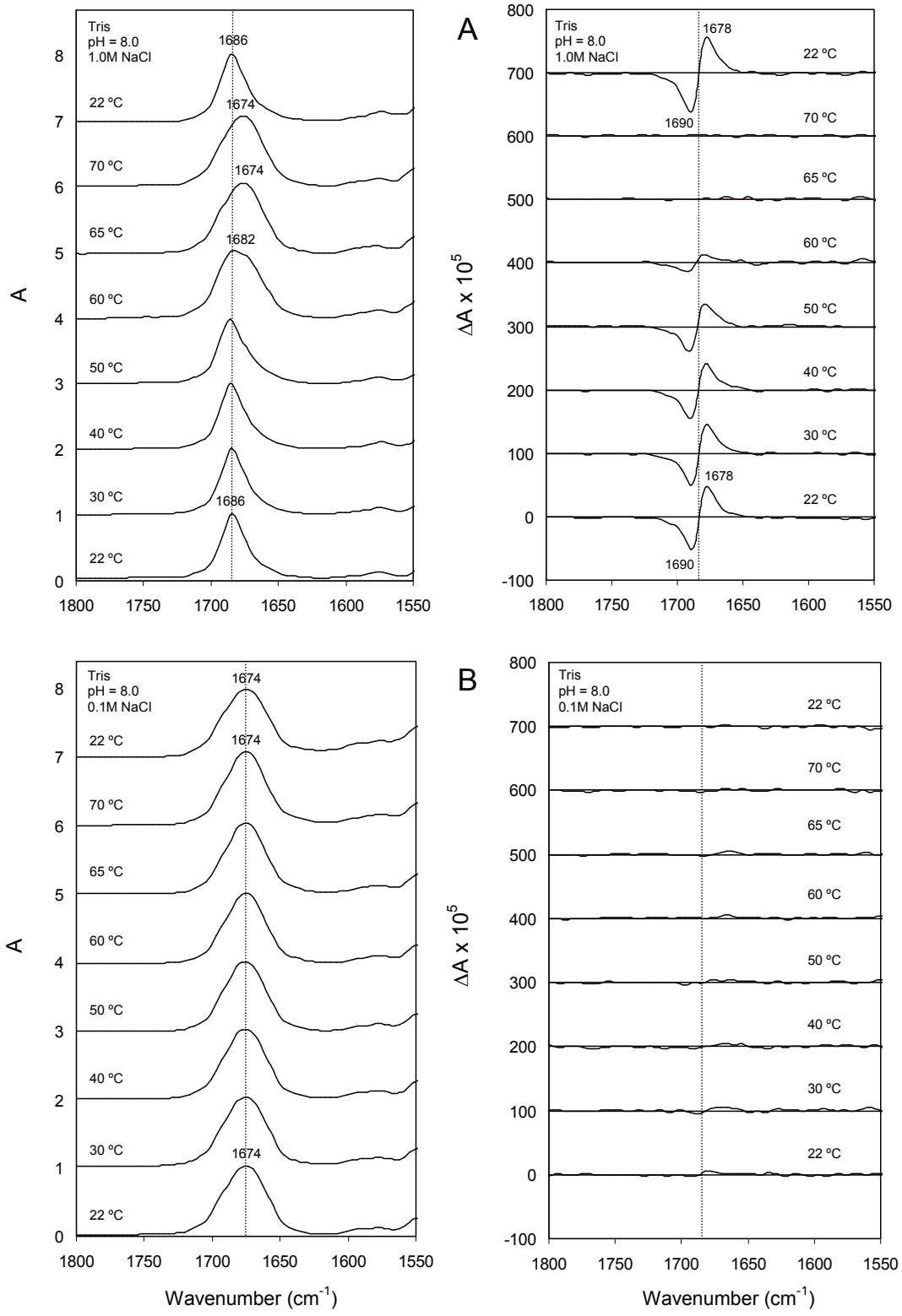

Figure 9-22: Heat-induced absorption (left) and VCD (right) spectral changes of polyI solution at pH = 8.0. NaCl concentrations associated with panels A and B are 1.0 M and 0.1 M NaCl respectively.

The downshift of the carbonyl absorption band (from 1686 to 1674 cm^{-1}) occurs at 60-65°C which is paralleled by a pronounced loss and then complete disappearance of the VCD couplet in this narrow temperature range. The spectral features of the quadruplex structure at room temperature (prior to heating) are completely restored at the end of heating cycle upon cooling the sample back to 22°C. However, this situation changes significantly at pH ~8.0 in the presence of 0.1 M NaCl. The spectra obtained at pH ~8.0 and 0.1M NaCl show carbonyl absorption band at a significantly downshifted frequency (1674 cm^{-1}) and absence of any significant VCD signal even prior to heating. The heating process has no influence on the spectral features under these conditions. These observations indicate that the quadruplex structure for polyI cannot be supported in the presence of 0.1 M Na^+ ions in a moderately alkaline environment.

In addition to the above mentioned solution-based spectra, we have also recorded the spectra for trehalose-assisted polyI film. Figure 9-23 displays the absorption and VCD spectra of polyI in the film state at 22°C and 70°C. Just as in solution-spectra, the carbonyl absorption band in the film state (at ~ 1701 cm^{-1}) is associated with a positive VCD couplet that can be indicative of quadruplex structure. The additional intense absorption band at 1589 cm^{-1} and corresponding negative VCD signal is likely to originate from C-N-H bending vibrations. Note that in D_2O solution, N-H protons exchange with deuterium, so C-N-H bending vibrational bands are not expected to be present, and therefore not seen, in solution spectra. As the polyI film sample is heated to 70°C only

minor changes are seen in the absorption and VCD spectra. The absorption band remained at the same position (1701 cm^{-1}) as that at room temperature and the corresponding positive VCD couplet remained with a slightly diminished intensity, unlike in solution spectra. From these observations it can be concluded that, unlike in solution state, the quadruplex structure is less prone to heat-induced disruptions in the trehalose-assisted polyI film.

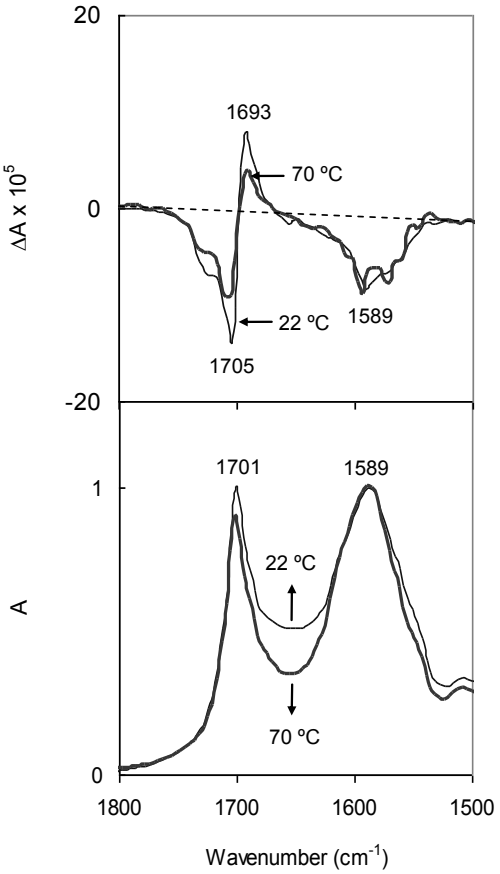

Figure 9-23: Absorption (bottom) and VCD (top) spectra of trehalose-assisted polyI film as a function of temperature.

Conclusion

From the vibrational absorption and VCD spectra of polyI as a function of alkali metal ion concentration, pH and temperature we conclude the following: a) A single positive VCD couplet associated with the carbonyl absorption band is the signature of quadruplex structure for polyI; b) The disruption of quadruplex structure with temperature increase or pH increase at low alkali metal ion concentration is evidenced by the disappearance of this positive VCD couplet; c) The absence of any VCD signal upon quadruplex disruption indicates that the newly formed structure lacks helical-chirality and is likely to be disordered; d) In the presence of 1 M NaCl or 0.1 M NaCl, the heat-induced quadruplex disruption is completely reversible; e) Mildly alkaline environment, in the presence of 0.1 M NaCl, is not sufficient to support the quadruplex structure of poly I. f) Trehalose-assisted polyI film at room temperature exhibits the same quadruplex spectral signature as that seen for solution at room temperature, but the qudruplex spectral signature for film stays intact at higher temperature, unlike in solution. This indicates that the quadruplex structure of polyI in the film state resists heat-induced disruptions.

CHAPTER X

VIBRATIONAL CIRCULAR DICHROISM INVESTIGATION OF A β-TURN FORMING WUGW-TETRAPEPTIDE

Introduction

Structures of biomolecules are typically investigated using X-ray crystallography, nuclear magnetic resonance (NMR), and/or electronic circular dichroism (ECD), depending on the applicability of these individual methods. Recently vibrational circular dichroism (VCD) spectroscopy has emerged as a powerful method for the structural elucidation of peptides and proteins in solution and film states. Although both ECD and VCD spectroscopies allow investigation of peptide and protein structures, the ECD spectral interpretations are sometimes ambiguous[361-363] when aromatic residues are present. This is because aromatic amino acids (Phe, Tyr, Trp) have electronic transitions in the far UV-region (190-230 nm) that overlap[361] with those of amide groups and, as a consequence, ECD associated with these two transitions can interfere with each other. On the other hand, as the vibrational transitions of aromatic amino acids and amide groups are well separated in frequency positions, VCD associated with these transitions do not interfere with each other. Thus VCD spectroscopy offers definite advantages for structural determination of peptide and proteins that contain aromatic residues. The tetrapeptide investigated here contains two aromatic residues.

A number of studies[364-378] have used VCD spectroscopy to derive conformationally sensitive information for protein/peptide systems. The

secondary structures are reflected in the recognizable VCD signatures associated with the amide I (C=O stretch) and amide II (N-H deformation) vibrations. Although a majority of structural elucidations of peptides/proteins using VCD spectroscopy have been accomplished with empirical spectra-structure correlations, some predictive calculations have also been attempted. Initial VCD predictions[361,379] have been based on extended coupled oscillator model[380], which assumes[263] dipole-dipole coupling between amide groups of amino acid units as the source of the optical activity. Keiderling and coworkers have promoted[381-388] correlations of the experimental VCD spectra with corresponding approximate quantum mechanical spectra using a transfer parameter method. This method relies on transferring parameters (geometry, force constants, and atomic tensors) obtained for smaller peptides, typically di- or tri-peptides, to larger polypeptides or proteins. This approach was deemed to give satisfactory predicted-experimental spectral correlations, while avoiding the high computational cost of fully quantum mechanical treatment for larger systems. This method has been implemented for α-helical[383,384], β-sheet[385,389] and β-hairpin[386-388] secondary structures. However, the transfer method does not address or verify fundamental rules such as the sum rules for force constants[390] and atomic tensors[391,392] following the transfer of these parameters. As a result it is not clear whether, or not, the transfer parameter method gives satisfactory predicted-experimental spectral correlations for the "right" reasons and the reliability of this method is difficult to judge. Furthermore for aromatic systems, such as the one considered here, the π- π interactions between aromatic

residues can dominate and such interactions are not likely to be represented correctly in the transfer parameter method.

Quantum mechanical optimizations and VCD predictions, without transferring parameters, have been performed on alanine-based decaamide[393], forming helical secondary structure, and alanine-based triamide[205], forming β-sheet arrangement. Such fully quantum mechanical VCD predictions have not been undertaken for hetero-amino-acid peptides or peptides capable of forming β-hairpin and β-turn type structures.

Among the secondary structures of peptides and proteins, turn geometry displays[379] considerable conformational variability. Turn is the non-repeating area where a polypeptide chain reverses its overall direction. In β-turn this area comprises four amino acid residues, while in γ-turns three residues. Several standard types of turns (ex. β-turn types I, I', II, II', III, III', etc.) and characteristic[394] dihedral angles have been defined[379], but some deviation from standard angles can be observed in practice. Unlike fairly well-established VCD signatures for α-helix, β-sheet, and random-coil secondary structures[381,395], characteristic VCD features for peptides exhibiting a turn motif have not been well defined. Xie *et al.* have reported[379] based on both experimental and theoretical considerations that cyclic-peptides display a positive couplet in the amide I region as a dominant signature of type I or type II β-turns. Specifically, type I turn was associated with the couplet at ~ 1675/1690 cm^{-1}, while type II turn was associated with a broader couplet at ~ 1635/1690 cm^{-1}. However, the positive VCD couplet in the amide I region can also be interpreted[396] as indicative

of a γ-turn for cyclic-peptides. A different study[397], performed by Wyssbrod *et al.*, has suggested that for cyclic peptides with at least four residues, β-turn characterizing VCD pattern in the amide I region is a negative-positive-negative signal. Experimentally and theoretically considered VCD spectra for turn-forming tetrapeptides, reported[398] by Hilario *et al.*, have displayed a negative VCD couplet in amide I region. It was also indicated in the literature[397] that linear hexapeptides exhibit amide I VCD pattern that is more complex than just a single couplet. Based on previous VCD studies[397,398] there is no prototypical VCD signature for turn as a secondary structural motif. VCD spectra may be able to distinguish among various types of turn conformations, but in order to establish conformational details of these turn conformations it is necessary to simultaneously obtain and compare the experimental and theoretical VCD spectra for peptides that have propensity for turn conformations.

β-hairpin structures result from a mixture of β-sheet and turn motifs. β-hairpins generally yield[361,362] an intense negative VCD band in the ~1645 cm^{-1} region and sometimes also a weak positive VCD band at ~1690 cm^{-1}. Parallel β-sheet structures typically give[363] one negative VCD signal at about ~1630 cm^{-1}. If both β-sheet and hairpin structures yield negative VCD signals then turn structure may also be associated with a negative VCD signal or no VCD signal at all. But to establish the VCD signature of turn motifs it is necessary to investigate the peptides that have only turn structure and no other secondary structural motif.

Although quantum mechanical VCD simulations for β-turn-forming tetrapeptides have been considered in the past[398], the tetrapeptides for which these simulations have been performed differ in residue-composition from the tetrapeptide used for experimental investigation. Specifically, experimentally investigated tetrapeptides were Ac-Val-Asn-Gly-Lys-NH_2 and Ac-Val-Pro-Gly-Lys-NH_2, while theoretical investigation were conducted for tetra peptides with all residues, other than Pro and Gly, substituted with Ala residue. Additionally, the geometry used for the calculations on these β-turn models is not a quantum mechanically optimized geometry, but a type I' turn geometry extracted from the NMR structure of a larger peptide.

From the literature background provided in the previous paragraphs, it is clear that both experimentally observed and quantum mechanically predicted VCD spectra for the same β-turn forming peptide have not been reported to date. In addition, no prior VCD theoretical study on β-turn forming peptides treated both structure-optimization and VCD spectral prediction entirely quantum mechanically at the same level of theory. This situation is remedied in the current study by presenting the first combined experimental and quantum mechanical investigation, including both geometry optimization and VCD spectral prediction, done on the entire tetrapeptide that is residue-for-residue equivalent to the tetrapeptide investigated experimentally. The tetrapeptide under investigation is Boc-Trp_1-Aib_2-Gly_3-Trp_4-OMe (WUGW) and it falls under a rare class of smallest tetrapeptides to exhibit turn structure. The reported[399] X-ray and NMR studies on this tetrapeptide suggest the presence of a turn in its structure. The quantum

mechanical predictions of stable conformations, and of the appearance of conformation dependent VCD spectra, along with vibrational origins of the dominant VCD signals, would be of significant importance for this tetrapeptide. The comparison of predicted VCD spectra for different conformers with the experimental VCD spectra for this tetrapeptide permits identification of characteristic VCD signatures for turn type structure.

Experimental Section

The vibrational absorption (VA) and VCD spectra were recorded in the 2000-900 cm^{-1} region using a commercial Fourier Transform VCD spectrometer modified[15] to reduce the level of artifacts. The VCD spectra were recorded with 3 hr data collection time at 4 cm^{-1} resolution. The sample was held in demountable cell with CaF_2 windows and a 100 μm spacer. Spectra were measured in $CHCl_3$ and CH_3OH solvents at ~ 20 mg/mL concentration (the actual amount used was ~ 2 mg in 100 μL). Baseline corrections for all spectra were made by subtracting the absorption (or VCD) of the corresponding solvent. Spectral region below ~1550 cm^{-1} has been omitted due to interference from the solvent absorption in CH_3OH.

All calculations were done using the Gaussian 03 program at National Center for Supercomputing Applications facility at the University of Illinois. Theoretical optimizations, VA and VCD predictions were done using B3LYP functional and 6-31G* basis set. Lorentzian bandshapes, with a bandwidth of 10 cm^{-1}, were used for spectral simulation. Predicted frequencies associated with

optimized conformations A and B have been scaled by a factor of 0.9613. No such scaling has been performed on frequencies predicted for un-optimized conformations I and II.

Results and Discussion

The WUGW tetrapeptide provides insight into how few residues with varying secondary-structure tendencies interact in conjunction to form a stable secondary structure. This tetrapeptide is terminated with two aromatic residues (Trp) whose π-stacking interactions along with hydrogen bonding between different residues result in propensity for turn formation. On the other hand, constrained Aib (α-aminoisobutyric acid, U) residue is known as helix nucleating moiety. In particular, there is X-ray crystallographic evidence[400-403] that Aib-containing short synthetic peptides are prone to adopt 3_{10}-helical conformation.

The X-ray structure of WUGW peptide indicates one turn conformation while NMR study[399] provided evidence for interconversion between two conformers with equal populations in solution, one of which is also observed in the X-ray analysis. In this report we investigate the secondary structure of WUGW tetrapeptide using combined experimentally observed and quantum mechanically predicted VCD spectra.

The geometry optimization of WUGW peptide involved consideration of three starting structures (conformations I-III as given in Figure 10-1). Each of the three starting structures represents a folded, fairly compact conformation with two hydrogen bonds. Conformation I is based on coordinates obtained from the

X-ray crystal study[399]. This initial conformation exhibits backbone folding aided by the formation of perpendicular or so-called T-shape aromatic interactions and it has been classified[399] as a type II-I' β-turn. Conformation II is one of the conformations suggested by the NMR study[399] and its dihedral angles resemble the conventional type I' β-turn. These two initial conformations are representatives of β-turn secondary structures and differ only in the φ dihedral angle of Trp_1 residue: this angle is -54.6° for conformation I and -149.8° for conformation II. Conformation III has been constructed to model a 3_{10}-helical structure, which is supported by Aib containing peptides. The main structural parameters of the three initial conformations are presented in Table 10-1. These parameters include dominant backbone dihedral angles (φ, ψ, ω) associated with each of the four amino acids and dihedral angles (χ_1, χ_2) associated with the orientation of two Trp residues.

The hydrogen bond specifications are presented in Figure 10-1. For conformation I, hydrogen bond length of 2.29 Å is between Trp_4 amine and Trp_1 carbonyl, while hydrogen bond length of 1.85 Å is between Gly_3 amine and Boc-ester carbonyl. For conformation II, hydrogen bond length of 2.29 Å is between Trp_4 amine and Trp_1 carbonyl, while hydrogen bond length of 2.32 Å is between Trp_1 amine and Trp_4 carbonyl. Lastly for conformation III, hydrogen bond length of 2.25 Å is between Trp_4 amine and Trp_1 carbonyl, while hydrogen bond length of 1.94 Å is between Gly_3 amine and Boc-ester carbonyl.

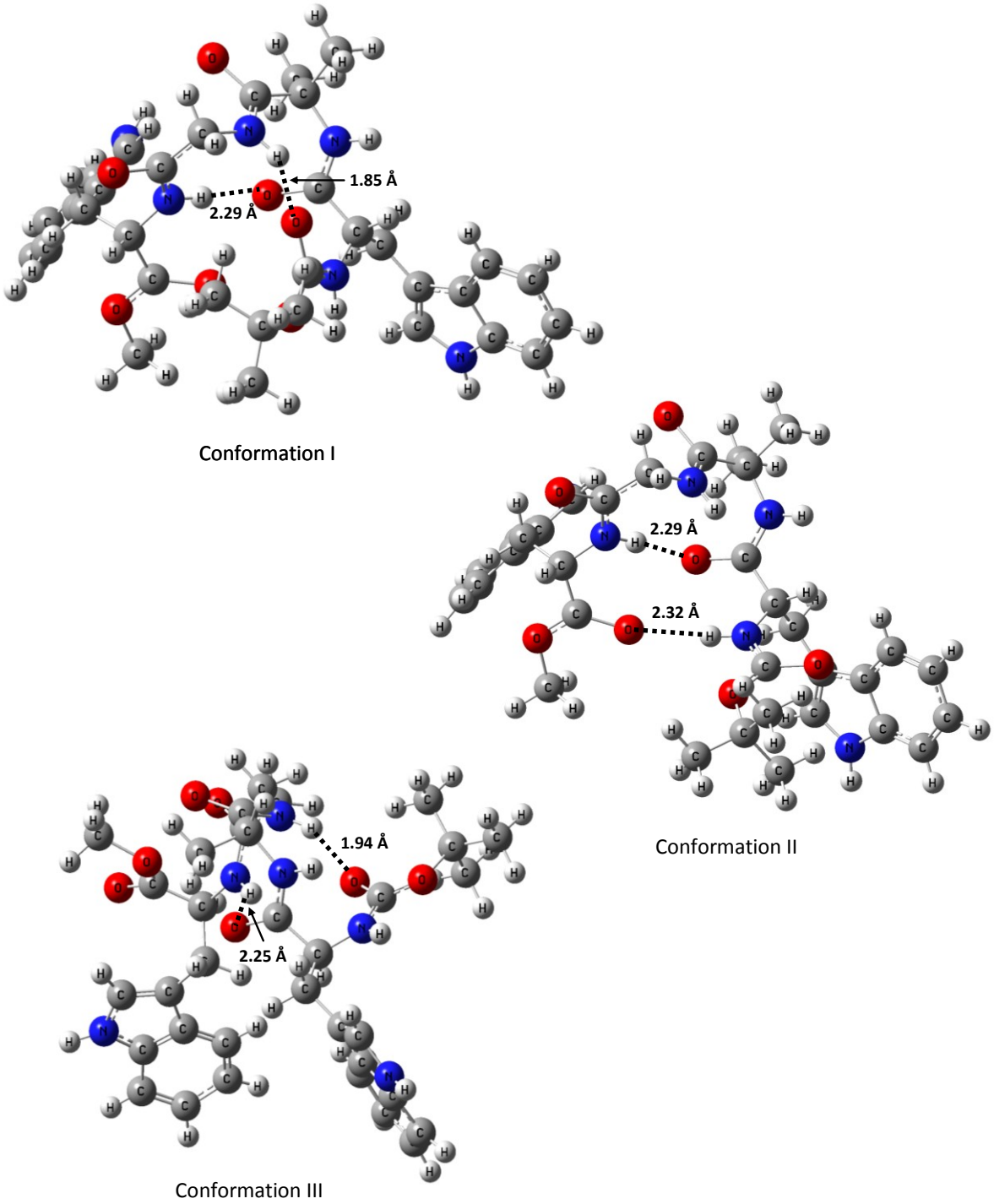

Figure 10-1: Structures of initial, non-optimized conformations of WUGW-tetrapeptide (Conformations I, II, and III).

Table 10-1: Dihedral angles (degrees) for Boc-Trp_1-Aib_2-Gly_3-Trp_4-OMe (WUGW) tetrapeptide for each of the three initial conformations.

Conformation I	ϕ	ψ	ω	χ^3	χ^4
Trp $_1$	-54.576	130.736	176.910	-56.727	130.884
Aib $_2$	61.455	19.813	175.321		
Gly $_3$	93.841	3.586	179.274		
Trp $_4$	-154.941	-177.221[1]	177.025[2]	71.284	-73.588

Conformation II	ϕ	ψ	ω	χ^3	χ^4
Trp $_1$	-149.774	130.736	176.910	-56.727	130.884
Aib $_2$	61.455	19.813	175.321		
Gly $_3$	93.841	3.586	179.274		
Trp $_4$	-154.941	-177.221[1]	177.025[2]	71.284	-73.588

Conformation III	ϕ	ψ	ω	χ^3	χ^4
Trp $_1$	-60.716	-30.548	176.905	-56.770	130.901
Aib $_2$	-59.975	-30.783	175.334		
Gly $_3$	-60.712	-30.764	179.282		
Trp $_4$	-60.223	-29.999[1]	177.019[2]	177.988	-73.605

[1] dihedral angle of N-C-C-O(Me)
[2] dihedral angle of C-C-O-C(Me)
[3] dihedral angle of N-C-C-C
[4] dihedral angle of C-C-C-C(N)

The optimization of these three conformations at B3LYP/6-31G* level theory has lead to their convergence into two structures that differ from each of the starting structures. The structural parameters of the new conformations are given in Table 10-2, while the structures themselves are displayed in Figure 10-2. Conformers I and II have converged into the same structure with φ dihedral angle of Trp_1 residue as -74.8°. This dihedral angle, in the optimized structure designated as conformation A, represents a compromise between the angles of the starting conformations I and II. However, as can be seen by comparison of

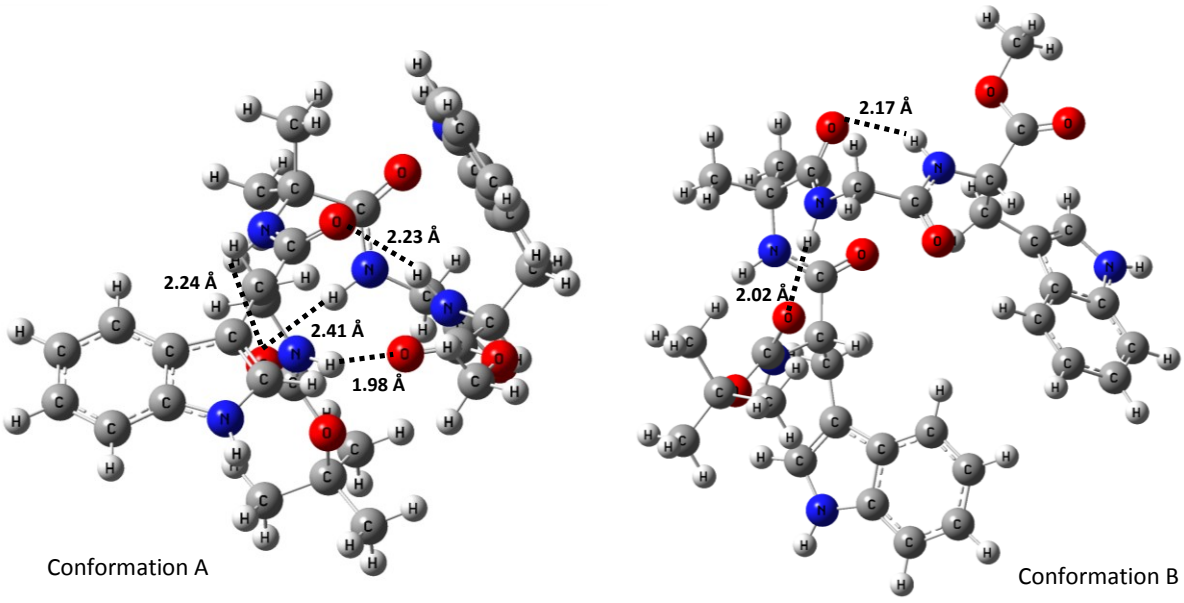

Figure 10-2: Structures of converged, optimized conformations of WUGW-tetrapeptide (Conformations A and B).

Table 10-2: Dihedral angles (degrees) for Boc-Trp_1-Aib_2-Gly_3-Trp_4-OMe (WUGW) tetrapeptide for the two converged conformations.

Conformation A	ϕ	ψ	ω	χ^3	χ^4
Trp 1	-74.795	99.302	-167.693	-58.035	100.664
Aib 2	49.548	38.540	176.472		
Gly 3	106.397	-25.330	-162.131		
Trp 4	-134.335	179.645[1]	179.864[2]	60.860	-81.497

Conformation B	ϕ	ψ	ω	χ^3	χ^4
Trp 1	-74.281	-12.953	169.528	-61.979	109.747
Aib 2	-52.366	-36.217	179.362		
Gly 3	-82.064	78.667	-172.290		
Trp 4	-146.571	-45.899[1]	-179.311[2]	-160.195	-107.866

[1] dihedral angle of N-C-C-O(Me)
[2] dihedral angle of C-C-O-C(Me)
[3] dihedral angle of N-C-C-C
[4] dihedral angle of C-C-C-C(N)

Tables 10-1 and 10-2, this is not the only dihedral angle that has been modified as a result of the optimization. Conformation A is coordinated by additional hydrogen bond length of 2.41 Å, between Aib_2 amine and Boc-ester carbonyl. However, the three hydrogen bonds between amine and carbonyl groups on the backbone, present in conformation A are preserved from conformations I and II. Specifically, hydrogen bond length of 2.23 Å is between Trp_4 amine and Trp_1 carbonyl; hydrogen bond length of 1.98 Å is between Trp_1 amine and Trp_4 carbonyl; and hydrogen bond length of 2.24 Å is between Gly_3 amine and Boc-ester carbonyl. Conformation III has also been modified as a result of optimization into structure designated as conformation B. One hydrogen bond (2.02 Å) present in conformation B is preserved from conformation III, while the second hydrogen bond (2.17 Å) is newly formed as a result of optimization. The hydrogen bond length of 2.02 Å is between Gly_3 amine and Boc-ester carbonyl, while the hydrogen bond length of 2.17 Å is between Trp_4 amine and Aib_2 carbonyl.

Based on the difference in predicted electronic energy values (ΔE=6.12 kcal/mol), conformer A is significantly more stable than conformer B. Despite the vastly different relative populations predicted for the two conformers, both forms have been subjected to VCD calculations in order to note the differences in theoretical spectra and evaluate the agreement with experimental spectra.

The comparison of the VA (bottom) and VCD (top) spectra obtained in $CHCl_3$ and CH_3OH solvents with the corresponding theoretical spectra of conformations A and B is displayed in Figure 10-3. As can be seen from this

figure, the dominant experimental VCD feature present in the amide I (C=O stretching) region is a negative band in both solvents at ~1660 cm^{-1} (1666 in $CHCl_3$ and 1655 in CH_3OH). These negative VCD bands, for both solvents, are associated with the highest intensity absorption bands (1674 and 1666 cm^{-1}) in the region considered. A negative VCD band in the ~1648-1658 cm^{-1} range was also seen[2] in longer analogous-peptide sequences with β-hairpin (β-sheet + β-turn) structures in chloroform solvent. This negative band appears[362] (see Figure 10-3) at a slightly lower frequency (by about 10 cm^{-1}) in methanol solvent. Since the present tetrapeptide does not have a β-sheet structural component but also gives a negative VCD signal in the amide I region at ~1650-1660 cm^{-1}, this negative signal can be interpreted as originating from the β-turn structure.

As the conformationally sensitive information is captured by VCD, the predicted VCD spectra provide an indication of characteristic signatures for turn structures. The turn structure represented by conformer A displays the characteristic features as a negative VCD signal at 1679 cm^{-1} and a positive VCD signal at 1730 cm^{-1}. On the other hand, the turn structure represented by conformer B displays very weak VCD signals.

Comparison between the experimental and predicted spectra help establish closer conformational details of the turn-structure present in solution. A comparison of predicted spectra for the two conformers leads to the conclusion that the turn-conformation present in solution can be represented by theoretical conformation A much more closely than conformation B. This conclusion results from considerably better qualitative agreement of the predicted VCD spectra of

conformation A with the experimental spectra. The dominant negative VCD signal at 1679 cm^{-1} for conformation A, correlates well in terms of position and intensity with the experimental negative VCD signals in both solvents. The predicted negative VCD signal originates from C=O stretching vibration of Trp_1 (see Table 10-3), coupled to C=O stretching motions of Boc-ester, Aib_2 and Gly_3, with a scaled frequency of 1681 cm^{-1}. The intensity of this simulated negative VCD band is reduced by a neighboring vibration with positive VCD at a scaled frequency of 1691 cm^{-1}, which originates from C=O stretching vibration of Gly3, coupled to C=O stretching motions of Trp_1 and Aib_2.

The simulated positive VCD signal at ~ 1730 cm^{-1} of conformer A doesn't have a corresponding experimental band for correlation. This positive VCD signal originates from two vibrations with scaled frequencies of 1700 cm^{-1} and 1729 cm^{-1} (Table 10-3). The origin of the 1700 cm^{-1} vibration is C=O stretching vibration of Aib_2 with coupling to C=O stretching motions of Trp_1 and Gly_3. The origin of the 1729 cm^{-1} vibration is C=O stretching of Trp_4.

The predicted VCD spectrum of conformation B doesn't have any satisfactory agreement with the experimental spectra. The most noticeable negative VCD signal of conformer B is present at 1764 cm^{-1} and it originates from C=O stretching vibration of Trp_4 residue (Table 10-4). Even for a qualitative level comparison, this negative VCD signal is too far-removed to be correlated with the negative experimental signal.

Although positions of weak VCD bands (positive band for conformation A and negative couplet for conformation B) have been labeled in Figure 10-3, they

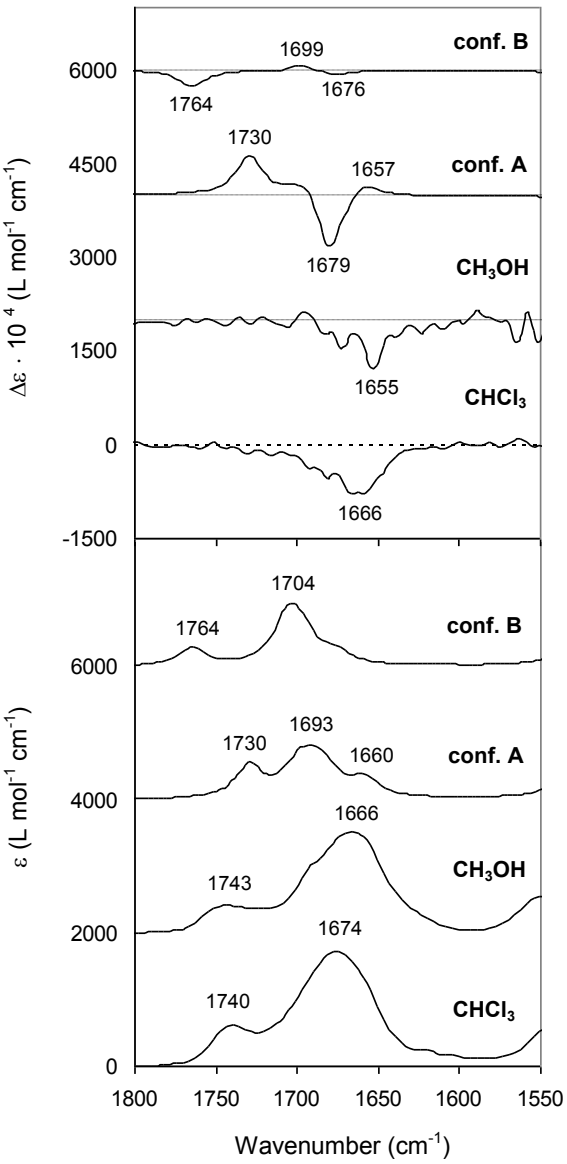

Figure 10-3: Comparison of experimental and predicted vibrational absorption (lower panel) and VCD (upper panel) traces. The predicted traces are for the two converged optimized conformations (Conformations A and B).

are not of much importance as there are no corresponding experimental bands. The origins of these weak predicted bands, nevertheless, have been identified based on data in Tables 10-3 and 10-4 as follows: the positive VCD signal at ~ 1657 cm^{-1} of conformation A originates from C=O stretching vibration of Boc-

ester with some coupling to C=O stretching motion of Trp_1; the predicted negative VCD band at ~ 1676 cm^{-1} for conformer B originates from C=O stretching vibration of Aib_2 with coupling to C=O stretching motions of Trp_1 andGly_3; the predicted positive VCD band at ~ 1699 cm^{-1} originates from three vibrations with a scaled frequencies of 1696 cm^{-1}, 1704 cm^{-1} and 1709 cm^{-1} (Table 10-4). Vibrations at 1696 cm^{-1} and 1704 cm^{-1} contribute to the intensity of the positive band, while vibration at 1709 cm^{-1} with negative rotational strength diminishes the positive VCD band intensity. The origin of the 1696 cm^{-1} is C=O stretching vibration of Trp_1 with coupling to the C=O stretching motion of Aib_2. The origin of the 1704 cm^{-1} vibration is C=O stretching vibration of Gly_3 with coupling to the C=O stretching motions of Boc-ester and Aib_2. The origin of the 1709 cm^{-1} vibration is C=O stretching vibration of Boc-ester with coupling to C=O stretching motion of Aib_2 and Gly_3.

It is disconcerting to note that the predicted VCD spectrum for conformer A also has a positive VCD band at 1730 cm^{-1} for which no corresponding experimental band is seen. A possible explanation for this mismatch is as follows: It is to be noted that the calculations are done for isolated molecules, while the experimental data are obtained in solution phase. The NMR spectral data for WUGW suggested[399] the presence of two conformers in equilibrium, while the geometry optimizations of these two conformers in vacuum lead to a single conformer A. Then it is to be construed that the NMR data are indicating solvent mediated stability of conformers I and II and that the calculations have to be done for these two conformers. The solvent influence on geometry

Table 10-3: Predicted parameters associated with five vibrations giving rise to the dominant VCD signals of Conformation A. The relative displacements are listed for carbonyl groups belonging to Boc, Trp_1, Aib_2, Gly_3 and Trp_4 residue in order to identify which residue(s) has the most pronounced C=O stretching for a given predicted vibration.

Simulated VCD bands (cm^{-1})	(+) , 1657	(−) , 1679		(+) , 1730	
Unscaled Freq. (cm^{-1})	1725	1749	1759	1769	1799
Scaled Freq. (cm^{-1})	1659	1681	1691	1700	1729
Dipole Strength (10^{-40} esu^2cm^2)	470.73	476.91	636.96	679.52	777.64
Rotational Strength (10^{-44} esu^2cm^2)	110.23	-476.46	155.36	61.28	267.94
Carbonyl Group	Relative Displacement				
Boc-ester	**1.0472**	-0.1516	0.0430	-0.0871	0.1022
Trp_1	0.1734	**0.9881**	-0.1733	0.3233	-0.0056
Aib_2	0.0277	-0.2971	0.1926	**1.0717**	0.0297
Gly_3	-0.0138	0.2119	**1.1165**	-0.1269	-0.1045
Trp_4	0.0874	-0.0457	-0.1004	0.0351	**-1.1764**

Table 10-4: Predicted parameters associated with five vibrations giving rise to the dominant VCD signals of Conformation B. The relative displacements are listed for carbonyl groups belonging to Boc, Trp_1, Aib_2, Gly_3 and Trp_4 residue in order to identify which residue(s) has the most pronounced C=O stretching for a given predicted vibration.

Simulated VCD bands (cm^{-1})	(−) , 1676	(+) , 1699			(−) , 1764
Unscaled Freq. (cm^{-1})	1743	1765	1773	1777	1836
Scaled Freq. (cm^{-1})	1676	1696	1704	1709	1765
Dipole Strength (10^{-40} esu^2cm^2)	282.44	607.07	754.22	433.09	425.81
Rotational Strength (10^{-44} esu^2cm^2)	-37.64	22.45	40.71	-32.15	-108.87
Carbonyl Group	Relative Displacement				
Boc-ester	0.1117	0.0441	0.4491	**0.9991**	-0.0075
Trp_1	-0.1975	**1.1394**	0.0459	-0.0481	-0.0192
Aib_2	**1.1108**	0.1657	0.1394	-0.1922	-0.0091
Gly_3	0.2038	0.0961	**-0.9815**	0.4263	0.0000
Trp_4	0.0079	0.0200	0.0087	0.0079	**1.2649**

optimizations can be incorporated using approximate models such as polarizable continuum model[404], but such models cannot represent the solvent-solute

interactions correctly. Explicit inclusion of solvent molecules[192] is one way to overcome this problem, but such calculations increase the number of basis functions leading to computational limitations. Therefore we have performed the calculations at the partially-optimized geometries of conformers I and II, obtained from crystal structure and NMR data with fixed backbone dihedral angles, ϕ, ψ, and ω. The partial optimization has involved completion of 65 cycles of optimization.

Comparison of experimental traces with those predicted for partially optimized conformations I and II is presented in Figure 10-4. With exception to a few positive contributions, the predicted VA and VCD signals display a satisfactory match with the experimental signals. The correlation between experimental and theoretical signatures are unambiguous for both conformers I and II since their predicted traces display predominantly a negative VCD signal which correspond to the negative signal observed in solution environment. Specifically, the experimental negative VCD signal at ~ 1650 cm^{-1} arising from the highest intensity absorption bands seem to correspond to the predicted negative VCD signal at ~ 1690 cm^{-1}, also arising from the highest intensity absorption bands. Since both partially optimized conformations display a good qualitative reproduction of experimental traces, based on VCD-study, both conformations are present in solution.

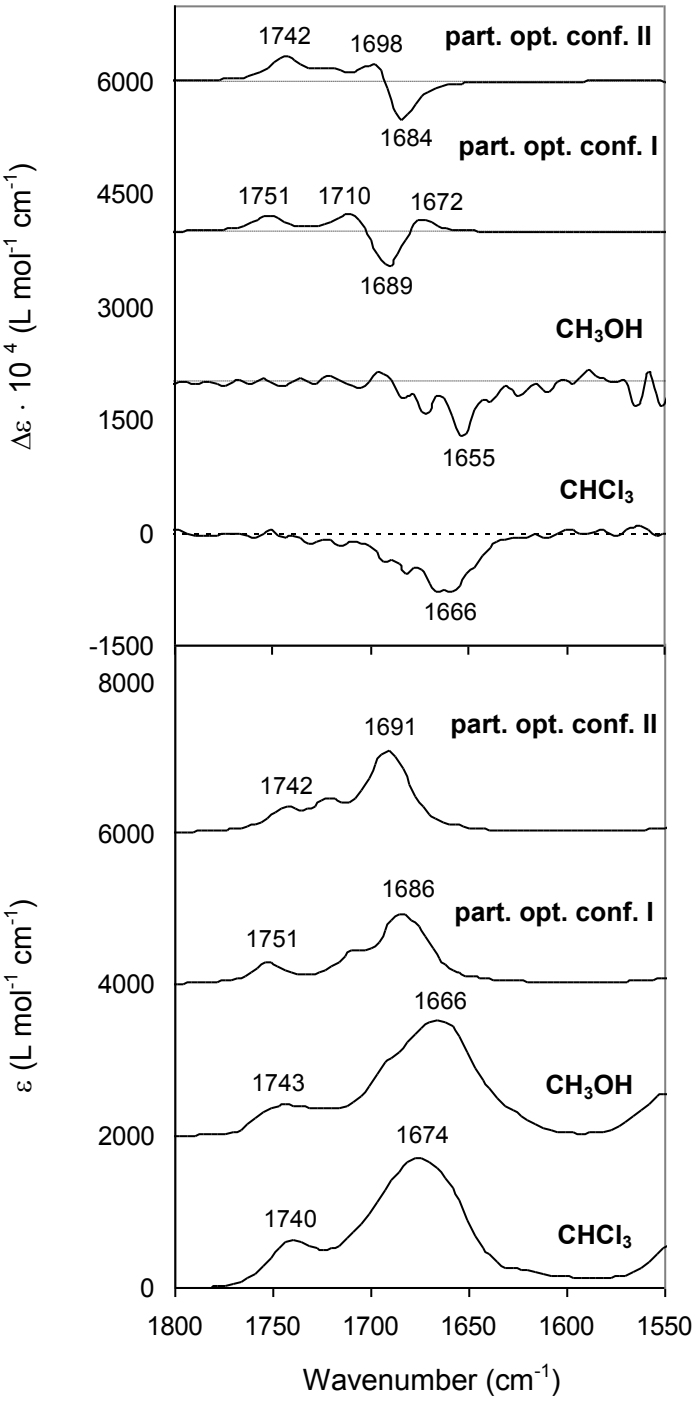

Figure 10-4: Comparison of experimental and predicted vibrational absorption (lower panel) and VCD (upper panel) traces. The predicted traces are for the two partially-optimized β-turn forming conformations (Conformations I and II).

The origins of the predicted bands for partially-optimized conformations I and II have been identified based on data in Tables 10-5 and 10-6, respectively. The correlated negative band at ~ 1689 cm^{-1} of partially optimized conformation I originates from two vibrations with a scaled frequencies of 1685 cm^{-1} and 1690 cm^{-1}. Vibrations at 1685 cm^{-1} with positive rotational strength diminish the intensity of the negative band, while vibrations at 1690 cm^{-1} contribute to the intensity the negative band. The origin of the 1685 cm^{-1} is C=O stretching vibration of Boc-ester with coupling to C=O stretching motion of Aib_2 and Gly_3. The origin of the 1690 cm^{-1} is C=O stretching vibration of Gly_3 with coupling to C=O stretching motion of Boc-ester and Trp_1. In terms of the correlated negative band at ~ 1684 cm^{-1} of partially-optimized conformation II, it originates from C=O stretching vibration of Trp_1 with coupling to C=O stretching motion of Boc-ester, Aib_2 and Gly_3.

Table 10-5: Predicted parameters associated with vibrations giving rise to the VCD signals of partially-optimized conformation I. The relative displacements are listed for different vibrations in order to identify which group(s) exhibits the most pronounced stretching.

Simulated VCD bands (cm^{-1})	(+) , 1672	(-) , 1689		(+) , 1710	(+) , 1751
Unscaled Freq. (cm^{-1})	1743	1753	1758	1778	1823
Scaled Freq. (cm^{-1})	1675	1685	1690	1710	1752
Dipole Strength (10^{-40} esu^2cm^2)	679.66	769.46	464.22	488.74	425.27
Rotational Strength (10^{-44} esu^2cm^2)	110.60	64.15	-299.30	133.65	85.55
Carbonyl Group	Relative Displacement				
Boc-ester	-0.3931	**-0.9904**	0.3777	-0.1760	-0.0371
Trp1	0.0699	0.1061	-0.2020	**-1.0770**	0.1336
Aib2	**-1.0506**	0.4049	-0.1456	-0.0074	0.0000
Gly3	-0.0127	-0.4316	**-1.0889**	0.1476	0.0871
Trp4	-0.0313	-0.0095	0.1238	0.1035	**1.2681**

Table 10-6: Predicted parameters associated with vibrations giving rise to the VCD signals of partially-optimized conformation II. The relative displacements are listed for different vibrations in order to identify which group(s) exhibits the most pronounced stretching.

Simulated VCD bands (cm^{-1})	(-) , 1684	(+) , 1698; (+), 1742			
Unscaled Freq. (cm^{-1})	1754	1761	1766	1791	1814
Scaled Freq. (cm^{-1})	1686	1693	1697	1722	1744
Dipole Strength (10^{-40} esu^2cm^2)	899.58	654.91	527.49	494.40	429.81
Rotational Strength (10^{-44} esu^2cm^2)	-374.70	217.68	64.08	48.76	122.77
Carbonyl Group	Relative Displacement				
Boc-ester	0.1953	0.0678	0.0286	**1.1477**	-0.1689
Trp1	**-1.0248**	-0.2275	-0.3562	0.2202	0.0904
Aib2	0.2321	**-1.1314**	0.0570	0.0287	-0.0191
Gly3	-0.3391	-0.0187	**1.1368**	0.0469	0.1109
Trp4	0.1445	0.0091	-0.0844	0.1445	**1.2450**

Conclusion

The first comparison of experimental VCD spectra with corresponding fully quantum mechanical, both optimization and VCD, predictions has been performed for a β-turn forming WUGW tetrapeptide. This report additionally establishes the vibrational origins of the signals for all of the predicted VCD spectra for the tetrapeptide under investigation. The predicted VCD spectrum of conformation A results in the reproduction of the dominant negative VCD signal observed experimentally. This comparison suggests a close resemblance of the conformation A to the dominant conformation of WUGW-tetrapeptide present in solution. However, a positive VCD signal predicted for conformer A did not have a corresponding band in the experimental spectrum. This mismatch has most

likely resulted from the lack of solvent influence in the quantum mechanical calculations.

Predicted VCD traces of partially-optimized conformations I and II display a satisfactory correlation of the negative band with the experimental spectra, indicating that both conformations are present in solution. It should be noted that optimizations should not be performed simply in vacuum, yet require accounting for a solvent influence. Incorporating the solvent-effect can be most reliably accomplished with explicit inclusion of solvent molecules[192]. Such calculations are not trivial and are out of our reach at this time, for the present investigation. The solvent influence for the partially optimized conformations I and II has been accounted for by fixing the empirically-derived (X-ray and NMR) dihedral angles of the backbone.

CHAPTER XI

SUMMARY

The significance of being able to reliably establish the structure of chiral molecules is manifested through the recognition that different enantiomers and diastereomers of the same compound can have vastly different effects with respect to a specific function. A portion of this Dissertation describes the configurational and conformational analysis of chiral molecules via experimental and theoretical applications of chiroptical spectroscopic methods. Three chiroptical spectroscopic techniques, Vibrational Circular Dichroism (VCD), Electronic Circular Dichroism (ECD), and Optical Rotatory Dispersion (ORD), complement each other in a quest for an unambiguous structural determination. A comparison between experimentally obtained and theoretically predicted chiroptical spectroscopic properties allows the stereochemical elucidation of chiral species. The first tandem application of the three methods has been demonstrated through structural investigations of several chiral organic and inorganic molecules: C_2–symmetric spiroselenurane (Chapter 2), trinickel(II) complex of dypiridylamine (Chapter 3), 2,2'-diphenyl-[3,3'-biphenanthrene]-4,4'-diol (Chapter 4), a set of sulfoxide-containing chiral molecules (Chapter 5), and t-butyl-phenyl-phosphinoamidate (Chapter 6). Progression from Chapter 2 to Chapter 6 adds to the complexity level of the investigation: progressing from analysis of molecules with single chiral centre and little conformational flexibility to analysis of molecules that are not only conformationally flexible but have 3

chiral centres and capability for intermolecular hydrogen-bonding interactions. Chapter 7 of the Dissertation evaluates the utility of ECD for the analysis of ORD in dimethyl tartrate using KK transform. The last three chapters of the Dissertation pertain to VCD based investigations on carbohydrates (Chapter 8), homopolynucleotides (Chapter 9), and tetrapeptide (Chapter 10). These chapters not only evaluate the applicability of the VCD method for elucidating the structures of these classes of biomolecules, but also introduce, film state measurements which, when applicable, can greatly aid the VCD-based structural analysis.

REFERENCES

1. Gergely, A., *J. Pharm. Biomed. Anal.* **1989,** 7, (5), 523-41.

2. Eliel, E. L.; Wilen, S. H., *Stereochemistry of Organic Compounds*. John Wiley & Sons, Inc.: New York, 1994.

3. Maier, N. M.; Franco, P.; Lindner, W., *J. Chromatogr., A* **2001,** 906, (1-2), 3-33.

4. Crawford, T. D., *Theor. Chem. Acc.* **2006,** 115, (4), 227-245.

5. Polavarapu, P. L., *Workshop on "Spectroscopic Methods for Determining Molecular and Suplramolecular Chirality: Optical Rotation and Molecular Stereochemistry". ISCD-16.* New York, July 2004.

6. Carter, R. L., *Molecular Symmetry and Group Theory*. John Wiley & Sons, Inc.: Hoboken, 1998.

7. Friedman, L.; Miller, J. G., *Science* **1971,** 172, (3987), 1044-6.

8. Knobloch, J.; Shaughnessy, J. D., Jr.; Ruether, U., *FASEB J.* **2007,** 21, (7), 1410-1421.

9. Polavarapu, P. L.; He, J., *Anal. Chem.* **2004,** 76, (3), 61A-67A.

10. Polavarapu, P. L., *Submitted for the special project: "Determination of Absolute Configuration"* **2007**.

11. Nakanishi, K.; Berova, N.; Woody, R. W., *Circular Dichroism: Principles and Applications*. VCH Publishers, Inc.: New York, 1994.

12. Nafie, L. A.; Vidrine, D. W., *Fourier Transform Infrared Spectroscopy*. Academic Press: New York, 1982.

13. Polavarapu, P. L., *Fourier Transform Infrared Spectroscopy*. Academic Press: New York, 1985.

14. Keiderling, T. A., *Fourier Transform Infrared Spectroscopy*. Academic Press: New York, 1990.

15. Shanmugam, G.; Polavarapu, P. L., *J. Am. Chem. Soc.* **2004,** 126, (33), 10292-10295.

16. Polavarapu, P. L., *Chem. Rec.* **2007,** 7, (2), 125-136.

17. Freedman, T. B.; Nafie, L. A., Infrared Circular Dichroism. In *Methods in Enzymology, Vol. 226*, Academic Press, Inc.: New York, 1993.

18. Harada, N.; Nakanishi, K., *Circular Dichroism Spectroscopy: Exciton Coupling in Organic Stereochemistry*. Science Books: Mill Valley, CA, 1983.

19. Landolt, H., *The Optical Rotation Power of Organic Substances and its Application*. Chemical Publishing: Easton, PA, 1902.

20. Lowry, T. M., *Optical Rotatory Power*. Dover Publications: New York, 1964.

21. Lakhtakia, A., *Selected Papers of Natural Optical Activity*. SPIE Optical Engineering Press: Bellingham, 1990.

22. Polavarapu, P. L.; Petrovic, A.; Wang, F., *Chirality* **2003,** 15, (9), 801.

23. Djerassi, C., *Optical Rotatory Dispersion*. McGraw-Hill: New York, 1960.

24. Polavarapu, P. L.; Chakraborty, D. K., *Journal of the American Chemical Society* **1998,** 120, (24), 6160-6164.

25. Polavarapu, P. L., *Molecular Physics* **1997,** 91, (3), 551-554.

26. Polavarapu, P. L., *Tetrahedron-Asymmetry* **1997,** 8, (20), 3397-3401.

27. Polavarapu, P. L., *Chirality* **2006,** 18, (5), 348-356.

28. Polavarapu, P. L., *International Journal of Quantum Chemistry* **2006,** 106, (8), 1809-1814.

29. Polavarapu, P. L., *Journal of Physical Chemistry A* **2005,** 109, (32), 7013-7023.

30. Krykunov, M.; Kundrat, M. D.; Autschbach, J., *Journal of Chemical Physics* **2006,** 125, (19), 194110/1-194110/13.

31. Ohta, K.; Ishida, H., *Appl. Spectrosc.* **1988,** 42, (6), 952-7.

32. Polavarapu, P. L.; Petrovic, A. G.; Zhang, P., *Chirality* **2006,** 18, (9), 723-732.

33. Levine, I. N., *Physical Chemistry*. Fifth ed.; McGraw-Hill Companies, Inc.: New York, 2002.

34. Frisch, M. J.; Trucks, G. W.; Schlegel, H. B.; Scuseria, G. E.; Robb, M. A.; Cheeseman, J. R.; Zakrzewski, V. G.; Montgomery, J. A.; Stratmann, J. R.; Burant, J. C.; Dapprich, S.; Millam, J. M.; Daniels, A. D.; Kudin, K. N.; Strain, M. C.; Farkas, O.; Tomasi, J.; Barone, V.; Cossi, M.; Cammi, R.; Mennucci, B.; Pomelli, C.; Adamo, C.; Clifford, S.; Ochterski, J.; Petersson, G. A.; Ayala, P. Y.; Cui, Q.; Morokuma, K.; Malick, D. K.; Rabuck, A. D.; Raghavachari, K.; Foresman, J. B.; Cioslowski, J.; Ortiz, J. V.; Stefanov, B. B.; Liu, G.; Liashenko, A.; Piskorz, P.; Komaromi, I.; Gomperts, R.; Martin, R. L.; Fox, D. J.; Keith, T.; Al-Laham, M. A.; Peng, C. Y.; Nanayakkara, A.; Gonzalez, C.; Challacombe, M.; Gill, P. M. W.; B. Johnson, W. C.; Wong, M. W.; Andres, J. L.; Gonzalez, C.; Head-Gordon, M.; Replogle, E. S.; Pople, J. A. *Gaussian 98*, Gaussian, Inc.: Pittsburgh PA, 1998.

35. Frisch, M. J.; Trucks, G. W.; Schlegel, H. B.; Scuseria, G. E.; Robb, M. A.; Cheeseman, J. R.; Montgomery, J. A.; Vreven, T.; Kudin, K. N.; Burant, J. C.; Millam, J. M.; Iyengar, S. S.; Tomasi, J.; Barone, V.; Mennucci, B.; Cossi, M.; Scalmani, G.; Rega, N.; Petersson, G. A.; Nakatsuji, H.; Hada, M.; Ehara, M.; Toyota, K.; Fukuda, R.; Hasegawa, J.; Ishida, M.; Nakajima, T.; Honda, Y.; Kitao, O.; Nakai, H.; Klene, M.; Li, X.; Knox, J. E.; Hratchian, H. P.; Cross, J. B.; Adamo, C.; Jaramillo, J.; Gomperts, R.; Stratmann, R. E.; Yazyev, O.; Austin, A. J.; Cammi, R.; Pomelli, C.; Ochterski, J. W.; Ayala, P. Y.; Morokuma, K.; Voth, G. A.; Salvador, P.; Dannenberg, J. J.; Zakrzewski, V. G.; Dapprich, S.; Daniels, A. D.; Strain, M. C.; Farkas, O.; Malick], D. K.; Rabuck, A. D.; Raghavachari, K.; Foresman], J. B.; Ortiz, J. V.; Cui, Q.; Baboul, A. G.; Clifford, S.; Cioslowski, J.; Stefanov, B. B.; Liu, G.; Liashenko, A.; Piskorz, P.; Komaromi, I.; Martin, R. L.; Fox, D. J.; Keith, T.; Al-Laham, M. A.; Peng, C. Y.; Nanayakkara, A.; Challacombe, M.; Gill, P. M.

W.; Johnson, B.; Chen, W.; Wong, M. W.; Gonzalez, C.; Pople, J. A. *Gaussian 03*, Gaussian, Inc.: Wallingford CT, 2004.

36. Claeson, S.; Langer, V.; Allenmark, S., *Chirality* **2000,** 12, (2), 71-75.

37. Lesser, R.; Weiss, R., *Ber. Dtsch. Chem. Ges.* **1914,** 47, 2510-25.

38. Dahlen, B.; Lindgren, B., *Acta Chem. Scand.* **1973,** 27, (6), 2218-20.

39. Ohno, F.; Kawashima, T.; Okazaki, R., *Chem. Commun.* **2001**, (5), 463-464.

40. Zhang, J.; Takahashi, S.; Saito, S.; Koizumi, T., *Tetrahedron: Asymmetry* **1998,** 9, (18), 3303-3317.

41. Drabowicz, J.; Luczak, J.; Mikolajczyk, M.; Yamamoto, Y.; Matsukawa, S.; Akiba, K.-Y., *Chirality* **2004,** 16, (9), 598-601.

42. Drabowicz, J.; Luczak, J.; Mikolajczyk, M.; Yamamoto, Y.; Matsukawa, S.; Akiba, K.-y., *Tetrahedron: Asymmetry* **2002,** 13, (19), 2079-2082.

43. Testa, B., *Principles of Organic Stereochemistry*. Marcel Dekker: New York, 1979.

44. Nasipuri, D., *Stereochemistry of Organic Compounds*. Wiley Eastern Limited: New Delhi, 1991.

45. Cahn, R. S.; Ingold, C.; Prelog, V., *Angew. Chem., Intern. Ed. Engl.* **1966,** 5, (4), 385-415.

46. Martin, J. C.; Balthazor, T. M., *J. Am. Chem. Soc.* **1977,** 99, (1), 152-62.

47. Gati, T.; Toth, G.; Drabowicz, J.; Moeller, S.; Hofer, E.; Polavarapu, P.; Duddeck, H., *Chirality* **2005,** 17, (Suppl.), S40-S47.

48. Bakiler, M.; Maslov, I. V.; Akyuz, S., *J. Mol. Struct.* **1999,** 476, (1-3), 21-26.

49. Douglas, B., *ACS Symp. Ser.* **1994,** 565, (Coordination Chemistry), 273-85.

50. Coe, B.; Curati, N., *Comments Inorg. Chem.* **2004,** 25, (5-6), 147-184.

51. Clerac, R.; Cotton, F. A.; Dunbar, K. R.; Lu, T.; Murillo, C. A.; Wang, X., *J. Am. Chem. Soc.* **2000,** 122, (10), 2272-2278.

52. Clerac, R.; Cotton, F. A.; Daniels, L. M.; Dunbar, K. R.; Kirschbaum, K.; Murillo, C. A.; Pinkerton, A. A.; Schultz, A. J.; Wang, X., *J. Am. Chem. Soc.* **2000,** 122, (26), 6226-6236.

53. Clerac, R.; Cotton, F. A.; Dunbar, K. R.; Murillo, C. A.; Pascual, I.; Wang, X., *Inorg. Chem.* **1999,** 38, (11), 2655-2657.

54. Aduldecha, S.; Hathaway, B., *J. Chem. Soc., Dalton Trans.* **1991**, (4), 993-8.

55. Hurley, T. J.; Robinson, M. A., *Inorg. Chem.* **1968,** 7, (1), 33-8.

56. Cotton, F. A.; Murillo, C. A., *Eur. J. Inorg. Chem.* **2006**, (21), 4209-4218.

57. Chae, D.-H.; Berry, J. F.; Jung, S.; Cotton, F. A.; Murillo, C. A.; Yao, Z., *Nano Lett.* **2006,** 6, (2), 165-168.

58. Berry, J. F., Extended Metal Atom Chains. In *Multiple Bonds Between Metal Atoms*, Cotton, F. A.; Murillo, C. A.; Walton, R. A., Eds. Springer Science and Business Media, Inc.: New York, 2005; pp 669-706.

59. Berry, J. F.; Cotton, F. A.; Lu, T.; Murillo, C. A.; Wang, X., *Inorg. Chem.* **2003,** 42, (11), 3595-3601.

60. Warnke, M. M.; Cotton, F. A.; Armstrong, D. W., *Chirality* **2007,** 19, (3), 179-183.

61. Polavarapu, P. L.; He, J.; Crassous, J.; Ruud, K., *ChemPhysChem* **2005,** 6, (12), 2535-2540.

62. Hay, P. J.; Wadt, W. R., *J. Chem. Phys.* **1985,** 82, (1), 270-83.

63. Shriver, D.; Atkins, P., *Inorganic Chemistry*. 3rd ed.; W.H. Freeman and Company: New York, 1999.

64. Bauernschmitt, R.; Ahlrichs, R., *Chem. Phys. Lett.* **1996,** 256, (4,5), 454-464.

65. Koumura, N.; Zijistra, R. W. J.; Van Delden, R. A.; Harada, N.; Feringa, B. L., *Nature (London)* **1999,** 401, (6749), 152-155.

66. Fujita, T.; Kuwahara, S.; Harada, N., *Eur. J. Org. Chem.* **2005**, (21), 4533-4543.

67. Bao, J.; Wulff, W. D.; Dominy, J. B.; Fumo, M. J.; Grant, E. B.; Rob, A. C.; Whitcomb, M. C.; Yeung, S.-M.; Ostrander, R. L.; Rheingold, A. L., *J. Am. Chem. Soc.* **1996,** 118, (14), 3392-405.

68. Becker, J. J.; White, P. S.; Gagne, M. R., *Organometallics* **2003,** 22, (16), 3245-3249.

69. Yu, S.; Rabalakos, C.; Mitchell, W. D.; Wulff, W. D., *Org. Lett.* **2005,** 7, (3), 367-369.

70. Heller, D. P.; Goldberg, D. R.; Wulff, W. D., *J. Am. Chem. Soc.* **1997,** 119, (43), 10551-10552.

71. Heller, D. P.; Goldberg, D. R.; Wu, H.; Wulff, W. D., *Can. J. Chem.* **2006,** 84, (10), 1487-1503.

72. Xue, S.; Yu, S.; Deng, Y.; Wulff, W. D., *Angew. Chem., Int. Ed.* **2001,** 40, (12), 2271-2274.

73. Antilla, J. C.; Wulff, W. D., *J. Am. Chem. Soc.* **1999,** 121, (21), 5099-5100.

74. Antilla, J. C.; Wulff, W. D., *Angew. Chem., Int. Ed.* **2000,** 39, (24), 4518-4521.

75. Loncaric, C.; Wulff, W. D., *Org. Lett.* **2001,** 3, (23), 3675-3678.

76. Zhang, Y.; Yeung, S.-M.; Wu, H.; Heller, D. P.; Wu, C.; Wulff, W. D., *Org. Lett.* **2003,** 5, (11), 1813-1816.

77. Yamamoto, K.; Noda, K.; Okamoto, Y., *J. Chem. Soc., Chem. Commun.* **1985**, (16), 1065-6.

78. Yamamura, K.; Ono, S.; Ogoshi, H.; Masuda, H.; Kuroda, Y., *Synlett* **1989**, (1), 18-19.

79. Koike, N.; Hattori, T.; Miyano, S., *Tetrahedron: Asymmetry* **1994,** 5, (10), 1899-900.

80. Toda, F.; Tanaka, K.; Stein, Z.; Goldberg, I., *J. Org. Chem.* **1994,** 59, (19), 5748-51.

81. Hattori, T.; Sakurai, K.; Koike, N.; Miyano, S.; Goto, H.; Ishiya, F.; Harada, N., *J. Am. Chem. Soc.* **1998,** 120, (35), 9086-9087.

82. Solladie-Cavallo, A.; Marsol, C.; Pescitelli, G.; Di Bari, L.; Salvadori, P.; Huang, X.; Fujioka, N.; Berova, N.; Cao, X.; Freedman, T. B.; Nafie, L. A., *Eur. J. Org. Chem.* **2002**, (11), 1788-1796.

83. Schettino, V.; Neto, N.; Califano, S., *J. Chem. Phys.* **1966,** 44, (7), 2724-34.

84. Schettino, V., *J. Chem. Phys.* **1967,** 46, (1), 302-8.

85. Bree, A.; Solven, F. G.; Vilkos, V. V. B., *J. Mol. Spectrosc.* **1972,** 44, (2), 298-319.

86. Godec, J.; Colombo, L., *J. Chem. Phys.* **1976,** 65, (11), 4693-700.

87. Cannon, C. G.; Sutherland, G. B. B. M., *Spectrochim. Acta* **1951,** 4, 373-95.

88. Cane, E.; Miani, A.; Palmieri, P.; Tarroni, R.; Trombetti, A., *Spectrochim. Acta, Part A* **1997,** 53A, (11), 1839-1851.

89. Langhoff, S. R., *J. Phys. Chem.* **1996,** 100, (8), 2819-41.

90. Martin, J. M. L.; El-Yazal, J.; Francois, J.-P., *J. Phys. Chem.* **1996,** 100, (38), 15358-15367.

91. Jaffe, H. H.; Orchin, M., *Theory and Applications of Ultraviolet Spectroscopy*. John Wiley and Sons: New York, 1962.

92. Hochstrasser, R. M.; Small, G. J., *J. Chem. Phys.* **1966,** 45, (6), 2270-84.

93. Platt, J. R., *J. Chem. Phys.* **1949,** 17, 484-95.

94. Klevens, H. B.; Platt, J. R., *J. Chem. Phys.* **1949,** 17, 470-81.

95. Harada, N.; Hattori, T.; Suzuki, T.; Okamura, A.; Ono, H.; Miyano, S.; Uda, H., *Tetrahedron: Asymmetry* **1993,** 4, (8), 1789-92.

96. Gottarelli, G.; Proni, G.; Spada, G. P.; Fabbri, D.; Gladiali, S.; Rosini, C., *J. Org. Chem.* **1996,** 61, (6), 2013-19.

97. Superchi, S.; Giorgio, E.; Rosini, C., *Chirality* **2004,** 16, (7), 422-451.

98. Galwas, P. A. Ph.D. Thesis. University of Cambridge, Cambridge, 1983.

99. Buckingham, A. D.; Fowler, P. W.; Galwas, P. A., *Chem. Phys.* **1987,** 112, (1), 1-14.

100. Stephens, P. J., *J. Phys. Chem.* **1985,** 89, (5), 748-52.

101. Polavarapu, P. L., *Chirality* **2003,** 15, (3), 284-285.

102. Bak, K. L.; Hansen, A. E.; Ruud, K.; Helgaker, T.; Olsen, J.; Joergensen, P., *Theor. Chim. Acta* **1995,** 90, (5/6), 441-58.

103. Grimme, S., *Chem. Phys. Lett.* **1996,** 259, (1,2), 128-137.

104. Pecul, M.; Ruud, K.; Helgaker, T., *Chem. Phys. Lett.* **2004,** 388, (1-3), 110-119.

105. Autschbach, J.; Ziegler, T.; van Gisbergen, S. J. A.; Baerends, E. J., *J. Chem. Phys.* **2002,** 116, (16), 6930-6940.

106. Pedersen, T. B.; Koch, H.; Ruud, K., *J. Chem. Phys.* **1999,** 110, (6), 2883-2892.

107. Diedrich, C.; Grimme, S., *J. Phys. Chem. A* **2003,** 107, (14), 2524-2539.

108. Furche, F.; Ahlrichs, R.; Wachsmann, C.; Weber, E.; Sobanski, A.; Voegtle, F.; Grimme, S., *J. Am. Chem. Soc.* **2000,** 122, (8), 1717-1724.

109. Stephens, P. J.; McCann, D. M.; Devlin, F. J.; Cheeseman, J. R.; Frisch, M. J., *J. Am. Chem. Soc.* **2004,** 126, (24), 7514-7521.

110. Price, C. P.; Matzger, A. J., *J. Org. Chem.* **2005,** 70, (1), 1-6.

111. Wang, F.; Polavarapu, P. L.; Drabowicz, J.; Kie-lbasinski, P.; Potrzebowski, M. J.; Miko-lajczyk, M.; Wieczorek, M. W.; Majzner, W. W.; Lazewska, I., *J. Phys. Chem. A* **2004,** 108, (11), 2072-2079.

112. Mikolajczyk, M.; Drabowicz, J.; Kielbasinski, P., *Chiral Sulfur Reagents: Applications in Asymmetric and Stereoselective Synthesis*. CRC Press: New York, 1997.

113. Metzner, P.; Thuillier, A., *Sulfur Reagents in Organic Synthesis*. Academic Press: London, 1994.

114. Satoh, T.; Kuramochi, Y.; Inoue, Y., *Tetrahedron Lett.* **1999,** 40, (50), 8815-8818.

115. Nakamura, S.; Yasuda, H.; Watanabe, Y.; Toru, T., *Tetrahedron Lett.* **2000,** 41, (21), 4157-4160.

116. Nakamura, S.; Watanabe, Y.; Toru, T., *J. Chem. Soc., Perkin Trans. 1* **1999**, (23), 3403-3404.

117. Cogan, D. A.; Liu, G.; Kim, K.; Backes, B. J.; Ellman, J. A., *J. Am. Chem. Soc.* **1998,** 120, (32), 8011-8019.

118. Owens, T. D.; Souers, A. J.; Ellman, J. A., *J. Org. Chem.* **2003,** 68, (1), 3-10.

119. Blum, S. A.; Bergman, R. G.; Ellman, J. A., *J. Org. Chem.* **2003,** 68, (1), 150-155.

120. Yuste, F.; Ortiz, B.; Carrasco, A.; Peralta, M.; Quintero, L.; Sanchez-Obregon, R.; Walls, F.; Garcia Ruano, J. L., *Tetrahedron: Asymmetry* **2000,** 11, (15), 3079-3090.

121. Colobert, F.; Tito, A.; Khiar, N.; Denni, D.; Medina, M. A.; Martin-Lomas, M.; Ruano, J.-L. G.; Solladie, G., *J. Org. Chem.* **1998,** 63, (24), 8918-8921.

122. Bravo, P.; Crucianelli, M.; Farina, A.; Meille, S. V.; Volonterio, A.; Zanda, M., *Eur. J. Org. Chem.* **1998**, (3), 435-440.

123. Senanayake, C. H.; Krishnamurthy, D.; Lu, Z.-H.; Han, Z.; Gallou, I., *Aldrichimica Acta* **2005,** 38, (3), 93-104.

124. Davis, F. A.; Chen, B.-C., *Chem. Soc. Rev.* **1998,** 27, (1), 13-18.

125. Evans, D. A.; Faul, M. M.; Colombo, L.; Bisaha, J. J.; Clardy, J.; Cherry, D., *J. Am. Chem. Soc.* **1992,** 114, (15), 5977-85.

126. Davis, F. A.; Liu, H.; Zhou, P.; Fang, T.; Reddy, G. V.; Zhang, Y., *J. Org. Chem.* **1999,** 64, (20), 7559-7567.

127. Pei, D.; Wang, Z.; Wei, S.; Zhang, Y.; Sun, J., *Org. Lett.* **2006,** 8, (25), 5913-5915.

128. Ellman, J. A., *Pure Appl. Chem.* **2003,** 75, (1), 39-46.

129. Davis, F. A.; Reddy, R. E.; Szewczyk, J. M.; Reddy, G. V.; Portonovo, P. S.; Zhang, H.; Fanelli, D.; Reddy, T.; Zhou, P.; Carroll, P. J., *J. Org. Chem.* **1997,** 62, (8), 2555-2563.

130. Davis, F. A.; Fanelli, D. L., *J. Org. Chem.* **1998,** 63, (6), 1981-1985.

131. Davis, F. A.; Szewczyk, J. M., *Tetrahedron Lett.* **1998,** 39, (33), 5951-5954.

132. Davis, F. A.; Szewczyk, J. M.; Reddy, R. E., *J. Org. Chem.* **1996,** 61, (6), 2222-5.

133. Lefebvre, I. M.; Evans, S. A., Jr., *J. Org. Chem.* **1997,** 62, (22), 7532-7533.

134. Mikolajczyk, M.; Lyzwa, P.; Drabowicz, J., *Tetrahedron: Asymmetry* **1997,** 8, (24), 3991-3994.

135. Han, Z.; Krishnamurthy, D.; Pflum, D.; Grover, P.; Wald, S. A.; Senanayake, C. H., *Org. Lett.* **2002,** 4, (23), 4025-4028.

136. Moreau, P.; Essiz, M.; Merour, J.-Y.; Bouzard, D., *Tetrahedron: Asymmetry* **1997,** 8, (4), 591-598.

137. Clennan, E. L.; Chen, M.-F.; Greer, A.; Jensen, F., *J. Org. Chem.* **1998,** 63, (10), 3397-3402.

138. Bharatam, P. V.; Amita; Kaur, D., *J. Phys. Org. Chem.* **2002,** 15, (4), 197-203.

139. Moree, W. J.; van der Marel, G. A.; Liskamp, R. J., *J. Org. Chem.* **1995,** 60, (16), 5157-69.

140. Liu, G.; Cogan, D. A.; Ellman, J. A., *J. Am. Chem. Soc.* **1997,** 119, (41), 9913-9914.

141. Liu, G.; Cogan, D. A.; Owens, T. D.; Tang, T. P.; Ellman, J. A., *J. Org. Chem.* **1999,** 64, (4), 1278-1284.

142. Dragoli, D. R.; Burdett, M. T.; Ellman, J. A., *J. Am. Chem. Soc.* **2001,** 123, (41), 10127-10128.

143. Weix, D. J.; Ellman, J. A., *Org. Lett.* **2003,** 5, (8), 1317-1320.

144. Qin, Y.; Wang, C.; Huang, Z.; Xiao, X.; Jiang, Y., *J. Org. Chem.* **2004,** 69, (24), 8533-8536.

145. Huang, Z.; Zhang, M.; Wang, Y.; Qin, Y., *Synlett* **2005**, (8), 1334-1336.

146. Berthod, A.; Xiao, T. L.; Liu, Y.; Jenks, W. S.; Armstrong, D. W., *J. Chromatogr.* **2002,** 955, (1), 53-69.

147. Petrovic, A. G.; He, J.; Polavarapu, P. L.; Xiao, L. S.; Armstrong, D. W., *Org. Biomol. Chem.* **2005,** 3, (10), 1977-1981.

148. Wong, M. W., *Chem. Phys. Lett.* **1996,** 256, (4,5), 391-399.

149. Giorgio, E.; Minichino, C.; Viglione, R. G.; Zanasi, R.; Rosini, C., *J. Org. Chem.* **2003,** 68, (13), 5186-5192.

150. Tanaka, M.; Aida, M., *Chem. Phys. Lett.* **2006,** 417, (4-6), 316-319.

151. Wang, F.; Polavarapu, P. L.; Drabowicz, J.; Mikolajczyk, M., *J. Org. Chem.* **2000,** 65, (22), 7561-7565.

152. Wang, F.; Polavarapu, P. L.; Drabowicz, J.; Mikolajczyk, M.; Lyzwa, P., *J. Org. Chem.* **2001,** 66, (26), 9015-9019.

153. Wang, F.; Wang, Y.; Polavarapu, P. L.; Li, T.; Drabowicz, J.; Pietrusiewicz, K. M.; Zygo, K., *J. Org. Chem.* **2002,** 67, (18), 6539-6541.

154. Nudelman, A.; Cram, D. J., *J. Amer. Chem. Soc.* **1968,** 90, (14), 3869-70.

155. Gamble, M. P.; Studley, J. R.; Wills, M., *Tetrahedron Lett.* **1996,** 37, (16), 2853-6.

156. Burns, B.; Gamble, M. P.; Simm, A. R. C.; Studley, J. R.; Alcock, N. W.; Wills, M., *Tetrahedron: Asymmetry* **1997,** 8, (1), 73-78.

157. Li, K.; Zhou, Z.; Wang, L.; Zhou, Q.; Tang, C., *Main Group Met. Chem.* **2002,** 25, (11), 663-667.

158. Li, K.; Zhou, Z.; Wang, L.; Chen, Q.; Zhao, G.; Zhou, Q.; Tang, C., *Tetrahedron: Asymmetry* **2003,** 14, (1), 95-100.

159. Harger, M. J. P., *J. Chem. Soc., Chem. Commun.* **1976**, (14), 555-6.

160. Sorensen, M. D.; Blaehr, L. K. A.; Christensen, M. K.; Hoyer, T.; Latini, S.; Hjarnaa, P.-J. V.; Bjorkling, F., *Bioorg. Med. Chem.* **2003,** 11, (24), 5461-5484.

161. Chan, M. F.; Verner, E. J. US Patent: Phosphoramidates, phosphinic amides and related compounds and the use thereof to modulate the activity of endothelin. Patent #: 5958905. 1999.

162. Lin, T. S.; Cai, G. L.; Sartorelli, A. C., *Nucleosides Nucleotides* **1988,** 7, (3), 403-8.

163. Drabowicz, J.; Lopusinski, A.; Mikolajczyk, M.; Polavarapu, P. L., *Manuscript to be submitted.*

164. He, J.; Polavarapu, P. L., *J. Chem. Theory Comput.* **2005,** 1, (3), 506-514.

165. Kuppens, T.; Herrebout, W.; van der Veken, B.; Bultinck, P., *J. Phys. Chem. A* **2006,** 110, (34), 10191-10200.

166. Chen, J. S.; Shirts, R. B., *J. Phys. Chem. A* **1985,** 89, (9), 1643-6.

167. Chen, J.-S.; Wu, C.-C.; Kao, D.-Y., *Spectrochim. Acta, Part A* **2004,** 60A, (10), 2287-2293.

168. *PeakFit (version 4.11)*, Aspire Software International: Ashburn, VA.

169. *KaleidaGraph (version 3.09)*, Synergy Software: Reading, PA.

170. Stawinski, J., *Handbook of Organophosphorus Chemistry*. Marcel Dekker: New York, 1992.

171. Smith, H. E., Circular Dichroism of the Benzene Chromophore. In *Circular Dichroism: Principles and Applications*, Nakanishi, K.; Berova, N.; Woody, R. W., Eds. VCH Publisher, Inc.: New York, 1994; pp 413-442.

172. Smith, H. E.; Willis, T. C., *J. Amer. Chem. Soc.* **1971,** 93, (9), 2282-90.

173. Smith, H. E.; Fontana, L. P., *J. Org. Chem.* **1991,** 56, (1), 432-5.

174. Neugebauer, J.; Jan Baerends, E.; Nooijen, M.; Autschbach, J., *J. Chem. Phys.* **2005,** 122, (23), 234305/1-234305/7.

175. Moscowitz, A., *Tetrahedron* **1961,** 13, 48-56.

176. Emeis, C. A.; Oosterhoff, L. J.; De Vries, G., *Proc. R. Soc. London, Ser. A* **1967,** 297, (1448), 54-65.

177. Cassim, J. Y.; Yang, J. T., *Biochemistry* **1969,** 8, (5), 1947-51.

178. Cassim, J. Y.; Yang, J. T., *Biopolymers* **1970,** 9, (12), 1475-502.

179. Carver, J. P.; Shechter, E.; Blout, E. R., *J. Am. Chem. Soc.* **1966,** 88, (11), 2550-61.

180. DeTar, D. F., *Anal. Chem.* **1969,** 41, (11), 1406-8.

181. Krueger, W. C.; Pschigoda, L. M., *Anal. Chem.* **1971,** 43, (6), 675-7.

182. Gawronski, J.; Gawronska, K.; Rychlewska, U., *Tetrahedron Lett.* **1989,** 30, (44), 6071-4.

183. Gawronski, J.; Gawronska, K.; Skowronek, P.; Rychlewska, U.; Warzajtis, B.; Rychlewski, J.; Hoffmann, M.; Szarecka, A., *Tetrahedron* **1997,** 53, (17), 6113-6144.

184. Gawronski, J.; Skowronek, P., *Curr. Org. Chem.* **2004,** 8, (1), 65-82.

185. Gawronski, J.; Dlugokinska, A.; Grajewski, J.; Plutecka, A.; Rychlewska, U., *Chirality* **2005,** 17, (7), 388-395.

186. Polavarapu, P. L.; Zhao, C., *Chem. Phys. Lett.* **1998,** 296, (1,2), 105-110.

187. Polavarapu, P. L.; Ewig, C. S.; Chandramouly, T., *J. Am. Chem. Soc.* **1987,** 109, (24), 7382-6.

188. Rychlewska, U.; Warzajtis, B.; Hoffmann, M.; Rychlewski, J., *Molecules* **1997,** 2, (7), 106-113.

189. Buffeteau, T.; Ducasse, L.; Brizard, A.; Huc, I.; Oda, R., *J. Phys. Chem. A* **2004,** 108, (18), 4080-4086.

190. Moscowitz, A., *Optical Rotatory Dispersion*. McGraw Hill: New York, 1960.

191. Wilson, S. M.; Wiberg, K. B.; Cheeseman, J. R.; Frisch, M. J.; Vaccaro, P. H., *J. Phys. Chem. A* **2005,** 109, (51), 11752-11764.

192. Zhang, P.; Polavarapu, P. L., *J. Phys. Chem. A* **2007,** 111, (5), 858-871.

193. Shallenberger, R. S., *Advanced Sugar Chemistry*. AVI publishing Co.: Westport, 1982.

194. Binkley, R. W., *Modern Carbohydrate Chemistry*. Marcel Dekker: New York, 1988.

195. Stephens, E. S., Carbohydrates. In *Circular Dichroism and the Conformational Analysis of Biomolecules*, Fasman, G. D., Ed. Plenum: New York, 1996.

196. Harada, T.; Kuroda, R., *Chem. Lett.* **2002**, (3), 326-327.

197. Kuroda, R.; Harada, T.; Shindo, Y., *Rev. Sci. Instrum.* **2001,** 72, (10), 3802-3810.

198. Holzwarth, G.; Hsu, E. C.; Mosher, H. S.; Faulkner, T. R.; Moscowitz, A., *J. Amer. Chem. Soc.* **1974,** 96, (1), 251-2.

199. Barron, L. D.; Bogaard, M. P.; Buckingham, A. D., *J. Amer. Chem. Soc.* **1973,** 95, (2), 603-5.

200. Barron, L. D., *Molecular Light Scattering and Optical Activity*. 2nd ed.; Cambridge University Press: Cambridge, 2004.

201. Diem, M., *Introduction to Modern Vibrational Spectroscopy*. John Wiley & Sons: New York, 1993.

202. Polavarapu, P. L., *Vibrational Spectra: Principles and Applications with Emphasis on Optical Activity*. Elsevier: New York 1998.

203. Freedman, T. B.; Cao, X.; Dukor, R. K.; Nafie, L. A., *Chirality* **2003,** 15, (9), 743-758.

204. Andrushchenko, V.; Wieser, H.; Bour, P., *J. Phys. Chem. B* **2004,** 108, (12), 3899-3911.

205. Bour, P.; Keiderling, T. A., *THEOCHEM FIELD* **2004,** 675, (1-3), 95-105.

206. Stephens, P. J.; Devlin, F. J., *Chirality* **2000,** 12, (4), 172-179.

207. Marcott, C.; Havel, H. A.; Overend, J.; Moscowitz, A., *J. Am. Chem. Soc.* **1978,** 100, (22), 7088-9.

208. Back, D. M.; Polavarapu, P. L., *Carbohydr. Res.* **1984,** 133, (1), 163-7.

209. Paterlini, M. G.; Freedman, T. B.; Nafie, L. A., *J. Am. Chem. Soc.* **1986,** 108, (7), 1389-97.

210. Tummalapalli, C. M.; Back, D. M.; Polavarapu, P. L., *J. Chem. Soc., Faraday Trans. 1* **1988,** 84, (8), 2585-95.

211. Bose, P. K.; Polavarapu, P. L., *Carbohydr. Res.* **1999,** 319, (1-4), 172-183.

212. Bose, P. K.; Polavarapu, P. L., *Carbohydr. Res.* **1999,** 322, (1-2), 135-141.

213. Bose, P. K.; Polavarapu, P. L., *Carbohydr. Res.* **2000,** 323, (1-4), 63-72.

214. Taniguchi, T.; Monde, K.; Miura, N.; Nishimura, S.-I., *Tetrahedron Lett.* **2004,** 45, (46), 8451-8453.

215. Monde, K.; Taniguchi, T.; Miura, N.; Nishimura, S.-I., *J. Am. Chem. Soc.* **2004,** 126, (31), 9496-9497.

216. Barron, L. D.; Gargaro, A. R.; Wen, Z. Q.; MacNicol, D. D.; Butters, C., *Tetrahedron: Asymmetry* **1990,** 1, (8), 513-16.

217. Barron, L. D.; Gargaro, A. R.; Wen, Z. Q., *Carbohydr. Res.* **1991,** 210, 39-49.

218. Wen, Z. Q.; Barron, L. D.; Hecht, L., *J. Am. Chem. Soc.* **1993,** 115, (1), 285-92.

219. Bell, A. F.; Barron, L. D.; Hecht, L., *Carbohydr. Res.* **1994,** 257, (1), 11-24.

220. Bell, A. F.; Hecht, L.; Barron, L. D., *J. Am. Chem. Soc.* **1994,** 116, (12), 5155-61.

221. Bell, A. F.; Hecht, L.; Barron, L. D., *Spectrochim. Acta, Part A* **1995,** 51A, (8), 1367-78.

222. Bell, A. F.; Hecht, L.; Barron, L. D., *J. Raman Spectrosc.* **1995,** 26, (12), 1071-4.

223. Bose, P. K.; Polavarapu, P. L., *J. Am. Chem. Soc.* **1999,** 121, (25), 6094-6095.

224. Shanmugam, G.; Polavarapu, P. L., *Biophys. J.* **2004,** 87, (1), 622-630.

225. Shanmugam, G.; Polavarapu, P. L., *Biophys. Chem.* **2004,** 111, (1), 73-77.

226. Nafie, L. A., *Appl. Spectrosc.* **2000,** 54, (11), 1634-1645.

227. Szejtli, J., *Cyclodextrin Technology*. Kluwer Academic: Budapest, 1988.

228. Bell, A. F.; Hecht, L.; Barron, L. D., *Chem. Eur. J.* **1997,** 3, (8), 1292-1298.

229. Rottman, F. M., Biochemistry of Nucleic Acids II. In *International Review in Biochemistry* Clark, B. F. B., Ed. University Park Press: Baltimore, 1978; Vol. 17.

230. Rich, A.; Davies, D. R.; Crick, F. H. C.; Watson, J. D., *J. Mol. Biol.* **1961,** 3, 71-86.

231. Luzzati, V.; Mathis, A.; Masson, F.; Witz, J., *J. Mol. Biol.* **1964,** 10, (1), 28-41.

232. Casassas, E.; Tauler, R.; Marques, I., *Macromolecules* **1994,** 27, (7), 1729-37.

233. Applequist, J.; Damle, V., *J. Am. Chem. Soc.* **1966,** 88, (17), 3895-3900.

234. Leng, M.; Felsenfeld, G., *J. Mol. Biol.* **1966,** 15, (2), 455-66.

235. Fresco, J. R.; Klemperer, E., *Ann. N. Y. Acad. Sci.* **1959,** 81, (Art. 3), 730-41.

236. Holcomb, D. N.; Tinoco, I., Jr., *Biopolymers* **1965,** 3, (2), 121-33.

237. Warshaw, M. M.; Bush, C. A.; Tinoco, I., Jr., *Biochem. Biophys. Res. Commun.* **1965,** 18, (4), 633-7.

238. Sarkar, P. K.; Yang, J. T., *J Biol Chem* **1965,** 240, 2088-93.

239. Poland, D.; Vournakis, J. N.; Scheraga, H. A., *Biopolymers* **1966,** 4, (2), 223-35.

240. Michelson, A. M.; Ulbricht, T. L. V.; Emerson, T. R.; Swan, R. J., *Nature (London, U. K.)* **1966,** 209, (5026), 873-4.

241. Hashizume, H.; Imahori, K., *J. Biochem. (Tokyo)* **1967,** 61, (6), 738-49.

242. Brahms, J.; Michelson, A. M.; van Holde, K. E., *J. Mol. Biol.* **1966,** 15, (2), 467-88.

243. Van Holde, K. E.; Brahms, J.; Michelson, A. M., *J. Mol. Biol.* **1965,** 12, (3), 726-39.

244. Hruska, F. E.; Danyluk, S. S., *J. Amer. Chem. Soc.* **1968,** 90, (12), 3266-7.

245. Chan, S. I.; Nelson, J. H., *J. Amer. Chem. Soc.* **1969,** 91, (1), 168-83.

246. Lerner, D. B.; Kearns, D. R., *Biopolymers* **1981,** 20, (4), 803-16.

247. Fresco, J. R.; Doty, P., *J. Am. Chem. Soc.* **1957,** 79, 3928-9.

248. Stevens, C. L.; Rosenfeld, A., *Biochemistry* **1966,** 5, (8), 2714-21.

249. McDonald, C. C.; Phillips, W. D.; Penman, S., *Science (Washington, DC, U. S.)* **1964,** 144, (3623), 1234-7.

250. Brahms, J.; Mommaerts, W. F. H. M., *J. Mol. Biol.* **1964,** 10, (1), 73-88.

251. Brahms, J., *Nature* **1964,** 202, (4934), 797-8.

252. Saenger, W., *Principles of Nucleic Acid Structure*. Springer-Verlag: New York, 1984.

253. Holcomb, D. N.; Timasheff, S. N., *Biopolymers* **1968,** 6, (4), 513-29.

254. Adler, A. J.; Grossman, L.; Fasman, G. D., *Biochemistry* **1969,** 8, (9), 3846-59.

255. Zarudnaya, M. I., *Mol. Biol. (Translation of Molekulyarnaya Biologiya (Moscow))* **1998,** 32, (3), 417-422.

256. Janik, B.; Sommer, R. G.; Bobst, A. M., *Biochim. Biophys. Acta, Nucleic Acids Protein Synth.* **1972,** 281, (2), 152-68.

257. Maggini, R.; Secco, F.; Venturini, M.; Diebler, H., *J. Chem. Soc., Faraday Trans.* **1994,** 90, (16), 2359-63.

258. Self, B. D.; Moore, D. S., *Biophys. J.* **1997,** 73, (1), 339-347.

259. Gunzler, H.; Gremlich, H. U., *IR Spectroscopy*. Wiley-VCH: Weinheim, Germany, 2002.

260. Yang, L.; Keiderling, T. A., *Biopolymers* **1993,** 33, (2), 315-27.

261. Annamalai, A.; Keiderling, T. A., *J. Am. Chem. Soc.* **1987,** 109, (10), 3125-32.

262. Duchense, J., *Physiochemical Properties of Nucleic Acids*. Academic Press: New York, 1973.

263. Xiang, T.; Goss, D. J.; Diem, M., *Biophys. J.* **1993,** 65, (3), 1255-1261.

264. Andrushchenko, V.; Leonenko, Z.; Cramb, D.; van de Sande, H.; Wieser, H., *Biopolymers* **2001,** 61, (4), 243-60.

265. Evdokimov, Y. M.; Platonov, A. L.; Tikhonenko, A. S.; Varshavskii, Y. M., *FEBS (Fed. Eur. Biochem. Soc.) Lett.* **1972,** 23, (2), 180-4.

266. Westcott, C., *pH Measurements*. Academic Press: New York, 1978.

267. Petrovic, A. G.; Bose, P. K.; Polavarapu, P. L., *Carbohydr. Res.* **2004,** 339, (16), 2713-2720.

268. Shanmugam, G.; Polavarapu, P. L., *Appl. Spectrosc.* **2005,** 59, (5), 673-681.

269. Mueller, O.; Deuter, R. German Patent Application DE 95-19530132. 1997.

270. Maruyama, A.; Akaike, T.; Goto, T.; Yonemura, K. Japanese Patent 96-146825. 1998.

271. Lopez de la Paz, M.; Vicent, C.; Gonzalez, C., *Chem. Commun.* **2000**, (5), 411-412.

272. Mei, E.; Tang, J.; Vanderkooi, J. M.; Hochstrasser, R. M., *J. Am. Chem. Soc.* **2003,** 125, (9), 2730-2735.

273. Arnott, S.; Chandrasekaran, R.; Leslie, A. G. W., *J. Mol. Biol.* **1976,** 106, (3), 735-48.

274. Langridge, R.; Rich, A., *Nature* **1963,** 198, (4882), 725-8.

275. Broido, M. S.; Kearns, D. R., *J. Am. Chem. Soc.* **1982,** 104, (19), 5207-16.

276. Green, G.; Mahler, H. R., *Biochemistry* **1970,** 9, (2), 368-87.

277. Brahms, J., *J. Am. Chem. Soc.* **1963,** 85, 3298-300.

278. Brahms, J.; Maurizot, J. C.; Michelson, A. M., *J. Mol. Biol.* **1967,** 25, (3), 465-80.

279. Guschlbauer, W., *Proc. Natl. Acad. Sci. U. S. A.* **1967,** 57, (5), 1441-8.

280. Hartman, K. A., Jr.; Rich, A., *J. Am. Chem. Soc.* **1965,** 87, (9), 2033-9.

281. Chaly, T., Jr.; Montrel, M., *Biosens. Bioelectron.* **2000,** 15, (1-2), 93-98.

282. Helmkamp, G. K.; Ts'o, P. O. P., *Biochim. Biophys. Acta, Spec. Sect. Nucleic Acids Relat. Subj.* **1962,** 55, 601-8.

283. Causley, G. C.; Johnson, W. C., Jr., *Biopolymers* **1982,** 21, (9), 1763-80.

284. Antao, V. P.; Gray, D. M., *J. Biomol. Struct. Dyn.* **1993,** 10, (5), 819-39.

285. Adler, A. J.; Grossman, L.; Fasman, G. D., *Biochemistry* **1968,** 7, (11), 3836-43.

286. Fasman, G. D.; Lindblow, C.; Grossman, L., *Biochemistry* **1964,** 3, (8), 1015-21.

287. Ts'o, P. O. P.; Helmkamp, G. K.; Sander, C., *Biochim. Biophys. Acta, Spec. Sect. Nucleic Acids Relat. Subj.* **1962,** 55, 584-600.

288. Akinrimisi, E. O.; Sander, C.; Ts'o, P. O. P., *Biochemistry* **1963,** 2, (2), 340-4.

289. Tsuboi, M.; Takahashi, S.; Harada, I., *Physicochemical Properties of Nucleic Acids*. Academic Press: New York, 1973.

290. Tsuboi, M.; Kyogoku, Y.; Shimanouchi, T., *Biochim Biophys Acta* **1962,** 55, 1-12.

291. Florian, J.; Baumruk, V.; Leszczynski, J., *J. Phys. Chem. A* **1996,** 100, (13), 5578-89.

292. Liu, H.; Yu, B.; Guo, H.; Wu, J.; Xu, G., *Mikrochim. Acta* **1988,** 1, (1-6), 365-8.

293. Miles, H. T., *Proc. Natl. Acad. Sci. U. S. A.* **1961,** 47, 791-802.

294. Chou, C. H.; Thomas, G. J., Jr., *Biopolymers* **1977,** 16, (4), 765-89.

295. Maleev, V.; Semenov, M.; Kashpur, V.; Bolbukh, T.; Shestopalova, A.; Anishchenko, D., *J. Mol. Struct.* **2002,** 605, (1), 51-61.

296. Shimanouchi, T.; Tsuboi, M.; Kyogoku, Y., *Advances in Chemical Physics: The Structure and Properties of Biomolecules in Biological Systems*. Interscience Publishers: London, 1964.

297. O'Connor, T.; Johnson, C.; Scovell, W. M., *Biochim. Biophys. Acta, Nucleic Acids Protein Synth.* **1976,** 447, (4), 484-94.

298. Tsankov, D.; Krasteva, M.; Andrushchenko, V.; van de Sande, J. H.; Wieser, H., *Biophys. Chem.* **2006,** 119, (1), 1-6.

299. Annamalai, A.; Keiderling, T. A., *J. Am. Chem. Soc.* **1987,** 109, (10), 3125-3132.

300. Guschlbauer, W., *Nucleic Acids Res.* **1975,** 2, (3), 353-60.

301. Zarudnaya, M. I.; Samijlenko, S. P.; Potyahaylo, A. L.; Hovorun, D. M., *Nucleosides, Nucleotides Nucleic Acids* **2002,** 21, (2), 125-137.

302. O'Connor, T.; Scovell, W. M., *Biopolymers* **1981,** 20, (11), 2351-67.

303. Michelson, A. M.; Massoulie, J.; Guschlbauer, W., *Progress in Nucleic Acid Research and Molecular Biology*. Academic Press: New York, 1967.

304. Hartman, K. A.; Lord, R. C.; Thomas, G. J., *Physicochemical Properties of Nucleic Acids*. Academic Press: New York, 1973.

305. Petrovic, A. G.; Polavarapu, P. L., *Journal of Physical Chemistry B* **2005,** 109, (49), 23698-23705.

306. Salomaa, P.; Schaleger, L. L.; Long, F. A., *J. Am. Chem. Soc.* **1964,** 86, (1), 1-7.

307. Tsuboi, M.; Kyogoku, Y.; Shimanouchi, T., *Biochimica et biophysica acta* **1962,** 55, 1-12.

308. Miles, H. T., *Nature (London, U. K.)* **1959,** 183, 1814.

309. Gehring, K.; Leroy, J. L.; Gueron, M., *Nature* **1993,** 363, (6429), 561-4.

310. Kang, C. H.; Berger, I.; Lockshin, C.; Ratliff, R.; Moyzis, R.; Rich, A., *Proc Natl Acad Sci U S A* **1994,** 91, (24), 11636-40.

311. Berger, I.; Egli, M.; Rich, A., *Proc. Natl. Acad. Sci. U. S. A.* **1996,** 93, (22), 12116-12121.

312. Gellert, M. F.; Lipsett, M. N.; Davies, D. H., *Proc. Natl. Acad. Sci.* **1962,** 48, 2013-2018.

313. Zimmerman, S. B.; Cohen, G. H.; Davies, D. R., *Journal of Molecular Biology* **1975,** 92, (2), 181-192.

314. Arnott, S.; Chandrasekaran, R.; Marttila, C. M., *Biochem. J.* **1974,** 141, (2), 537-543.

315. Laughlan, G.; Murchie, A. I.; Norman, D. G.; Moore, M. H.; Moody, P. C.; Lilley, D. M.; Luisi, B., *Science* **1994,** 265, (5171), 520-524.

316. Phillips, K.; Dauter, Z.; Murchie, A. I. H.; Lilley, D. M. J.; Luisi, B., *Journal of Molecular Biology* **1997,** 273, (1), 171-182.

317. Lesnik, E. A.; Kochkina, I. M.; Tikhonenko, A. S.; Varshavskii, Y. M., *Molekulyarnaya Biologiya (Moscow)* **1980,** 14, (4), 820-829.

318. Lesnik, E. A.; Maslova, R. N.; Varshavskii Ia, M., *Molekuliarnaia biologiia* **1981,** 15, (1), 161-166.

319. Chantot, J. F.; Haertle, T.; Guschlbauer, W., *Biochimie* **1974,** 56, (4), 501-507.

320. Howard, F. B.; Frazier, J.; Miles, H. T., *Biopolymers* **1977,** 16, (4), 791-809.

321. Miles, H. T.; Frazier, J., *Biochimica et Biophysica Acta, Specialized Section on Biophysical Subjects* **1964,** 79, (1), 216-220.

322. Srivastava, S.; Srivastava, S.; Singh, S.; Gupta, V. D.; Gupta, V. P., *European Polymer Journal* **2002,** 39, (2), 341-354.

323. Simard, C.; Savoie, R., *Biopolymers* **1994,** 34, (1), 91-100.

324. Delabar, J. M.; Guschlbauer, W., *Biopolymers* **1979,** 18, (8), 2073-2089.

325. Yamada, A.; Akasaka, K.; Hatano, H., *Biopolymers* **1978,** 17, (3), 749-757.

326. Kononov, A. I.; Bakulev, V. M., *J. Photochem. Photobiol., B* **1996,** 34, (2-3), 211-216.

327. Chowdhury, S.; Bansal, M., *J. Phys. Chem. B* **2001,** 105, (31), 7572-7578.

328. Blackburn, E. H., *Nature* **1991,** 350, (6319), 569-573.

329. Sen, D.; Gilbert, W., *Nature* **1988,** 334, (6180), 364-366.

330. Sundquist, W. I.; Heaphy, S., *Proc. Natl. Acad. Sci. U. S. A.* **1993,** 90, (8), 3393-3397.

331. Arya, S. K.; Helser, T. L.; Carter, W. A.; Ts'o, P. O. P., *Mol. Pharmacol.* **1976,** 12, (5), 844-853.

332. Zhang, Z.; Fauser, U.; Schluesener, H. J., *NeuroReport* **2006,** 17, (15), 1579-1583.

333. Qi, H.; Lin, C.-P.; Fu, X.; Wood, L. M.; Liu, A. A.; Tsai, Y.-C.; Chen, Y.; Barbieri, C. M.; Pilch, D. S.; Liu, L. F., *Cancer Res.* **2006,** 66, (24), 11808-11816.

334. Sun, D.; Thompson, B.; Cathers, B. E.; Salazar, M.; Kerwin, S. M.; Trent, J. O.; Jenkins, T. C.; Neidle, S.; Hurley, L. H., *Journal of Medicinal Chemistry* **1997,** 40, (14), 2113-2116.

335. Ou, T.-M.; Lu, Y.-J.; Zhang, C.; Huang, Z.-S.; Wang, X.-D.; Tan, J.-H.; Chen, Y.; Ma, D.-L.; Wong, K.-Y.; Tang, J. C.-O.; Chan, A. S.-C.; Gu, L.-Q., *J. Med. Chem.* **2007,** 50, (7), 1465-1474.

336. Phan, A. T.; Kuryavyi, V.; Burge, S.; Neidle, S.; Patel, D. J., *J. Am. Chem. Soc.* **2007,** 129, (14), 4386-4392.

337. Kotlyar, A. B.; Borovok, N.; Molotsky, T.; Cohen, H.; Shapir, E.; Porath, D., *Adv. Mater.* **2005,** 17, (15), 1901-1905.

338. Keniry, M. A., *Biopolymers* **2001,** 56, (3), 123-146.

339. Fresco, J. R.; Massoulie, J., *J. Am. Chem. Soc.* **1963,** 85, 1352-1353.

340. Petrovic, A. G.; Polavarapu, P. L., *Journal of Physical Chemistry B* **2006,** 110, (45), 22826-22833.

341. Wang, F.; Zhao, C.; Polavarapu, P. L., *Biopolymers* **2004,** 75, (1), 85-93.

342. Sarkar, P. K.; Yang, J. T., *Biochemistry* **1965,** 4, (7), 1238-1244.

343. Brahms, J.; Sadron, C., *Nature* **1966,** 212, (5068), 1309-1312.

344. Cech, C. L.; Tinoco, I., Jr., *Nucleic Acids Res* **1976,** 3, (2), 399-404.

345. Chou, C. H.; Thomas, G. J., Jr.; Arnott, S.; Smith, P. J. C., *Nucleic Acids Res.* **1977,** 4, (7), 2407-2419.

346. Ulicny, J.; Ghomi, M.; Tomkova, A.; Miskovsky, P.; Chinsky, L.; Turpin, P. Y., *J. Raman Spectrosc.* **1994,** 25, (7-8), 507-514.

347. Rich, A., *Biochim. Biophys. Acta* **1958,** 29, 502-509.

348. Pan, B.; Shi, K.; Sundaralingam, M., *J. Mol. Biol.* **2006,** 363, (2), 451-459.

349. Hall, C. E., *Ann. N. Y. Acad. Sci.* **1959,** 81, (Art. 3), 723-729.

350. Hinz, H. J.; Haar, W.; Ackermann, T., *Biopolymers* **1970,** 9, (8), 923-936.

351. Srivastava, S.; Srivastava, S.; Khan, I. A.; Pandey, M. K.; Gupta, V. D., *Indian J. Biochem. Biophys.* **2004,** 41, (6), 311-321.

352. Simard, C.; Gaudreau, E.; Savoie, R., *Biopolymers* **1996,** 38, (3), 329-338.

353. Mukerji, I.; Sokolov, L.; Mihailescu, M.-R., *Biopolymers* **1998,** 46, (7), 475-487.

354. Small, E. W.; Peticolas, W. L., *Biopolymers* **1971,** 10, (1), 69-88.

355. Neumann, J. M.; Tran Dinh, S., *Biopolymers* **1981,** 20, (1), 89-109.

356. Thiele, D.; Guschlbauer, W., *Biophysik* **1973,** 9, (3), 261-277.

357. Salomaa, P.; Schaleger, L. L.; Long, F. A., *J. Am. Chem. Soc.* **1964,** 86, (1), 1-7.

358. Petrovic, A. G.; Polavarapu, P. L., *J. Phys. Chem. B* **2005,** 109, (49), 23698-23705.

359. Petrovic, A. G.; Polavarapu, P. L., *J. Phys. Chem. B* **2006,** 110, (45), 22826-22833.

360. Shanmugam, G.; Polavarapu, P. L., *J. Am. Chem. Soc.* **2004,** 126, (33), 10292-10295.

361. Zhao, C.; Polavarapu, P. L.; Das, C.; Balaram, P., *J. Am. Chem. Soc.* **2000,** 122, (34), 8228-8231.

362. Mahalakshmi, R.; Shanmugam, G.; Polavarapu, P. L.; Balaram, P., *ChemBioChem* **2005,** 6, (12), 2152-2158.

363. Krittanai, C.; Johnson, W. C., Jr., *Anal. Biochem.* **1997,** 253, (1), 57-64.

364. Lal, B. B.; Nafie, L. A., *Biopolymers* **1982,** 21, (11), 2161-83.

365. Sen, A. C.; Keiderling, T. A., *Biopolymers* **1984,** 23, (8), 1533-45.

366. Lipp, E. D.; Nafie, L. A., *Biopolymers* **1985,** 24, (5), 799-812.

367. Yasui, S. C.; Keiderling, T. A.; Bonora, G. M.; Toniolo, C., *Biopolymers* **1986,** 25, (1), 79-89.

368. Narayanan, U.; Keiderling, T. A.; Bonora, G. M.; Toniolo, C., *J. Am. Chem. Soc.* **1986,** 108, (9), 2431-7.

369. Pancoska, P.; Wang, L.; Keiderling, T. A., *Protein Sci.* **1993,** 2, (3), 411-19.

370. Pancoska, P.; Yasui, S. C.; Keiderling, T. A., *Biochemistry* **1989,** 28, (14), 5917-23.

371. Nafie, L. A.; Freedman, T. B., *Enantiomer* **1998,** 3, (4-5), 283-97.

372. Zhao, C.; Polavarapu, P. L., *Biospectroscopy* **1999,** 5, (5), 276-283.

373. Zhao, C.; Polavarapu, P. L., *J. Am. Chem. Soc.* **1999,** 121, (48), 11259-11260.

374. Zhao, C.; Polavarapu, P. L., *Biopolymers* **2001,** 62, (6), 336-340.

375. Keiderling, T. A., *Curr. Opin. Chem. Biol.* **2002,** 6, (5), 682-688.

376. Borics, A.; Murphy Richard, F.; Lovas, S., *Biopolymers* **2003,** 72, (1), 21-4.

377. Mazaleyrat, J.-P.; Wright, K.; Gaucher, A.; Toulemonde, N.; Wakselman, M.; Oancea, S.; Peggion, C.; Formaggio, F.; Setnicka, V.; Keiderling, T. A.; Toniolo, C., *J. Am. Chem. Soc.* **2004,** 126, (40), 12874-12879.

378. Taniguchi, T.; Miura, N.; Nishimura, S.-I.; Monde, K., *Mol. Nutr. Food Res.* **2004,** 48, (4), 246-254.

379. Xie, P.; Zhou, Q.; Diem, M., *J. Am. Chem. Soc.* **1995,** 117, (37), 9502-8.

380. Gulotta, M.; Goss, D. J.; Diem, M., *Biopolymers* **1989,** 28, (12), 2047-58.

381. Bour, P.; Keiderling, T. A., *J. Am. Chem. Soc.* **1993,** 115, (21), 9602-7.

382. Bour, P.; Sopkova, J.; Bednarova, L.; Malon, P.; Keiderling, T. A., *J. Comput. Chem.* **1997,** 18, (5), 646-659.

383. Bour, P.; Kubelka, J.; Keiderling, T. A., *Biopolymers* **2000,** 53, (5), 380-395.

384. Silva, R. A. G. D.; Kubelka, J.; Bour, P.; Decatur, S. M.; Keiderling, T. A., *Proc. Natl. Acad. Sci. U. S. A. FIELD Full Journal Title:Proceedings of the National Academy of Sciences of the United States of America* **2000,** 97, (15), 8318-8323.

385. Kubelka, J.; Keiderling, T. A., *J. Am. Chem. Soc.* **2001,** 123, (25), 6142-6150.

386. Hilario, J.; Kubelka, J.; Syud, F. A.; Gellman, S. H.; Keiderling, T. A., *Biopolymers* **2002,** 61, (3), 233-236.

387. Bour, P.; Keiderling, T. A., *J. Phys. Chem. B* **2005,** 109, (49), 23687-23697.

388. Kim, J.; Huang, R.; Kubelka, J.; Bour, P.; Keiderling, T. A., *J. Phys. Chem. B* **2006,** 110, (46), 23590-23602.

389. Kubelka, J.; Keiderling, T. A., *J. Am. Chem. Soc.* **2001,** 123, (48), 12048-12058.

390. King, W. T.; Zelano, A. J., *J. Chem. Phys.* **1967,** 47, (9), 3197-9.

391. Polavarapu, P. L., *J. Chem. Phys.* **1986,** 84, (1), 542-3.

392. Polavarapu, P. L., *Chem. Phys. Lett.* **1990,** 174, (5), 511-16.

393. Bour, P.; Kubelka, J.; Keiderling, T. A., *Biopolymers* **2002,** 65, (1), 45-59.

394. Csaszar, A. G.; Perczel, A., *Prog. Biophys. Mol. Biol.* **1999,** 71, (2), 243-309.

395. Polavarapu, P. L.; Zhao, C., *Fresenius' J. Anal. Chem.* **2000,** 366, (6-7), 727-734.

396. Xie, P.; Zhou, Q.; Diem, M., *Faraday Discuss* **1994**, (99), 233-43.

397. Wyssbrod, H. R.; Diem, M., *Biopolymers* **1992,** 32, (9), 1237-42.

398. Hilario, J.; Kubelka, J.; Keiderling, T. A., *J. Am. Chem. Soc.* **2003,** 125, (25), 7562-7574.

399. Mahalakshmi, R.; Sengupta, A.; Raghothama, S.; Shamala, N.; Balaram, P., *Biopolymers* **2007,** 88, (1), 36-54.

400. Karle, I. L.; Balaram, P., *Biochemistry* **1990,** 29, (29), 6747-56.

401. Toniolo, C.; Crisma, M.; Bonora, G. M.; Benedetti, E.; Di Blasio, B.; Pavone, V.; Pedone, C.; Santini, A., *Biopolymers* **1991,** 31, (1), 129-38.

402. Karle, I. L.; Flippen-Anderson, J. L.; Gurunath, R.; Balaram, P., *Protein Sci.* **1994,** 3, (9), 1547-55.

403. Mammi, S.; Rainaldi, M.; Bellanda, M.; Schievano, E.; Peggion, E.; Broxterman, Q. B.; Formaggio, F.; Crisma, M.; Toniolo, C., *J. Am. Chem. Soc.* **2000,** 122, (47), 11735-11736.

404. Tomasi, J.; Cammi, R.; Mennucci, B., *Int. J. Quantum Chem.* **1999,** 75, (4/5), 783-803.